

Sorbonne Université

Ecole Doctorale Astronomie et Astrophysique d'Ile-de-France

Thèse de doctorat

réalisée

à l'Institut d'Astrophysique de Paris

sous la direction de Kumiko Kotera

présentée par

Claire Guépin

CHASING THE COSMIC ACCELERATORS WITH HIGH ENERGY ASTROPARTICLES

Soutenue publiquement le **14 juin 2019**, devant un jury composé de :

Frédéric Daigne, Professeur - Sorbonne Université, Président du Jury

Marianne Lemoine-Goumard, Chargée de recherche CNRS - CENBG, Rapportrice

Francis Halzen, Hildale and Gregory Breit Professor - University of Wisconsin-Madison, Rapporteur

Sera Markoff, Associate Professor - University of Amsterdam, Examinatrice

Benoît Cerutti, Chargé de recherche CNRS - IPAG, Examineur

Kumiko Kotera, Chargée de recherche CNRS - IAP, Directrice de thèse

Acknowledgements

Kumiko, tu m'as transmis un souffle. Petit à petit, grâce à ton oeil aiguisé de chercheuse et ton soutien infaillible, je prends confiance. Les premiers rayons illuminent ce qui me semblait incompréhensible, et l'insurmontable se teinte de défi. Merci d'avoir été une fantastique directrice de thèse, merci de rendre la recherche si exceptionnelle et si belle.

Je tiens à remercier les relecteur et relectrice de cette thèse, Francis et Marianne, pour leurs suggestions et leurs encouragements, ainsi que Frédéric, Sera et Benoît pour leur présence et questions éclairantes lors de ma soutenance. Merci à Florence, Jacques et Thierry, et à toute l'école doctorale pour leur accompagnement. Je remercie aussi toutes celles et ceux qui m'ont accueillie à l'institut d'astrophysique de Paris, dans l'administration ou la recherche.

Au cours de cette thèse, j'ai pu aborder des sujets variés et passionnants, grâce aux projets et discussions partagées avec Kumiko, mais aussi Enrico, Ke et Kohta, Emmanuel, Joe, Lucia et Tanguy, et Benoît. Merci pour votre gentillesse et ces partages. En parallèle de projets plus théoriques, les collaborations GRAND et POEMMA m'ont ouvert de larges perspectives. Au sein de POEMMA, ce fut un plaisir travailler avec Angela, Fred et John, et de guider quelques temps Jacqueline et Ashley. Au sein de GRAND, Anne m'a ouvert la voie de la reconstruction radio ; merci pour tes explications et ta patience. Un GRAND merci à toute l'équipe APACHE, à Olivier, Anne et Nicolas, Matías et Simon qui nous ont rejoint, pour leur enthousiasme, les discussions chaleureuses, pleines des expériences et découvertes de demain. Merci Valentin, pour ces voyages souriants en ta compagnie, dans les chaises volantes, les hôtels spatiaux, en courant, en nageant, en survolant quelques rares erreurs de compilation.

J'ai eu la chance de pouvoir voyager au cours de ma thèse, grâce au soutien financier de l'ILP et de la fondation CFM, et de découvrir de nombreux instituts de recherche en France et à l'étranger : l'institut de planétologie et d'astrophysique de Grenoble, les universités Columbia et Princeton, l'université d'état de l'Ohio, l'école des mines du Colorado ; et surtout les universités de Chicago et de Penn State. Je remercie chaleureusement les chercheurs et chercheuses qui m'ont reçue au cours de ces visites. Je pense en particulier à Angela et Kohta, qui resteront pour moi deux grands modèles d'engagement scientifique. Ce fut également un plaisir de participer à des conférences, séminaires, écoles et rencontres, qui mettent en avant la convivialité et l'entraide, comme c'est le cas des Entretiens pulsars. J'ai pu y découvrir une science variée, des astroparticules et pulsars aux questions d'égalité et biais inconscients. J'espère sincèrement que dans un futur proche, tous les doctorants ainsi que toutes les doctorantes auront les moyens d'effectuer leur thèse dans d'aussi bonnes conditions, et d'être traité.e.s sur un pied d'égalité.

À l'institut, dans la solidarité et l'amitié, nous partageons chocolat, philosophie et science avec la même passion. Un immense merci à celles et ceux qui m'ont fait tant méditer et rire ces trois années, dans nos débats, nos questionnements et nos indignations égalitaires et écologiques, Adèle, Corentin, Gohar, Hugo. Sans oublier des anciens et ancienne, Alba, Jesse, Oscar, Tanguy, des nouveaux et nouvelles, Amaël, Raphaël, Sandrine, Shweta, Simon, et une pensée pour toutes celles et ceux avec qui j'ai pu échanger dans le respect et la bienveillance.

Sylvie, Jean, Raphaëlle, Julien, Damien, Françoise, Max, pas de nouvelle planète en vue mais toujours l'estime et l'humour. Vous donnez du sens à mes choix. Puis ces dernières années, les trébuchements, les émerveillements, les contradictions, les paysages intérieurs et montagneux grandioses, la neige puis le soleil, Paulin. Avec toi, je reste en équilibre sur l'horizon.

Contents

Acknowledgements	i
Introduction	1
1 The vibrant context of transient multi-messenger astronomy	3
1.1 The advent of a multi-messenger era	3
1.2 Acceleration and interaction processes	9
1.2.1 Particle acceleration, a delicate process	9
1.2.2 Inevitable interlink between acceleration and interactions	12
1.2.3 Numerical treatment of photohadronic interactions	19
1.3 Can we identify the cosmic accelerators?	20
2 Comparing explosive transients: the production of high-energy neutrino flares	23
2.1 Specificities of neutrino production in transients	24
2.2 Maximum accessible proton energy and indicative maximum neutrino energy . .	25
2.2.1 Acceleration process	25
2.2.2 Energy losses	26
2.2.3 Decay of secondaries and neutrino maximum energy	28
2.2.4 Results	29
2.3 Neutrino flux and detectability limit	31
2.3.1 Maximum neutrino flux	31
2.3.2 Minimum photon flux $\Phi_{\gamma,\min}$ for neutrino detectability	32
2.3.3 Can we detect a neutrino flare?	34
2.4 Implications for categories of transients and specific case studies	36
2.4.1 Census of existing transients	36
2.4.2 Case studies	41
2.4.3 From cosmic-ray to neutrino spectra	45
2.5 Discussion	51

2.5.1	Competing processes for neutrino production	51
2.5.2	Optically thick envelopes and choked flares	51
2.6	Conclusion	52
3	The acceleration of protons in pulsar magnetospheres	54
3.1	Particle extraction and magnetosphere generation	57
3.1.1	Initial electromagnetic fields and particle extraction	57
3.1.2	Energy losses and pair production	58
3.1.3	A parameter space to be explored	60
3.1.4	Structure of the magnetosphere	61
3.2	Particle acceleration and energy dissipation	63
4	Millisecond pulsars as pevatrons: multi-wavelength signatures in the galactic center region	70
4.1	Multi-wavelength observations of the galactic center	71
4.1.1	The galactic center region	71
4.1.2	The diffuse TeV emission	72
4.1.3	The diffuse GeV emission	73
4.2	Millisecond pulsars as pevatrons	74
4.3	Cosmic-ray spatial density distribution	76
4.3.1	Cosmic-ray density for a single source	76
4.3.2	Millisecond-pulsar distributions	77
4.3.3	Total cosmic-ray density	79
4.4	Diffuse gamma-ray emission	81
4.4.1	Uniform power-law cosmic-ray injection	82
4.4.2	Transient monoenergetic cosmic-ray injection	83
4.4.3	Bulge population of pulsars	85
4.5	Discussion	86
4.6	Conclusion	88
5	Tidal disruptions by massive black holes, as promising source candidates of ultra-high-energy cosmic rays and high-energy neutrinos	89
5.1	Interaction of UHE nuclei inside TDE jets	90
5.1.1	UHECR injection and energetics	91
5.1.2	Modeling the TDE spectral energy distribution	92
5.1.3	Interaction processes	92

5.2	UHECRs and neutrinos from single TDEs	95
5.3	Modeling the population of TDEs contributing to UHECR and neutrino fluxes .	97
5.3.1	TDE rate per galaxy	98
5.3.2	Identifying the black hole masses leading to observable TDEs	98
5.3.3	Relation between black hole mass and jet luminosity	99
5.3.4	Redshift evolution of the black hole mass function	100
5.4	Diffuse UHECR and neutrino fluxes from a TDE population	103
5.4.1	Final spectrum and composition of cosmic rays	104
5.4.2	Diffuse neutrino flux	107
5.5	Discussion and conclusion	107
6	Future detection and reconstruction challenges for very-high energy neutrinos and ultra-high energy cosmic rays	109
6.1	Towards space detection	110
6.1.1	General characteristics of space-based VHE neutrino detector	110
6.1.2	Effective field of view and sky exposure estimates	113
6.1.3	Strategy to achieve full sky coverage	118
6.1.4	Target of opportunity follow-up	120
6.1.5	Conclusion	121
6.2	Towards radio detection with a gigantic ground array	124
6.2.1	The X_{max} reconstruction procedure	126
6.2.2	Reconstruction performance	129
	Conclusion	132
	Acronyms	134
	Bibliography	135
	Abstract	157

Introduction

The most energetic phenomena of our universe produce extremely luminous bursts of particles, that can be observed with ground-based or satellite-borne telescopes, or other kinds of detectors such as radio antenna arrays, despite their tremendous distances from the Earth. They show a large diversity in luminosity and duration, and new classes of phenomena are regularly discovered. Over the past century, many intriguing astrophysical objects have been related to these energetic phenomena by the joint work of astronomers and astrophysicists, observers and theorists: dying massive stars, coalescing binary systems of compact dead stars, stars disrupted by the tidal forces when they approach massive black holes in the center of galaxies, for instance. However, they are so powerful that they cannot be reproduced in terrestrial laboratories, and so distant that the available information about them is most of the time very scarce. Many puzzles remain concerning their nature and properties.

Before the 20th century, astronomy was limited to the detection of optical photons. Progressively, fundamental advances in technologies made possible the detection of photons at various wavelengths and today radio, infrared, ultra-violet, X-ray and gamma-ray photons are observed with high-sensitivity instruments. Moreover, additional messengers coming from space were discovered. Cosmic rays, that are protons and nuclei coming from space, were progressively detected over a large energy range, up to ultra-high energies. Cosmic neutrinos, these scarcely interacting and nearly massless particles, were only detected at high-energies in 2013. Finally, the detection of space-time distortions, the so-called gravitational waves, was performed in 2015 as the result of several decades of technological challenges. The discovery of these multiple messengers marked a turning point in astrophysics, with the possibility of combining complementary information to better understand astrophysical phenomena: the 21st century has seen the advent of multi-messenger astronomy.

The fantastic energies of some of the detected messengers, and especially ultra-high-energy cosmic rays, but also gamma rays and high-energy neutrinos, link them naturally to energetic phenomena. They provide us with precious information about these phenomena, even if it is sometimes difficult to decipher the message that they are carrying. Indeed, the reconstruction of the direction, the energy, or the precise nature of the particle (especially for cosmic rays, if it is a proton or a nucleus) can be difficult due to the specific properties of the messengers and the detection techniques. In this context, the advent of time-domain astronomy open promising perspectives. The recent improvements of the time resolution of telescopes and detectors and the possibility of follow-up observations allow to study the time-dependency of energetic phenomena, but more importantly to combine more easily signals coming from one given source. A recent brilliant example was the joint detection of gravitational waves and photons across the entire electromagnetic spectrum from the neutron star merger GW170817. The future of multi-messenger and time-domain astronomy promises to be captivating.

Intense theoretical efforts are required to follow this sudden leap of observation techniques. In particular, the precise modeling of multi-messenger and contingently time-dependent emissions of energetic phenomena is essential. This requires a good knowledge of physical processes producing the multiple messengers, and especially the ones at the highest energies. Concretely,

as high-energy cosmic rays appear to play a key role in high-energy emissions, it is therefore crucial to understand how they get accelerated and how they produce the secondary high-energy photons and neutrinos that are observed. We underline some important properties of cosmic messengers, and present some basis of particle acceleration and interactions in chapter 1. Moreover, high-energy neutrinos appear as powerful probes for the acceleration and interaction of high-energy cosmic rays in astrophysical environments. Therefore it is of great interest to compare various kind of sources from the point of view of their high-energy neutrino emissions, a topic that is developed in chapter 2. To go further in the characterization of energetic phenomena, we explore theoretical aspects of cosmic ray acceleration and interactions with numerical simulations in chapter 3. From this, several observational signatures can be predicted, from a Galactic population of rapidly rotating and highly magnetized neutron stars in chapter 4, and from an extragalactic population of stars disrupted by massive black holes in chapter 5. Finally, we conclude in chapter 6 by discussing some observational challenges of future neutrino and cosmic-ray observatories, aiming at accessing yet unreached energy domains and improving the reconstruction of the particle properties. This journey across theoretical and observational markers of cosmic-ray acceleration and interactions, guided by ultra-high-energy cosmic rays, gamma rays and high-energy neutrinos, hopefully sheds more light on our understanding of cosmic accelerators.

Chapter 1

The vibrant context of transient multi-messenger astronomy

Astronomical observatories detect a plethora of energetic phenomena occurring in the Universe. These phenomena exhibit luminous electromagnetic emissions, sometimes at very-high energies. They are characterized by quiescent or transient emissions, and show diverse properties. In particular, transient emissions are short (up to months), violent, and irregular emissions, that occur sometimes in addition to a quiescent emission. With their improved sensitivity and time resolution together with the possibility of fast follow-up, current instruments allow the observation of Galactic and extragalactic transient phenomena (blazar flares, gamma-ray bursts, magnetar flares, superluminous supernovae, to cite but a few) over a wide energy range. These powerful bursts and flares have attracted the attention of the scientific community as they allow to study in great detail the time-dependency of energetic emissions and infer some properties concerning the underlying astrophysical sources and the physical phenomena at play, such as the acceleration, propagation, interaction and escape of particles related to the observed emissions. These energetic emissions are often related to the acceleration of leptonic particles (for instance electrons) and/or hadronic particles (for instance protons) within the source. In this case, the observed photon spectra are modeled by synchrotron radiation of leptons; hadrons are less frequently invoked, although they also lead to consistent pictures in specific cases, for example, for some blazars where leptons alone fail to provide a satisfactory explanation to the data (e.g., Oikonomou et al., 2014; Petropoulou et al., 2016a; Petropoulou et al., 2016b). Combined radio, optical, X-ray, or gamma-ray observations are a valuable source of information on the emission mechanisms, as they allow a precise comparison with the models.

1.1 The advent of a multi-messenger era

The recent advances in the detection of photons at multiple wavelengths, cosmic rays, neutrinos and gravitational-waves, and the combination of these complementary signals open promising perspectives for multi-messenger studies of energetic phenomena. At the highest energies, the levels of the detected gamma-ray, neutrino and cosmic-ray fluxes in $E^2 dN/dE dA d\Omega dt$ could suggest a potential common origin of these messengers from one source population, see figure 1.1. In this perspective, multi-messenger studies of energetic sources provide strong constraints on the source properties and emission mechanisms, so as not to overshoot one of the components. A particular attention should thus be paid to the development of messengers cascades and the production of secondary messengers: for instance, cosmic rays at the highest energies propagating in the extragalactic medium produce the so-called cosmogenic gamma rays and neutrinos. In the following, we will describe in more detail some important properties of the different messengers.

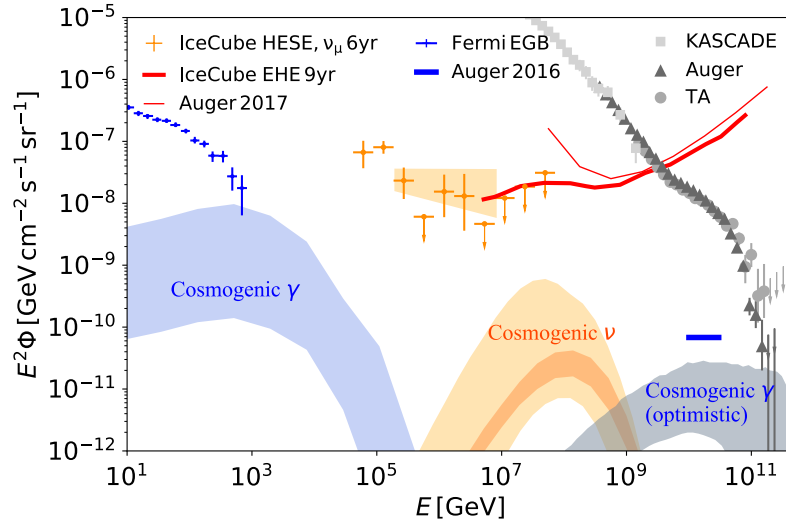


Figure 1.1: Gamma-ray, neutrino and cosmic-ray spectra, at the highest energies detected. From Alves Batista et al. (2019) and references therein. Overlaid are predictions of the cosmogenic gamma rays from the ultra-high-energy cosmic-ray flux, see text for more detail.

Photons are the historical astrophysical messengers. They can be considered as the most obvious messengers as we can detect them in the visible band with our eyes. The additional various wavelengths that we can observe today, from radio to gamma, bring complementary information about the Universe. We note that the observation techniques are very different depending on the photon energy. The interaction with the environment, such as the atmosphere, can alter a part of the signal, and thus some detections can only be made from the upper atmosphere or from space, which is the case for UV, X-ray, gamma-ray, and most of the infrared observations. Ground-based observatories focus mainly on radio detection, performed with antennas, and optical observations, performed with optical instruments. At the highest energies, photons can interact with the atmosphere and produce an extensive air shower, and can be indirectly detected. For instance, the Cherenkov signal produced by relativistic particles (in the UV) can be detected by Cherenkov telescopes like HESS in Namibia.

To study energetic phenomena, it is fundamental to detect high-energy photons as they provide important information about acceleration processes and radiation. The information given by photons at lower energies is also very important to unveil acceleration processes, but also to characterize the radiative background in the vicinity of the source, as they can lead to energy losses and interactions of accelerated particles. Non-thermal spectra, characterized by power-law spectra, are indicative of particle acceleration and give some information about the radiation processes at play. The example of Fermi acceleration is developed in section 1.2, showing how to particle acceleration can produce power-law particle spectra. As a consequence, the photons radiated by accelerated particles also have a power-law spectrum.

Cosmic rays are charged particles, primarily protons or nuclei, that constantly bombard the Earth. Since their discovery by Victor Hess at the beginning of the 20th century, these particles have been detected over a wide energy range. The first observation of an ultra-high-energy cosmic ray (UHECR) with energy above 10^{20} eV was only made in 1962 (Linsley, 1963). As illustrated in figure 1.2, the cosmic-ray flux decreases strongly with energy, which make their detection difficult at the highest energies. We receive approximately 1 particle/m² s at 10^{11} eV, 1 particle/m² yr at 10^{16} eV and 1 particle/km² yr at 10^{18} eV. Cosmic rays can be detected directly, by particle detectors located in space, for instance aboard the International Space Station. They

can also be detected indirectly, especially at high energies, by the detection of secondary particles produced when a cosmic ray interacts with the atmosphere, such as muons or photons. A census of the existing detectors for air-shower measurements is shown in figure 1.2. UHECR, that are currently detected by the Pierre Auger observatory (Pierre Auger Collaboration, 2015) and the Telescope Array experiment (Abu-Zayyad et al., 2012), are of particular interest as they give information about the most powerful accelerators of the Universe and about fundamental physics at energies that are yet unexplored. They reach energies 10^6 times higher than the maximum energies of individual protons produced in the Large Hadron Collider (LHC) and involve proton-proton interactions with center-of-mass energies up to 10^3 times higher than the ones obtained at LHC.

Cosmic rays below $\sim 10^{15}$ eV are thought to be of galactic origin, whereas cosmic rays above $\sim 10^{18}$ eV are thought to be of extragalactic origin (Abbasi et al., 2017; Aab et al., 2018). We note that above 10^{18} eV, cosmic rays cannot be confined in the Galaxy as their Larmor radii are comparable to the Galactic disc thickness for a Galactic magnetic field of $B \approx 3 \mu\text{G}$. The different features that appear on the cosmic-ray spectrum (see figure 1.2) can be related to a transition from Galactic to extragalactic populations of sources. In the most topical scenario, the maximum energy of Galactic accelerators induces a first transition at the knee, and the second knee is related to a transition to heavy primaries. The ankle marks the transition to an extragalactic population of accelerated particles. Finally, the high-energy cut-off of the cosmic-ray spectrum is thought to be due to inelastic interactions of UHECR with the cosmic microwave background, and is called the GZK cut-off (Zatsepin and Kuzmin, 1966; Greisen, 1966). This feature could also be related to a maximum rigidity of cosmic rays accelerated in extragalactic sources.

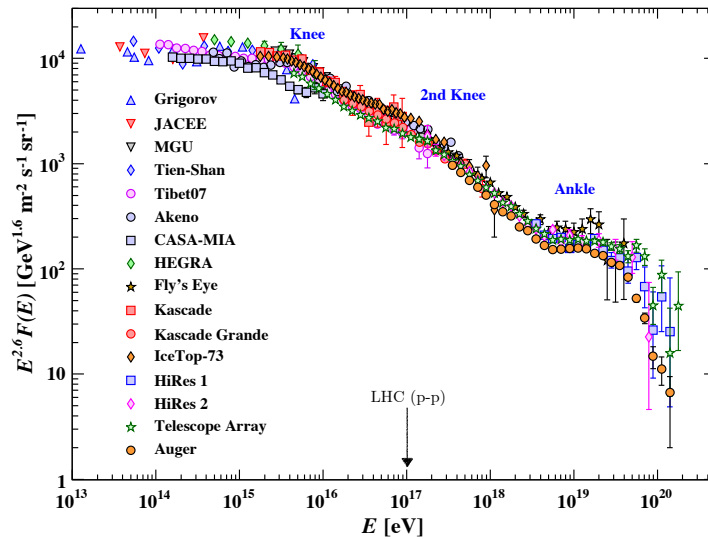


Figure 1.2: Cosmic-ray spectrum $E^{2.6}dN/dE$ as a function of energy, adapted from Tanabashi et al. (2018).

Historically, the ankle feature has also been interpreted as the marker of $p\gamma \rightarrow e^+ + e^-$ energy losses of protons interacting with the cosmic microwave background (Berezinsky and Zatsepin, 1969). However, this model has been weakened by composition measurements performed above 10^{18} eV by the Pierre Auger observatory, which found a composition becoming heavier above 2×10^{18} eV (Aab et al., 2016), see figure 1.3. The elementary composition of UHECR is encoded for instance in the atmospheric depth of the maximum development of the air shower that they initiate in the atmosphere, called X_{max} . Statistical reconstruction is performed by comparing the mean and standard deviation of the measured X_{max} distribution with simulation

outputs (Ostapchenko, 2011; Pierog et al., 2015a; Riehn et al., 2015). There is still some debate about this point as the Telescope Array experiment still finds data compatible with a proton composition below 10^{19} eV and with a mixed composition above.

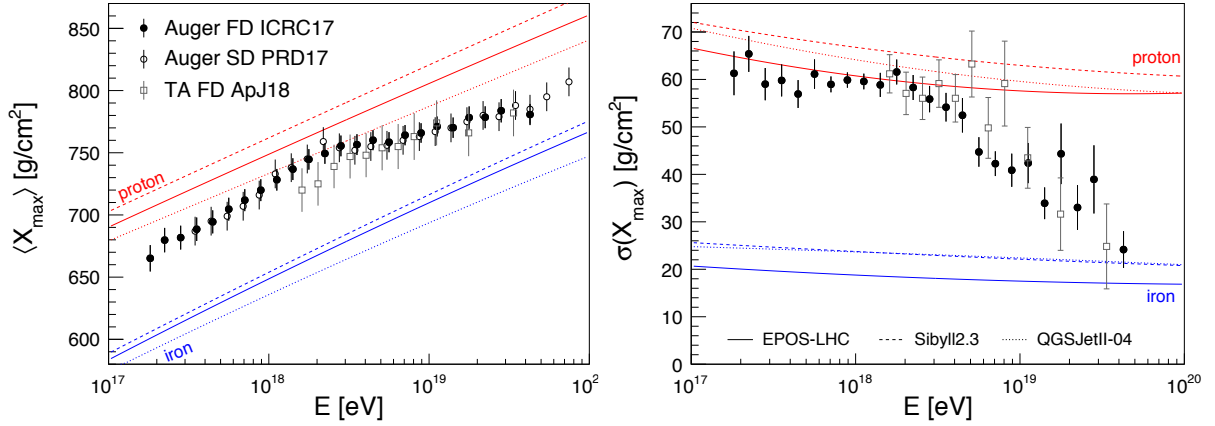


Figure 1.3: Mean and standard deviation of the distribution of shower maximum X_{\max} as a function of energy (respectively left and right), from Alves Batista et al. (2019), The Pierre Auger Collaboration et al. (2017), Bellido (2018), and Abbasi et al. (2018). The data points from the Pierre Auger Observatory and the Telescope Array experiment are shown with statistical and systematic uncertainties, and can be compared with simulation results of air showers initiated by proton and iron, respectively red and blue lines, for different hadronic interaction models (Ostapchenko, 2011; Pierog et al., 2015a; Riehn et al., 2015).

Before they reach the Earth, cosmic rays propagate in the interstellar and/or intergalactic medium. Because of their charge, they interact with the interstellar and intergalactic electromagnetic fields during their propagation, and are thus deflected from their initial direction. As our knowledge concerning the interstellar and intergalactic magnetic fields are limited, the reconstruction of the source direction is dire. Cosmic rays are thus of limited use for transient studies, but can provide useful information for diffuse flux studies about the flux, energy range and composition of particles accelerated in one source or a population of sources. In particular, several UHECR source models have been proposed in the literature, such as radio-loud active galactic nuclei (AGN), cluster accretion shocks for steady objects, gamma-ray bursts (GRB), fast-rotating neutron stars, or giant AGN flares for transient candidates (see, e.g., Kotera and Olinto, 2011 and references therein). Most of these models can successfully fit the observational data of the Auger and Telescope Array experiments for specific choices of astrophysical parameters. With the current set of data, however, there is no evidence that allows us to strongly favor one particular scenario over the others.

Neutrinos are fermions with no electric charge and very small masses. They only interact via the weak and gravitational interactions. They were originally predicted by Wolfgang Pauli in 1930 and observed only in 1956 by the experiment of Frederick Reines and Clyde Cowan. Nowadays, various experiments detect neutrinos over a wide energy range. To detect neutrinos, several experiments use the Cherenkov radiation emitted by the lepton produced by the interaction between a neutrino and water or ice. The detected neutrinos have one of the three leptonic flavors, electron, muon or tau, which are quantum superpositions of the three mass states. Therefore, when they propagate, they oscillate between different flavors.

Neutrinos are used to study various topics, from particle physics to astrophysics. They can be generated in nuclear reactors by nuclear fission, in the Sun by nuclear fusion, in supernovae by energy dissipation into neutrino-antineutrino pairs. The interaction of cosmic rays with

radiative or hadronic backgrounds can also produce neutrinos, for instance in the atmosphere, in various astrophysical sources accelerating particles, and during the propagation of UHECR in the intergalactic medium by their interaction on the cosmic microwave background and the extragalactic background light. High-energy neutrinos are expected to play a key role in multi-messenger studies of energetic phenomena as undeflected signatures of hadronic acceleration: the detection of neutrinos would be an (almost) unquestionable indicator of the acceleration of hadrons and of their interaction within the source environment, and the direction of the neutrino would allow to localize the source.

Neutrino astronomy started with the detection of solar neutrinos, and the detection of neutrinos from the supernova SN 1987A located in the Large Magellanic Cloud, by Kamiojande II, Irvine-Michigan-Brookhaven and Baksan detectors (Arnett et al., 1989). Gigantic detectors have been built to look for neutrinos at higher energies, such as the IceCube Neutrino Observatory in the south pole (Halzen and Klein, 2010), or ANTARES in the Mediterranean sea (Ageron et al., 2011) for instance. In 2013, IceCube started to detect cosmic neutrinos above 10^{13} eV (Aartsen et al., 2013a). This exciting discovery was made possible by the gigantic size of the detector, comprised of thousand of sensors deployed under the Antarctic ice over a cubic kilometer. This detection was also challenging because of the high atmospheric neutrino flux below 10^{14} eV and the muon background. Over 7 years of operation, IceCube has detected more than 100 cosmic neutrinos between 10^{13} eV and 10^{16} eV, for more than a million of atmospheric neutrinos. The flux of high-energy neutrinos detected by IceCube is illustrated in figure 1.4. A second-generation detector is being envisioned by the IceCube collaboration to enhance the sensitivity (The IceCube-Gen2 Collaboration et al., 2015).

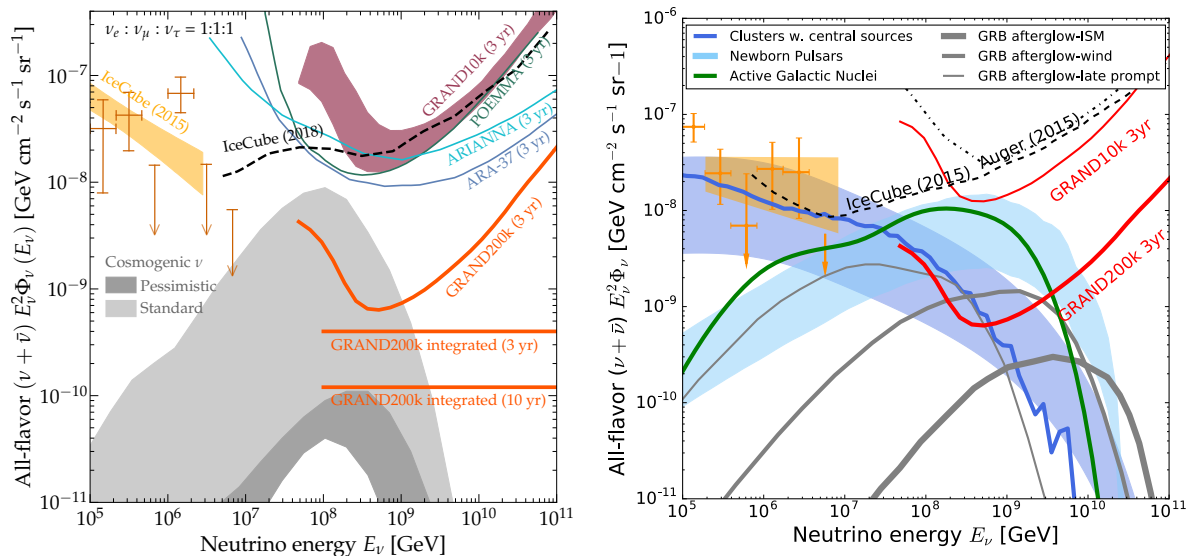


Figure 1.4: Predicted all-flavor very-high-energy (VHE) neutrino spectra for cosmogenic neutrinos (left) and neutrinos from source models (right). Overlaid are the high-energy (HE) neutrino flux detected by IceCube, and sensitivities of current and future experiments. From GRAND Collaboration et al. (2018).

In the same way as for UHECR, current observations and models do not allow yet to clearly identify the sources of high-energy neutrinos. The various UHECR source models predict associated high-energy neutrino fluxes that could be observed in the next decade by existing and future experiments. However, neutrinos are better suited than cosmic rays for transient studies, because they have no electric charge and are not deflected (thus not delayed) during their propagation. Over the past years, the IceCube collaboration has developed and enhanced methods for time-variable searches (e.g., Abbasi et al., 2012b; Abbasi et al., 2012a; Aartsen et al., 2013b; Aartsen et al., 2015). Several bright sources are being constantly monitored for flaring activities

(see Aartsen et al., 2015 for the latest public list). The very recent hint of a high-energy neutrino in coincidence with a blazar flare (IceCube Collaboration et al., 2018) confirms what has been expected for decades, namely that neutrino astronomy will reveal new and unique insights on the highest energy astrophysics in the universe, thus fully opening the multi-messenger window.

No neutrinos have been detected above 10^{16} eV. However, the interactions of UHECR during their propagation in the intergalactic medium are expected to produce neutrinos at very-high-energies Berezhinsky and Zatsepin (1969), Hill and Schramm (1985), and Engel et al. (2001), and the interactions of UHECR with radiative or hadronic backgrounds in cosmic accelerators are also expected to produce such neutrinos, see figure 1.4. These neutrinos could provide us with unprecedented insight into the cosmic ray acceleration processes, the distribution and evolution of the UHECR sources and the UHECR elementary composition Kotera et al. (2010). In particular, very-high-energy (VHE) neutrinos with energies above 10^{17} eV, provide a measure of UHECR sources beyond the GZK horizon of ~ 50 Mpc due to the minuscule neutrino interaction cross sections (see Block et al. (2014) for a recent calculation). IceCube has set significant limits on the flux of VHE neutrinos for $E_\nu \lesssim 10$ PeV. Auger observations extend these limits above ~ 500 PeV Zas and Pierre Auger Collaboration (2017) while the Antarctic Impulsive Transient Antenna (ANITA) experiment defines the limits above ~ 30 EeV Tanabashi et al., 2018, figure 29.10. These sensitivities only constrain the highest flux levels of the wide range of cosmogenic neutrino fluxes modeled for example by Kotera et al. (2010). Therefore, new projects emerge that aim at detecting these VHE neutrinos and increasing the sensitivity to UHECR, such as for instance the Giant Radio Array for Neutrino Detection (GRAND, GRAND Collaboration et al., 2018), the Probe of Extreme Multi-Messenger Astrophysics (POEMMA, Olinto, 2017) and the Antarctic Ross Ice-Shelf ANTenna Neutrino Array (ARIANNA, Barwick et al., 2015). As neutrino detection becomes even more challenging with increasing energy, ground-breaking detection techniques need to be developed, such as the radio detection or very-inclined air showers on the ground, or Cherenkov emissions from space. In the current context of multi-messenger astronomy, these observations will be decisive to identify the sources of the UHECR and VHE neutrinos and better understand the underlying high-energy astrophysics.

Gravitational waves are perturbations in the spacetime structure that are generated by accelerated objects and propagate at the speed of light. Predicted at the beginning of the 20th century by Henri Poincaré and Albert Einstein, they have only been detected indirectly in 1993 by Russell Hulse and Joseph Taylor, who studied the decay of the orbit of a binary star system (a pulsar and a neutron star). In 2015, thanks to the efforts deployed by the Laser Interferometer Gravitational-Wave Observatory (LIGO) and Virgo collaborations to build gigantic interferometers, the first direct detection of gravitational waves from a binary black hole merger was performed (Abbott et al., 2016b). Since then, several gravitational wave events have been detected for a binary black hole mergers and one binary neutron star merger (Abbott et al., 2017). A gravitational wave background related to the asymmetric explosions of supernovae is also expected. In the future, gigantic space interferometers, such as the Laser Interferometer Space Antenna (LISA, Amaro-Seoane et al., 2017; eLISA Consortium et al., 2013) will allow to explore other frequencies ranges and study for instance massive black hole binaries or cosmological inflation. Moreover, major efforts are being deployed to detect a stochastic gravitational-wave background with pulsar timing arrays (e.g. Foster and Backer, 1990; Verbiest et al., 2016).

Aside from further strengthening the success of general relativity, gravitational waves allow to explore strong gravity regimes and properties of compact objects. In particular, they can provide information about the populations of binary black holes, binary black hole and neutron star and binary neutron stars. They can be used as probes to evaluate the energies at play in the mergers of compact objects (e.g. Kotera and Silk, 2016). Moreover, as demonstrated by the observation of the binary neutron star merger GW170817, these events are of particular interest from a multi-

messenger point of view. GW170817 was detected with numerous electromagnetic counterparts across the spectrum, and has been also associated with a short gamma-ray burst. Neutron star mergers are also very promising sources for the production of HE neutrinos. Therefore, the study of correlations between gravitational wave and HE neutrino signals will certainly open interesting perspectives in the near future.

1.2 Acceleration and interaction processes

From this brief review of cosmic rays, neutrinos and gravitational waves properties, it appears that the messengers at the highest energies, and especially photons, high-energy cosmic rays and neutrinos, provide unique information about acceleration and interaction processes at play in energetic phenomena. Before going further, a closer look at acceleration and interaction models is therefore required.

1.2.1 Particle acceleration, a delicate process

The study of particle acceleration is crucial to understand energetic nonthermal radiation. A large variety of particle acceleration processes have been invoked in energetic sources, such as nonrelativistic or mildly relativistic shock acceleration (e.g., Bednarek and Idec, 2011; Metzger et al., 2015 and Bykov et al., 2012; Marcowith et al., 2016 for reviews), wake-field acceleration (Tajima and Dawson, 1979; Chen et al., 2002), or reacceleration in sheared jets (de Gouveia dal Pino and Lazarian, 2005; Giannios, 2010). Magnetic reconnection is a great favorite, however, for the modeling of explosive phenomena, that exhibit very rapid time variability and impulsive character (e.g., Lyutikov, 2006; Baty et al., 2013; Cerutti et al., 2014 and Zweibel and Yamada, 2009; Uzdensky, 2011; Uzdensky, 2016 for reviews).

In this section, we discuss the basics of the extensively studied Fermi acceleration mechanisms, which successfully predict nonthermal power-law particle spectra with spectral indices around 2. We also discuss the basics of magnetic reconnection in relativistic collisionless plasmas, that can also accelerate particles and thus power high-energy emission in various astrophysical systems. Finally, we present how the characteristics of acceleration processes can be accounted for in large-scale phenomenological models of energetic phenomena.

Fermi acceleration involves the scattering of charged particles by moving scattering centers. In the original mechanism developed by Fermi, called second-order Fermi acceleration (Fermi, 1949; Fermi, 1954), the scattering centers (clouds for instance) move in random direction. In first-order Fermi acceleration (e.g. Bell, 1978a; Bell, 1978b; Blandford and Ostriker, 1978), particles gain energy by cycling across a shock front, between unshocked upstream regions and shocked downstream regions. Fermi processes rely on several assumptions. First, a continuous injection mechanism of particles has to be considered. One other important assumption in these models is the existence of scattering centers (for instance magnetic) in the fluid that allow to isotropize the particle distributions upstream and downstream. Moreover, in the test particle approach, the impact of nonthermal particles on the shock structure, that could induce nonlinear effects, is not taken into account.

We consider a fluid moving at the speed βc , with bulk Lorentz factor Γ . This speed represents the mean speed of scattering centers for second-order Fermi acceleration and upstream speed in the downstream frame for first-order Fermi acceleration. Two Lorentz transformations allow to express the final Lorentz factor of a particle after a cycle as a function of its initial Lorentz

factor:

$$\gamma_f = \Gamma^2 \gamma (1 - \beta \beta_{\text{part}} \mu) (1 + \beta \beta_{\text{part}} \mu') \quad (1.1)$$

where $\beta_{\text{part}} c$ is the speed of the particle, $\theta = \arccos(\mu)$ and $\theta' = \arccos(\mu')$ are the angles of the particle entering and exiting the scattering region. For $\beta_{\text{part}} c > \beta c$ and $\beta_{\text{part}} \rightarrow 1$, the fractional energy gain is

$$\frac{\Delta\gamma}{\gamma} = \Gamma^2 (1 - \beta\mu + \beta\mu' - \beta^2\mu\mu') - 1. \quad (1.2)$$

By averaging over the entrance and exit angle distributions, we obtain

$$\frac{\Delta\gamma}{\gamma} = \frac{4}{3} \beta^2 \Gamma^2 \xrightarrow{\beta \ll 1} \frac{4}{3} \beta^2, \quad (1.3)$$

for second-order Fermi acceleration and

$$\frac{\Delta\gamma}{\gamma} = \frac{4}{3} \beta \Gamma^2 + \frac{13}{9} \beta^2 \Gamma^2 \xrightarrow{\beta \ll 1} \frac{4}{3} \beta, \quad (1.4)$$

for first-order Fermi acceleration. The fundamental difference between these two processes is related to the geometry, as first-order Fermi acceleration involves an infinite planar shock.

In what follows we concentrate on first-order Fermi acceleration. The spectrum of accelerated particles can be determined from probability arguments, by considering the competition between acceleration and escape. The downstream escape probability $P_{\text{esc}} = 4\beta/(\chi - 1)$ is obtained by taking the ratio between the convective flux downstream and the flux from upstream Bell (1978a). The compression ratio χ is the ratio between upstream to downstream speeds in the frame of the shock. For N_0 particles injected at an energy E_0 , the number and energies of particles that have completed n cycles are $N_n = (1 - 4\beta/(\chi - 1))^n N_0$ and $E_n = (1 + 4\beta/3)^n E_0$. This leads to the differential spectrum of accelerated particles

$$\frac{dN}{dE} \propto E^{-\alpha} \text{ with } \alpha = 1 - \frac{\log(1 - 4\beta/(\chi - 1))}{\log(1 + 4\beta/3)} \xrightarrow{\beta \ll 1} \frac{\chi + 2}{\chi - 1}. \quad (1.5)$$

For strong nonrelativistic shocks with monoatomic ideal gas, $\chi \rightarrow 4$, thus $\alpha \rightarrow 2$, which allows to distribute energy over a large range, with limits imposed by the size and lifetime of the system. Several effects can affect this simple picture, such as diffusion in a finite medium which softens the spectrum, an energy dependent diffusion coefficient that softens the spectrum above a characteristic energy, nonlinear effects caused by the cosmic-ray pressure which induce a spectral hardening. Moreover, the upstream magnetic field can be amplified by particle streaming instabilities and influence the cosmic ray maximum energy. In ultra-relativistic shocks, the energy of the particle is increased by a factor Γ^2 in the first cycle, and by only a factor of two in the next cycles (Gallant and Achterberg, 1999) due to high anisotropies of the nonthermal particle distribution Kirk and Schneider (1987). Still, this would be enough to reach ultra-high energies. However, strong amplification of the small-scale magnetic power is required to prevent particles from escaping the system in the case of ultra-relativistic shocks (Lemoine et al., 2006). In the case of successful acceleration, α can vary between 2 and 2.3 (e.g. Bednarz and Ostrowski, 1998; Kirk et al., 2000) or even 2.6 – 2.7 due to shock compression and anisotropic scattering downstream (Lemoine and Revenu, 2006). Particle-in-cell simulations (see chapter 3 for more detail) facilitate the modeling of nonlinear effects in shocks, with a precise treatment of various instabilities, such as Weibel instability (e.g. Spitkovsky, 2008; Sironi et al., 2013; Vanthieghem et al., 2018), which might play a decisive role in the formation of shocks and particle acceleration.

Magnetic reconnection is a rapid rearrangement of magnetic field geometry, often leading to an intense release of magnetic energy that can be converted into plasma kinetic energy. This

phenomenon is important in many laboratory and astrophysical plasmas (see e.g. Yamada et al., 2010, for a review). The Sweet-Parker model (Sweet, 1958; Parker, 1963) and the Petschek model (Petschek, 1964) were the first theoretical frameworks of magnetic reconnection developed in the resistive magnetohydrodynamic (MHD) framework, illustrated in figure 1.5. Near neutral points of the magnetic field, electric current density is concentrated in current sheets, and ohmic dissipation changes the shape of the magnetic field lines. Thus they develop a strong curvature in the current layer, forming a X point feature, and subsequently accelerate the plasma, converting magnetic energy into plasma kinetic energy. In the Petschek model, slow shocks developing near the X point were introduced, increasing the reconnection rates.

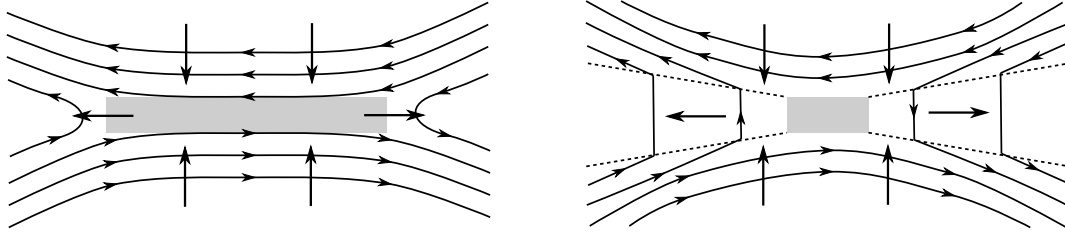


Figure 1.5: Illustration of magnetic field line configurations in the Sweet-Parker (left) and Petschek (right) models of magnetic reconnection. Large arrows indicate plasma flow and the dissipation regions are shaded. Dashed lines indicate slow shocks. Adapted from Yamada et al. (2010).

In high-energy astrophysical environments, such as magnetospheric plasmas near black holes or neutron stars, relativistic magnetic reconnection can occur when the magnetic energy density exceeds the plasma energy density, which corresponds to a large magnetization parameter $\sigma \equiv B^2/4\pi nmc^2$, with n and m the density and the mass of the particles. As the Alfvén velocity $V_A = [\sigma/(1 + \sigma)]^{1/2}c$ becomes relativistic for large magnetizations, magnetic reconnection is in the relativistic regime (Blackman and Field, 1994; Lyutikov and Uzdensky, 2003; Lyubarsky, 2005), and produces relativistic outflows. This process is usually seen as a good candidate for efficient particle acceleration (Hoshino and Lyubarsky, 2012). The recent progress of numerical studies of kinetic plasma processes allows to treat self consistently non-thermal particle acceleration as they account for the retroactive effect of non-thermal particles on electromagnetic fields. In particular, a large number of particle-in-cell simulations (see chapter 3 for more detail) have explored particle acceleration in relativistic collisionless reconnection in electron-positron pair and electron-ion plasmas (e.g. Sironi and Spitkovsky, 2014; Guo et al., 2014; Werner et al., 2016; Werner et al., 2018). They demonstrate the production of a power-law spectra of accelerated particles. For ultrarelativistic reconnection in electron-positron plasmas, very hard spectral indexes $\alpha = 1$ can be obtained, which is very promising to explain short and energetic flares such as Blazar flares or pulsar flares. Electron-ion plasmas should exhibit similar behaviour in the ultrarelativistic regime (Werner et al., 2016). Semirelativistic reconnection in electron-ion plasmas (where electrons are ultrarelativistic and ions subrelativistic) produce softer spectral indexes for electrons $\alpha \gtrsim 2$, and the acceleration of protons remains to be precisely characterised (Werner et al., 2018).

Phenomenological modeling of energetic phenomena require an accurate treatment of acceleration. All the refinements of the acceleration processes described above cannot be directly applied to large-scale systems. However, they can allow to derive simple estimates of important quantities, such as the acceleration timescale or the spectrum of accelerated particles, that can be used for the modeling of energetic sources. The acceleration timescale of a particle of charge e and energy E experiencing an electric field \mathcal{E} reads $t_{\text{acc}} = E/(e\mathcal{E}c)$. Astrophysical plasmas are almost perfectly conducting, implying $\mathcal{E} + \mathbf{v} \times \mathbf{B}/c = 0$ for a plasma moving at velocity \mathbf{v} , hence $\mathcal{E} \leq B$. Therefore, unless one invokes peculiar non-conducting plasmas, the acceleration timescale can be related to the particle Larmor time $t_L \equiv E/(eBc)$: $t_{\text{acc}} = \eta_{\text{acc}}^{-1}t_L$. As argued

in detail in Lemoine and Waxman (2009), for instance, it is impossible to have $\eta_{\text{acc}}^{-1} < 1$, and in most cases $\eta_{\text{acc}}^{-1} \gg 1$. $\eta_{\text{acc}}^{-1} \sim 1$ might be achieved in high-voltage drops that can occasionally be found in some regions of the magnetosphere or the wind of neutron stars, or near black holes and their accretion disks. Even in such extreme regions, however, the efficiency of acceleration depends on the (often highly speculative) mechanism of dissipation of energy.

The maximum energy of an accelerated particle can be estimated by comparing the acceleration timescale to the energy-loss timescales, that are described in the next section. Synchrotron losses are often a competitive process at the highest energies. Moreover, acceleration can occur if the particle can be confined in the system, namely if its Larmor radius is smaller than the typical size of the system. These criteria allow to simply assess the energy of accelerated particles without entering into the detail of acceleration mechanisms.

1.2.2 Inevitable interlink between acceleration and interactions

Various interactions can impact the nature and energy of accelerated particles. The interaction with electromagnetic fields and hadrons can lead to strong energy losses but can also produce a large amount of secondary photons, leptons and hadrons, and contribute to the generation of new interaction backgrounds, on which particles can further interact. In general, leptons contribute more than hadrons to the generation of radiation fields, because of the mass dependence of relativistic dipole radiation. In the following, we focus on hadronic processes.

In the following, symbols marked with a bar refer to the rest frame of the incident proton or nucleus, symbols with a prime refer to the scattering frame (i.e. the comoving frame of the region considered) and unmarked symbols refer to the observer frame. For instance, for an interaction between a photon and a proton, $\bar{\epsilon}$, ϵ' and ϵ are the incident photon energies in the frames mentioned above.

A glimpse into secondary nuclear production

Purely hadronic processes are of particular interest for astrophysical applications in the specific context of secondary nuclear production, which refers to the inelastic production of pions, kaons, hyperons, baryonic resonances, baryons, baryon-antibaryon pairs or spallation. Secondary nuclear production can influence significantly the observed composition of cosmic rays with respect to the composition injected at the source, and produce secondary particles as gamma rays and neutrinos, by the decay of neutral and charged pions. These processes may occur in dense regions, in the interstellar gas, the ejecta from a supernova, an accretion disk or an atmosphere. They are particularly important for the description of extensive air showers produced by cosmic ray hitting the Earth atmosphere (Pierog et al., 2013), or cosmic ray transport in the interstellar medium (di Mauro et al., 2014; Giesen et al., 2015). However, $\sqrt{s} = 13$ TeV is the highest collision energy reached so far at particle accelerators (achieved at the Large Hadron Collider) and quantum chromodynamics cannot yet be solved in the nonperturbative regime. Therefore, at the highest energies, secondary nuclear production cross sections cannot yet be measured nor modeled, and extrapolations of the existing models are needed. We note that photonuclear processes are certainly dominant over purely hadronic interactions in most of the astrophysical phenomena involving winds or jets, apart from the cases of beam-on-target models and mass-loaded winds or jets. Considering the simplest cases of $p + p \rightarrow \pi + X$ production, where X can be any kind of secondary particle produced during the interaction, the total inelastic cross section above $E' = 10$ GeV (Aharonian and Atoyan, 1996) is given by

$$\sigma_{pp}(E') \simeq 30 [0.95 + 0.06 \log(E')] \text{ mb}, \quad (1.6)$$

where E' is the proton energy in GeV units. The inelasticity of pp interactions is important (~ 0.5) and therefore the protons lose their kinetic energy after only a few collision. For nuclei, the spallation cross section (Hörandel et al., 2007) can be written

$$\sigma_{\text{sp}}(E') \simeq [50.44 - 7.93 \log(E') + 0.61 \log^2(E')] A^{\beta_{\text{sp}}} \text{ mb}, \quad (1.7)$$

where E' is the nucleus energy in eV units and $\beta_{\text{sp}} = 0.97 - 0.022 \log(E')$. The typical spallation timescale is $t_{\text{sp}} \sim (n_p \sigma_{\text{sp}} c)^{-1}$, where n_p is the target density. To study the specific production of gamma rays or neutrinos, the use of differential production cross sections is preferred.

Highlights of photohadronic interactions

A general classification of photonuclear interactions has been proposed in Rachen (1996), following the general concepts from Jackson (1975) and Rybicki and Lightman (1979). For coherent electromagnetic interactions, the nucleus acts as a classical charge, whereas its structure is essential to describe incoherent interactions. Among the mechanisms of interest in an astrophysical context, relativistic dipole radiation, Inverse-Compton and Bethe-Heitler processes are considered as coherent processes, whereas photodisintegration and photomeson production are considered as incoherent interactions. Moreover, processes characterized by a large cross section with a small incidence on the cosmic ray at each interaction (small energy losses, no nucleon ejection) can be considered as quasi-continuous processes, and thus we estimate their energy-loss timescales instead of their interaction timescales.

Relativistic dipole radiation. In an electromagnetic field (E, B) , an accelerated charge radiates the total power

$$P_{\text{rad}} = \frac{2e^2\gamma}{3m^2c^3} [(E + \beta \times B)^2 - (\beta \cdot E)^2], \quad (1.8)$$

where $e, m, \beta = v/c$ and γ are respectively the charge, the mass, the speed and the Lorentz factor of the particle. In a pure magnetic field, if $E = 0$, this radiation is called synchrotron radiation, and in the comoving frame the synchrotron cooling timescale averaged over the particle pitch angle reads

$$t'_{\text{syn}} = \frac{3m_p c}{4\sigma_{\text{T,p}} U'_B} \frac{A^3}{Z^4} \frac{1}{\gamma'}, \quad (1.9)$$

where $U'_B = B'^2/8\pi$. The quantum electrodynamic interpretation of electromagnetic interactions as the exchange of virtual photons highlights the similarity between the interaction of a relativistic charge with an electromagnetic field and a photon background. An estimate of the virtual photon energy allows to find the classical limit of synchrotron radiation $\gamma' B' \lesssim 10^{17} \text{ G}$, the threshold of pair production. We note that for strong magnetic fields, the energy losses become so strong that the pitch angle of the particle changes rapidly, and the strong damping of its motion perpendicular to the magnetic field direction induces a transition from synchrotron to curvature regime.

Inverse Compton scattering involves a charged particle, as an electron, a proton or a charged nucleus, and a photon. We focus on the case of protons or charged nuclei $N + \gamma \rightarrow N + \gamma$. In the proton rest frame, the energy of the incident photon is $\bar{\epsilon}$. In the scattering frame, the incident photon energy is $\epsilon' = \bar{\epsilon} / [\gamma' (1 + \cos \theta')]$ where γ' is the Lorentz factor of the incident proton or nucleus and θ' is the scattering angle, thus on average $\bar{\epsilon} = \gamma' \epsilon'$. If the region moves relativistically towards the observer, with a bulk Lorentz factor Γ , the energy of photons in the

observer rest frame is $\epsilon \sim \Gamma \epsilon'$ and therefore $\bar{\epsilon} = \epsilon \gamma' / \Gamma$. For a nucleus of mass Am_u and charge Ze , where m_u the atomic mass unit, the total cross section is

$$\sigma = \frac{3}{8x^2} \left[4 + \frac{2x^2(1+x)}{(1+2x)^2} + \frac{x^2-2x-2}{x} \ln(1+2x) \right] \sigma_{T,N} \quad (1.10)$$

where $\sigma_{T,N} = \sigma_T (m_e / Am_u)^2 Z^4$ and $x = \bar{\epsilon} / Am_u c^2$. We recall that $\sigma_T = 8\pi r_e^2 / 3 = 6.6524 \times 10^{-25} \text{ cm}^2$ is the Thomson cross section for an electron and $r_e = e^2 / m_e c^2$ is the electron classical radius. In the **Thomson regime** ($x \ll 1$) the cross section is $\sigma \sim \sigma_{T,N} = \sigma_T (m_e / m_p)^2$. In the **Klein-Nishina regime** ($x \gg 1$) the cross section is $\sigma \sim 3/8 \sigma_T (m_e / m_p)^2 x^{-1} (\ln 2x + 1/2)$. The transition between the two regimes occurs at $\epsilon' \sim Am_u c^2 / \gamma'$. For $\gamma' = 10^9$, we obtain $\epsilon' \sim 0.9 \text{ eV}$ for proton and $\epsilon' \sim 5 \times 10^1 \text{ eV}$ for iron. The Inverse Compton cross section is illustrated in figure 1.6.

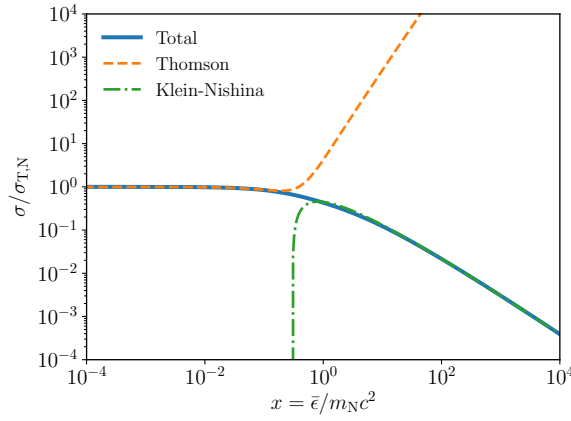


Figure 1.6: Inverse Compton scattering cross section for charged nuclei, normalized by the Thomson cross section, as a function of the photon energy in the proton rest frame normalized by the nucleus rest energy. We show the total cross section (blue solid line), the Thomson regime (orange dashed line) and the Klein-Nishina regime (green dot-dashed line).

Following Dermer and Menon (2009), the energy-loss timescale of Inverse Compton scattering is given by

$$t'_{IC}{}^{-1} = \frac{c}{2\gamma'^3} \int_0^\infty \frac{d\epsilon'}{\epsilon'^2} \frac{dn'_\gamma}{d\epsilon'}(\epsilon') \int_0^{2\gamma'\epsilon'} d\bar{\epsilon} \bar{\epsilon} \left(\langle \epsilon'_s{}^1 \sigma \rangle - \epsilon' \langle \epsilon'_s{}^0 \sigma \rangle \right) / m_N c^2, \quad (1.11)$$

where $dn'_\gamma/d\epsilon' = dN_\gamma/d\epsilon' dV$ is the photon energy density in the scattering frame, ϵ'_s is the scattered photon energy in the scattering frame, and $\langle \epsilon'_s{}^0 \sigma \rangle$ and $\langle \epsilon'_s{}^1 \sigma \rangle$ are respectively the 0 and 1 moments of the differential cross section. For this calculation, we consider the head-on approximation in which the scattered photon travels in the direction of the scattering charged particle. In the Thomson regime, the energy-loss timescale is

$$t'_{IC} = \frac{3m_p c}{4\sigma_{T,p} U'_{rad}} \frac{A^3}{Z^4} \frac{1}{\gamma'}, \quad (1.12)$$

where $U'_{rad} = \int_0^{m_N c^2 / \gamma'} d\epsilon' \epsilon' dn'_\gamma / d\epsilon'$. We note the dependency of the nuclei mean free paths compared to the proton mean free path. The transition between the Thomson and the Klein-Nishina regimes also depend on the mass number.

Bethe-Heitler scattering corresponds to the scattering of a photon on a virtual photon from the Coulomb field around a nucleus $N\gamma \rightarrow Ne^+e^-$. Approximations of the cross section in the

ultra-relativistic case give

$$\sigma_{\text{BH}} = \frac{\alpha_e \sigma_{\text{T}}}{32} Z^2 \left(\frac{\bar{\epsilon}}{m_e c^2} - 2 \right)^3 \quad \text{for } \frac{\bar{\epsilon}}{m_e c^2} - 2 \ll 1 \quad (1.13)$$

$$\sigma_{\text{BH}} = \frac{7\alpha_e \sigma_{\text{T}}}{6\pi} Z^2 \left(\log \frac{\bar{\epsilon}}{m_e c^2} - \frac{109}{42} \right) \quad \text{for } \frac{\bar{\epsilon}}{m_e c^2} \gg 2, \quad (1.14)$$

where $\alpha_e = 1/137$ is the fine-structure constant. More accurate approximations have been obtained by Maximon (1968) using series expansions. We note that these expressions are exact in the first Born approximation, if electrons and positrons do not interact with the nuclear Coulomb field after their production, which might be inaccurate for very heavy nuclei.

The energy loss timescale is computed in the isotropic case, following Chodorowski et al. (1992):

$$t_{\text{BH}}^{-1} = \frac{3}{8\pi} \frac{\alpha_e \sigma_{\text{T}} c (m_e c^2)^3}{\gamma' m_{\text{N}} c^2} \int_{2m_e c^2}^{\infty} \frac{d\epsilon'}{\epsilon'^2} \frac{dn'_{\gamma}}{d\epsilon'} \left(\frac{\epsilon'}{2\gamma'} \right) \varphi(\epsilon'/m_e c^2), \quad (1.15)$$

where φ is a fitting function

$$\varphi(x) = \frac{\pi}{12} \frac{(x-2)^4}{1 + \sum_{i=1}^{i=4} c_i (x-2)^i} \quad \text{for } 2 \leq x < 25, \quad (1.16)$$

$$= \frac{x \sum_{i=0}^{i=3} d_i (\ln x)}{1 - \sum_{i=1}^{i=3} f_i x^{-i}} \quad \text{for } x \geq 25. \quad (1.17)$$

The values of the parameters c_i , d_i and f_i are given in Chodorowski et al. (1992). We note that $t'_{\text{BH}} \propto A/Z^2$, thus a simple rescaling of the proton energy-loss timescale can be performed to calculate the nuclei energy-loss timescales.

Photomeson production and photodisintegration are of particular interest in astrophysical contexts as they produce a large amount of secondary hadrons, photons and also neutrinos above the pion production threshold. The cross sections we show are based on the phenomenological approach detailed in Rachen (1996), where experimental data are mixed with simple theoretical concepts in order to develop a parametrization that can be used in astrophysical contexts. We distinguish between the cases of protons, light nuclei and heavier nuclei (respectively below and above $A = 10$). In these interactions, protons are subject to Lorentz factor change, whereas nuclei only experience mass changes. In nuclei, the energy deposited by the photon can be seen as heating, leading to nucleon evaporation or fragmentation of the nucleus.

The total cross sections for proton and iron are illustrated in figure 1.7, where we show the contribution from various channels. Resonances play an important role in photomeson production and photodisintegration at the lowest incident photon energies $\bar{\epsilon}$. They usually occur in a small energy range, around $\bar{\epsilon} \sim E_{\text{b}}$ where E_{b} is the system binding energy. In the case of nuclei, every nucleon acts as an oscillator in the joint potential well of all nucleons, and the photon resonant absorption can lead to the emission of particles, such as nucleons or pions. The giant dipole resonance (GDR) corresponds to a dipole absorption related to the collective vibrations of protons and neutrons. Moreover, baryon resonances (BR) correspond to baryon excited states, and in the total γp and γN cross sections, the $\Delta(1232)$ resonance is the dominant feature at low $\bar{\epsilon}$ near the pion production threshold. We also note the contribution of direct interactions in the proton and nuclei cross sections, such as the scattering of virtual pions around a nucleon, which occurs in the energy range $\bar{\epsilon} \sim m_{\pi} c^2$, or the interaction of the photon with parts of the system (nucleons or even quark structure). Among the direct channels involving nuclei, the quasi deuteron regime (QD) corresponds to the absorption of a virtual pion by a nucleon pair.

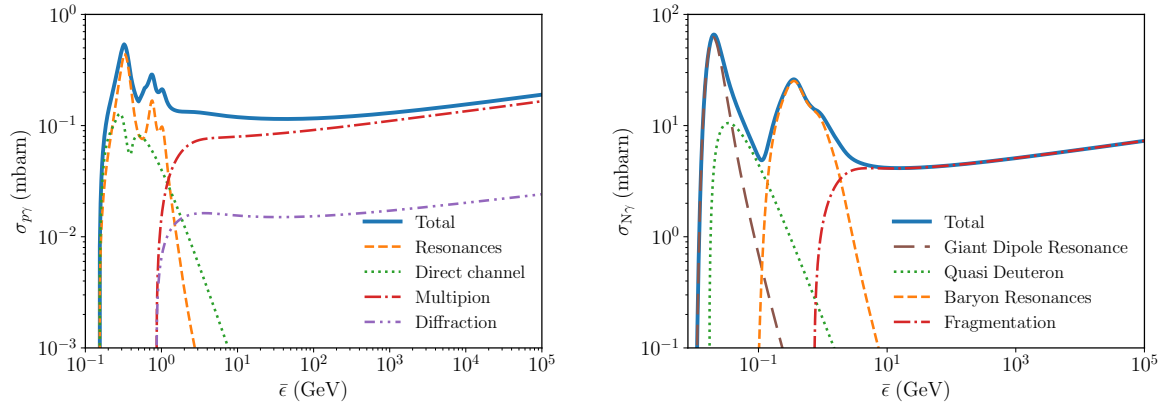


Figure 1.7: Total photohadronic cross sections for proton (left) and for iron (right). We show the total cross section (blue thick line) and the contributions from various channels. The cross section models are from Mücke et al. (2000) and Rachen (1996).

At the highest energies, the fragmentation of a “fireball” into quark-antiquark pairs corresponds to statistical multipion production.

The proton energy-losses depend on the regime of photomeson production. The inelasticity characterizes the energy loss of the primary particle during the interaction. From Atoyan and Dermer (2003), the total cross section and inelasticity can be approximated by two step functions, accounting for resonances and direct channels in the low energy part, and for multipion production in the high energy part

$$\sigma_{p\gamma}(\bar{\epsilon}) = \begin{cases} 340 \mu\text{b}, & \bar{\epsilon}_{\text{th}} < \bar{\epsilon} < 500\text{MeV}, \\ 120 \mu\text{b}, & \bar{\epsilon} > 500\text{MeV}, \end{cases} \quad (1.18)$$

$$\kappa_{p\gamma}(\bar{\epsilon}) = \begin{cases} 0.2, & \bar{\epsilon}_{\text{th}} < \bar{\epsilon} < 500\text{MeV}, \\ 0.6, & \bar{\epsilon} > 500\text{MeV}, \end{cases} \quad (1.19)$$

with $\bar{\epsilon}_{\text{th}} = 0.2\text{ GeV}$ the interaction threshold energy in the proton rest frame. We note the lower cross section at high energies, but with larger proton energy losses at each interaction.

The nuclei mass-losses also depend on the photodisintegration regime. At the lowest energies, one or a few nucleons can be ejected from the heated nucleus. The branching ratios for nucleon emissions have been studied in Puget et al. (1976), in the range $\bar{\epsilon} = 30 - 150\text{ MeV}$. As data get sparser with increasing energy, it is difficult to treat the production of secondary nuclei in great detail, which induces large uncertainties on the nuclear cascades. In the fragmentation regime, nuclei might be fragmented into multiple pieces and the choice of the heaviest fragment might be ambiguous. In the case of light nuclei, the various interaction channels can be considered individually. As $\bar{\epsilon} \sim \epsilon' \gamma'$, high-energy regimes can be dominant for very hard photon spectra, which might be the case for instance if accelerated cosmic rays interact with a gamma-ray burst prompt emission. The propagation and interactions of nuclei in systems should therefore be treated carefully.

For the various aforementioned regimes, the photodisintegration interaction timescales are calculated as follows, in the case of isotropic photon spectra:

$$t'^{-1}_{N\gamma} = \frac{c}{2\gamma'^2} \int_0^\infty \frac{d\epsilon'}{\epsilon'^2} \frac{dn'_\gamma}{d\epsilon'}(\epsilon') \int_0^{2\gamma'\epsilon'} d\bar{\epsilon} \bar{\epsilon} \sigma_{N\gamma}(\bar{\epsilon}), \quad (1.20)$$

where $\sigma_{N\gamma}(\bar{\epsilon})$ is the photodisintegration cross section. Benchmark calculations of interaction and energy-loss timescale are illustrated in section 2.4.3, with analytic or numerical approaches.

Secondary gamma rays and neutrinos carry important information about the astrophysical sources and their environments. In the following we describe in more detail the production of secondaries in the case of photomeson production. We recall that purely hadronic interactions can also produce similar secondary particles, involving for instance baryonic resonances; we focus here on photomeson production for illustration purposes.

At the lowest energies, the dominant channels are the single-pion resonance channel $p + \gamma \rightarrow \Delta^+$ and the direct single-pion production. The delta baryon decay gives $\Delta^+ \rightarrow p + \pi^0$ and $\Delta^+ \rightarrow n + \pi^+$. The non-charge-changing reactions (producing $p\pi^0$) and charge-changing reactions (producing $n\pi^+$) occur with the same probability. At the highest energies, the multipion channel is the dominant channel.

GAMMA RAYS. When a neutral pion is produced, it decays into two gamma rays, which carry approximately 10% of the initial proton energy. They can also be produced by secondary electrons and positrons generated by the decay of charged pions. Many processes can affect gamma rays, such as $\gamma\gamma$ pair production, and can initiate a cascade of pairs. Gamma rays propagating in the interstellar and intergalactic media interact with the Extragalactic Background Light (EBL) in the infrared and optical wavelengths, and with the Cosmic Microwave Background (CMB). In the sources, they can interact with the ambient photon field and can thus be completely absorbed. As these interactions produce $e^+ - e^-$ pairs, the subsequent synchrotron or Compton emissions of the pairs can produce new gamma rays and the process starts over again. As one of the produced leptons gets a large fraction of the gamma-ray energy, many generations of gamma rays are formed in the electromagnetic cascade. The cross section of $\gamma\gamma$ pair production (Jauch and Rohrlich, 1976; Gould, 2005) reads

$$\sigma_{\gamma\gamma}(s) = \frac{\pi r_e^2}{2} (1 - \beta_{\text{cm}}^2) \left[(3 - \beta_{\text{cm}}^4) \ln \left(\frac{1 + \beta_{\text{cm}}}{1 - \beta_{\text{cm}}} \right) - 2\beta_{\text{cm}} (2 - \beta_{\text{cm}}^2) \right], \quad (1.21)$$

where $\beta_{\text{cm}} = \sqrt{1 - s^{-1}}$ and $\sqrt{s} = \gamma_{\text{cm}}$ is the Lorentz factor of the produced pairs in the center-of-momentum frame. For a collision between a gamma ray of energy ϵ_γ and a photon of energy ϵ with an interaction angle θ , $s = [\epsilon\epsilon_\gamma(1 - \cos\theta)]/2$. The approximation $s = \epsilon\epsilon_\gamma/2$ gives good estimates for isotropic target photons. In this case, the gamma-ray absorption probability per unit pathlength is

$$\frac{d\tau_{\gamma\gamma}(\epsilon_\gamma)}{dx} = \frac{2}{\epsilon_\gamma^2} \int_{1/\epsilon_\gamma}^{\infty} \frac{d\epsilon}{\epsilon^2} \frac{dn_\gamma}{d\epsilon}(\epsilon) \int_1^{\epsilon\epsilon_\gamma} ds s \sigma_{\gamma\gamma}(s). \quad (1.22)$$

This absorption probability can be used to infer the attenuation of the gamma ray flux for specific cases. For a given path and without additional gamma ray sources, the source flux is reduced by the factor $\exp(-\tau_{\gamma\gamma})$.

HIGH-ENERGY NEUTRINOS. When a charged pion is produced, it decays into three neutrinos $\pi^+ \rightarrow \mu^+ + \nu_\mu \rightarrow e^+ + \nu_e + \bar{\nu}_\mu + \nu_\mu$. Additionally, the neutron decay produces one neutrino $n \rightarrow p + e^- + \bar{\nu}_e$. Without accounting for additional energy losses, the charged pion carries $\approx 20\%$ of the proton initial energy, the charged muon $\approx 10\%$ and the neutrinos $\approx 5\%$. The neutrino produced by neutron decay carries $\approx 50\%$ less energy than the others. Finally, the produced ν_μ and ν_e spectrum of neutrinos is further mixed during propagation due to neutrino oscillations yielding $\nu_e:\nu_\mu:\nu_\tau$ flavor ratios of 1:1:1. Unlike gamma rays, neutrinos have a very small interaction probability and therefore neutrino fluxes reflect directly the conditions of their production.

A simple estimate of the all-flavor neutrino flux can be derived following Waxman and Bahcall (1999),

$$E_\nu^2 F_\nu(E_\nu) = \frac{3}{8} f_{p\gamma} E_p^2 F_p(E_p), \quad (1.23)$$

where $E_p^2 F_p$ is the energy spectrum of accelerated proton, $f_{p\gamma}$ is the photo-pion production efficiency, and typically $E_\nu \simeq 0.05 E_p$. If all the protons lose their energy through these interactions, $f_{p\gamma} = 1$, which corresponds to a maximum efficiency of photo-pion production. The 3/8 factor arises from the fact that only a fraction of the proton luminosity is converted into neutrino luminosity. As mentioned before, approximately half of the pions produced are charged pions. Moreover, muon and anti-muon neutrinos produced in the charged pion decay carry about half of the pion energy. For a similar flux contribution of the three neutrino species, this leads to the 3/8 factor used to calculate the all-flavor neutrino flux. Several factors can be added to this simple formula to account for additional processes leading to a suppression of the neutrino flux, such as secondary energy losses or interactions of pions and muons, e.g. synchrotron losses or $\pi\gamma$ interactions before they decay. In particular, $\pi\gamma$ interactions can lead to the development of pion cascades. In the opposite, pion or muon acceleration could lead to an enhancement of the neutrino energy (Koers and Wijers, 2007).

We note that neutrinos could be produced through purely leptonic processes, such as $\gamma\gamma \rightarrow \mu^+\mu^-$ or $\gamma\gamma \rightarrow \pi^+\pi^-$, and that in some cases this processes could contribute to the observed neutrino flux (Razzaque et al., 2006).

The production of high-energy neutrinos requires dense target photon fields. Therefore, the peak of neutrino production should be related to a maximum gamma ray absorption in the source, thus a detection of low gamma-ray fluxes and high target photon fluxes, for instance optical or X-ray fluxes (Dermer et al., 2007). This should play an important role in target searches and source follow-ups.

A comparison of the different cross sections mentioned above is shown in figure 1.8, for proton and iron. We see that the inverse Compton scattering cross section is very low compared to the Bethe-Heitler scattering cross section. Thus for hadrons, the energy losses due to inverse Compton scattering can be neglected in most of the cases. A comparison between the interaction and energy-loss lengths is required to better grasp the relative importance of these processes. For this purpose, benchmark examples are presented in section 2.4.3.

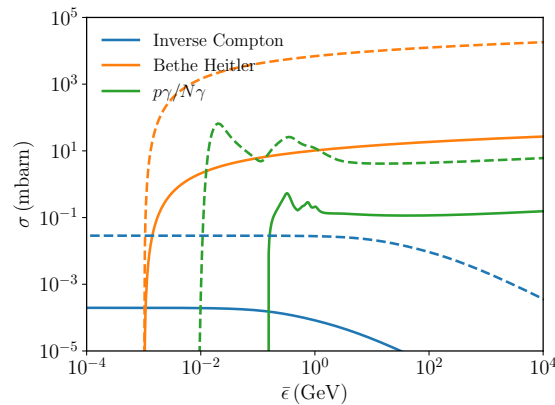


Figure 1.8: Comparison between cross sections for proton and iron (respectively solid and dashed lines), for inverse compton scattering (blue lines), Bethe-Heitler process (orange lines), photomeson production or photodisintegration (green lines).

1.2.3 Numerical treatment of photohadronic interactions

A large number of particle interaction mechanisms can be at play in energetic astrophysical environments. An accurate description of the subsequent energy losses and the production of secondary particles is essential to describe the observed emissions. As stated before, interactions can also have a large impact on particle acceleration, and a precise description of interactions is thus critical. Due to the variety of interactions at play, analytical treatments require simplifications by identifying the dominant processes (see for instance chapter 2), which can already lead to accurate predictions. However, more refined treatments are required to fully understand the great complexity of particles cascades, for instance electron positron cascades, or nuclear cascades, with the subsequent energy losses. In particular, an accurate description of the production of secondary nuclei and nucleons is important for cosmic-ray studies, to compare with the measured composition of cosmic rays for instance at ultra-high energies.

In order to characterize the interactions of accelerated cosmic rays with any type of radiative background, for instance the cosmic microwave background or a theoretical photon field produced in a source, we have developed a mean free path generator, starting from a basis developed by Ke Fang. As stated before, the interaction cross sections and interaction products are obtained from analytical formula (e.g. Rachen, 1996) or from numerical codes: SOPHIA (Mücke et al., 2000) for photopion, TALYS (Koning et al., 2005) for photonuclear and EPOS (Werner et al., 2006) for purely hadronic interactions. For light nuclei, we consider the following channels for Deuteron, Trinucleon, Alpha particle and Beryllium 9: $d(\gamma, np)$, $T_3(\gamma, N)D_2$, $T_3(\gamma, 3N)$, $He_4(\gamma, n)T_3$, $He_4(\gamma, np)d$ and $Be_9(\gamma, n)2\alpha$.

For a given photon field, this code computes the interaction or energy-loss length of proton and nuclei as a function of their Lorentz factor. The Romberg integration method is implemented for fast integration (Press et al., 1992). The mean free paths tables generated with this code are then used in a general propagation and interaction setup, comprised of modules from CRPROPA and a Monte Carlo code (e.g. Armengaud et al., 2007; Kotera et al., 2009), to generate the spectra of ultra-high-energy cosmic rays and high-energy neutrinos from various astrophysical sources. Protons and nuclei up to iron can be propagated, and all the primary and secondary hadrons are tracked until a given distance at which they escape the radiation region.

The different channels for the production of secondary nucleons and nuclei are included in tables for the photomeson production of protons and the giant dipole resonance regime of photodisintegration (respectively generated by SOPHIA and TALYS), whereas they are analytically implemented for the quasi deuteron and baryon resonance regimes of photodisintegration (Puget et al., 1976). For the fragmentation regime, due to the lack of current data and the difficulty to distinguish between photodisintegration and spallation reactions in this high-energy regime (Rachen, 1996), we use branching ratios from hadronic interaction tables (from EPOS) occurring at the same energy in the center of mass.

We emphasize that we also account for energy losses of charged secondary particles, such as pions and muons, before their decay, as it can strongly influence the neutrino spectra. In particular, they can experience strong synchrotron losses as their masses are smaller than the proton and nuclei energies, as shown in chapter 2. Moreover, pions can interact with the photon field; an accurate treatment of $\pi\gamma$ is yet to be implemented. Analytical estimates or simulation outputs can be used as inputs for the radiation field properties or for the value of the mean magnetic field for instance.

1.3 Can we identify the cosmic accelerators?

Today, despite the successes of multimessenger astronomy, the detection of UHECR and high-energy neutrinos seems to raise more questions than answers. As developed in Alves Batista et al. (2019), a plethora of salient open questions remain on the origin of the UHECR, their mass composition, the features appearing at the highest energies in the cosmic ray spectrum (the ankle, the GZK cut-off), the propagation of UHECR and the effect of magnetic fields, their anisotropies, the characteristics of hadronic interactions and discovery potentials for secondary particles, such as photons and neutrinos, and new physics.

As stated before, the acceleration of hadrons to very-high energies in energetic sources is still an open question. This question is absolutely fundamental as the Galactic and extragalactic populations of sources producing the cosmic rays detected from 10^{14} eV to more than 10^{20} eV are yet to be found, as well as the sources of the cosmic high-energy neutrinos detected above 10^{13} eV. Depending on their evolution model, comoving rate densities, cosmic ray injection spectrum and elementary composition, these sources could contribute to the extragalactic gamma-ray background and produce a variable amount of VHE neutrinos. Solving this question requires a careful modeling of acceleration and interaction processes, in a constant dialogue with observations.

A large variety of candidate sources for the acceleration of hadrons have been identified and studied. As a first step, a simple energy requirement, known as the Hillas condition (Hillas, 1984) allows to identify the sources able to accelerate cosmic rays up to a given energy. By comparing the gyroradius $r_g = \gamma mc^2 \beta_{\perp} / ZeB$ of a particle of charge Z , mass m , Lorentz factor γ and speed $v_{\perp} = c\beta_{\perp}$ perpendicular to the magnetic field B , to the typical size of the source R , this criterion puts constraints on the size and the magnetic field of sources allowing to produce efficient cosmic-ray acceleration, with $E_{\max} \lesssim \eta_{\text{acc}} ZeBR$, where η_{acc} is added to account for the acceleration efficiency which can be low for non-relativistic outflows. This criterion can be extended to relativistic outflows, for which we compare the Larmor radius and typical size in the comoving frame, which gives $E_{\max} \lesssim \eta_{\text{acc}} ZeB'R'\Gamma$ where R' and B' are the typical size and magnetic field in the comoving frame, as illustrated in figure 1.9 for a maximum energy $E_{\max} = 10^{20}$ eV.

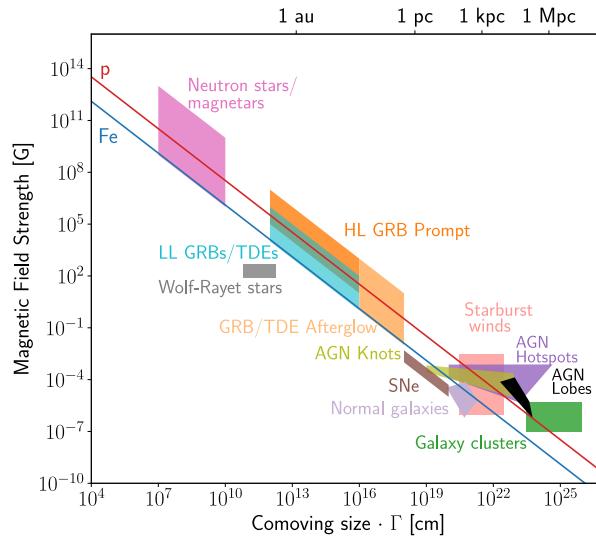


Figure 1.9: Hillas diagram for various sources classes, as a function of $R'\Gamma$ and B' , adapted from Alves Batista et al. (2019). Above the solid red and blue lines, sources can accelerate respectively protons and iron above $E_{\max} = 10^{20}$ eV.

Detailed analysis and modeling of the source properties is then required to reach more precise conclusions. Several UHECR source models have been proposed in the literature, such as radio-

loud active galactic nuclei (AGN), cluster accretion shocks for steady objects, gamma-ray bursts (GRBs), fast-rotating neutron stars, or giant AGN flares for transient candidates (see, e.g., Kotera and Olinto, 2011 and references therein). Most of these models can successfully reproduce the observational data of the Auger and Telescope Array experiments for specific choices of astrophysical parameters, and predict associated high-energy neutrino fluxes that could be observed in the next decade by existing and future experiments. The UHECR composition as measured by the Pierre Auger Observatory indicate a transition towards nuclei heavier than proton above 10^{18} eV. Given the scarcity of heavy elements in the Universe, this puts strong constraints on the elementary composition of hadronic raw material at the source. If interactions backgrounds at the source are too dense, on the one hand ultra-high energies might not be reached due to strong energy losses, but on the other hand heavy elements might be fragmented. However, even with the current set of data, there is no evidence that allows us to strongly favor one particular scenario over the others.

Many theoretical aspects and observational signatures of cosmic ray acceleration and interactions remain to be explored to unveil the cosmic accelerators. The advent of multi-messenger transient astronomy could help distinguish between the existing scenarios, by the joint identification of markers of the acceleration and interaction of hadrons, for instance the detection of high-energy neutrinos and optical/X-ray flux enhancement at the same time and from the same direction. However follow-up studies are still at an early stage and in particular no burst of high-energy neutrinos (i.e. several neutrinos at the same time and from the same source) have been detected yet. Network of observatories, such as the Astrophysical Multimessenger Observatory Network (AMON, Smith et al., 2013) for instance, emerge in order to facilitate the communication between different collaborations and source follow-up. A good coordination of the observations is required, in order to collect as many observations as possible. It is also necessary to prioritize the observations if several events occur at the same time.

We tackle the question of cosmic acceleration by a systematic and analytic comparison between various kinds of transient sources in chapter 2. We focus on their multi-messenger emissions, with a special highlight on high-energy neutrinos produced through photohadronic interactions. The detection of high-energy neutrino bursts is a timely topic in that the gain of sensitivity of existing and upcoming high-energy neutrino detectors will open the era of neutrino astronomy. Moreover, many types of transient powerful events have been discovered lately thanks to unprecedented instrumental performance in terms of time resolution and sensitivity. This general (and mostly prospective) work does not allow to break the degeneracy between the candidate sources, but allows to identify promising source populations, in terms of particle acceleration, production of detectable high-energy neutrino fluxes, but also typical detectability distance from the Earth.

This work serves as a stepping stone for more detailed exploration of hadron acceleration and interactions in energetic sources. Among all the fascinating populations of energetic sources, we identify two categories that appear particularly promising for cosmic-ray acceleration: rapidly rotating and highly magnetized neutron stars, better known as pulsars, and tidal disruptions of stars by massive black holes than are powering relativistic jets. The first population is Galactic and the second extragalactic and they could therefore contribute to the cosmic-ray and neutrino spectra at the highest energies, over a large energy range. However, the modeling of these sources and their emissions raise additional theoretical challenges. First, the simple and general description of acceleration mechanisms should be adapted to the system considered, and in the case of pulsars, we study therefore in more detail the acceleration of hadrons in the vicinity of the neutron star, called the magnetosphere, presented in chapter 3. In the case of tidal disruption events, we consider standard shock acceleration and can therefore adopt simple prescription. Second, a detailed study of the interactions of cosmic rays in the vicinity of the sources appeared as a necessary step to better characterize their emissions. In particular, we follow the idea that UHECR and HE neutrinos could be produced in the same transient sources but in different

states (for instance depending on their luminosities), and our numerical treatment is a first step to account for the time-dependency of a system. Thus we developed a code allowing to simulate the propagation and interaction of UHECR in any type of radiative background. Using these two theoretical tools, we then studied observational markers of cosmic-ray acceleration and interaction for our two source populations. We predict gamma-ray emissions linked to a population of pulsars located in the Galactic center region in chapter 4, and also UHECR and HE neutrino spectra for a population of tidal disruption events in chapter 5.

In parallel, keeping in mind the great interest of developing future HE and VHE neutrino astronomy, we focus on the following question in chapter 6: what kind of techniques do we need to develop and what challenges will we face in order to reconstruct the properties of the UHECR and VHE neutrinos detected in future VHE neutrino detectors? In this context, the development of future experiments aiming at accessing yet unreached energy domains, especially by the detection of VHE neutrinos, is of prime importance. With the projects POEMMA and GRAND, we tackle the questions of the sky coverage of a VHE neutrino space detector, and the reconstruction of UHECR elementary composition with a sparse array of radio antenna.

This manuscript is based on several articles written during the last three years: chapter 2 is based on Guépin and Kotera (2017), chapter 3 is based on Guépin et al. (2019b), in preparation, chapter 4 on Guépin et al. (2018a), chapter 4 on Guépin et al. (2018b) and the first part of chapter 6 is based on Guépin et al. (2019a). Their content is often unchanged, but sometimes updated or increased, and the entire manuscript has been redesigned to contextualise and highlight this work.

Chapter 2

Comparing explosive transients: the production of high-energy neutrino flares

High-energy neutrinos are key messengers in the search for cosmic-ray accelerators, as their main production channels involve accelerated hadrons interacting with a radiative or a hadronic background. Moreover, given the large variety of explosive transients that are currently observed and the increasing sensitivities of observing facilities, the derivation of general criteria for the detectability of neutrinos from transient sources appears as a powerful comparison tool. It can be successfully applied by current and upcoming instruments to target the most promising sources for follow-ups. Conversely, our criteria can also be used to easily distinguish false associations of neutrino events with a flaring source – if the source does not pass the necessary conditions for detectability.

From a theoretical perspective, many studies concentrate on one specific type of source (e.g., on gamma-ray bursts – GRBs – or active galactic nucleus – AGN – flares), for which they give detailed estimates of the neutrino flux (see Section 2.4). Rachen and Mészáros (1998) more broadly discussed the maximum energy of neutrinos and the spectrum for transient sources, but focused in particular on GRBs and AGN. Here, in a more general approach, we aim at constraining the parameter space of bursts and flares detectable in neutrinos by providing necessary conditions on the background fields of the source. Predicting neutrino flux levels is not the scope of this work; we focus here on estimating lower limits on the photon flux of the flare, which is required for efficient neutrino production.

For the purpose of deriving these necessary conditions, we demonstrate that we can describe the large variety of existing sources with a handful of variables: the luminosity distance from the source D_s , the isotropic bolometric luminosity of the source measured during the flare L_{bol} and its peak emission energy ϵ_{peak} , the variability timescale of the emission t_{var} , and the bulk Lorentz factor of the outflow Γ (and the corresponding velocity β in units of c for nonrelativistic cases). Using these quantities, we calculate in the $L_{\text{bol}} - t_{\text{var}}$ parameter-space the maximum accessible neutrino energy in these sources and the minimum flux of photons in a flare required at a specific given wavelength, in order to allow detectability with IceCube.

After recalling the high-energy neutrino production mechanisms and discussing the specificities related to explosive transients in Section 2.1, we derive the maximum accessible neutrino energies in the luminosity-time variability parameter space in Section 2.2. We calculate the photon flux requirements for detectability in Section 2.3 and discuss the case of general categories of transients and of particular sources in Section 2.4 in light of these results. Our results are summarized in Tables 2.1 and 2.2.

This chapter is based on Guépin and Kotera (2017), with a few modifications: several formulae have been adapted to better describe relativistic cases, figures and tables have been changed

accordingly. These changes make our detectability criteria more constraining. We have discussed more precisely the impact of efficient neutrino production. Moreover, we have studied the influence of the cosmic ray injection spectrum on transient neutrino production analytically and numerically, as presented in section 2.4.3.

2.1 Specificities of neutrino production in transients

Bursts or flares of astronomical sources can be associated with the acceleration of leptonic and hadronic particles. In presence of hadrons, neutrinos can be produced through photo-hadronic and hadronic interactions. In this study, we aim at identifying the conditions under which a detectable neutrino flare can be produced by a photon flare.

The searches for time-dependent neutrino signals follow distinctive procedures compared to time-integrated point-source searches. For example, in IceCube, atmospheric neutrinos and muons being the main limiting factor for detection, time-dependent analyses tend to reduce the background (Aartsen et al., 2015). Real-time analysis and follow-ups on alerts can also drastically increase the significance of results. For these observational reasons, we concentrate here on the production of non-steady neutrino signals from flaring sources with typical durations of less than a few months ($t_{\text{var}} \lesssim 10^7$ s).

In the following, all primed quantities are in the comoving frame of the emitting region. Quantities are labeled $Q_x \equiv Q/10^x$ in cgs units unless specified otherwise, and except for particle energies, which are in $E_x \equiv E/10^x$ eV. Numerical applications are given as an illustration for benchmark parameters of GRBs. We consider protons of energy $E_p = \gamma_p m_p c^2$, accelerated in a one-zone region of bulk Lorentz factor $\Gamma = (1 - \beta^2)^{-1/2}$ (with βc the bulk velocity), and of comoving magnetic field strength B' , in a source located at redshift z .

Focussing on flares has some important theoretical consequences. The distance of the emitting region from the central object is estimated to be $r \sim \beta(1 + \beta)\Gamma^2 c t_{\text{var}}/(1 + z)$, where Γ is the bulk Lorentz factor of the outflow, βc its velocity, and z the redshift of the source. This distance is estimated by considering that t_{var} corresponds to the delay between photons emitted towards the observer and photons emitted with an angle Γ^{-1} , or between photons emitted at r and $2r$ (e.g. Piran, 2004). For relativistic outflows, it yields $r \sim \Gamma^2 c t_{\text{var}}(1 + z)^{-1} \lesssim 0.1 \text{ pc } \Gamma^2 (t_{\text{var}}/10^7 \text{ s}) (1 + z)^{-1}$, which implies that the particle escape timescale is limited by the dynamical time of the system $t_{\text{dyn}} = r/\beta c = \Gamma^2 t_{\text{var}}(1 + z)^{-1}$. In particular, magnetic diffusion of particles only intervenes in the acceleration timescale. Rachen and Mészáros (1998) discussed that finite injection or radiation timescales can introduce emission delays and affect this causality relation. The orientation and the geometry of the region could also influence variability timescales (Protheroe, 2002). In the following we assume a homogeneous and instantaneous emission. The comoving size of the radiation region R' is related to the variability timescale of the emission by the Doppler factor $\delta = 1/[\Gamma(1 - \beta \cos \theta)]$, where θ is the jet viewing angle. In the following, we consider a jet pointing towards the observer, therefore $R' = (1 + \beta)\Gamma c t_{\text{var}}(1 + z)^{-1} \sim 6.0 \times 10^{11} \text{ cm } \Gamma_2 t_{\text{var},-1}$.

We consider only photo-hadronic interactions of accelerated hadrons on the *flaring* radiation (the flaring material being usually optically thinner to neutrino production through hadronic interactions, as is demonstrated in Section 2.5). Although accelerated nuclei can also interact with the steady baryon and photon fields in the source or in the cosmic medium, this occurs over a timescale $t \gg t_{\text{var}}$ because the source is larger than the flaring region and because of the magnetic diffusion of particles. In this configuration, the neutrino emission will be diluted over time and can be viewed as a steady emission stemming from the quiescent source.

Relativistically boosted acceleration regions emit radiation and particles within a narrow cone. Although charged particles could be significantly isotropized by intervening magnetic fields, neutrinos produced through interaction with the beamed photon fields cannot be emitted significantly off-axis. Hence neutrino flares from beamed sources cannot be observed off-axis.

In order to set our detectability requirements on a source, we calculate its maximum achievable neutrino flux, $E_\nu^2 F_\nu|_{\max}$, for a given luminosity L_{bol} , time variability t_{var} , and assumed bulk Lorentz factor Γ (and the corresponding velocity β for nonrelativistic cases), without further refined knowledge of the acceleration environment. For each set of $(L_{\text{bol}}, t_{\text{var}}, \Gamma)$, we work under the most optimistic and/or reliable assumptions to maximize all our variables, except for the flare photon flux level, which is left as a free parameter. By setting the calculated neutrino maximal flux to instrument sensitivities, we then derive the minimum level of background photon flux in the flare that is required at a specified wavelength for a successful detection.

2.2 Maximum accessible proton energy and indicative maximum neutrino energy

The magnetic field strength can be derived by setting $U_B = \eta_B U_{\text{rad}}$, where $U_{\text{rad}} = L'_{\text{bol}}/4\pi R'^2 c$ is the comoving photon energy density of the flare and $U_B = B'^2/8\pi$ is the comoving magnetic energy density

$$\begin{aligned} B' &= \left[\frac{2\eta_B L_{\text{bol}}(1+z)^2}{(1+\beta)^6 \Gamma^6 c^3 t_{\text{var}}^2} \right]^{1/2} \\ &\sim 3.4 \times 10^4 \text{ G } \eta_B^{1/2} L_{\text{bol},52}^{1/2} \Gamma_2^{-3} t_{\text{var},-1}^{-1} (1+z). \end{aligned} \quad (2.1)$$

Typically, only a fraction of the total jet luminosity, which is comprised of the magnetic luminosity and the kinetic luminosities of leptons and hadrons, is channelled into radiation, as shown for the case of blazar jets (e.g. Ghisellini et al., 2010).

For maximization reasons, we concentrate on the proton case, which should lead to the highest rates of neutrino production compared to heavier nuclei. The case of heavier nuclei can be derived at the cost of scaling down the expected fluxes in the proton case by a factor of 5 – 10 (Murase and Beacom, 2010).

2.2.1 Acceleration process

Given the complexity of the existing acceleration models and the wide range of parameters that have to be accounted for, we stick to our maximization strategy and consider in the following the maximally efficient acceleration timescale, with $\eta_{\text{acc}} \sim 1$ (see section 1.2). The acceleration timescale can thus be expressed

$$\begin{aligned} t'_{\text{acc}} &= \frac{E'_p}{c e B'} = \left(\frac{c}{2\eta_B e^2} \right)^{1/2} \frac{E_p (1+\beta)^2 \Gamma^2 t_{\text{var}}}{L_{\text{bol}}^{1/2}} \\ &\sim 1.6 \times 10^{-2} \text{ s } \eta_B^{-1/2} E_{p,18} \Gamma_2^2 t_{\text{var},-1} L_{\text{bol},52}^{-1/2}. \end{aligned} \quad (2.2)$$

As already described, this timescale is usually overly optimistic in terms of efficiency, but could be adequate for magnetic reconnection. This timescale is conservative to derive the necessary condition for detectability. The nonrelativistic case is delicate, however, as shock acceleration processes becomes significantly less efficient for low shock velocities β_{sh} , as $\eta_{\text{acc}} \propto \beta_{\text{sh}}^2$. As described in the next section, this could directly affect the maximum accessible energy and the neutrino flux.

2.2.2 Energy losses

The maximum energy of accelerated particles is obtained by comparing the acceleration and energy loss timescales. In presence of strong magnetic fields (and thus for a high source luminosity) synchrotron cooling competes with the adiabatic energy losses.

In the comoving frame, the adiabatic loss timescale, corresponding to the dynamical timescale, can be determined by a condition of causality: $t'_{\text{dyn}} = R'/c$, where R' is the comoving size of the emitting region, thus we obtain

$$t'_{\text{dyn}} = \frac{(1 + \beta)\Gamma t_{\text{var}}}{(1 + z)} \sim 20 \text{ s } \Gamma_2 t_{\text{var},-1} (1 + z)^{-1}. \quad (2.3)$$

We note that this estimate can be influenced by the structure of the emitting region, for instance in the case of subjets. For simplicity, these specific cases are not considered in the following. The proton synchrotron cooling timescale reads

$$\begin{aligned} t'_{\text{syn}} &= \frac{6\pi(m_p c^2)^2}{(m_e/m_p)^2 \sigma_T c E_p' B'^2} \\ &= \frac{3\pi m_p^4 c^6}{m_e^2 \sigma_T} \frac{(1 + \beta)^7 \Gamma^7 t_{\text{var}}^2}{E_p \eta_B L_{\text{bol}}} (1 + z)^{-3} \\ &\sim 3.9 \times 10^2 \text{ s } \eta_B^{-1} E_{p,18}^{-1} \Gamma_2^7 t_{\text{var},-1}^2 L_{\text{bol},52}^{-1} (1 + z)^{-3}. \end{aligned} \quad (2.4)$$

The condition $t_{\text{acc}} < \min(t_{\text{dyn}}, t_{\text{syn}})$ leads to an estimate of the maximum proton energy. Two regimes can be distinguished. If $t_{\text{dyn}} < t_{\text{syn}}$

$$\begin{aligned} E_{p,\text{max}}^{\text{dyn}} &\sim \frac{e}{(1 + \beta)\Gamma} \left(\frac{2\eta_B}{c} \right)^{1/2} L_{\text{bol}}^{1/2} (1 + z)^{-1} \\ &\sim 8.7 \times 10^{20} \text{ eV } \eta_B^{1/2} \Gamma_2^{-1} L_{\text{bol},52}^{1/2} (1 + z)^{-1}, \end{aligned} \quad (2.5)$$

and if $t_{\text{dyn}} > t_{\text{syn}}$

$$\begin{aligned} E_{p,\text{max}}^{\text{syn}} &\sim \frac{(3\sqrt{2}\pi)^{1/2} m_p^2 c^{11/4} e^{1/2}}{m_e \sigma_T^{1/2} (1 + z)^{3/2}} \frac{(1 + \beta)^{5/2} \Gamma^{5/2} t_{\text{var}}^{1/2}}{\eta_B^{1/4} L_{\text{bol}}^{1/4}} \\ &\sim 2.2 \times 10^{20} \text{ eV } \Gamma_2^{5/2} \eta_B^{-1/4} L_{\text{bol},52}^{-1/4} t_{\text{var},-1}^{1/2} (1 + z)^{-3/2}. \end{aligned} \quad (2.6)$$

We note that $E_{p,\text{max}}^{\text{dyn}}$ is independent of t_{var} . In the following, we set $\eta_B = 1$: we assume that the magnetic luminosity of the considered region is fully radiated during the flare. This hypothesis is valid if the dominant emission process is synchrotron radiation. Values of $\eta_B < 1$ are possible and could lead to higher $E_{p,\text{max}}$ if $t_{\text{dyn}} > t_{\text{syn}}$ (Eq. 2.6). We note the mild dependency on η_B in Eq. (8), however. Hence no significant enhancement of the maximum accessible energy is expected from this prefactor.

We caution that in the nonrelativistic case, $\eta_{\text{acc}}^{-1} \propto \beta_{\text{sh}}^2 \gg 1$, and a more realistic picture gives $E_{p,\text{max}}^{\text{dyn}} \propto \beta_{\text{sh}}^2$. Therefore, the energy of protons is limited by the loss of efficiency of the acceleration process.

Other energy-loss processes can influence the maximum energy of particles. We choose to neglect them here, out of generality (some processes require a more refined knowledge of the background fields and structure) or for simplicity when they have limited impact. In all cases, neglecting energy losses preserves the *maximum achievable* nature of $E_{p,\text{max}}$. We also show in the next section that this is consistent with our derivations of our necessary conditions for neutrino flare detectability. We briefly discuss some of the neglected cooling processes below.

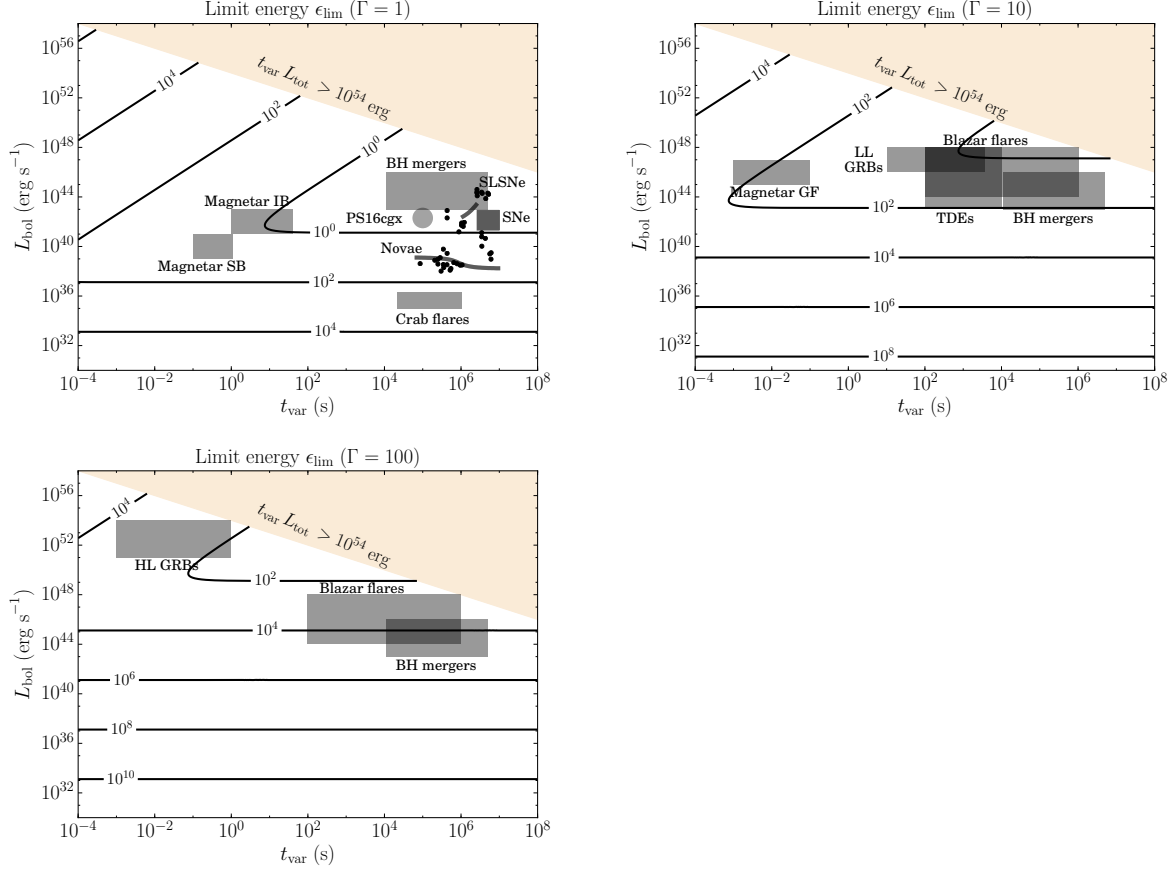


Figure 2.1: Limit energy ϵ_{lim} in parameter space $L_{\text{bol}}, t_{\text{var}}$ for $\Gamma = 1, 10, 100$ allows approximately assessing the effect of inverse-Compton losses for each category of sources. For a break energy in the photon spectrum $\epsilon_b \geq \epsilon_{\text{lim}}$, inverse-compton losses can be neglected against synchrotron losses.

Inverse-compton scattering on the flare photon field can also participate in proton cooling at the level of synchrotron radiations in the Thomson regime. However, in the Klein-Nishina regime, inverse-compton losses become quickly negligible with respect to synchrotron losses. As the inverse-compton regime depends on the photon energy in the proton rest frame (and in particular on ϵ_b), the relative importance of inverse-compton and synchrotron losses can only be estimated on a case-by-case basis. We discuss this process applied to specific source categories, by identifying the dominant inverse-compton regime (Thomson or Klein-Nishina). We can consider that for $x = \epsilon''/m_p c^2 \gg 1$, where ϵ'' is the photon energy in the proton rest frame, inverse-compton losses can be neglected (Klein-Nishina regime), and for $x \lesssim 1$, they have a similar effect as synchrotron losses (Thomson regime).

We assume that the maximum proton energy $E_{p,\text{max}}$ is established by the competition between acceleration, synchrotron, and adiabatic losses and evaluate the effect of inverse-compton losses on these protons. If inverse-compton losses are significant, they can influence the maximum neutrino energy. As $x = \epsilon E_p / \Gamma^2 (m_p c^2)^2$, inverse-compton losses are significant for $\epsilon \leq \epsilon_{\text{lim}} = \Gamma^2 (m_p c^2)^2 / E_p$. Typically, they can be neglected when $\epsilon_b \gtrsim \epsilon_{\text{lim}}$. In figure 2.1 we plot ϵ_{lim} in the $L_{\text{bol}} - t_{\text{var}}$ parameter space and compare for each category of transients its value with the break energy ϵ_b quoted in Section 2.4.

We conclude that blazars are expected to experience large inverse-compton losses. As suggested in (Murase et al., 2014), these objects are also expected to experience other energy loss processes, for instance, strong Bethe-Heitler losses. For GRBs the inverse-compton losses can be neglected as $\epsilon_b \sim 10^3$ keV is quite high. The uncertainty on the value of ϵ_b for magnetar flares is too high to

conclude. In the case of the Crab flares, as $\epsilon_b \sim 400$ MeV, inverse-compton losses can be easily neglected. They may also be neglected for Tidal Disruption Events (TDE) as their emission peaks in hard X-rays or soft gamma rays. Last, for novae and supernovae, inverse-compton losses may not be negligible as the values of ϵ_b can be borderline, but refined case-by-case studies are required to conclude. In order to keep this study as general as possible, we choose to neglect inverse-compton losses in the following. We recall that in any case, neglecting inverse-compton losses preserves the maximum achievable nature of $E_{p,\max}$ and thus the validity of the necessary minimum flux $\Phi_{\gamma,\min}$.

Bethe-Heitler electron-positron pair production from interactions of protons on photon fields is usually a subdominant cooling process compared to photopion production (e.g., Sikora et al., 1987 for AGN), because of its low inelasticity ($\xi_{\text{BH}} \sim 10^{-3}$ at the threshold $\epsilon''_{\text{BH}} \sim 1$ MeV) and mild cross-section ($\sigma_{\text{BH}} \sim 1.2$ mb at threshold). It can become significant over some high-energy range windows for very specific photon spectra (Murase et al., 2014; Petropoulou and Mastroianni, 2015), however – see also the detailed analytical discussion by (Rachen and Mészáros, 1998). We note that the cooling effect itself is limited even in these situations, although the production of secondary pairs can have an important influence on the resulting gamma-ray spectra. For simplicity, we therefore neglect Bethe-Heitler losses in this study.

2.2.3 Decay of secondaries and neutrino maximum energy

Photohadronic interactions can generate neutrinos through the production of charged pions and their subsequent decay: $p + \gamma \rightarrow n + \pi^+$ and $\pi^+ \rightarrow \mu^+ + \nu_\mu$ followed by $\mu^+ \rightarrow e^+ + \nu_e + \bar{\nu}_\mu$. The decay of secondary neutrons can also generate neutrinos, although their photodisintegration has a higher occurrence rate. This description is simplified as other photohadronic interaction channels contribute to the production of neutrinos, for instance, multi-pion productions (see, e.g., the SOPHIA code, Mücke, 1999), but it suffices in our framework. The resulting flavor composition is $\nu_e : \nu_\mu : \nu_\tau = 1 : 2 : 0$, as we neglect the effect of energy losses or acceleration of pions and muons (e.g., Kashti and Waxman, 2005). The expected flavor composition at Earth is $1 : 1 : 1$ when long-baseline neutrino oscillations are accounted for. In the following the fluxes account for all neutrino flavors.

As charged pions carry 20% of the proton energy and neutrinos carry 25% of the pion energy, neutrinos produced by photohadronic interactions typically carry 5% of the initial energy of hadrons: $E_\nu = 0.05E_p$. The maximum accessible energy of neutrinos therefore depends on the maximally accessible energy of accelerated protons, which is determined by a competition between acceleration and energy losses. Moreover, the charged pions and muons can experience energy losses such as adiabatic or synchrotron cooling before decaying and producing neutrinos, which influences the maximum accessible energy of neutrinos.

The pion and muon decay times depend on their energies E_π and E_μ . In the comoving frame, their decay times read $t'_\pi(E_\pi) = \tau_\pi E_\pi (1+z) ((1+\beta)\Gamma m_\pi c^2)^{-1} \sim 0.9 \text{ s } E_{\pi,18} \Gamma_2^{-1}$ and $t'_\mu(E_\mu) = \tau_\mu E_\mu (1+z) ((1+\beta)\Gamma m_\mu c^2)^{-1} \sim 10^2 \text{ s } E_{\mu,18} \Gamma_2^{-1}$, where the pion and muon lifetimes and masses are $\tau_\pi = 2.6 \times 10^{-8} \text{ s}$, $\tau_\mu = 2.2 \times 10^{-6} \text{ s}$, $m_\pi = 140 \text{ MeV } c^{-2}$ and $m_\mu = 106 \text{ MeV } c^{-2}$, respectively. As $\tau_\mu > \tau_\pi$, the muon decay time is usually the main limiting factor for neutrino production. Muons satisfying $t'_\mu(E_\mu) < \min(t'_{\text{dyn}}, t'_{\text{syn}})$ have time to decay and produce neutrinos. If $t'_\mu > \min(t'_{\text{dyn}}, t'_{\text{syn}})$, we derive the maximum energy of muons that can produce neutrinos during the flare by equating $t'_\mu = \min(t'_{\text{dyn}}, t'_{\text{syn}})$. If $t_{\text{dyn}} < t_{\text{syn}}$

$$\begin{aligned} E_{\mu,\max}^{\text{decay}} &= \frac{m_\mu c^2}{\tau_\mu} (1+\beta)^2 \Gamma^2 t_{\text{var}} (1+z)^{-2} \\ &\sim 1.9 \times 10^{17} \text{ eV } \Gamma_2^2 t_{\text{var},-1} (1+z)^{-2}, \end{aligned} \quad (2.7)$$

and if $t_{\text{dyn}} > t_{\text{syn}}$

$$\begin{aligned} E_{\mu, \text{max}}^{\text{decay}} &= \frac{(3\pi)^{1/2} m_{\mu}^{5/2} c^4}{m_e \tau_{\mu}^{1/2} \sigma_T^{1/2} \eta_B^{1/2}} (1 + \beta)^4 \Gamma^4 L_{\text{bol}}^{-1/2} t_{\text{var}} (1 + z)^{-2} \\ &\sim 3.4 \times 10^{16} \text{ eV } \Gamma^4 \eta_B^{-1/2} L_{\text{bol}, 52}^{-1/2} t_{\text{var}, -1} (1 + z)^{-2}. \end{aligned} \quad (2.8)$$

The maximum neutrino energy can then be deduced as $\sim 50\%$ of the muon energy.

For dense photon backgrounds, pions and muons could undergo further $\mu\gamma$ or $\pi\gamma$ interactions, creating more pions and muons, that would lead to a cascade and thus to a suppression in neutrino flux (see, e.g., Fang et al., 2016). Such cascades are expected to have an effect only if photo-pion production is already highly efficient, that is to say, for dense fields, as the cross-sections of $p\gamma$ and $\pi\gamma$ processes can be considered as similar. We neglect these cascades for simplicity, as we estimate the neutrino *maximum achievable* energy.

Before decaying, secondary pions and muons could undergo reacceleration processes in the same region as for the parent proton, as was discussed, for example, in (Koers and Wijers, 2007; Murase et al., 2012; Winter et al., 2014). These effects could have an impact if the acceleration process is very efficient. They should be taken into account to maximize the achievable neutrino energy and calculate the pion, muon, and neutrino energies self-consistently. We leave these calculations for further studies, as we aim here at giving a range of observable neutrino energies, and further refinements are not required for the purpose of calculating the minimum detectability flux (for this, we show that the maximum achievable proton energy is the crucial parameter).

2.2.4 Results

The maximum accessible energy of protons (left panels) and an indicative (i.e., neglecting possible reacceleration) maximum energy of neutrinos (right panels) as a function of the variability timescale and the total luminosity are displayed in figure 2.2 for three bulk Lorentz factors $\Gamma = 1, 10, 100$ from top to bottom. The beige region is excluded in all figures as it corresponds to an energetic budget $t_{\text{var}} L_{\text{bol}} > 10^{54} \text{ erg}$: this exceeds the energetic budget of GRBs, which are the most energetic transient events observed with photons in our Universe. White and gray patches locate typical transient sources discussed in Section 2.4.1 in the parameter space.

We can distinguish two regimes in the $L_{\text{bol}} - t_{\text{var}}$ parameter space: adiabatic (synchrotron) cooling is dominant at low (high) luminosity. The transition between the two regimes depends on the bulk Lorentz factor: it is shifted toward higher luminosities when Γ increases. The limits set by pion and muon energy losses appear as vertical lines in the righthand column of figure 2.2. As expected, they play an important role for low-variability timescales. We also note the influence of synchrotron secondary losses, as the contour lines tend to tighten up at high luminosities.

For nonrelativistic outflows ($\Gamma \sim 1$), mild luminosities $L_{\text{bol}} > 10^{36} \text{ erg s}^{-1}$ and variability timescales longer than $t_{\text{var}} \sim 10 \text{ s}$ are required to reach $E_{\nu} > 100 \text{ TeV}$, which is the lower limit of the IceCube detection range. This limit is related to the high fluxes of atmospheric neutrinos at $E_{\nu} \lesssim 100 \text{ TeV}$, although the experiment endeavors to lower this limit (Aartsen et al., 2016b). Sensitivities of future experiments such as ARA, ARIANNA, or GRAND, aiming at energies $E_{\nu} > 1 \text{ EeV}$, would be reached for higher luminosities $L_{\text{bol}} > 10^{42} \text{ erg s}^{-1}$ and longer variability timescales $t_{\text{var}} > 10^6 \text{ s}$. Our results are consistent with the dedicated studies that can be found in the literature for particular sources with mildly and ultrarelativistic outflows ($\Gamma = 10$ and 100 in our examples). We find that high-luminosity (HL) GRBs can accelerate protons up to 10^{20} eV , which corresponds to classical estimates (e.g., Waxman and Bahcall, 2000; Murase et al., 2008; Bustamante et al., 2016). They could in principle produce very high energy neutrinos,

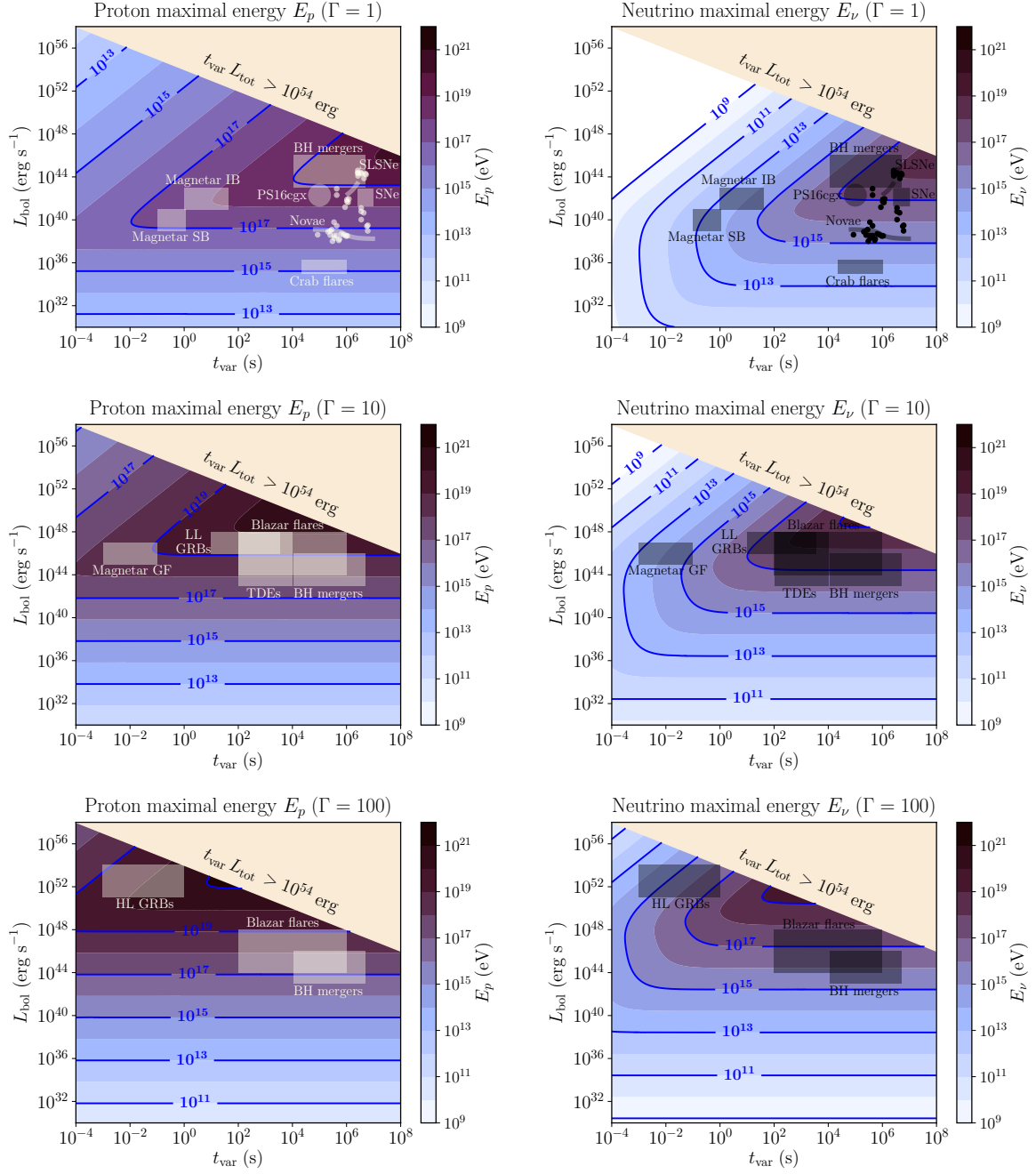


Figure 2.2: Maximum accessible proton energy $E_{p,\text{max}}$ (left column) and corresponding maximum accessible neutrino energy $E_{\nu,\text{max}}$ (right column) as a function of the variability timescale t_{var} and the bolometric luminosity L_{bol} of a flaring source, with bulk Lorentz factor $\Gamma = 1, 10, 100$ (from top to bottom). Overlaid are examples of the location of benchmark explosive transients in the $L_{\text{bol}} - t_{\text{var}}$ parameter space (see Section 2.4). The beige region indicates the domain where no source is expected to be found because of the excessive energy budget. The dots locate recently discovered categories of transients (Kasliwal, 2011), superluminous supernovae (SLSNe), peculiar supernovae, and luminous red novae. The small square box (labeled SNe) and the short diagonal line on its upper left indicate core-collapse and thermonuclear supernovae, respectively. Low-luminosity GRBs and type Ibc supernovae should be treated with care (see Section 2.5.2).

with $E_\nu \lesssim 10^{18}$ eV. In this case, muon energy losses constitutes a very strong limiting factor and hence the maximum energy strongly depends on the variability timescale. Blazars, low-luminosity (LL) GRBs, and tidal disruption events (TDE) are also powerful accelerators with $E_{p,\max} \sim 10^{19}$ eV and associated maximum neutrino energy $E_\nu \sim 10^{18}$ eV. We note that muon energy losses are not a limiting factor for blazars.

We caution again that these estimates are indicative and constitute maximum achievable neutrino energies, neglecting possible secondary reacceleration. In the next section, we evaluate the neutrino fluxes associated with these various flaring events in order to assess their detectability.

2.3 Neutrino flux and detectability limit

2.3.1 Maximum neutrino flux

As a first approximation, we consider that the flare photon spectrum follows a broken power-law over the energy range $[\epsilon_{\min}, \epsilon_{\max}]$, with an observed break energy ϵ_b , corresponding observed (isotropic equivalent) luminosity set as L_b , and spectral indices $a < b$, with $b > 2$:

$$L_\gamma(\epsilon) = \epsilon^2 \frac{d\dot{N}_\gamma}{d\epsilon} = \begin{cases} L_b (\epsilon/\epsilon_b)^{2-a} & \epsilon_{\min} \leq \epsilon \leq \epsilon_b, \\ L_b (\epsilon/\epsilon_b)^{2-b} & \epsilon_b < \epsilon < \epsilon_{\max}. \end{cases} \quad (2.9)$$

This type of spectrum is adequate to model nonthermal processes such as synchrotron emission. It is quite appropriate in many cases, for instance, for most GRBs or for the Crab flares. However, the spectral energy distribution (SED) of explosive transients shows great diversity, and our approach should be refined by using more realistic SED, adapted to several typical sources such as blazars or magnetars. We leave this issue for further studies.

Following the simple approach described in section 1.2.2 (Waxman and Bahcall, 1999), the all-flavor neutrino flux can be estimated from the proton energy spectrum $E_p^2 F_p$:

$$E_\nu^2 F_\nu = \frac{3}{8} f_{p\gamma} E_p^2 F_p, \quad (2.10)$$

where the photo-pion production efficiency $f_{p\gamma} \equiv \min(1, t'_{\text{dyn}}/t'_{p\gamma})$ is the key parameter to determine. The photo-pion production timescale in the comoving frame $t'_{p\gamma}$ can be written

$$t_{p\gamma}'^{-1} = c \langle \sigma_{p\gamma} \kappa_{p\gamma} \rangle \int_{\epsilon'_{\text{th}}}^{\infty} d\epsilon' \frac{dn'_\gamma}{d\epsilon'}(\epsilon'), \quad (2.11)$$

with ϵ'_{th} the interaction threshold energy in the comoving frame. We can approximate the cross-section $\sigma_{p\gamma}$ and inelasticity $\kappa_{p\gamma}$ profiles by the sum of two step functions, as shown in section 1.2.2. The photon energy density in the comoving frame, $dn'_\gamma/d\epsilon'$, associated with the flaring event, is estimated from the observations, using Eq. (2.9)

$$\frac{dn'_\gamma}{d\epsilon'}(\epsilon') = \frac{L'_b}{4\pi R'^2 c \epsilon_b'^2} \times \begin{cases} (\epsilon'/\epsilon'_b)^{-a} & \epsilon' < \epsilon'_b, \\ (\epsilon'/\epsilon'_b)^{-b} & \epsilon' > \epsilon'_b. \end{cases} \quad (2.12)$$

We can obtain an equivalent expression regardless of the geometry of the emitting region, for a spherical blob or wind-type spherical shell geometries (Dermer and Menon, 2009). As $R' = \delta(1+z)^{-1} c t_{\text{var}}$, $L' = \delta^{-4} L$ and $\epsilon'_b = \delta^{-1}(1+z)\epsilon_b$, we derive the photo-pion production timescale

$$t_{p\gamma}'^{-1} \simeq \frac{\langle \sigma_{p\gamma} \kappa_{p\gamma} \rangle L_b}{4\pi(1+\beta)^5 \Gamma^5 c^2 t_{\text{var}}^2 \epsilon_b} \frac{1}{1-a} \left[\frac{a-b}{1-b} - \left(\frac{\epsilon_{\text{th}}}{\epsilon_b} \right)^{1-a} \right]. \quad (2.13)$$

The term $(a-b)/(1-b)$ being of order unity, we can readily see that $t'_{p\gamma}$ will simplify depending on whether the flare photon spectrum before the break energy is soft ($a > 1$) or hard ($a < 1$):

$$t'^{-1}_{p\gamma} \simeq \frac{\langle \sigma_{p\gamma} \kappa_{p\gamma} \rangle}{4\pi(1+\beta)^5 \Gamma^5 c^2 t_{\text{var}}^2} \frac{1}{|a-1|} \times \begin{cases} (L_{\text{th}}/\epsilon_{\text{th}}) & a > 1, \\ (L_{\text{b}}/\epsilon_{\text{b}}) & a < 1, \end{cases} \quad (2.14)$$

where we have defined the observed photon luminosity at threshold energy $L_{\text{th}} \equiv L_{\gamma}(\epsilon_{\text{th}}) = L_{\text{b}}(\epsilon_{\text{th}}/\epsilon_{\text{b}})^{2-a}$. The photon energy threshold for photo-pion production reads

$$\epsilon_{\text{th}} = \epsilon''_{\text{th}} \frac{(1+\beta)^2 \Gamma^2 m_p c^2}{(1+z)^2 E_p} \sim 7.5 \times 10^3 \text{ eV } \Gamma_2^2 E_{p,18}^{-1} (1+z)^{-2}, \quad (2.15)$$

hence $t'_{p\gamma}$ depends on E_p through ϵ_{th} .

We note that Eq. (2.13) was obtained by assuming $\epsilon_{\text{th}} < \epsilon_{\text{b}}$. However, this is not always the case as ϵ_{th} depends on the proton energy and the bulk Lorentz factor (Eq. 2.15). The condition $\epsilon_{\text{th}} < \epsilon_{\text{b}}$ implies $E_p > E_{p,\text{min}}$ with $E_{p,\text{min}} = (1+\beta)^2 \Gamma^2 \epsilon''_{\text{th}} m_p c^2 / (1+z)^2 \epsilon_{\text{b}} \sim 1.8 \times 10^9 \text{ eV } (1+\beta)^2 \Gamma^2 (1+z)^2 (\epsilon_{\text{b}}/100 \text{ MeV})^{-1}$. For $\epsilon_{\text{th}} > \epsilon_{\text{b}}$, $t'^{-1}_{p\gamma} \propto (L_{\text{b}}/\epsilon_{\text{b}})(\epsilon_{\text{th}}/\epsilon_{\text{b}})^{1-b} = L_{\text{th}}/\epsilon_{\text{th}}$. As we have assumed $b > 1$, we recover the soft spectrum case ($a > 1$) of Eq. (2.14) when $\epsilon_{\text{th}} > \epsilon_{\text{b}}$.

We assume that a fraction η_p of the bolometric source luminosity is channeled into a population of accelerated protons, with a peak luminosity $x_p \eta_p L_{\text{bol}}$, where $x_p \leq 1$ is a bolometric correction prefactor that depends on the proton spectral index, peak, and maximum energies. The proton spectrum is modeled as a simple power law with spectral index α , between $E_{p,\text{min}}$ and $E_{p,\text{max}}$

$$E_p^2 F_p = \frac{1}{4\pi D_L^2} \frac{(2-\alpha)\eta_p L_{\text{bol}}}{E_{p,\text{max}}^{2-\alpha} - E_{p,\text{min}}^{2-\alpha}} E_p^{2-\alpha}, \quad (2.16)$$

for a transient source located at luminosity distance D_L (redshift z). A maximum achievable time-integrated neutrino flux $E_{\nu}^2 F_{\nu}|_{\text{max}} = \frac{3}{8} \max(f_{p\gamma} E_p^2 F_p)$ can then be derived from Eq. (2.10). The energy $E_{p,\text{high}}$ maximizing $f_{p\gamma} E_p^2 F_p$ depends on the source characteristics.

If $a > 1$, the higher the proton energy E_p , the lower the corresponding ϵ_{th} , and the higher the associated photon luminosity and the efficiency $f_{p\gamma}$. If $a < 1$, $t'_{p\gamma}$ does not depend on E_p . Hence $f_{p\gamma}(E_{p,\text{max}}) = f_{p\gamma}|_{\text{max}}$. As we maximize the neutrino flux, we also set $x_p = 1$.

Expressing $f_{p\gamma} \equiv \min(1, t'_{\text{dyn}}/t'_{p\gamma})$ using Eqs. (2.3) and (2.14) yields the maximum achievable neutrino flux. If $f_{p\gamma}(E_{p,\text{high}}) = 1$, the neutrino flux is simply a fraction of the proton flux:

$$E_{\nu}^2 F_{\nu}|_{\text{max}} \simeq \frac{3}{8} \frac{(2-\alpha)\eta_p L_{\text{bol}} E_{p,\text{high}}^{2-\alpha}}{4\pi D_L^2 (E_{p,\text{max}}^{2-\alpha} - E_{p,\text{min}}^{2-\alpha})}. \quad (2.17)$$

If $f_{p\gamma}(E_{p,\text{high}}) < 1$,

$$E_{\nu}^2 F_{\nu}|_{\text{max}} \simeq \frac{3}{8} \frac{\langle \sigma_{p\gamma} \kappa_{p\gamma} \rangle (1+z)^{-1}}{4\pi(1+\beta)^4 \Gamma^4 c^2 t_{\text{var}} |a-1|} \frac{(2-\alpha)\eta_p L_{\text{bol}} E_{p,\text{high}}^{2-\alpha}}{E_{p,\text{max}}^{2-\alpha} - E_{p,\text{min}}^{2-\alpha}} \begin{cases} \Phi_{\gamma}^{\text{th}} & a > 1 \\ \Phi_{\gamma}^{\text{b}} & a < 1 \end{cases}, \quad (2.18)$$

where we have defined $\Phi_{\gamma}^x \equiv L_x / (4\pi D_L^2 \epsilon_x)$ with $x=\text{th}$ or b , the observed photon flux of the source at threshold energy ϵ_{th} and break energy ϵ_{b} , respectively. We note that the threshold energy depends on $E_{p,\text{high}}$. The flux Φ_{γ}^x is a directly measurable quantity.

2.3.2 Minimum photon flux $\Phi_{\gamma,\text{min}}$ for neutrino detectability

We consider a neutrino detector of flux sensitivity s_{exp} and corresponding sensitivity in terms of fluence \mathcal{S}_{exp} . We assume that the detector points toward the source during the entire flaring

event, that is, during $t \sim t_{\text{var}}$. The experimental detection limit then depends on the variability timescale: $s_{\text{exp}} \sim \mathcal{S}_{\text{exp}}/t_{\text{var}}$. By equating the maximum achievable neutrino flux to the detector sensitivity in flux $E_{\nu}^2 F_{\nu}|_{\text{max}} = s_{\text{exp}}$, we can deduce several conditions for neutrino flare detectability. First, we note that as all known acceleration processes lead to proton spectral indexes such as $|\alpha - 2| < 1$, we always have $[(2 - \alpha)E_{p,\text{high}}^{2-\alpha}/E_{p,\text{max}}^{2-\alpha} - E_{p,\text{min}}^{2-\alpha}] \leq 1$. Therefore, we can consider an upper bound for the neutrino flux, by setting the aforementioned quantity to 1. In the case where $f_{p\gamma}(E_{p,\text{high}}) = 1$, the detectability criterion does not involve the photon flux, and neutrinos can only be detected if

$$D_{\text{eff}} \equiv \frac{8}{3} \frac{\eta_p L_{\text{bol}} t_{\text{var}}}{4\pi D_L^2 \mathcal{S}_{\text{exp}}} \geq 1. \quad (2.19)$$

If this first detectability criterion is met, the energetic budget is sufficient to reach neutrino flare detectability for an efficient neutrino production. In the case where $f_{p\gamma}(E_{p,\text{high}}) < 1$, we calculate the minimum photon flux required to reach the experimental detection limit:

$$\Phi_{\gamma,\text{min}} \simeq \frac{8}{3} \frac{4\pi(1+\beta)^4 \Gamma^4(1+z) c^2 \mathcal{S}_{\text{exp}} |a-1|}{\langle \sigma_{p\gamma} \kappa_{p\gamma} \rangle \eta_p L_{\text{bol}}} \frac{E_{p,\text{max}}^{2-\alpha} - E_{p,\text{min}}^{2-\alpha}}{(2-\alpha)E_{p,\text{high}}^{2-\alpha}}. \quad (2.20)$$

As stated before, we always have $(E_{p,\text{max}}^{2-\alpha} - E_{p,\text{min}}^{2-\alpha})/[(2-\alpha)E_{p,\text{high}}^{2-\alpha}] > 1$, and we can define a minimum detectability criterion which does not depend on $E_{p,\text{high}}$,

$$\begin{aligned} \Phi_{\gamma,\text{min}} &= \frac{8}{3} \frac{4\pi(1+\beta)^4 \Gamma^4(1+z) c^2 \mathcal{S}_{\text{exp}}}{\langle \sigma_{p\gamma} \kappa_{p\gamma} \rangle \eta_p L_{\text{bol}}} \\ &\simeq 30 \text{ Jy } \eta_p^{-1} \Gamma^4 L_{\text{bol},52}^{-1} (1+z). \end{aligned} \quad (2.21)$$

For a fixed cosmic-ray loading factor η_p and a bulk Lorentz factor Γ of the emitting region chosen following a theoretical model for the source, the minimum photon flux density for neutrino detection is a function of two observed quantities: the bolometric luminosity L_{bol} , and the variability timescale of the flaring event t_{var} .

This minimum flux should be compared with the observed flux estimated

1. for soft photon spectra ($a > 1$), at the minimum threshold energy (obtained from the maximum energy of accelerated protons): $\epsilon_{\text{th}} = \epsilon_{\text{th}}'' (1+\beta)^2 \Gamma^2 m_p c^2 / (1+z)^2 E_{p,\text{high}}$;
2. for hard photon spectra ($a < 1$), at the observed spectral break energy ϵ_b . Here, we have also assumed $|a-1|^{-1} \sim \mathcal{O}(1)$.

For IceCube, the sensitivity is characterized by a minimum fluence $\mathcal{S}_{\text{IC}} = 5 \times 10^{-4} \text{ TeV cm}^{-2}$ over an energy range 10 TeV–10 PeV, which corresponds to a detection limit $s_{\text{IC}} \sim 10^{-11} \text{ TeV cm}^{-2} \text{ s}^{-1}$ for a one-year data collection (Aartsen et al., 2015). The IceCube-Gen2 project could reach a sensitivity of one order of magnitude better (The IceCube-Gen2 Collaboration et al., 2015). The planned sensitivities for ARA, ARIANNA (Allison et al., 2012; Barwick, 2011), CHANT (Neronov et al., 2016), or GRAND (Martineau-Huynh, 2016) are 1, 1.5, or 2 orders of magnitude better, respectively, than IceCube, at $E_{\nu} \sim 1 \text{ EeV}$.

All types of events (tracks or showers) should be considered for detection, and our predictions are given for all flavors. However, energies below 100 TeV are strongly disfavored because of atmospheric background. Furthermore, track events give more information about the arrival direction and therefore allow us to identify coincident photon flares or coincident neutrino events more precisely. If arrival directions are not available (in the case of shower events), temporal coincidence could also help to associate events, with less certainty.

We note that the factors η_p and β can strongly influence the minimum photon flux density $\Phi_{\gamma,\min}$. The factor η_p is an unknown parameter that could take values up to $\eta_p \sim 100$, which are required for GRBs and blazar populations to reach the flux of observed UHECRs (e.g., Murase et al., 2006). In the following, we set $\eta_p = 1$ as a standard estimate, but most conservative limits should be obtained by multiplying $\Phi_{\gamma,\min}$ by $\eta_p = 100$ (Eq. 2.21). Moreover, we note that in the nonrelativistic case ($\beta < 1$) the minimum flux should be strongly suppressed and therefore the detectability for nonrelativistic outbursts should be favored. However, the inefficiency of acceleration processes in nonrelativistic cases could compensate for this effect, and values of $\beta \lesssim 10^{-2}$ are not favored to produce neutrinos above ~ 100 TeV.

2.3.3 Can we detect a neutrino flare?

We show in figure 2.3 the minimum photon flux required to reach the IceCube detection limit in the $L_{\text{bol}} - t_{\text{var}}$ parameter space for $\Gamma = 1, 10$, and 100 from top to bottom. We set $\eta_p = \eta_B = 1$. Depending on the SED of the emission (soft or hard before the break energy, see Sections 2.3.1 and 2.3.2), this minimum flux $\Phi_{\gamma,\min}$ should be evaluated at the minimum threshold energy ϵ_{th} indicated in red contours (for soft spectra, $a > 1$) or at the observed spectral break energy ϵ_b (for hard photon spectra, $a < 1$). For simplicity, the threshold energy has been set to its minimum value $\epsilon_{\text{th}} = \epsilon_{\text{th}}'' (1 + \beta)^2 \Gamma^2 m_p c^2 / (1 + z)^2 E_{p,\max}$.

We locate concrete examples of explosive transients in the parameter space: for $\Gamma \sim 1$ Crab flares, supernovae, and novae (list of sources taken from Kasliwal, 2011). For $\Gamma \sim 10$ and $\Gamma \sim 100$ we give the example of blazars, magnetar giant flares, TDEs, LL GRBs, and classical GRBs. These categories and specific source cases are discussed in Section 2.4 and our results are reported in Table 2.1.

In practice, here we describe how these figures can be used to determine whether an explosive transient could have a chance to be detected in neutrinos with IceCube.

1. Choose a bulk Lorentz factor Γ for the outflow.¹
2. Identify a broken power-law shape in the source emission, roughly measure the break energy ϵ_b and whether the spectrum is soft ($a > 1$) or hard ($a < 1$) below the break.
3. Locate the source in the $L_{\text{bol}} - t_{\text{var}}$ parameter space and read the required flux $\Phi_{\gamma,\min}$ (colored contours).
4. Compare $\Phi_{\gamma,\min}$ with the observed flux of the source $\Phi_{\gamma,\text{obs}}$, around the threshold energy indicated in red contours, ϵ_{th} , for soft spectra ($a > 1$), or at the break energy ϵ_b for hard spectra ($a < 1$). We recall that a neutrino flare associated with the photon flare *can* be detectable if $\Phi_{\gamma,\text{obs}} \gtrsim \Phi_{\gamma,\min}$.

We note that for many sources, $\Phi_{\gamma,\text{obs}} \ll \Phi_{\gamma,\min}$ over the whole radiation spectrum, thus the knowledge of ϵ_{th} or ϵ_b is not necessary to conclude on the non-detectability. For more refined cases, however, we caution that ϵ_{th} is a minimum value because it was derived from $E_{p,\max}$. When checking detectability, one might wish to extend the comparison between $\Phi_{\gamma,\text{obs}}$ and $\Phi_{\gamma,\min}$ for $\epsilon_{\text{th}} > \epsilon_{\text{th},\min}$, in case the neutrino spectrum reaches its peak below the energy $E_\nu = 0.05 E_{p,\max}$. Extrapolation of spectra should be conducted with care, always trying to maximize the photon flux, in order to avoid missing a detectable case. For greater accuracy, in the case of a soft photon spectrum, $E_{p,\text{high}}$ should be determined in order to calculate the threshold energy ϵ_{th}

¹ In general, for a given luminosity, a higher Γ implies a higher $\Phi_{\gamma,\min}$ (Eq. 2.21), and is thus worse in terms of constraints. This can be kept in mind for sources with large uncertainties on Γ .

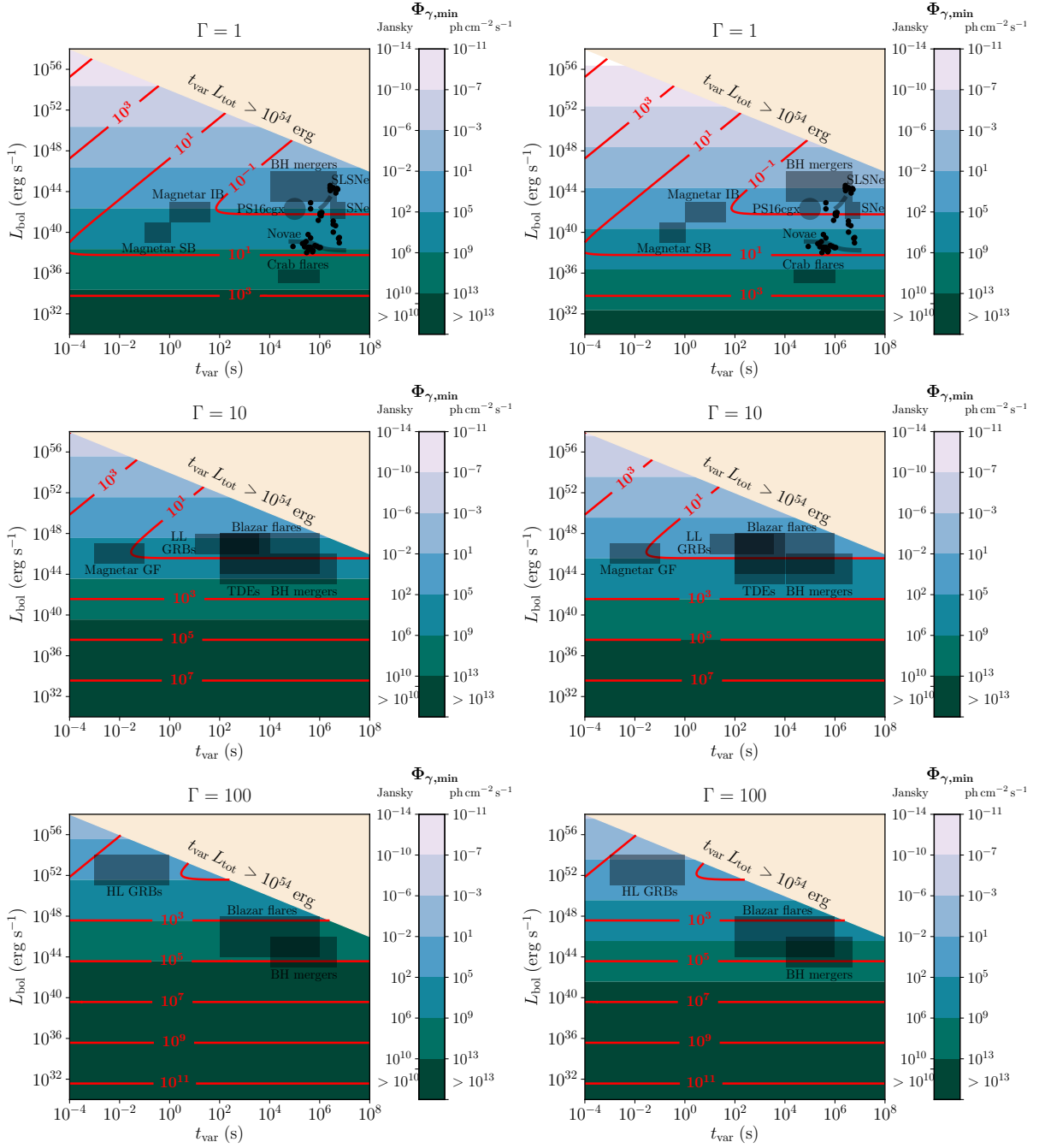


Figure 2.3: What is the minimum source photon flux required to enable neutrino detection with IceCube? The color map shows the minimum photon flux $\Phi_{\gamma, \min}$ (in Jy and ph cm $^{-2}$ s $^{-1}$) as a function of the bolometric luminosity L_{bol} and the variability timescale t_{var} of the flaring event for an outflow bulk Lorentz factor $\Gamma = 1, 10, 100$. A neutrino flare *can* be detectable if the observed photon flux $\Phi_{\gamma, \text{obs}} \gtrsim \Phi_{\gamma, \min}$, above the minimum threshold energy ϵ_{th} (red lines) for soft photon spectra, and at the observed photon break energy ϵ_b for hard spectra. Here $\eta_B = 1$. On the left $\eta_p = 1$ and on the right $\eta_p = 100$. Overlaid objects as in figure 2.2. Type Ibc supernovae should be treated with care (see Section 2.5.2).

and evaluate the observed photon flux at this energy. This point is developed in the next section, where we give several examples of neutrino spectra in our simple setup.

A quiescent photon flux from the source could be dominating the flare radiation in some regions of the spectrum. Taking these photons into account by mistake when evaluating $\Phi_{\gamma,\text{obs}}$ to compare to $\Phi_{\gamma,\text{min}}$ does not lead to false negatives (missing detectable sources) as this simply overestimates the observed flux.

The observation of type Ibc SNe with no associated GRB emission (corresponding to completely choked and misaligned GRBs) constitutes a limitation of our model. As discussed in Section 2.5.2, the material surrounding the outburst could prevent the observer from detecting it and from correctly assessing the total amount of energy and the variability of the outburst. Thus our criteria do not apply and these sources should be examined in more detail in order to conclude on their detectability.

2.4 Implications for categories of transients and specific case studies

The general approach presented up to this point allows us to evaluate the detectability in neutrinos of a large variety of explosive transients. We study the implications for general source categories in Section 5.1 and examine several concrete examples in Section 2.4.2.

2.4.1 Census of existing transients

We summarize the typical ranges of key parameters (the bolometric luminosity for equivalent isotropic emission, the variability timescale, and the bulk Lorentz factor) that intervene in the evaluation of the detectability of neutrino flares for several categories of transients. For each type of sources, we evaluate the maximum luminosity distance $D_{\text{L,max}}$ or maximum redshift z_{max} at which we can expect to detect an associated neutrino flare with IceCube. From the expression of the maximum neutrino flux, we obtain

$$D_{\text{L,max}} = \left(\frac{3}{8} f_{p\gamma} \frac{\eta_p L_{\text{bol}}}{4\pi s_{\text{exp}}} \right)^{1/2} \quad (2.22)$$

with $s_{\text{exp}} \sim S_{\text{exp}}/t_{\text{var}}$, which gives $D_{\text{L,max}} = \max(L_{\text{b}}/\epsilon_{\text{b}}, L_{\text{th}}/\epsilon_{\text{th}})^{1/2} (4\pi\Phi_{\gamma,\text{min}})^{-1/2}$ for $f_{p\gamma} < 1$. The results are reported in Table 2.1 and can be compared with the distance of real sources in Table 2.2. As the minimum photon flux $\Phi_{\gamma,\text{min}}$ is proportional to the detector sensitivity, this threshold will decrease by one or two orders of magnitude for future detectors such as IceCube-Gen2, ARA, ARIANNA, or GRAND.

Novae, supernovae, and luminous supernovae

Thermonuclear SNe, core-collapse SNe, and classical novae have been extensively studied (e.g., Kasliwal (2011) for a review). These events are well characterized by their peak luminosity ($L_{\text{b}} \sim 10^{38} - 10^{39} \text{ erg s}^{-1}$ for novae and $L_{\text{b}} \sim 10^{40} - 10^{43} \text{ erg s}^{-1}$ for ordinary SNe) and duration (between 1 and 100 days). The classical objects only populate limited regions of the parameter space, but new classes of transients with properties intermediate between novae and SNe are being discovered.

Many studies focus on quiescent neutrino emissions from supernova remnants or from hadronic interactions during the early evolution of classical supernovae (see, e.g., Bednarek et al., 2005,

for a more general review of Galactic sources of high-energy neutrinos). The low-energy neutrino emissions throughout the explosion have also been extensively studied. The early production of transient high-energy neutrinos from classical SNe or novae has scarcely been examined so far (but see, e.g., Beall and Bednarek, 2002); authors concentrate on superluminous supernovae instead, which seem indeed promising in terms of detectability following our criterion (see Table 2.1).

The radiation processes related to these explosions are generally considered as thermal emissions; the radiated energy is mainly observed in optical and UV wavelengths. However, nonrelativistic shocks may also occur during these outbursts and lead to nonthermal shock-emissions. In this case, a significant fraction of the optical emission could be shock powered. We emphasize that shocks are mainly expected to occur in dense regions, but gamma-ray emissions have also been detected from novae only a few days after the peak of the optical radiation (Ackermann et al., 2014). Therefore, particle acceleration may be at play in these objects (Metzger et al., 2015). If hadrons are accelerated at high energies, it may lead to neutrino production, but the density of hadronic background could favor purely hadronic over photohadronic neutrino production.

Hypernovae or superluminous supernovae (SLSNe) constitute a rare class of bright transients, with luminosities ten to hundreds of times that of usual core-collapse or thermonuclear SNe (Quimby, 2012). Mainly three scenarios have been proposed to explain these exceptionally luminous light curves: they could be powered by the interaction of the supernova (SN) ejecta with the circumstellar medium (e.g., Ofek et al., 2007; Quimby et al., 2011; Chevalier and Irwin, 2011; Murase et al., 2011), neutron-star-driven (Kasen and Bildsten, 2010; Dessart et al., 2012; Kotera et al., 2013; Metzger et al., 2014; Murase et al., 2015), or pair-instability-driven (Gal-Yam et al., 2009; Gal-Yam and Leonard, 2009). In the two former scenarios, associated gamma-ray emission is expected and implies shock regions that would be favorable for cosmic-ray acceleration to very high energies, and subsequent neutrino production. In particular, for neutron-star powered SNe, neutrinos can be produced by pp or $p\gamma$ interactions on the nonthermal, thermal, or baryonic fields of the ejecta (Murase et al., 2009; Fang et al., 2013a; Fang et al., 2016). Only magnetars can lead to reasonably short $t_{\text{var}} < 10^7$ s transient emissions, however, thanks to their rapid electromagnetic energy losses. For these objects, the dominant process for neutrino production is $p\gamma$ interactions on background photons that should be mostly directly observed (Kasen and Bildsten, 2010; Kotera et al., 2013).

We caution that some stripped core-collapse SNe (types Ibc, superluminous or more ordinary) could be associated with gamma-ray bursts (e.g., Modjaz, 2011; Hjorth and Bloom, 2012 for reviews). In this case, a different neutrino production mechanism (likely more efficient) might have occurred (see next sections and references therein). As discussed in Section 2.5.2, such scenarios imply that the neutrinos are a precursor of the SN emission, and our minimum flux criterion cannot be applied because the relevant radiation field could be processed in the environment and diluted over the emission timescale.

Gamma-ray bursts

Gamma-ray bursts are the most energetic and violent events observed in our Universe. In the popular fireball model, the observed photons stem from the acceleration of electrons in internal shocks of a relativistic outflow of typical bulk Lorentz factor $\Gamma \sim 10^2 - 10^3$. These events last approximately $t_{\text{GRB}} \sim 10^{-1} - 10^2$ s. They show short and puzzling variability timescales $t_{\text{var}} \sim 10^{-3} - 1$ s and very high bolometric luminosities $L_{\text{bol}} \sim 10^{49} - 10^{54}$ erg s $^{-1}$. Different categories of GRBs can be distinguished depending on their luminosity or duration. Here we focus on high-luminosity GRBs (HL GRBs), and the question of low-luminosity GRBs is discussed in Section 2.4.1. Long GRBs, with $t_{\text{GRB}} > 2$ s, are supposedly associated with the death of massive

stars, while short GRBs, with $t_{\text{GRB}} < 2\text{ s}$, are associated with compact-object binary mergers. Hence, unlike long GRBs, short GRBs are not associated with supernovae. Ghirlanda et al. (2009) highlighted similarities between the variability, the spectrum, the luminosity, and the $E_{\text{peak}} - L_{\text{iso}}$ correlation (corresponding to $E_{\text{b}} - L_{\text{bol}}$ with our notations) of short GRB and the first seconds of long GRB emission. However, the $E_{\text{peak}} - E_{\text{iso}}$ correlation (with E_{iso} the total isotropic equivalent energy) defined by long GRBs does not seem to be followed by short GRBs. Moreover, except for exceptional detections, short GRBs seem to be located at lower redshift than long GRBs – although the number of precise measurements for short GRBs remains a major limitation.

The prompt HL GRB spectra are well described by broken power-laws with typical low- and high-energy spectral indices $a \sim -1 - 2$ and $b \sim 2 - 3$ and a break at $\epsilon_{\text{b}} \sim 10 - 1000\text{ keV}$ (Ghirlanda et al., 2005). However, in many cases, the spectrum exhibits a high-energy cut-off. Therefore different spectral models have been suggested to fit the GRBs spectra, such as the ‘Band’ function, exponential cutoff power-laws, or smoothly connected broken power-laws. With these models, systematic spectral analyses of GRBs have been performed to better characterize the distribution of low- and high-energy spectral indices and of peak energies (Goldstein et al., 2013).

Numerous studies have been conducted to precisely evaluate the expected flux of neutrinos from HL GRBs (e.g., Waxman and Bahcall, 1997; Murase and Nagataki, 2006b; Murase et al., 2008 and Mészáros, 2015 for a review). Our criteria given in Table 2.1 are consistent with these works. The production of high-energy neutrinos from GRB early afterglows has also been addressed (e.g., Dermer, 2002; Murase, 2007). The detection of GeV-TeV neutrinos coincident with the prompt emission, guaranteed by recent GRB models (Murase et al., 2013), could also help constrain GRB emission mechanisms.

The IceCube searches for neutrinos produced during the prompt emission of GRBs (Aartsen et al., 2016a) have revealed no excess against the expected atmospheric background. It allows us to constrain the current models for the production of UHECRs and neutrino in GRBs (e.g., He et al., 2012; Baerwald et al., 2015).

Low-luminosity GRBs, trans-relativistic supernovae, and off-axis GRBs

Low-luminosity GRBs (LL GRBs) have been suggested as a separate population from high-luminosity GRBs (HL GRBs) (e.g., Virgili et al., 2009; Bromberg et al., 2011). LL GRBs show longer variability timescales, $t_{\text{var}} \sim 10 - 10^3\text{ s}$, lower bolometric luminosities $L_{\text{bol}} \sim 10^{46} - 10^{48}\text{ erg s}^{-1}$, a softer spectrum, and a lower break energy. They may also be characterized by lower Lorentz factors $\Gamma \sim 10$. However, other authors invoke a unified picture by interpreting LL GRBs as GRBs that are observed off-axis (Salafia et al., 2016) or as semi-choked GRBs (Nakar, 2015).

In the latter case, the singular characteristics of LL GRBs associated with SNe could be explained by the trans-relativistic shock breakout model (Soderberg et al., 2006; Nakar and Sari, 2012). When a stellar explosion occurs, the breakout of the shock going through the object generates the first observable light. In the case of a compact object or a very energetic explosion, the breakout could become mildly or ultra relativistic. Several studies focus on the cosmic rays and high-energy neutrinos from trans-relativistic supernovae shock breakouts (e.g., Budnik et al., 2008; Kashiyama et al., 2013).

The value of $\Phi_{\gamma, \text{min}}$ given in Table 2.1 assumes that neutrinos are produced in the region emitting the LL GRB radiation. However, as discussed in Section 2.5.2, the actual bolometric luminosity and the target radiation for neutrino production could be difficult to evaluate. This criterion

should therefore be viewed with care.

Blazar flares

Blazars are a subset of AGN whose jet is pointed toward the observer. Unification models (Urry and Padovani, 1995) allow to set their mean bulk Lorentz factor to $\Gamma_j \sim 10$. A blazar flare is a very fast and short increase in blazar luminosity that occurs in addition to its “quiescent” emission. In simple models, the bulk Lorentz factor Γ of the region associated with a flare is assumed to be the same as the mean bulk Lorentz factor. However, the rapid variability of blazar flares has led to more realistic scenarii where $\Gamma > \Gamma_j$ (e.g., Ghisellini et al., 2005; Giannios et al., 2009) with $\Gamma \gtrsim 100$. These models predict orphan TeV flares and TeV flares with simultaneous far-UV/soft X-ray flares, respectively.

Blazar SEDs exhibit two nonthermal peaks, at low and high energies. The low-energy part extends from radio to X-rays (in the most extreme cases), while the high-energy part extends from X-rays to gamma rays. Blazars show strongly variable emissions correlated over frequencies, with a typical variation timescale of months. They also experience flaring events with shorter timescales (e.g., Aharonian et al., 2007); thus we set $t_{\text{var}} \sim 10^2 - 10^6$ s. In some cases, Blazar flaring emissions can be described by a soft power-law from submillimeter to X-rays, with typically $L_b \sim 10^{45}$ erg s $^{-1}$ at $\epsilon_b \sim 1$ keV (Rachen and Mészáros, 1998). Hadronic and leptonic models still coexist to explain the emissions from these objects, although IceCube is expected to soon start constraining the contribution of hadrons (e.g., Petropoulou et al., 2016c).

Our estimates of $\Phi_{\gamma, \text{min}}$ show that ultrarelativistic cases with $\Gamma = 100$ are less favorable than cases with $\Gamma = 10$. Furthermore, for $\Gamma = 100$ the threshold energy falls in the low-flux region of the blazar emission.

Magnetars

Magnetars are strongly magnetized pulsars ($B \gtrsim 10^{14}$ G) with high spin-down rates. They are historically divided into two classes: soft gamma-ray repeaters (SGRs) and anomalous X-ray pulsars (AXPs). SGRs are of significant importance in this study as they exhibit several types of flaring events: short bursts (SB), intermediate bursts (IB), and giant flares (GF). Short bursts are characterized by $t_{\text{var}} \sim 10^{-1} - 1$ s, $L_b = 10^{39} - 10^{41}$ erg s $^{-1}$ with soft spectra at ~ 10 keV. Intermediate bursts are characterized by $t_{\text{var}} \sim 1 - 40$ s, $L_b = 10^{41} - 10^{43}$ erg s $^{-1}$ with similar spectra. Giant flares are rarer, with a first violent emission (the initial spike) followed by a longer pulsating tail lasting $t \sim 100$ s (Woods and Thompson, 2006; Mereghetti, 2008; Turolla et al., 2015). The initial spike is characterized by $t_{\text{var}} \sim 10^{-1}$ s, $L_b = 10^{44} - 10^{47}$ erg s $^{-1}$ and a very hard spectrum, detected up to 2 MeV, with a peak around 10^5 eV. It is not clear whether a cooling blackbody or an exponentially cutoff power-law fits the observed spectra best. Moreover, the value of Γ is uncertain and strongly depends on the model adopted to describe the flares. A bulk Lorentz factor $\Gamma = 10$ is sometimes assumed for giant flares, see, for example, Lyutikov (2006).

Ioka et al. (2005) estimated neutrino fluxes from magnetar giant flares by considering proton-proton interactions and photohadronic interactions with photospheric thermal radiation. Photohadronic interactions with nonthermal photon fields are considered to be negligible. The case of SGR 1806-20 is also studied by using a fireball model, and promising estimates are calculated, see Section 2.4.2 for more detail. As we consider flaring emissions of neutrinos and not steady emissions (the variability timescale of the neutrino flare should be in the order of the variability timescale of the giant flares), and as we do not consider a specific model for magnetar giant

flares, we focus here on photohadronic interactions with the main radiation field, assumed to be nonthermal.

Tidal disruption events

Tidal disruption events are assumed to result from the disruption of a star approaching a supermassive black hole. Numerous TDE candidates are known today (Komossa, 2015), but several events, referred to as jetted TDEs, show very interesting properties, for example, Swift J1644+57 (Cummings et al., 2011) and Swift J1112-8238 (Brown et al., 2015). Compared to the GRBs, these transients have extremely long durations: the flare rise time is approximately ~ 100 s and its duration $\sim 10^3 - 10^4$ s. Typical peak luminosities are $L_b \sim 10^{43} - 10^{48} \text{ erg s}^{-1}$ (e.g., Donley et al., 2002a; Burrows et al., 2011) with a peak in hard X-rays or soft gamma rays. The lack of spectral information about jetted TDEs does not allow us to characterize the TDE spectra precisely. However, from the observation of Swift J1644+57, we assume that jetted TDEs are characterized by nonthermal and hard spectra ($a < 1$). The emission is most likely relativistic, with a bulk Lorentz factor $\Gamma \sim 10$. Several studies predict a possible acceleration of UHECRs in TDE, for instance, Farrar and Gruzinov (2009), Farrar and Piran (2014), and Pfeffer et al. (2015). Others directly address the question of neutrino production (Dai and Fang, 2016; Lunardini and Winter, 2016; Senno et al., 2016b).

Black hole, neutron star, and white dwarf mergers

The recent detection of gravitational waves by the LIGO collaboration (Abbott et al., 2016b; Abbott et al., 2016a) has generated considerable interest in mergers of compact objects. Black hole (BH) mergers are at the origin of most of the detected emissions. Mergers of other compact objects, such as neutron star (NS) or white dwarf (WD) mergers, can also produce gravitational waves. Given the huge amount of energy released during the merger of two compact objects, electromagnetic counterparts are often contemplated.

The existence of an electromagnetic counterpart to BH mergers as well as a counterpart in ultrahigh-energy cosmic rays and neutrinos have been proposed by Kotera and Silk (2016) and Murase et al. (2016). In this scenario, a powerful electromagnetic outflow is generated through the Blandford-Znajek process (Blandford and Znajek, 1977), and an associated luminosity can be roughly estimated (Lyutikov, 2011): $L_{\text{BZ}} \sim 3.2 \times 10^{46} \text{ erg s}^{-1} M_{100}^3 B_{11}^2 R_s/R$, where M is the mass of the final black hole, B is the external magnetic field strength, and the orbital radius is approximated by the Schwarzschild radius R_s . Therefore, we set $L_{\text{bol}} \sim 10^{43} - 10^{46} \text{ erg s}^{-1}$ for BH mergers. A variability timescale for electromagnetic emissions $t_{\text{var}} \sim 10^4 - 5 \times 10^6$ can be postulated, as it allows us to reproduce the observed ultrahigh-energy cosmic-ray flux with a population of BH mergers. This represents a comfortable fraction of the maximum duration of the BZ process: $t_{\text{BZ}} \sim 22 \text{ yr} M_{100} B_{11}^{-2} (R_s/R)^2$, which can be sustained as long as accretion is sustained – through disruption of planetary or asteroidal debris, for example.

Neutron star mergers are also studied in a multi-messenger perspective. They are associated with the production of short GRBs or have been proposed as possible candidates for the production of UHECR and neutrinos if the merger produces a magnetar (Piro and Kollmeier, 2016). The typical spin-down time and spin-down luminosity of magnetars allows us to roughly estimate the variability timescale and maximum bolometric luminosity of the emissions: $t_{\text{var}} \sim 10^3 - 10^4$ s and $L_{\text{bol}} \sim 10^{46} - 10^{48} \text{ erg s}^{-1}$.

Last, WD mergers have been proposed as a source of high-energy neutrinos (Xiao et al., 2016). The variability timescale is obtained from the viscous time, and we take a rough estimate $t_{\text{var}} \sim 10^2 - 10^4$ s. The maximum bolometric luminosity is obtained from the magnetic luminosity

Category	Γ	t_{var} (s)	L_{bol} (erg s $^{-1}$)	$E_{p,\text{max}}$ (PeV)	$E_{\nu,\text{max}}$ (PeV)	$\epsilon_{\text{th}} [\epsilon_{\text{b}}]$ (eV)	$\eta_p \Phi_{\gamma,\text{min}}$ (ph cm $^{-2}$ s $^{-1}$)	$D_{\text{L,max}} [z_{\text{max}}]$
HL GRBs	300	$10^{-3} - 1$	10^{49-54}	10^{4-6}	$1 - 10^3$	$10 - 10^3$	10^{4-9}	2 Gpc
HL GRBs	100	$10^{-3} - 1$	10^{49-54}	10^{3-5}	$10^{-2} - 10^3$	$10 - 10^3$	10^{2-7}	2 Gpc
Blazar flares		$10^2 - 10^6$	10^{44-48}	10^{2-4}	$10 - 10^3$	$10^3 - 10^5$	10^{8-12}	2 Gpc
BH mergers		$10^4 - 10^{6.7}$	10^{43-46}	10^{1-3}	$1 - 10^2$	$10^4 - 10^5$	10^{10-13}	—
NS mergers		$10^3 - 10^4$	10^{46-48}	10^{3-4}	$10^2 - 10^3$	$10^3 - 10^4$	10^{8-10}	—
WD mergers		$10^2 - 10^4$	10^{44-46}	10^{2-3}	$1 - 10^2$	$10^4 - 10^5$	10^{10-12}	—
Blazar flares	10	$10^2 - 10^6$	10^{44-48}	10^{3-5}	$10 - 10^4$	$0.1 - 10$	10^{4-8}	2 Gpc
LL GRBs		$10 - 10^3$	10^{46-48}	10^{4-5}	$10 - 10^3$	$0.1 - 1$	10^{4-6}	60 Mpc
Magnetar GF		$10^{-3} - 0.1$	10^{44-47}	10^{3-4}	$10^{-3} - 1$	$[10^5]$	10^{5-8}	200 kpc
TDEs		$10^2 - 10^4$	10^{43-48}	10^{2-5}	$10 - 10^3$	$[10^4]$	10^{4-9}	200 Mpc
BH mergers		$10^4 - 10^{6.7}$	10^{43-46}	10^{2-4}	$10 - 10^3$	$1 - 10^2$	10^{6-9}	—
NS mergers		$10^3 - 10^4$	10^{46-48}	10^{4-5}	$10^2 - 10^4$	$10^{-1} - 10$	10^{4-6}	—
WD mergers		$10^2 - 10^4$	10^{44-46}	10^{3-4}	$10^2 - 10^3$	$1 - 10^2$	10^{6-8}	—
SLSNe	1	$10^5 - 10^7$	10^{43-45}	10^{4-5}	$10 - 10^3$	$10^{-3} - 10^{-2}$	10^{2-4}	200 Mpc
SNe		$10^5 - 10^7$	10^{40-43}	10^{2-4}	$10 - 10^3$	$10^{-2} - 1$	10^{4-7}	20 Mpc
Novae		$10^5 - 10^7$	10^{38-40}	10^{1-2}	$1 - 10$	$1 - 10$	10^{7-9}	4 kpc
Magnetar IB		$1 - 40$	10^{41-43}	10^3	$0.1 - 1$	$0.1 - 1$	10^{4-6}	40 kpc
Magnetar SB		$0.1 - 1$	10^{39-41}	10^2	10^{-2}	0.1	10^{6-8}	600 pc
BH mergers		$10^4 - 10^{6.7}$	10^{43-46}	10^{3-5}	$1 - 10^2$	$10^{-3} - 10^{-2}$	10^{1-4}	—
NS mergers		$10^3 - 10^4$	10^{46-48}	10^{2-3}	$10^{-2} - 1$	$10^{-2} - 10^{-1}$	10^{-1-1}	—
WD mergers		$10^2 - 10^4$	10^{44-46}	10^{2-4}	$10^{-2} - 10$	$10^{-2} - 10^{-1}$	10^{1-3}	—

Table 2.1: Typical properties of different flaring source categories. We recall the ranges of values for the bulk Lorentz factor Γ , time variability t_{var} , and apparent bolometric luminosity L_{bol} for each category and the derived maximum energy of protons $E_{p,\text{max}}$, maximum energy of neutrinos $E_{\nu,\text{max}}$, threshold energy ϵ_{th} (for soft photon spectra), and the required flux for detectability $\Phi_{\gamma,\text{min}}$. The flux can be converted from ph cm $^{-2}$ s $^{-1}$ into Jy by multiplying by $\sim 10^{-3}$. $D_{\text{L,max}}$ or z_{max} are the order of magnitude of the maximum distance or redshift at which we can expect to detect an associated neutrino flare with IceCube. Here $\eta_B = \eta_p = 1$, but the most conservative estimate should use $\eta_p = 100$. Starred types of sources should be viewed with care because of possible hidden radiation (Section 2.5.2).

$L_{\text{bol}} \sim 10^{44} - 10^{46}$ erg s $^{-1}$. In these cases, if the debris disk surrounding the central object is optically thick, the high-energy photons can be hidden from the observer. However, a bright optical counterpart with $L \sim 10^{41} - 10^{42}$ erg s $^{-1}$ may be observable (Beloborodov, 2014).

The Lorentz factors for these mergers being difficult to infer from current data and theory (their acceleration region could equally resemble GRBs or blazar jets, or have $\Gamma \sim 1$), we show in Table 2.1 the estimates for different Γ . Maximum distances are not calculated because we lack of information on the spectral shape of the radiation.

2.4.2 Case studies

Naked-eye GRB 080319B

An exceptional burst was detected on 2008 March 19 by the Swift and Konus-Wind satellites (Racusin et al., 2008b). This long-duration burst, with $t \sim 50$ s, was characterized by an extreme isotropic equivalent luminosity at peak: $L_{\text{iso,peak}} \sim 10^{53}$ erg s $^{-1}$ at $\epsilon_{\text{b}} \sim 540 - 740$ keV (Racusin et al., 2008a), with a redshift $z \sim 0.937$ (Vreeswijk et al., 2008). It was the brightest GRB ever detected in optical and reached a magnitude $m_{\text{V,peak}} \sim 5.3$ (Bloom et al., 2009). Observations suggested a very high bulk Lorentz factor $\Gamma = 300 - 1400$. The burst time variability depends on the energy (Margutti et al., 2008; Abbasi et al., 2009), here we consider a broad range: $t_{\text{var}} \sim 0.01 - 1$ s. The photon index deduced from high-energy data softens rapidly with time:

Source	Γ	t_{var} (s)	L_{bol} (erg s $^{-1}$)	$E_{p,\text{max}}$ (PeV)	$E_{\nu,\text{max}}$ (PeV)	$\epsilon_{\text{th}} [\epsilon_b]$ (eV)	$\Phi_{\gamma,\text{min}}$ (ph cm $^{-2}$ s $^{-1}$)	$\Phi_{\gamma,\text{obs}}$ (ph cm $^{-2}$ s $^{-1}$)	$D_L [z]$
GRB 080319B	300	$10^{-2} - 1$	10^{53}	10^{5-6}	$10 - 10^3$	$10 - 10^2$	4×10^5	$10 - 10^4$	[0.937]
GRB 100316D	10	$10^2 - 10^3$	10^{47}	10^{4-5}	$10^2 - 10^3$	1	5×10^5	$10^{-1} - 1$	260 Mpc
PKS 1424-418	10	$10^4 - 10^5$	2×10^{48}	10^5	$10^3 - 10^4$	0.1	3×10^4	3×10^2	[1.522]
SGR 1806-20	10	$10^{-3} - 10^{-2}$	2×10^{47}	10^2	$10^{-3} - 10^{-2}$	[10 5]	3×10^5	[10 7]	15 kpc
Swift J1644+57	10	10^2	4×10^{48}	10^5	10	[10 4]	1×10^4	[0.6]	1.8 Gpc
PS16cgx	1	10^5	$10^{42} - 10^{43}$	10^{3-4}	10^2	$10^{-2} - 0.1$	3×10^4	8×10^{-1}	[0.1 - 0.2]
Crab Flares	1	$10^4 - 10^6$	$10^{35} - 10^{36}$	1	$10^{-2} - 10^{-1}$	10^2	3×10^{11}	$< 10^{-2}$	1.9 kpc

Table 2.2: Properties of concrete sources as an illustration of the categories presented in Table 2.1. The luminosity distance D_L or the redshift z of each source is also specified. The flux $\Phi_{\gamma,\text{min}}$ is the minimum flux required to reach the IceCube sensitivity limit, at threshold energy ϵ_{th} or at break ϵ_b , to be compared with the observed flux of the source $\Phi_{\gamma,\text{obs}}$ at that energy. Fluxes calculated at ϵ_b are indicated in brackets. Here $\eta_B = \eta_p = 1$, but the most conservative estimate should use $\eta_p = 100$. Starred sources should be viewed with care because of possible hidden radiation (Section 2.5.2).

$a = 1.0 - 2.1$ (Racusin et al., 2008a, figure 2). The IceCube detector performed searches for muon neutrinos from GRB 080319B, but did not find significant deviation from the background (Abbasi et al., 2009).

From the properties of GRB 080319B, with the assumption $\Gamma \sim 300$, we obtain $E_{p,\text{max}} \sim 10^{20} - 10^{21}$ eV, $E_{\nu,\text{max}} \sim 10^{15} - 10^{17}$ eV, $\epsilon_{\text{th}} \sim 10 - 100$ eV (soft case), $D_{\text{eff}} \sim 10^{-2}$ and $\eta_p \Phi_{\gamma,\text{min}} \sim 10^5 - 10^6$ ph cm $^{-2}$ s $^{-1}$. The flux of the source at 10 and 100 eV is difficult to estimate because we lack data at these energies. However, we note that the source reached a flux $10 \text{ Jy} \sim 10^4$ ph cm $^{-2}$ s $^{-1}$ at 5 eV and $10^{-2} \text{ Jy} \sim 10$ ph cm $^{-2}$ s $^{-1}$ at 10 5 eV (Racusin et al., 2008a, figure 3). We note that a baryon loading $\eta_p \sim 10^2$ is required to reach the first detection criterion with efficient pion production. Therefore, despite its extreme brightness, this GRB lies below the IceCube detection limit for $\eta_p < 10^2$.

GRB 100316D

The GRB 100316D was detected on 2010 March 16 by the Swift satellite (Starling et al., 2011; Fan et al., 2011). This long-duration (~ 1300 s) and low-luminosity GRB was associated with the energetic SN 2010bh (Wiersema et al., 2010), identified as a type Ic supernova. This LL GRB could therefore be related to a semi-choked jet (see Section 2.5.2). It was located nearby, at $z = 0.059$ (Vergani et al., 2010), and was characterized by a low bolometric luminosity $L_{\text{bol}} \sim 10^{47}$ erg s $^{-1}$ at peak energy $\epsilon_b \sim 20$ keV. As the event showed a smooth rise, we set $t_{\text{var}} \sim 10^2 - 10^3$ s.

As a first estimate, we consider that the emission of GRB 100316D was not choked. We assume $\Gamma \sim 10$ (it may be lower, see, e.g., Margutti et al., 2013), and we obtain $E_{p,\text{max}} \sim 10^{19} - 10^{20}$ eV, $E_{\nu,\text{max}} \sim 10^{16} - 10^{17}$ eV, $\epsilon_{\text{th}} \sim 0.1$ eV, $D_{\text{eff}} \sim 6 \times 10^{-3}$ and $\eta_p \Phi_{\gamma,\text{min}} \sim 100 \text{ Jy} \sim 10^5 - 10^6$ ph cm $^{-2}$ s $^{-1}$. No counterpart was detected at ~ 0.1 eV, so that we can only give a rough estimate of the source flux: at peak $\Phi_{\gamma,\text{obs}}(\epsilon_b) \sim 10^{-1}$ ph cm $^{-2}$ s $^{-1}$ and at 1 eV, $\Phi_{\gamma,\text{obs}}(1 \text{ eV}) \lesssim 1$ ph cm $^{-2}$ s $^{-1}$. For lower values of the bulk Lorentz factor, for example, $\Gamma = 2$, $\Phi_{\gamma,\text{min}} \sim 10^2 - 10^3$ ph cm $^{-2}$ s $^{-1}$. In any case, a baryon loading $\eta_p \gtrsim 200$ is required to reach the first detection criterion $D_{\text{eff}} \geq 1$, and thus the source flux is far below the IceCube sensitivity limit for $\Gamma = 10$.

We note that if GRB 100316D was a semi-choked jet, neutrinos should be searched around 100 - 1000 s before the onset of photon emission (Senno et al., 2016a). The reported absence of precursor neutrinos with IceCube could be used to constrain the thickness of the extended

material around the source in the semi-choked model of LL GRBs.

Candidate cosmic neutrino and PS16cgx

After the detection of the candidate cosmic neutrino IceCube-160427A (Blaufuss, 2016), Pan-STARRS, the Fermi Gamma-ray Burst Monitor and the Palomar 48-inch Oschin telescope carried out a follow-up in order to identify potential sources (Smartt et al., 2016; Blackburn et al., 2016; Singer et al., 2016). Pan-STARRS identified seven supernova candidates (Smartt et al., 2016). We focus on the most interesting candidate, PS16cgx, consistent with a type Ic supernova, and possibly a choked-jet or an off-axis GRB.

Its apparent magnitude $i = 21.84$ rose by 0.4 during two days. Therefore we set $t_{\text{var}} \sim 10^5$ s. The flux is approximately $F_{\text{obs}} \sim 7.5 \times 10^{-14}$ erg cm $^{-2}$ s $^{-1}$. If the object is indeed a Ic supernova at $z \sim 0.1 - 0.2$, its peak luminosity is $L_b \sim 10^{42} - 10^{43}$ ergs $^{-1}$. If the candidate is indeed a supernova, the outflow is nonrelativistic and the bulk Lorentz factor is $\Gamma \sim 1$. We obtain $E_{\nu, \text{max}} \sim 100$ PeV, $\epsilon_{\text{th}} \sim 0.1$ eV, $D_{\text{eff}} \sim 4 \times 10^{-6}$ and $\Phi_{\gamma, \text{min}} \sim 10^5$ ph cm $^{-2}$ s $^{-1}$. These values are rough estimates as the uncertainty on the distance is high. Assuming that the whole observed luminosity is emitted at the threshold energy $\epsilon_{\text{th}} \sim 0.1$ eV, we calculate that the flux at this energy is $\Phi_{\gamma, \text{obs}} \sim 0.8$ ph cm $^{-2}$ s $^{-1} \ll \Phi_{\gamma, \text{min}}$. But even in the most favorable case with efficient photohadronic interactions, a baryon loading $\eta_p \gtrsim 10^5$ would be required for detectability, which seems unlikely. We conclude that we should not observe neutrino flares from this source with IceCube (produced through photohadronic interactions).

However, PS16cgx could have hosted a choked GRB jet. In that case, we expect that the neutrino event has been detected before the SN radiation emission, which seems to be compatible with the observations. More details on the light curve of the source and its spectral evolution are necessary to conclude. We cannot exclude either that the neutrino event was part of a relatively long emission ($>$ months) produced by pp interactions on the SN ejecta. PS16cgx could also be an off-axis GRB that seeded magnetically isotropized accelerated protons in its environment, producing a neutrino flux through interactions on the photon or baryonic backgrounds in the GRB cocoon or the SN ejecta, again on longer timescales. In these cases, more events should be found after integration over several months.

‘BigBird’ and PKS 1424-418 major outburst

The IceCube Collaboration has detected astrophysical neutrinos up to PeV energies (Aartsen et al., 2014a). For the third PeV event (IC 35, $E_\nu \sim 2$ PeV), searches for coincidence with AGN flares revealed a possible association with the major outburst of the Blazar PKS 1424-418 (Kadler et al., 2016), located at redshift $z = 1.522$. A bright gamma-ray emission (Ojha and Dutka, 2012) and an increase in X-ray (Ciprini and Cutini, 2013), optical (Hasan et al., 2013), and radio (Nemenashi et al., 2013) emissions were observed between 2012 and 2013.

The outburst lasted more than six months; we consider a time variability comparable with the initial rise time: $t_{\text{var}} \sim 10^4 - 10^5$ s. The peak luminosity is $L_b \sim 2 \times 10^{48}$ ergs $^{-1}$. In the case $\Gamma \sim 10$ (as is commonly assumed for blazar flares; for estimates of the bulk Lorentz factors of blazar jets, see, e.g., Lähteenmäki and Valtaoja, 1999; Ghisellini et al., 1993; Britzen et al., 2007; Readhead, 1994; Hovatta et al., 2009; Jorstad et al., 2005), the threshold energy is $\epsilon_{\text{th}} \sim 0.1$ eV (for $E_p = E_{p, \text{max}} \sim 10^{20}$ eV), $D_{\text{eff}} \sim 6 \times 10^{-3}$ and $\Phi_{\gamma, \text{min}} \sim 3 \times 10^4$ ph cm $^{-2}$ s $^{-1}$. The detected flux is $\Phi_{\gamma, \text{obs}}(\epsilon_{\text{th}}) \sim 3 \times 10^2$ ph cm $^{-2}$ s $^{-1}$. We see that $\eta_p \gtrsim 10^2 - 10^3$ would be required for detectability with IceCube. We note that Kadler et al. (2016) calculated a maximum number of PeV neutrinos of 4.5 for the three-year IceCube period. According to our calculations, this

would require a high baryon loading factor in the source. Therefore, the association between the neutrino event and the blazar outburst remains unclear.

SGR 1806-20

A magnetar giant flare was detected on 2004 December 27 by INTEGRAL and GRB detectors (Borkowski et al., 2004; Hurley et al., 2004; Boggs et al., 2005; Mazets et al., 2004; Palmer et al., 2005). This is the third of the three magnetar giant flares that have been detected until now. They are usually characterized by a short initial spike and a long pulsating tail. The initial spike lasted approximately 0.2 s, with a rise time $\sim 10^{-3}$ s and a fall time ~ 0.065 s, therefore we consider $t_{\text{var}} \sim 10^{-3} - 10^{-2}$ s. From Corbel and Eikenberry (2004), $D_L \sim 15$ kpc and therefore $L_{\text{iso,b}} \sim 2 \times 10^{47} \text{ erg s}^{-1}$ with $\epsilon_b \sim 10^5$ eV (Hurley et al., 2005; Terasawa et al., 2005).

Assuming $\Gamma \sim 10$, as suggested in (Lyutikov, 2006), we obtain $E_{p,\text{max}} \sim 10^{17} - 10^{18}$ eV, $E_{\nu,\text{max}} \sim 10^{11} - 10^{12}$ eV, $\epsilon_{\text{th}} \sim 10 - 10^2$ eV, $D_{\text{eff}} \sim 3 \times 10^1$ and $\eta_p \Phi_{\gamma,\text{min}} \sim 10^5 \text{ ph cm}^{-2} \text{ s}^{-1}$. A low-energy power law $\epsilon^{-1} dN/d\epsilon \propto \epsilon^{-0.2}$ has been used to fit observations (Palmer et al., 2005). This is a very hard spectrum, therefore we calculate the observed flux at break $\Phi_{\gamma,\text{obs}}(\epsilon_b) \sim 10^7 \text{ ph cm}^{-2} \text{ s}^{-1}$. The parameter $D_{\text{eff}} > 1$ is significantly high and leaves room for a possible detection for $\eta_p \gtrsim 3 \times 10^{-2}$. We note that $E_{\nu,\text{max}}$ lies just above the energy for which the IceCube sensitivity is diminished by the atmospheric neutrino background. Following the method presented in section 2.4.3, we can examine the possible neutrino spectral shapes. We see that we can have $E_{\nu,\text{high}} > E_{\nu,\text{max}}$, but at the cost of a neutrino flux suppression compared to its maximum achievable value.

If a higher Lorentz factor of the outflow is assumed, for example, $\Gamma \sim 10^2$ (Ioka et al., 2005), we obtain $E_{\nu,\text{max}} \sim 10^{15} - 10^{16}$ eV, $\epsilon_{\text{th}} \sim 10^2$ eV, and $\eta_p \Phi_{\gamma,\text{min}} \sim 10^8 \text{ ph cm}^{-2} \text{ s}^{-1}$. A baryon loading $\eta_p \gtrsim 10$ is therefore required for detectability.

Ioka et al. (2005) calculated the neutrino energies and fluxes for a baryon-poor model (BP) and a baryon-rich model (BR). They obtained $\Phi_{\nu,p\gamma}^{\text{BP}} \sim 7 \times 10^{-13} \text{ GeV}^{-1} \text{ cm}^{-2} \text{ s}^{-1}$ for the baryon-poor model, with a typical neutrino energy at $E_{\nu}^{\text{BP}} \sim 8 \times 10^5 \text{ GeV}$. It yields a fluence of $4 \times 10^{-5} \text{ GeV cm}^{-2}$. The BR case is more favorable as the fluence is about three orders of magnitude above the IceCube detection limit (as in our estimates). In this model the neutrino typical energy is lower (around 10 TeV), however, and hadronic emissions dominate.

Swift J1644+57

An interesting flaring event, initially discovered as GRB 110328A, was detected on March 28, 2011 by Swift-BAT (Cummings et al., 2011). The detection of consecutive bursts during the following 48 hours by Swift-BAT (Suzuki et al., 2011) and of a quiescent optical counterpart by the Palomar Transient Factory (Cenko et al., 2011) disfavored the hypothesis of a cosmological long-duration GRB. A precursor of the first flare was also discovered in archival data. The observations suggested a sudden accretion onto a massive black hole with a mildly relativistic outflow $\Gamma \sim 10$ (Bloom et al., 2011). Several X-ray flares lasting $\sim 10^3 - 10^4$ s occurred during $\sim 10^7$ s. They were separated by quiescent periods of $\sim 5 \times 10^4$ s and exhibited very short rise times ~ 100 s, therefore we set $t_{\text{var}} \sim 100$ s. From optical, near-infrared, and radio observations, the emission came from a source located within 150 pc of the center of a compact galaxy at redshift of $z = 0.354$ (Levan et al., 2011). The flares were characterized by an isotropic luminosity at break $L_{\text{iso,b}} \sim 4 \times 10^{48} \text{ erg s}^{-1}$ at $\epsilon_b \sim 10$ keV (Burrows et al., 2011).

With our model we obtain $E_{p,\text{max}} \sim 10^{19}$ eV, $E_{\nu,\text{max}} \sim 10^{15} - 10^{16}$ eV, $\epsilon_{\text{th}} \sim 1$ eV, $D_{\text{eff}} \sim 5 \times 10^{-4}$ and $\eta_p \Phi_{\gamma,\text{min}} \sim 10^4 \text{ ph cm}^{-2} \text{ s}^{-1}$. As the spectrum is hard ($a < 1$) between near-infrared and

X-rays, we evaluate the flux of the source at break energy: $\Phi_{\gamma,\text{obs}}(\epsilon_b) \sim 0.6 \text{ ph cm}^{-2} \text{ s}^{-1}$. This observed flux, as well as the parameter D_{eff} are far from the IceCube detection requirement, for which $\eta_p \gtrsim 10^3$ would be required.

Crab flares and the April 2011 superflare

Since 2010, violent and brief gamma-ray emissions have been detected in the Crab nebula by AGILE and Fermi/LAT. They led to numerous theoretical models, involving stochastic acceleration processes or magnetic reconnection (Clausen-Brown and Lyutikov, 2012; Cerutti et al., 2012; Cerutti et al., 2013a; Cerutti et al., 2014). The first flares were detected in September 2010 (Tavani et al., 2010, Buehler et al., 2010, Tavani et al., 2011 and Abdo et al., 2011), and indications of optical and X-ray counterparts were detected afterward by HST and Chandra experiments (Tennant et al., 2010, Ferrigno et al., 2010, Horns et al., 2010 and Tavani et al., 2011). Other flaring events were identified afterward in the 2007 and 2009 archival data. In April 2011, a particularly intense flare was also observed (Striani et al., 2011 and Buehler et al., 2012). Another flare was detected during the next years (e.g., Ojha et al., 2013, Verrecchia et al., 2013), but without exceeding the intensity of the 2011 superflare. These flares last approximately a week, but can also exhibit internal variability or very short rise-time (Balbo et al., 2011; Striani et al., 2011). The shortest variability timescale reported is in the range of 6 to 10 hours, thus, $t_{\text{var}} \sim 2 \times 10^4 - 6 \times 10^5 \text{ s}$. The peak luminosity during the flaring events are typically $L_b \sim 10^{35} - 10^{37} \text{ erg s}^{-1}$ at $\epsilon_b \sim 200 \text{ MeV}$. These events can reach more than three times the averaged luminosity of the Crab nebula.

Here we focus on the most extreme 2011 superflare. It is characterized by $t_{\text{var}} \sim 6 \text{ h}$ and $L_{\text{bol}} \sim 2 \times 10^{36} \text{ erg s}^{-1}$. Models propose $\Gamma = 1 - 5$ (e.g., Bednarek and Idec, 2011; Komissarov and Lyutikov, 2011; Clausen-Brown and Lyutikov, 2012). This case is on the border between soft and hard spectra: $a = 1.27 \pm 0.12$ (Weisskopf et al., 2013, figure 8).

The maximum energy of neutrinos is slightly above 100 TeV, which is in the IceCube detection range; but atmospheric neutrinos could make the detection difficult. The detectability parameter is $D_{\text{eff}} \sim 1$. The flux required for detection is about $\Phi_{\gamma,\text{min}} \sim 10^8 \text{ Jy}$ at a threshold energy $\epsilon_{\text{th}} \sim 100 \text{ eV}$. The flux associated with the flares at $\epsilon_{\text{th}} \sim 100 \text{ eV}$ can be estimated to be $\Phi_{\gamma,\text{obs}}^{\text{th}} \sim 10^{-7} - 10^{-5} \text{ Jy}$. The difference between the required and observed fluxes exceeds thirteen orders of magnitude; this result does not seem very promising for the detection of neutrinos from Crab flares, because of the very low efficiency neutrino production in these objects.

2.4.3 From cosmic-ray to neutrino spectra

In order to illustrate the various cases mentioned above, we calculate indicative neutrino spectral shapes, for various photon and proton spectral indexes and identify several characteristic energies. The lowest energy neutrinos are produced by the interaction between low energy protons and high energy photons, above the spectral break. As $b > 2$ and given the theoretical constraints on α , the neutrino spectrum $E_\nu^2 F_\nu \propto E_\nu^{1-\alpha+b}$ has a positive slope at these energies. The neutrino energy corresponding to the break in the photon spectrum is given by

$$E_{\nu,\text{break}} \simeq 0.05 \frac{\delta^2 m_p c^2 \epsilon_{\text{th}}''}{(1+z)^2 \epsilon_b}. \quad (2.23)$$

At higher energies, several additional effects need to be considered, and lead to a large variety of neutrino spectra. The spectral shape differs if the neutrino energy is below or above the break energy and if the photon spectrum above the spectral break is hard or soft. Without additional

effects, $E_\nu^2 F_\nu \propto E_\nu^{1-\alpha+b}$ below $E_{\nu,\text{break}}$, and above $E_\nu^2 F_\nu \propto E_\nu^{1-\alpha+a}$ for a soft spectrum and $E_\nu^2 F_\nu \propto E_\nu^{-\alpha}$ for a hard spectrum, until the exponential suppression at $E_{\nu,\text{cutoff}} = 0.05 E_{p,\text{max}}$, as illustrated in figure 2.4. Efficient pion production with $f_{p\gamma} = 1$ leads to $E_\nu^2 F_\nu \propto E_\nu^{2-\alpha}$. If the photon spectrum is soft, the energy above which photohadronic interactions become very efficient, i.e. $t'_{\text{dyn}}/t'_{p\gamma} > 1$, is given by

$$E_{\nu,\text{eff}} = 0.05 \left[\frac{a-b}{1-b} + \frac{4\pi c^2 \delta^4 (1+z) t_{\text{var}} (a-1) \epsilon_b}{\langle \sigma_{p\gamma} \kappa_{p\gamma} \rangle L_b} \right]^{\frac{1}{a-1}} \frac{\delta^2 m_p c^2 \epsilon''_{\text{th}}}{(1+z)^2 \epsilon_b}, \quad (2.24)$$

above $E_{\nu,\text{break}}$ and

$$E_{\nu,\text{eff}} = 0.05 \left[\frac{4\pi c^2 \delta^4 (1+z) t_{\text{var}} (b-1) \epsilon_b}{\langle \sigma_{p\gamma} \kappa_{p\gamma} \rangle L_b} \right]^{\frac{1}{b-1}} \frac{\delta^2 m_p c^2 \epsilon''_{\text{th}}}{(1+z)^2 \epsilon_b}, \quad (2.25)$$

below $E_{\nu,\text{break}}$. Moreover, suppression can add a E_ν^{-1} or E_ν^{-2} factor, for adiabatic or synchrotron cooling respectively, and occurs at $E_{\nu,\text{sup}} = 0.5 E_{\mu,\text{max}}^{\text{decay}}$ for adiabatic or synchrotron cooling of muons, as defined in section 2.2.3. We note that the indicative neutrino maximum energy calculated previously is given by $E_{\nu,\text{max}} = \min(E_{\nu,\text{sup}}, E_{\nu,\text{cutoff}})$. Two additional examples of spectra are illustrated in figure 2.4 where we can see the impact of efficient pion production and cooling. We emphasize that the spectra shown in this section are only indicative: the shape of realistic neutrino spectra can be influenced by additional effects, as pions and muons could experience additional cooling mechanisms (e.g. $\pi\gamma$ interactions), and as all neutrino are not produced by muons but also by pions, which experience less energy losses than muons.

In order to determine the peak energy of the neutrino spectrum $E_{\nu,\text{high}}$ and the corresponding proton energy $E_{p,\text{high}} = 20 E_{\nu,\text{high}}$, one needs to consider the aforementioned effects. For one given source, calculating the energies mentioned above allows already to constrain the peak energy, as $\min(E_{\nu,\text{break}}, E_{\nu,\text{eff}}, E_{\nu,\text{sup}}) \leq E_{\nu,\text{high}} \leq E_{\nu,\text{cutoff}}$. Finding the precise value of the peak energy is difficult without the knowledge of the proton spectra characteristics. For example, we consider the case where $E_{\nu,\text{break}} < \min(E_{\nu,\text{eff}}, E_{\nu,\text{sup}}, E_{\nu,\text{cutoff}})$ for a hard photon spectrum ($a < 1$). Without suppression due to secondary losses, $E_\nu^2 F_\nu \propto E_\nu^{2-\alpha}$ above $E_{\nu,\text{break}}$. Suppression can bring an additional E_ν^{-1} or E_ν^{-2} factor, for adiabatic or synchrotron cooling respectively. Due to the acceptable range for α , cooling leads to negative slope of the spectrum $E_\nu^2 F_\nu$. Thus, if $\alpha < 2$ $E_{\nu,\text{high}} = E_{\nu,\text{break}}$ and if $\alpha > 2$ $E_{\nu,\text{high}} = \min(E_{\nu,\text{sup}}, E_{\nu,\text{cutoff}})$.

For short flares, nonthermal spectra can broadly be approximated by a broken power-law. In the case of a peculiar spectrum with a double bump (e.g., blazar spectra) at ϵ_{b1} and ϵ_{b2} with photon indices a_1 , b_1 , a_2 , and b_2 , several cases are to be considered. A schematic double-bump spectrum is illustrated in figure 2.5. In practice, we need to compare the minimum photon flux $\Phi_{\gamma,\text{min}}$ with $\max[\Phi_{\text{obs}}(\epsilon_{\text{th}}), \Phi_{\text{obs}}(\epsilon_{b1}), \Phi_{\text{obs}}(\epsilon_{b2})]$ if $\epsilon_{\text{th}} < \epsilon_{b1}$, with $\max[\Phi_{\text{obs}}(\epsilon_{\text{th}}), \Phi_{\text{obs}}(\epsilon_{b2})]$ if $\epsilon_{b1} < \epsilon_{\text{th}} < \epsilon_{b2}$ and with $\Phi_{\text{obs}}(\epsilon_{\text{th}})$ if $\epsilon_{\text{th}} > \epsilon_{b2}$.

The analytical estimates presented above can be completed by using the numerical approach described in section 1.2.3. It gives more precise estimates of the cosmic-ray and neutrino spectra as it accounts for the large variety of interaction processes. It also allows to illustrate the mean free path calculation, and the subsequent computation of cosmic-ray propagation and interactions in our Monte-Carlo code. Therefore, we consider two fiducial examples and use the typical properties of magnetar giant flares and tidal disruption events. We highlight some interesting properties of the photohadronic mean free paths and comment on the detectability of the produced neutrino flares, with the IceCube experiment and future generation VHE neutrino detectors.

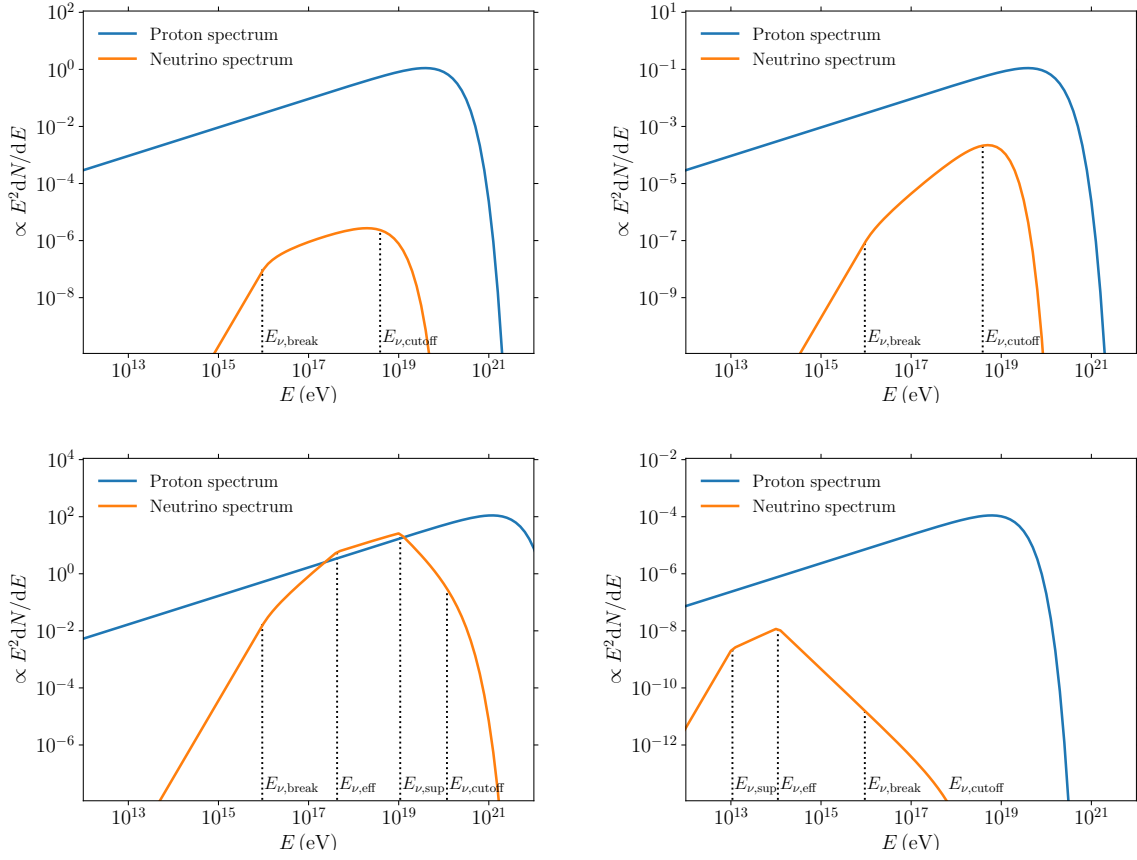


Figure 2.4: Top panel: two examples of proton and neutrino spectra, for a hard photon spectrum (left) and for a soft photon spectrum (right). Bottom panel: two examples of proton and neutrino spectra, showing the impact of efficient pion production and energy losses of secondaries, above or below $E_{\nu, \text{break}}$ (respectively right and left).

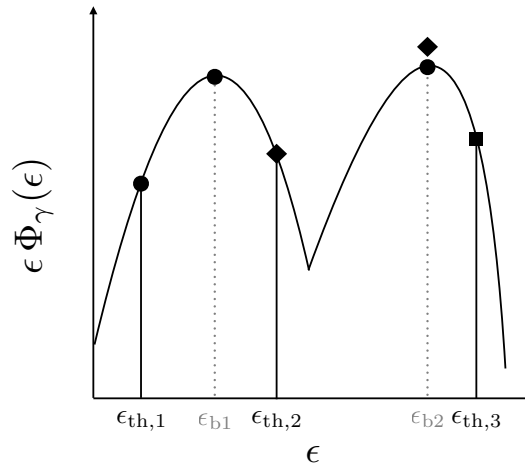


Figure 2.5: In this schematic spectrum with a double bump at ϵ_{b1} and ϵ_{b2} , we indicate for three different values of threshold energy $\epsilon_{\text{th},1}$, $\epsilon_{\text{th},2}$ and $\epsilon_{\text{th},3}$ the energies $\epsilon \geq \epsilon_{\text{th}}$ at which the observed photon flux can be maximum. These values are marked by circles for $\epsilon_{\text{th},1}$, diamonds for $\epsilon_{\text{th},2}$, and by squares for $\epsilon_{\text{th},3}$.

Magnetar giant flares

In this first example, we consider an explosive transient with a bolometric luminosity $L_{\text{bol}} = 2 \times 10^{47} \text{ erg s}^{-1}$, a bulk Lorentz factor $\Gamma = 10$, a variability timescale $t_{\text{var}} = 10^{-2} \text{ s}$ and a total duration $t_{\text{dur}} = 1 \text{ s}$. The photon spectrum used as a target for photohadronic interactions is a power law characterized by a very hard spectral index $a = 0.1$ below $\epsilon'_b = 5 \text{ keV}$ and $b = 3.1$ above. The mean free paths for photohadronic interactions are illustrated in figure 2.6, together with the typical size of the radiation region and the acceleration timescale, for a maximally efficient acceleration process $\eta_{\text{acc}} = 1$. We see that efficient pion production is expected above $\gamma' \sim 10^4$. Due to the hard photon spectrum, mainly photons at and above the break energy contribute to photopion production. This leads to $t_{p\gamma} \propto \gamma'^{1-b}$ below the break Lorentz factor $\gamma'_{\text{break}} \sim \bar{\epsilon}_{\text{th}}/\epsilon'_b \sim 4 \times 10^4$ and a constant $t_{p\gamma}$ above the break Lorentz factor. Synchrotron losses dominate above $\gamma' \sim 10^8$. Moreover, acceleration is limited by synchrotron losses. Inverse-Compton and Bethe-Heitler losses are subdominant except for $\gamma' \lesssim 10^3$ where Bethe-Heitler interactions are the dominant process.

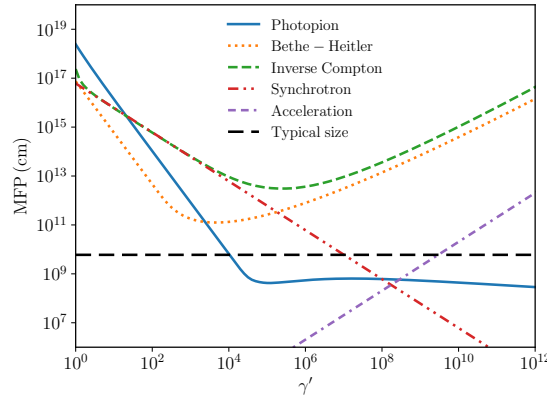


Figure 2.6: Proton energy-loss and interaction lengths for the magnetar example. We show the acceleration length and typical size of the radiation region.

The cosmic-ray and neutrino spectra are illustrated in figure 2.7, for a source located at $D_L = 15 \text{ kpc}$. We consider a power law injection spectrum of index 1.5 for protons, between $E'_{p,\text{min}}$ and $E'_{p,\text{max}}$. The minimum energy is not well constrained, and we consider $E'_{p,\text{min}} \sim 10^{12} \text{ eV}$ in this example. The maximum energy is deduced from the competition between acceleration and energy-loss processes, which gives $E'_{p,\text{max}} \sim 10^{17} \text{ eV}$. Thus we consider that the acceleration process is able to produce a power-law spectrum over a large energy range. As expected, the cosmic-ray spectrum is strongly affected by the photopion production. The high-energy cut-off is due to synchrotron losses, preventing protons above $\sim 10^{18} \text{ eV}$ from escaping the source. Moreover, the neutrino spectrum is strongly affected by secondary losses (mainly synchrotron losses of muons). Without secondary losses, the neutrino spectrum peaks around 10^{16} eV whereas it peaks around 10^{14} eV when secondary losses are accounted for. Below 10^{13} eV , the spectral index is not exactly given by $E_\nu^2 F_\nu \propto E_\nu^{1-\alpha+b}$, which is certainly a consequence of the accumulation of protons below 10^{14} eV due to photopion energy losses. Without secondary losses, the intermediate spectral index between 10^{13} eV and 10^{16} eV is given by $E_\nu^2 F_\nu \propto E_\nu^{2-\alpha}$, as expected for efficient photopion production. Interestingly, this category of explosive transients could produce a large amount of high-energy neutrinos in the energy range $10^{13} - 10^{15} \text{ eV}$, where the IceCube experiment has the highest sensitivity. The source model used in this simple example would lead to the production of neutrino flares detectable with IceCube, and would be at the detectability limit for a baryon loading of $\eta_p = 0.1$.

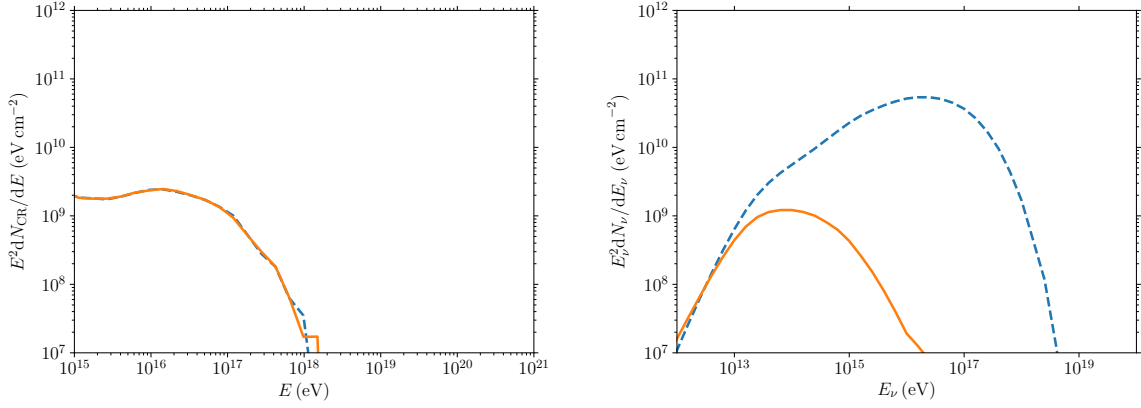


Figure 2.7: Cosmic-ray and neutrino spectra produced by a magnetar giant flare located at $D_L = 15$ kpc, without and with secondary losses accounted for (respectively dashed blue and solid orange lines).

Tidal disruptions

For this second example, we consider an explosive transient with a bolometric luminosity $L_{\text{bol}} = 10^{48} \text{ erg s}^{-1}$, a bulk Lorentz factor $\Gamma = 10$, a variability timescale $t_{\text{var}} = 10^2 \text{ s}$ and a total duration $t_{\text{dur}} = 10^5 \text{ s}$. Regarding the photon spectrum used as a target for the interactions in the radiation region, we first compare two benchmark examples of broken power-law spectra (hard or soft). In this sense we illustrate in more detail the approach of chapter 2. The spectra are characterized by their break energy ($\epsilon'_b = 0.5 \text{ keV}$), their spectral index below the break ($a = 0.1$ and $a = 1.8$) and above the break ($b = 3.1$). The energy-loss and interaction lengths for proton are illustrated in figure 2.8. We note that the Inverse-Compton energy-loss are negligible above $\gamma' > 10^2$. Energy losses due to Bethe-Heitler process are dominant between $\gamma' = 10^2$ and $\gamma' = 10^4$, thus may play an important role at low energies. However, the Bethe-Heitler energy-loss length is very large compared to the typical size of the radiation region, and thus do not play an important role in this precise example. At higher energies, the interaction length of photopion production is larger than the energy-loss lengths mentioned above, thus photopion production is an important cooling process, as each photopion interaction induces significant energy losses. Moreover, in the soft photon spectrum case, at the highest energies the photopion interaction length becomes comparable to the typical size of the radiation region, inducing an efficient pion production. Finally, acceleration is limited by the typical size of the region and synchrotron losses induce strong energy-losses at the highest energies.

Focussing on photopion production, we retrieve some results from chapter 2: below the break Lorentz factor $\gamma'_{\text{break}} \sim \bar{\epsilon}_{\text{th}}/\epsilon'_b \sim 200$, $t_{p\gamma} \propto \gamma'^{1-b}$ and above the break Lorentz factor, $t_{p\gamma} \propto \gamma'^{1-a}$ for a soft spectrum and $t_{p\gamma}$ is constant for a hard spectrum. We see that for a soft spectrum, the minimum energy of the photon spectrum acts as a spectral break, with a transition to the hard spectrum case. The Inverse-Compton energy-loss length is comparable to the synchrotron energy-loss length in the Thomson regime, and the transition from Thomson to Klein-Nishina regime occurs at $\gamma' \sim m_p c^2/\epsilon'_b$ for a hard photon spectrum and at $\gamma' \sim m_p c^2/\epsilon'_{\text{min}}$ for a very soft photon spectrum. The soft spectrum case shown in figure 1.8 lies in between. The transition in the Bethe-Heitler energy-loss length occurs at $\gamma' \sim 25m_e c^2/2\epsilon'_b$ for a hard photon spectrum and at $\gamma' \sim 25m_e c^2/2\epsilon'_{\text{min}}$ for a soft photon spectrum.

We show in figure 2.9 the spectra of cosmic rays and neutrinos obtained after the propagation of cosmic rays inside the radiation region, in the case of a soft spectrum. A power-law spectrum of cosmic rays is injected in the radiation region, with spectral index $\alpha = 1.5$, minimum and maximum energy $E'_{p,\text{min}} \sim 6 \times 10^{12} \text{ eV}$ and $E'_{p,\text{max}} \sim 6 \times 10^{17} \text{ eV}$. In this example, the injection

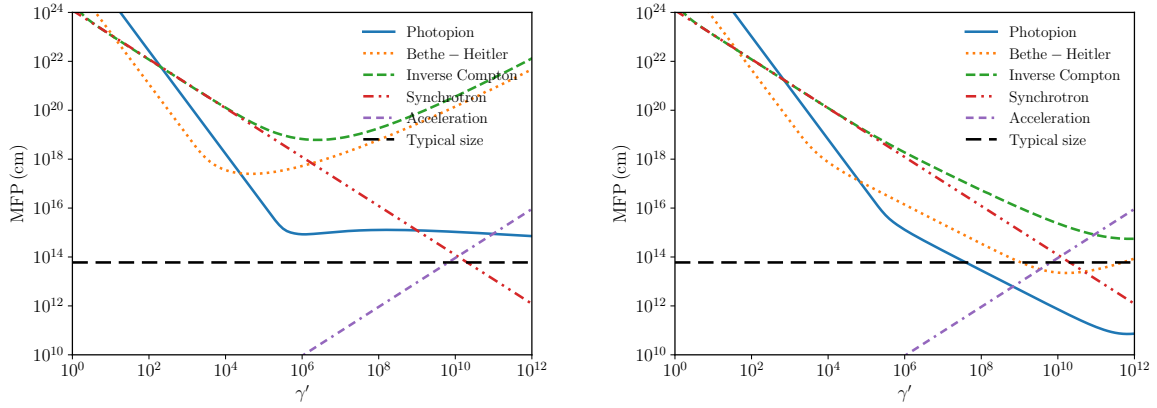


Figure 2.8: Comparison between proton energy-loss and interaction lengths for a hard photon spectrum ($a < 1$, left) and a soft photon spectrum ($a > 1$, right). We add the acceleration length and typical size of the radiation region.

spectral index can be seen in the low-energy tail of the cosmic-ray spectrum, as it is not strongly affected by interactions at these energies. We do not account for diffusion and trapping of low energy particles in the radiation region. At the highest energies, because of the small photopion interaction length, which becomes comparable to the typical size of the radiation region, a large amount of neutrinos are produced. As expected, the neutrino spectrum has a low-energy spectral index $E_\nu^2 F_\nu \propto E_\nu^{1-\alpha+a}$. The flattening of the spectrum before the high energy cut-off is due to efficient photopion production. We also note the influence of secondary energy losses, which reduce the neutrino flux at the highest energies. These secondary losses are less strong than in the previous example, and the neutrino spectrum peaks at very-high energies 10^{17} eV, even after accounting for secondary losses. A source with similar characteristics and a baryon loading $\eta_p > 0.1$ could produce neutrinos detectable with IceCube above 10^{15} eV. Due to the energies of the neutrino produced, the best sensitivity would be obtained with future generation VHE neutrino detectors, such as GRAND.

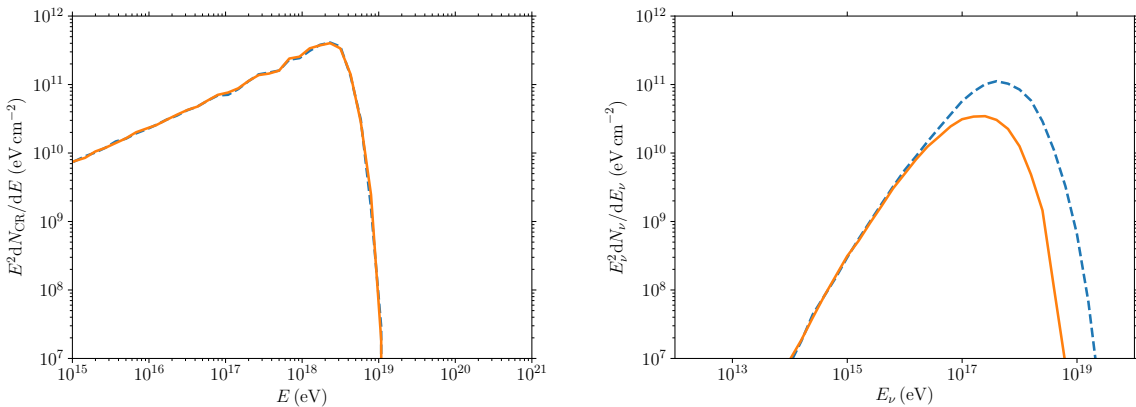


Figure 2.9: Cosmic-ray and neutrino spectra produced by a tidal disruption located at $D_L = 10$ Mpc, without and with secondary losses accounted for (respectively dashed blue and solid orange lines).

These simple examples allow to visualize basic features of photopion production, and illustrate the tools that we developed to describe high-energy cosmic-ray propagation in radiative backgrounds. Beyond these simple features, this powerful tool allows to study the propagation of nuclei in radiative backgrounds and the development of nuclear cascades, which is difficult to treat analytically. It is applied in chapter 5 to the interesting case of tidal disruption of stars by

massive black holes. In the future, this setup should be enriched with additional features, such as an approximate treatment of diffusion at the lowest energies, a better description of secondary losses with a tracking of charged pions and muons and eventually a self-consistent treatment of radiation background generation. It could also be coupled with more accurate treatments of particle acceleration and propagation, such as particle-in-cell (PIC) simulations, which would require higher computing power.

2.5 Discussion

2.5.1 Competing processes for neutrino production

Hadronic interactions are invoked as dominant processes over photohadronic interactions in dense source environments (e.g., in some GRB and transrelativistic SN shock-breakout scenarios Murase, 2008b; Kashiyama et al., 2013). As explained in Section 2.1, we do not consider the steady baryon background as a target for the production of neutrino flares because it is bound to produce a diluted emission over time.

The hadronic energy loss timescale is given by $t'_{pp} = (cn'_p \sigma_{pp} \kappa_{pp})^{-1}$, where σ_{pp} is the interaction cross-section, κ_{pp} its elasticity, and n_p is the proton density in the considered region. As $f_{p\gamma} = t'_{\text{dyn}}/t'_{p\gamma}$, $f_{pp} = t'_{\text{dyn}}/t'_{pp}$, and $\sigma_{pp} \kappa_{pp} / \langle \sigma_{p\gamma} \kappa_{p\gamma} \rangle \sim 10^2$, we can compare the interaction efficiencies by comparing the proton and photon number densities in the comoving frame:

$$\frac{f_{p\gamma}}{f_{pp}} \sim 10^{-2} \frac{1}{n'_p} \int_{\epsilon'_{\text{th}}}^{\infty} d\epsilon' (dn'_\gamma/d\epsilon') \quad (2.26)$$

$$\sim \Gamma \left(\frac{\epsilon_x}{10 \text{ MeV}} \right)^{-1} \frac{L_x}{L_{\text{bol}}} \frac{1}{|a-1|}, \quad (2.27)$$

with $x=\text{th}$ or b , at threshold energy ϵ_{th} and break energy ϵ_{b} , respectively. This estimate assumes that $n'_p = U'_\gamma/(m_p c^2)$, with the flare bolometric energy density $U'_\gamma = L_{\text{bol}}/(4\pi R^2 \Gamma^2 c)$. For hard photon spectra ($a < 1$), we can see that only emissions that are peaked at an energy $\epsilon_{\text{b}} \gg 10 \text{ MeV}$ will be dominated by pp interaction for transient neutrino production. For soft spectra ($a > 1$), the expression of ϵ_{th} (Eq. 2.15) indicates that extreme values of $\Gamma \gtrsim 100$ combined with low $E_{p,\text{max}} \lesssim 100 \text{ TeV}$ (that would produce neutrinos below the lower energy threshold for IceCube due to atmospheric backgrounds) could lead to $\epsilon_{\text{th}} \gg 1$ and thus to $f_{p\gamma}/f_{pp} \ll 1$. This is illustrated in the alternative photospheric model for GRB prompt emission by Murase (2008b) or Kashiyama et al. (2013), for example, who find that neutrinos from the pp interactions can be important at energies around 10 TeV.

Although the relative efficiencies of $p\gamma$ to pp processes depend on each source, it appears in our framework that neutrino production is strongly dominated by pp interactions in only a few marginal cases.

2.5.2 Optically thick envelopes and choked flares

Many classes of explosive transients are associated with the death of massive stars, with their major source of radiation emitted inside an optically thick stellar envelope. This envelope prevents the emitted photons from escaping until a diffusion timescale t_{d} , and/or the electromagnetic outflow to escape from the environment until the break-out time t_{b} . In these cases, it has been discussed that copious neutrino production could occur without a simultaneous radiative smoking gun. Such orphan neutrino scenarios have been developed in particular for LL GRBs and choked GRBs (Murase and Ioka, 2013; Senno et al., 2016a; Tamborra and Ando,

2016), which could appear as ordinary or superluminous type Ibc SNe. As argued in Dai and Fang (2016), TDE are not likely to be choked, however. The orientation of the jet compared to the distribution of the surrounding material makes it unlikely that it collides with high-density media (Senno et al., 2016b also demonstrated that even assuming the presence of a surrounding envelope, only low-luminosity TDEs ($L \lesssim 2 \times 10^{44}$ erg/s) could be choked). Similar arguments can be applied to blazar flares that could hardly be hidden.

When the GRB jet drives into the stellar envelope, it could emerge or remain choked. In the former case, we witness a successful GRB. If the jet is choked, its energy is deposited in a cocoon, creating a head of thermal photons that usually constitutes the main target to produce neutrino emission (Murase and Ioka, 2013; Senno et al., 2016a). For powerful jets and not too thick stellar envelopes, a transrelativistic shock can be driven out of the envelope and lead to an observable shock-breakout. It is difficult to relate this emission to the target photon background leading to neutrino production, however, and we have to be careful when applying our detectability criteria. On the other hand, if the jet is choked deep inside the material, neutrino production could still occur on the thermal photons of the jet head, but it is not guaranteed that we can observe this target background. Cocoon signatures should be observed in optical/UV/X (Nakar and Piran, 2016), but probably at a lower flux level than the actual target because of dilution over time. A jet-boosted SN should be observed (typically a SN Ibc), but it is difficult to relate this emission to the photons that efficiently produced neutrinos.

We note, however, that for all these objects, neutrinos should be *precursors* of the radiation. For LL GRBs, for example, a delay of 100 – 1000 s is expected between the neutrino emission and the escape of the radiation (Senno et al., 2016a). More generally, the diffusion timescale for a shell of mass $M_{-2} \equiv M/(10^{-2} M_{\odot})$ expanding adiabatically with velocity v is on the order of $t_d = (M\kappa/4\pi v c)^{1/2} \sim 10^5 \text{ s } M_{-2}^{1/2} \kappa_{0.2}^{1/2} v_9^{-1/2}$ (Arnett, 1980), with the opacity-to-electron scattering taken as $\kappa_{0.2} \equiv \kappa/(0.2 \text{ g}^{-1} \text{ cm}^2)$ for optical photons. For the sources considered in this framework, figure 2.3 shows that the relevant background photon energy ranges from 0.1 eV to 100 eV for nonrelativistic to mildly relativistic outflows, and reaches $\gtrsim 10^3$ eV for ultrarelativistic cases. An opacity of $\kappa_{0.2}$ can then be considered as a lower value, as we can expect that for IR and for UV and energies above, free-free interactions and Compton and pair production processes will cause the medium to be more opaque. Thus the delay between the neutrino and photon emissions should be significant ($\delta t \gg t_{\text{var}}$).

When applying our criteria, sources associated with the onset of type Ibc SNe without an associated GRB therefore need to be considered with caution. If a neutrino has been detected in coincidence with such a source, if the arrival time of the neutrino event is before the supernova peak time, our minimum flux criterion should not be used. A dedicated analysis is required to determine whether the coincidence is true.

2.6 Conclusion

We have derived the minimum photon flux necessary for neutrino detection from explosive transients, based on two main observables: the bolometric luminosity L_{bol} , and the time variability t_{var} of the flaring emission. Our results also depend on the photon spectrum associated with the emission, modeled by a broken power-law and a photon index a below the break energy. The bulk Lorentz factor of the emitting region Γ is also a key parameter to set according to the source model.

We wish to emphasize that the scope of this work is to obtain *necessary conditions* for neutrinos detection, and we did not calculate a precise neutrino spectrum or present a neutrino flux estimate. Our minimum photon flux requirement can be compared at around the indicated

energy to the observed photon flux from various transient sources, in order to assess their detectability in neutrinos.

We find that for nonrelativistic and mildly relativistic outflows, only the photon fields between IR to UV wavelengths ($\epsilon \sim 0.1 - 100$ eV) are relevant for neutrino production. Sources flaring at very high energy with no optical counterparts will not be observed. Of the NR transient sources, SLSNe appear to be the most promising candidates.

The production of very high energy neutrinos, up to $E_\nu = 1$ EeV, requires relativistic outflows. Such neutrinos could be produced by HL GRBs, LL GRBs, blazars, or TDEs. As computed by several authors, very luminous short bursts (GRBs, magnetar flares) have a good chance of being observed. However, cooling processes could prevent detection by strongly reducing the flux at the highest energies. Pions or muons could also leave the flaring region before decaying, and thereby delay the neutrino flare.

Several concrete examples are given as an illustration of our criterion in Section 2.4. Simple order-of-magnitude estimates allow us to conclude on the non-detectability with IceCube of many specific popular bright sources. In particular, no flaring neutrino emission in correlation with neither Swift J1644+57 or the Crab flares can be detected by IceCube or other future experiments. Our results are summarized in Tables 2.1 and 2.2.

However, our criterion should not be directly applied to low-luminosity GRBs or type Ibc supernovae because these objects could be off-axis GRBs or have hosted a choked GRB, leading to neutrino emission without a relevant radiation counterpart. We note that if neutrinos are emitted by such sources, they are probably precursors of the radiation.

This study can be applied to a wide range of well-known sources and sensitivities of projected instruments. Our results indicate that with an increase of one to two orders of magnitude in sensitivity, next-generation neutrino detectors could have the potential to discover neutrino flares in PeV or EeV energy ranges.

Chapter 3

The acceleration of protons in pulsar magnetospheres

The comparison between various categories of explosive transients allows to identify promising candidates for the acceleration of cosmic rays and for the production of related detectable high-energy neutrino signals. High-energy neutrinos are definitely a good signature for the acceleration of cosmic rays but also their efficient interaction in radiative or hadronic backgrounds. In order to go further and better comprehend the properties of energetic phenomena, a precise modeling of these two aspects seems critical. In this chapter, we study the early life of cosmic rays, in close interaction with electromagnetic and radiation fields.

The existence of very energetic cosmic rays requires some raw hadronic material, and a large energy reservoir in order to accelerate these particles. The steps required for the acceleration of particles are far from being trivial, and the existing models show a large diversity and complexity. An invariant of these models is the fundamental role of electromagnetic fields in the acceleration process, and the strong coupling between the particles and the field. Combining the two required ingredients, several benchmark configurations can come to mind: a compact object or some material orbiting a compact object, on which a strong magnetic field is anchored. In the case of rotating systems, the rotation can induce a strong electric field, and particles extracted from the object itself or the orbiting material can form a plasma of particles in constant interplay with the electromagnetic fields. In order to precisely understand the extraction, trajectories, and principally the acceleration and escape of hadrons in such large scale systems, we focus on the first configuration, where particles are extracted from the surface of a strongly magnetized and rotating central object. Neutron stars display all these characteristics and often show energetic emissions, which are clear manifestations of the radiation of accelerated particles, and are therefore of particular interest to test the observational implications of these models. Moreover, in the vicinity of the source, due to their interaction with the electromagnetic fields, the particles can get accelerated but also lose energy through radiation. Most of the radiation is emitted by electrons and positrons, due to the mass dependence of radiation processes such as synchrotron radiation for instance. Accelerated particles also interact with radiation fields, which influence mainly their energies and the production of secondary particles. It is therefore of particular importance to assess precisely the impact of these interactions, as they can strongly affect the properties of particles escaping the system and thus the detectable signals.

Numerical simulations can help to capture the complexity of the aforementioned aspects. In this chapter, we focus on particle-in-cell simulations of proton acceleration in pulsar magnetospheres. This study allows to explore the acceleration and escape of ions but also their feedback on the magnetosphere.

Proton acceleration in the vicinity of highly magnetized and rapidly rotating objects

The observation of broad non-thermal particle distributions indicate acceleration processes at play in astrophysical sources. We can mention for instance the detection of non-thermal photon spectra from specific sources, such as blazars or pulsars, which is imputed to the production of non-thermal spectra of accelerated particles and their radiation in the vicinity of the sources. We can also mention the detection of the diffuse non-thermal cosmic ray spectrum, which remains to be clearly associated with one or several population of sources at the highest energies, above 10^{14} eV. As stated before, plasmas interacting with electromagnetic fields can lead to particle acceleration, for instance through shocks or magnetic reconnection. In astrophysical environments, these plasmas are dilute thus effectively collisionless, which means that the particle distribution is not thermalized by collisions and that non-thermal distributions can be produced. Important collective plasma phenomena are at play in acceleration processes.

These collective phenomena occur on small scales, for instance below the plasma skin depth, the Debye length, or the particle gyroradius. The plasma skin depth is the depth to which low-frequency electromagnetic radiation can penetrate, and is given by $l_s = c/\omega_{pe}$. In this formula, the electron plasma frequency $\omega_{pe} = (4\pi n_e e^2/m_e)^{1/2}$ is the characteristic frequency of oscillations of the electron density when thermal motion is neglected, where n_e , e and m_e are respectively the number density, charge and mass of electrons. The Debye length λ_D is the distance over which charged particles screen out the electric field. In a mildly relativistic plasma, thermal motion can be neglected, and the Debye length is equal to the plasma skin depth. The particle gyroradius is $r_g = \gamma m c v_\perp / |q| B$, where γ , m , v_\perp and q are respectively the Lorentz factor, mass, speed perpendicular to the magnetic field direction and charge of the particle, and B is the magnetic field strength. Typically, $l_s \sim 2 \text{ cm } B_9^{-1/2} P_{-3}^{1/2}$ for a millisecond pulsar with magnetic field $B_9 = 10^9 \text{ G}$ and rotation period $P_{-3} = 10^{-3} \text{ s}$, where the electron density is set to the Goldreich-Julian density (defined in the following). Moreover, for the same parameters and $\gamma v_\perp / c \sim 1$, we obtain $r_g \sim 2 \times 10^{-6} \text{ cm } B_9^{-1}$ for electrons. These scales are very small when compared to the typical size of the systems. It is required to resolve kinetic scales in order to treat self-consistently the interaction between electromagnetic fields and particles, and model precisely acceleration processes. Concretely, a self-consistent resolution of the Maxwell equations for the electromagnetic fields and the Vlasov equation for the particle distribution function is required. The high complexity of this problem requires a numerical treatment, and a large variety of methods have been developed. We emphasize that in this context, magnetohydrodynamic approaches are not appropriate as they do not allow to resolve kinetic scales. Vlasov and Particle-In-Cell (PIC) simulations, that allow to solve directly or indirectly the Vlasov equation, are successful alternatives that become more competitive.

Due to the necessity of resolving kinetic scales and the high computational costs of the aforementioned simulations, the details of particle acceleration is usually studied in small-scale systems such as a small box around a shock front, which allows for a detailed study of plasma instabilities for instance. As described in section 1.2, several key quantities such as the acceleration timescale or the spectrum of accelerated particles can then be used as an input in global source models. However, a complete understanding of particle acceleration in astrophysical sources requires a comprehensive modeling of the system, to characterize the global configuration of the plasma and the electromagnetic fields, and identify acceleration sites. Large-scale effects can significantly affect the acceleration process, as different sites in the source can be involved in plasma generation or acceleration of different particle species. We emphasize that the global modeling of particle acceleration is challenging due to the huge separation of scales between the size of the system and kinetic scales.

Nevertheless, large-scale simulations of astrophysical sources start to emerge, such as the modeling of pulsar magnetospheres with PIC simulations (e.g. Chen and Beloborodov, 2014; Philippov

and Spitkovsky, 2014; Cerutti et al., 2015), on which we will focus in the following. The simplicity of this system makes it particularly attractive as it only involves a rapidly rotating central object on which a strong magnetic field is anchored. The central object is considered as the primary source of plasma as the strong electric field induced by the rotation leads to particle extraction from the surface. Despite its apparent simplicity, this configuration shows a very complex behavior, due to the interaction of particles with the electromagnetic fields and for instance plasma generation through pair cascades. Moreover, from an astrophysical perspective, due to their huge reservoir of rotational energy, pulsars are seen as interesting candidates for particle acceleration (e.g. Arons, 1981; Kirk et al., 2009). Since their discovery in the late 1960s, they have been extensively studied. Pulsars have been detected across the entire electromagnetic spectrum, from radio to gamma rays (see e.g. Abdo et al., 2013 for a Fermi-LAT catalog of gamma-ray pulsars and Aliu et al., 2008; VERITAS Collaboration et al., 2011; Aleksić et al., 2012 for the detection of the Crab pulsar above 100 GeV), and their high-energy emissions have been associated with the radiation of accelerated leptons (e.g. Arons, 1983; Cheng et al., 1986; Romani, 1996; Muslimov and Harding, 2003 for acceleration by unscreened electric fields close to the neutron star surface). Many open questions remain concerning these objects, which are actively studied. A description of the structure of the magnetosphere from first principles, accounting for the feedback of particles on the electromagnetic fields, is still to be established (e.g. Spitkovsky, 2006; Pétri, 2012; Philippov and Spitkovsky, 2014; Philippov et al., 2015; Cerutti et al., 2015). The various particle interactions occurring in the magnetosphere and in particular the production of pairs (e.g. Daugherty and Harding, 1982; Gurevich and Istomin, 1985; Zhang and Harding, 2000; Medin and Lai, 2010; Timokhin, 2010; Timokhin and Arons, 2013), are still to be fully understood and self-consistently implemented in large-scale systems. This could have a critical influence on the understanding of pair multiplicities and high-energy emissions of pulsars, and might help to improve the models for energy dissipation and spin down. One fundamental question is related to the nature of the wind around pulsars. The location of the energy dissipation, where the Poynting flux is dissipated into particle kinetic energy, is still to be clearly identified (e.g. Coroniti, 1990; Kirk and Skjæraasen, 2003; Komissarov, 2013; Porth et al., 2013). Finally, the mechanisms for cosmic-ray acceleration in pulsars, studied for instance in Venkatesan et al. (1997), Blasi et al. (2000), Arons (2003), Fang et al. (2012a), Fang et al. (2013a), Lemoine et al. (2015), and Kotera et al. (2015), should be modeled from first principles, to infer more precisely the contribution of these sources to the observed cosmic-ray flux. Interestingly, most of the existing studies have focused on magnetospheres filled with a plasma of electrons and positrons, without ion injection, and the injection of ions has been only considered in recent work (Chen and Beloborodov, 2014; Philippov and Spitkovsky, 2018). It is therefore timely to study the fate of protons in pulsar magnetospheres.

In the following, we consider the simplified configuration where the magnetic and rotation axis or the object are aligned, as the cylindrical symmetry of the system reduces the computational costs. This work relies on simulations performed with the PIC code Zeltron (Cerutti et al., 2013b). PIC simulations (see e.g. Pritchett, 2003) are based on a phase space sampling with particles: the motion of a large number of particles is solved, which allows to probe the Vlasov equation. Due to computational costs, the number of particles is significantly lower than the number of particles in real plasmas, and each simulation particle (macroparticle) represents a large number of physical particles. Particles evolve in phase-space whereas electromagnetic fields are known on the grid, and particles interact with each other indirectly via the grid, on which current and charge densities are deposited. For each timestep, particles are evolved with the Boris push, current and charge densities are deposited on the grid, and Maxwell equations are solved with the finite-difference time-domain Yee method (Birdsall and Langdon, 1991; BORIS, 1970; Yee, 1966). If the charge is not strictly conserved, Poisson's equation is solved periodically to prevent small errors from accumulating in the electric fields, which is the case in the code Zeltron. We highlight that accelerated particles can lose energy through their interaction with

electromagnetic fields for instance, as seen in section 1.2. These effects should be considered to ensure an accurate treatment of particle propagation and acceleration. In our work, only the radiation reaction force due to the radiation of accelerated particles and an approximate treatment of pair creation are included.

3.1 Particle extraction and magnetosphere generation

3.1.1 Initial electromagnetic fields and particle extraction

In the following, we consider an axisymmetric spherical grid and r, θ, ϕ are the usual spherical coordinates. The initial setup is a perfectly conducting neutron star in vacuum, with a magnetic dipole anchored at its surface

$$B_r(r, \theta, \phi) = \frac{B_\star R_\star^3}{r^3} \cos \theta, \quad (3.1)$$

$$B_\theta(r, \theta, \phi) = \frac{B_\star R_\star^3}{2r^3} \sin \theta, \quad (3.2)$$

$$B_\phi(r, \theta, \phi) = 0, \quad (3.3)$$

where R_\star is the radius of the neutron star, θ is the angle from the rotation axis, and B_\star is the polar magnetic field. For a perfect conductor rotating at angular velocity Ω , $\mathbf{E}' = \mathbf{E} + (\boldsymbol{\Omega} \times \mathbf{r}) \times \mathbf{B}/c = 0$ in the co-rotating frame, where \mathbf{E} and \mathbf{B} are the electric and magnetic fields in the observer frame, and $\boldsymbol{\Omega}$ is along the rotation axis. It allows to estimate the electric field inside the star $(E_r^{\text{int}}, E_\theta^{\text{int}}, E_\phi^{\text{int}}) = (r \sin \theta / R_{\text{LC}})(B_\theta, -B_r, 0)$, which gives

$$E_r^{\text{int}}(r, \theta, \phi) = \frac{B_\star R_\star^3}{2R_{\text{LC}} r^2} \sin^2 \theta, \quad (3.4)$$

$$E_\theta^{\text{int}}(r, \theta, \phi) = -\frac{B_\star R_\star^3}{2R_{\text{LC}} r^2} \sin 2\theta, \quad (3.5)$$

$$E_\phi^{\text{int}}(r, \theta, \phi) = 0, \quad (3.6)$$

for a dipolar magnetic field inside, where $R_{\text{LC}} = c/\Omega$ is the light cylinder radius, defined as the distance at which the corotating speed reaches the speed of light. At $t = 0$, the rotation of the neutron star is forced by imposing at its surface the poloidal and toroidal electric fields induced by the rotation of a perfect conductor. The radial electric field can be discontinuous for a non-zero surface charge density. The outer boundary condition is defined by an absorbing layer, to mimic an open boundary with no information coming back inwards (Birdsall and Langdon, 1991). Apart from these boundary conditions, there are no constraints on the external electric field, which evolves self-consistently during the simulation. We emphasize that several analytical estimates of the electric field outside of the neutron star have been derived, and in particular for an aligned rotator in vacuum, the electric field is given by Deutsch (1955) and Michel (1982)

$$E_r(r, \theta, \phi) = \frac{B_\star R_\star^5}{2R_{\text{LC}} r^4} (1 - 3 \cos^2 \theta), \quad (3.7)$$

$$E_\theta(r, \theta, \phi) = -\frac{B_\star R_\star^5}{2R_{\text{LC}} r^4} \sin 2\theta, \quad (3.8)$$

$$E_\phi(r, \theta, \phi) = 0. \quad (3.9)$$

We note that at the surface of the star, the electric field is of the order $E_\star \sim B_\star R_\star / R_{\text{LC}} \sim 10^8 \text{ statV cm}^{-1}$ for a millisecond pulsar with $B_\star = 10^9 \text{ G}$. Due to this high electric field, charged particles can be extracted from the neutron star surface. Indeed, the molecular or gravitational

attraction are often neglected (Pétri, 2016). However, we note that an inefficient extraction has also been suggested (Ruderman and Sutherland, 1975). In this study, we consider three particle species: electrons, positrons and protons. Electrons and protons are extracted from the surface and positrons are created through pair production process. In order to avoid overinjection, particles can be extracted when the local charge density does not exceed the Goldreich-Julian number density $n_{\text{GJ}} \simeq B_\star(3\cos^2\theta - 1)/4\pi R_{\text{LC}}e$. This charge density has been derived in Goldreich and Julian (1969) by considering a magnetosphere filled with plasma, in the context of ideal magnetohydrodynamics and force-free limit. In this model, the plasma is perfectly conducting and in strict corotation with the neutron star. The electromagnetic field dominates the dynamics and thus the Lorentz force on a plasma element for a one-component fluid is null, $\rho_e \mathbf{E} + \mathbf{j} \times \mathbf{B}/c = 0$, where ρ_e is the charge density and \mathbf{j} the current density. Due to the absence of dissipation (the conductivity is infinite), $\mathbf{E} + \mathbf{v} \times \mathbf{B}/c = 0$ where \mathbf{v} is the flow velocity. For a strict corotation, $\mathbf{v} = \boldsymbol{\Omega} \times \mathbf{r}$ and $\mathbf{j} = \rho_e \boldsymbol{\Omega} \times \mathbf{r}$, and using the Maxwell-Gauss equation

$$\rho_e = \frac{-\mathbf{B} \cdot \boldsymbol{\Omega}}{2\pi c [1 - (\boldsymbol{\Omega} \times \mathbf{r})^2/c^2]}. \quad (3.10)$$

The denominator adds a relativistic correction due to the modification of the magnetic field structure by currents, and is very important when approaching the light cylinder. At the neutron star surface, for a dipole magnetic field and a rotation around the vertical axis

$$\rho_e = \frac{-B_\star(3\cos^2\theta - 1)}{4\pi R_{\text{LC}} [1 - (R_\star \sin\theta/R_{\text{LC}})^2]}. \quad (3.11)$$

The denominator correction is small as $R_\star/R_{\text{LC}} \simeq 0.2$ for a millisecond pulsar. Thus we retrieve the Goldreich-Julian number density $n_{\text{GJ}} = \rho_e/e$ defined above for electrons.

The presence of a plasma in the magnetosphere influences the configuration of the electromagnetic fields. Indeed there is a large discrepancy between the vacuum solution and the force-free magnetosphere. The aligned force-free magnetosphere is described by the solution of a scalar non-linear partial differential equation, the ‘pulsar equation’ (Michel, 1973; Scharlemann and Wagoner, 1973)

$$\frac{\partial^2 \psi}{\partial r^2} + \frac{\partial^2 \psi}{\partial z^2} - \frac{1}{r} \frac{R_{\text{LC}}^2 + r^2}{R_{\text{LC}}^2 - r^2} \frac{\partial \psi}{\partial r} = -\frac{A(\psi)A'(\psi)}{R_{\text{LC}}^2 - r^2}, \quad (3.12)$$

where ψ is the flux function of the poloidal magnetic field, with $\mathbf{B} = \nabla\psi \times \mathbf{e}_\phi/r$, and $A(\psi)$ is an arbitrary function verifying some regularity conditions. This equation has been extensively studied, and significant progress has been made by Contopoulos et al. (1999) and Timokhin (2007) with numerical treatments. Several solutions have been found and one is illustrated in figure 3.1. Some interesting features appear such as the transition between closed field lines and open field lines, the direct volume currents at the poles, the return currents along the last closed field line (the equatorial current sheet) and possibility additional open field lines.

3.1.2 Energy losses and pair production

As stated previously, two additional effects influence the acceleration of particles: the radiation of accelerated particles and the pair production of leptons. The motion of a particle is governed by the Abraham-Lorentz-Dirac equation

$$\frac{d\mathbf{p}}{dt} = q(\mathbf{E} + \boldsymbol{\beta} \times \mathbf{B}) + \mathbf{g}, \quad (3.13)$$

where $\mathbf{p} = \gamma m \mathbf{v}$ is the particle momentum, $\gamma = 1/\sqrt{1 - \beta^2}$ the particle Lorentz factor, $\mathbf{v} = \boldsymbol{\beta}c$ the particle 3-velocity, m the particle mass and q the particle electric charge. The first right-hand

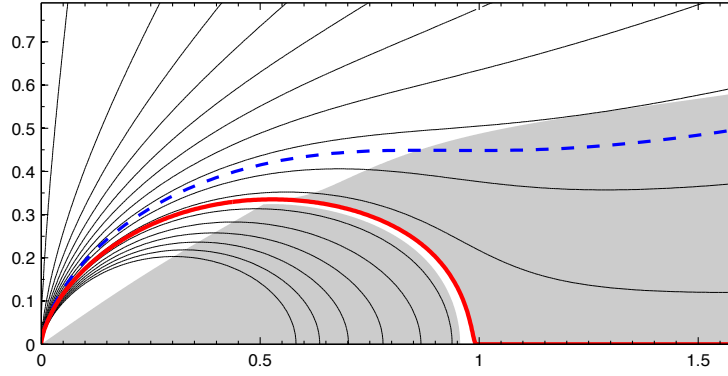


Figure 3.1: Structure of the magnetosphere, adapted from Timokhin (2007). The horizontal and vertical axis are the equatorial and rotation axis. The black lines show the magnetic flux surfaces, the grey area indicates a positive Goldreich-Julian charge density, the dashed line separates the direct and return volume currents (respectively above and below) and the red thick line is the last closed field line.

side term is the usual Lorentz force and \mathbf{g} is the radiation reaction force due to the radiation of accelerated particles, curvature and synchrotron radiation, given by the Landau-Lifshitz formula in the framework of classical electrodynamics (Landau and Lifshitz, 1975)

$$\mathbf{g} = \frac{2}{3} \frac{q^4}{m^2 c^4} [(\mathbf{E} + \boldsymbol{\beta} \times \mathbf{B}) \times \mathbf{B} + (\boldsymbol{\beta} \cdot \mathbf{E}) \mathbf{E}] - \frac{2}{3} \frac{q^4 \gamma^2}{m^2 c^4} [(\mathbf{E} + \boldsymbol{\beta} \times \mathbf{B})^2 + (\boldsymbol{\beta} \cdot \mathbf{E})^2] \boldsymbol{\beta}, \quad (3.14)$$

where the terms containing the time derivative of the fields are neglected (Tamburini et al., 2010).

The configuration of the magnetosphere, especially its filling with a dense plasma and the existence of gaps, relies primarily on the production of electron and positron pairs. The pairs are also thought to contribute to the high-energy radiation of Pulsar Wind Nebulae (PWNe), through synchro-curvature and inverse Compton radiation. A precise understanding of the pair production process is therefore critical for the modeling of pulsars. However, the amount of pair production in pulsar magnetospheres is scarcely constrained. The pairs are thought to be mainly produced in the polar cap regions (Ruderman and Sutherland, 1975), by the conversion of high-energy gamma rays into pairs in strong magnetic fields (i.e. $B \gtrsim 10^{11}$ G) and the subsequent development of a pair cascade. In the classical model, gamma rays are initially produced through curvature radiation. In the outer gaps, the interaction of gamma-ray photons with X-ray photons from the neutron star surface could also make a significant contribution to the production of pairs in the pulsar magnetospheres (Cheng et al., 2000). The pair multiplicity $\kappa = (n^+ + n^-)/2n_0$, which describes the number of electron and positron pairs produced by each primary particle, is a poorly constrained parameter that could range between 1 and 10^7 . From observations and PWNe emission models, the multiplicity has been estimated to be about $10^5 - 10^7$ for the Crab PWN and 10^5 for the Vela PWN (e.g. de Jager, 2007; Bucciantini et al., 2011). However, recent theoretical predictions limit the pair multiplicity to about a few 10^5 (Timokhin and Harding, 2018), achieved for magnetic fields $4 \times 10^{12} \lesssim B \lesssim 10^{13}$ G and hot neutron star surfaces $T \gtrsim 10^6$ K, which questions the existing models of PWNe emissions requiring very high pair multiplicities.

The electron-positron pair plasma generation is a subject of active research (Timokhin and Arons, 2013; Chen and Beloborodov, 2014). In this study, as described in Philippov et al. (2015), a simplified treatment is adopted. Pairs are directly produced at the location at the parent lepton if its Lorentz factor exceeds the threshold $\gamma > \gamma_{\min}$ and the produced pairs have a Lorentz factor $\gamma_f \sim f_\gamma \gamma_i$, which is a fraction $f_\gamma = 0.1$ of the Lorentz factor of the parent particle γ_i . The threshold $\gamma_{\min} = f_{\text{pp}} \gamma_0$ is a fraction f_{pp} of the maximum Lorentz factor $\gamma_0 = e\Phi_0/mc^2$

obtained by the acceleration of a particle through the full vacuum potential drop from pole to equator

$$\Phi_0 = - \int_0^{\pi/2} d\theta R_\star E_\theta(R_\star) = \frac{R_\star^2 B_\star}{2R_{\text{LC}}}. \quad (3.15)$$

The threshold is constant in the whole magnetosphere, and does not depend on the curvature of the magnetic field lines. This corresponds to a maximization of pair production as all the regions where leptons can get accelerated to sufficiently high energies are active pair producing regions. Thus, pair production can take place for instance in the equatorial current sheet (Lyubarskii, 1996), and not only in the polar cap regions near the surface of the neutron star. This simplified approach allows to explore various regimes of the magnetosphere by adjusting the parameter f_{pp} , without entering into a detailed modeling of the radiative backgrounds that could significantly contribute to the production of pairs. The connection between the implemented parameter f_{pp} governing the pair production in the entire magnetosphere, and the pair multiplicity κ at the polar cap is intricate. A straightforward comparison can be made by computing κ at the poles directly in the simulation and comparing the results with theoretical and observed values. This is one on-going study. The modeling of gamma-ray emissions could also help to establish a clearer link between these quantities.

Several additional effects such as photohadronic interactions could impact the particle motion and contribute to energy losses and pair production, and could be included in future work. For instance, we do not account for Bethe-Heitler processes that could contribute to the production of pairs. Depending on the radiation backgrounds, inverse-Compton scattering could also lead to significant energy losses.

3.1.3 A parameter space to be explored

As explained above, the transition between a charge separated magnetosphere and a force-free magnetosphere can be explored by changing the amount of pair production, which has a strong influence on particle acceleration. In the first configuration, the production of pairs is not sufficient to populate completely the magnetosphere with plasma and charges should be separated in different regions. The second configuration is the one described by Goldreich and Julian (1969). In this perspective, two fundamental questions can be addressed: what is the energy of the protons, especially for the ones escaping the magnetosphere, and what is their contribution to the cosmic-ray fluxes? We focus on the impact of two crucial parameters: the pair production strength f_{pp} and the magnetization $\sigma_{\text{LC}} = B_{\text{LC}}^2 / 4\pi n_{\text{LC}} \Gamma_{\text{LC}} m_e c^2$ at the light cylinder radius R_{LC} , where n_{LC} and Γ_{LC} are the plasma density and the wind Lorentz factor at the light cylinder.

In these simulations, the radius R_\star , the magnetic field B_\star and the mass ratio $m_r = m_p/m_e$ are scaled down in order to maintain acceptable computation costs, and typically $R_\star = 10^2$ cm, $B_\star = 1.1 \times 10^5$ G and $m_r = 18.36$. As a reminder, realist values give $R_\star \sim 10^6$ cm, $B_\star \sim 10^8 - 10^{15}$ G and $m_p/m_e \simeq 1836$, and for millisecond pulsars, we have $R_{\text{LC}}/R_\star = cP/2\pi R_\star \sim 5 P_{-3} R_{\star,6}^{-1}$. We adopt this typical value of R_{LC}/R_\star in the simulations. The radiation reaction force is amplified (within the limits of time resolution) by considering an effective magnetic field $B_{\text{eff}} \sim 10^9$ G, in order to reduce the synchrotron cooling time. We conserve a mass separation between electrons and protons, in order to identify its consequences on acceleration. From a technical perspective, a non-uniform spherical grid is used, logarithmically spaced in r and uniformly in θ and ϕ .

The system is strongly perturbed at the beginning of the simulation, due to the sudden injection of particles and the subsequent reconfiguration of electromagnetic fields. In order to capture the system behavior when the stationary regime is established, we evolve the system during at least five rotation periods.

3.1.4 Structure of the magnetosphere

The variation of the parameters f_{pp} and σ_{LC} produce different configurations of the magnetosphere, between two extreme regimes illustrated in figure 3.2. These examples are obtained for a high production of pairs ($f_{\text{pp}} = 0.01$) and for a low production of pairs ($f_{\text{pp}} = 0.30$) after five rotation periods, both with $R_\star = 10^2 \text{ cm}$, $R_{\text{LC}}/R_\star = 5$, $B_\star = 1.1 \times 10^5 \text{ G}$, $B_{\text{eff}} \sim 2.5 \times 10^9 \text{ G}$ and $m_\tau = 18.36$. The simulation box extends to $5R_{\text{LC}}$ and the simulation captures five rotation periods P .

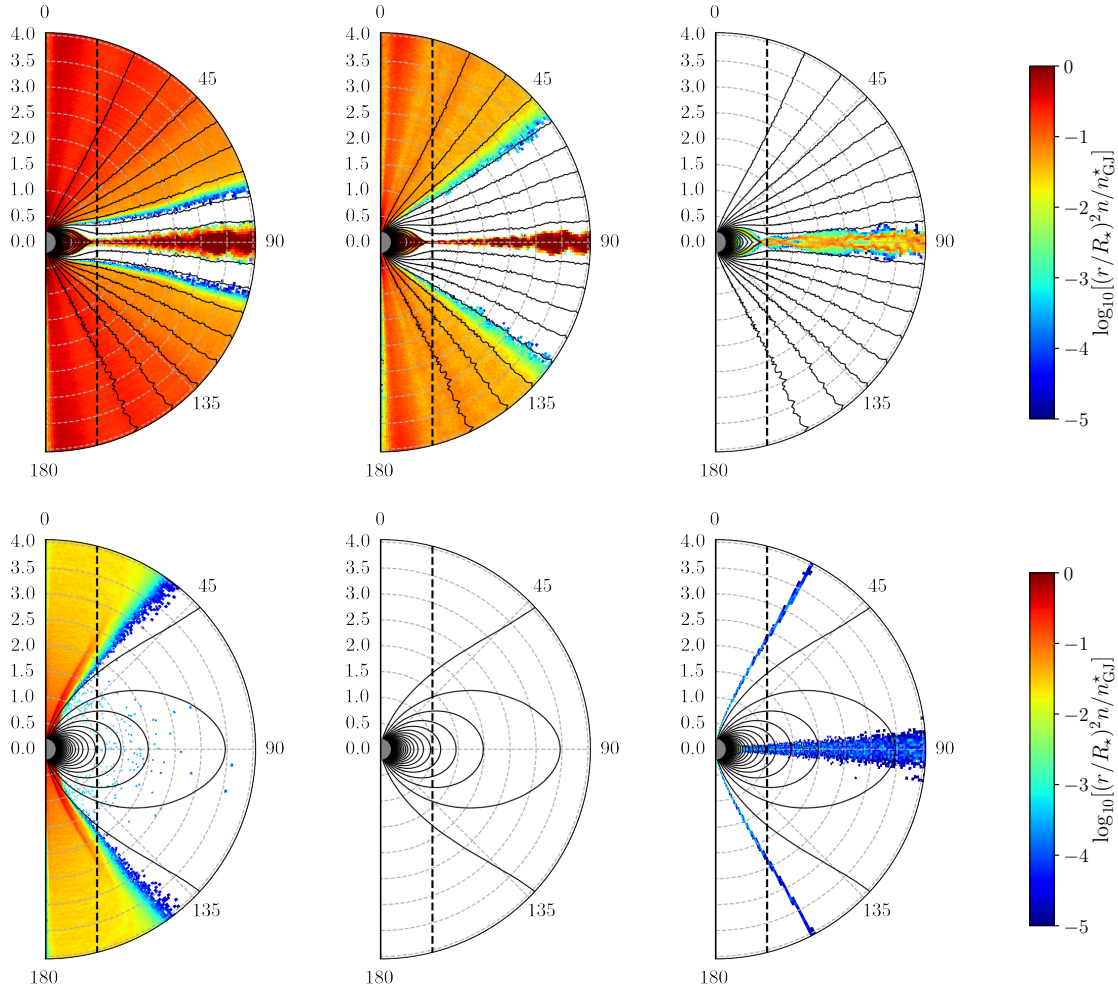


Figure 3.2: Density maps for electrons, positrons and protons (from left to right), for a high production of pairs $f_{\text{pp}} = 0.01$ (top) and a low production of pairs $f_{\text{pp}} = 0.30$ (bottom), as a function of r/R_{LC} and θ , for $t = 5P$. We show the normalized logarithmic densities $\log_{10}[(r/R_\star)^2 n/n_{\text{GJ}}^*]$ where $n_{\text{GJ}}^* = B_\star/2\pi R_{\text{LC}}e$ is the polar Goldreich-Julian number density. Solid black lines are the magnetic field lines and the dashed black line indicate the distance from the rotation axis $r \sin \theta = R_{\text{LC}}$. The grey semi-disk represents the neutron star.

Low values of f_{pp} lead to a strong production of pairs and thus allow to study magnetospheres close to the force-free regime. This configuration is characterized by number densities of electrons and positrons in the polar region and in the equatorial region (the current sheet) in the order of the polar Goldreich-Julian number density $n_{\text{GJ}}^* = B_\star/2\pi R_{\text{LC}}e$ multiplied by the quantity $(R_\star/r)^2$. Moreover protons are propagating in the equatorial region, with number densities around 1 to 10% of the pondered Goldreich-Julian number density. We note that small gaps with densities below $10^{-5}n_{\text{GJ}}^*$ separate the polar flows and the current sheet. The magnetic field, initially in a dipolar configuration, is strongly affected by the dense plasma outflow. A

closed magnetic field line region is maintained at low latitudes below the light cylinder radius, whereas magnetic field lines open up at high latitudes, which is similar to the configuration in the force-free regime (e.g. Contopoulos et al., 1999; Timokhin, 2007). Theoretically, the magnetic field lines have been predicted to present a Y-shape at the point where the last closed field line intersects the equatorial plane (called the Y-null point or Y-point), which seems to be the case in these simulations.

For high values of f_{pp} , the production of pairs is almost absent and allows to study magnetospheres close to the electrosphere configuration, which is characterized by a dome of negative charges and a disk of positive charges. In the example with $f_{pp} = 0.30$, there are no positrons in the magnetosphere. Electrons are essentially confined in the polar regions and characterized by number densities around 10% of $n_{GJ}^*(R_*/r)^3$, with higher number densities close to the star surface and in high-latitude elongated regions. In these regions, it appears that electrons are trapped and are going back and forth before escaping or falling back to the star surface. Large gaps of densities below $10^{-5}n_{GJ}^*$ separate the bulk of electrons and protons. A high density of protons is confined near the neutron star surface, with $n \sim n_{GJ}^*$. Low number densities of protons, below $10^{-3}n_{GJ}^*$, propagate in the equatorial region and along the separation region between the bulk of electrons and the gaps. The magnetic field lines that open up at the beginning of the simulation, because of the transitory dense plasma outflow, tend to return to a dipolar configuration, because of the low plasma density in the stationary regime. High electric fields contribute to maintain the equatorial flow of protons, but the subsequent current is not sufficiently large to modify the dipolar structure. The few open field lines are anchored to the star near the poles, where the electrons are extracted.

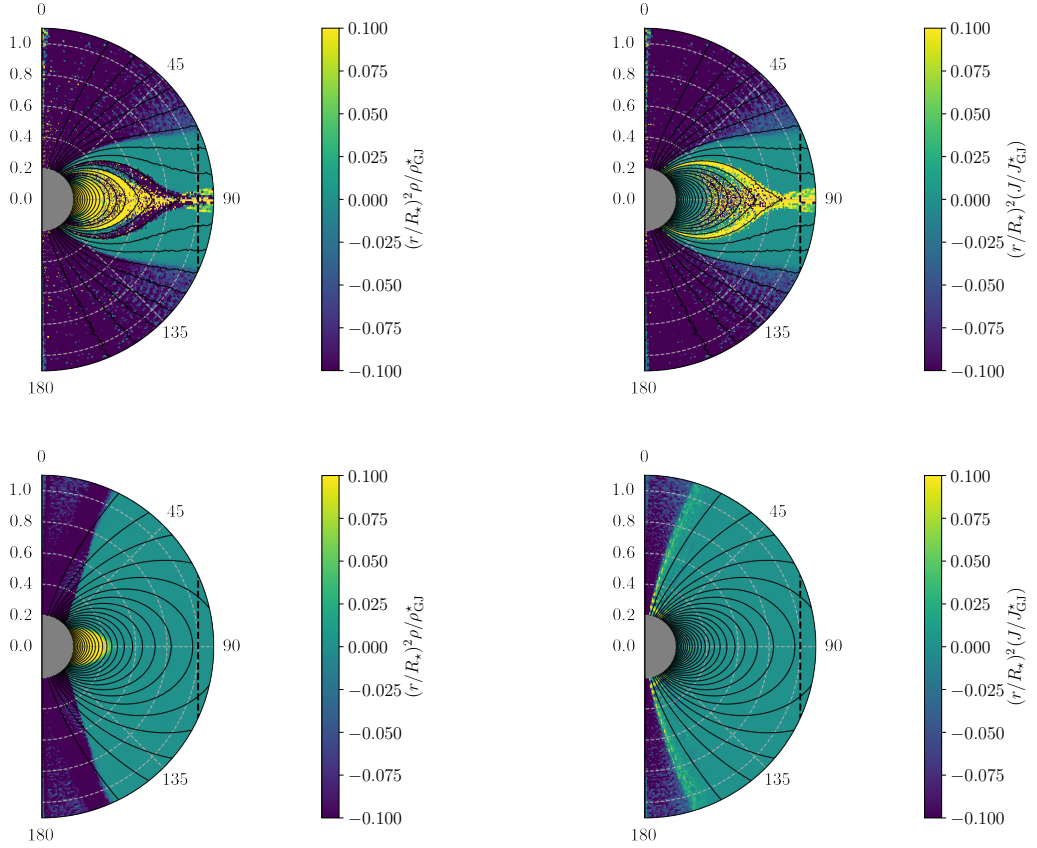


Figure 3.3: Charge density and radial current maps (respectively left and right) for a high production of pairs $f_{pp} = 0.01$ (top) and a low production of pairs $f_{pp} = 0.30$ (bottom), for $r \leq R_{LC}$. ρ_{GJ}^* and J_{GJ}^* are the Goldreich-Julian charge and current densities at the pole.

We note that none of these two configurations perfectly match the theoretical descriptions. In particular, the charge densities and radial currents present some interesting features, due to the mixing of particle species, as illustrated in figure 3.3. For $f_{pp} = 0.01$, the poles are dominated by negative charge densities, which carry a negative radial current out of the polar caps. The equator is mostly dominated by positive charge densities, and a positive current density. Just above the last closed field line, a small region is dominated by negative charge densities. The corresponding radial current shows that these negative charges are the main contributors to the return current (they carry a positive radial current), closing on the polar caps. The closed field line region is dominated by positive charge densities, which do not seem to contribute much to the radial current. For $f_{pp} = 0.3$ the situation is more simple, with negative charge densities at the poles and positive charge densities at the equator. Interestingly, only high latitudes seem to contribute to radial currents, with a small return current just next to the negative current. Protons and electrons in this region seem thus to contribute more to the return current than protons in the equatorial region.

3.2 Particle acceleration and energy dissipation

From a theoretical point of view, a magnetized rotating conductor develops a potential difference between the pole and the equator. Particles that experience all or a fraction of the voltage drop can get accelerated through unipolar induction. This is the case for rotating and magnetized neutron stars, that are considered as perfect conductors in our model. As shown in section 3.1.2 and in particular in equation 3.15, particles can get accelerated up to $\gamma_0 = e\Phi_0/mc^2$, where $\Phi_0 = B_\star R_\star^2/2R_{LC}$, if they experience the full potential drop. For the force-free regime, a typical fraction is given by the potential drop across the polar cap, the surface of the neutron star on which open field lines are anchored. As the typical polar cap angle is $\sin^2 \theta_{pc} \sim R_\star/R_{LC}$, it gives $\Phi_{pc} = -\int_0^{\theta_{pc}} d\theta R_\star E_\theta(R_\star) = R_\star^3 B_\star/2R_{LC}^2$. Interestingly, in this case $\gamma \sim \sigma_{LC}$ (Cerutti and Beloborodov, 2017), where we neglect the bulk Lorentz factor of the wind and the pair multiplicity of the pair plasma. For the vacuum case, another estimate can be calculated by considering particles following magnetic field lines from an injection angle θ_{inj} up to the equator. The trajectory is thus characterised by $r/\sin^2 \theta = C$ where C is a constant. Considering the Deutsch solution for a dipole in vacuum, $\Phi_{||} = -\int \mathbf{ds} \cdot \mathbf{E} = B_\star R_\star^2 (2 - 3 \sin^2 \theta_{inj} + \sin^6 \theta_{inj})/6R_{LC}$, which varies between 0 for $\theta_{inj} = \pi/2$ and $B_\star R_\star^2/3R_{LC}$ for $\theta_{inj} = 0$. These estimates can be applied in a variety of contexts. However, the detail of particle trajectories and structure of the electromagnetic field is important to precisely determine their acceleration.

In all our simulations, there is always a part of the protons that can get accelerated and can escape the magnetosphere. We illustrate in figure 3.4 and 3.5 the trajectories of 2400 protons projected in a poloidal plane, for $f_{pp} = 0.01$ and $f_{pp} = 0.30$. All the protons are injected at the same time all over the neutron star surface, and most of the protons directly fall back on the neutron star surface. Only protons injected at high latitudes escape, protons injected at lower latitudes are trapped in the closed field line region. Trapped protons wrap around the neutron star, whereas protons that escape have quasi-radial trajectories at large distances. We do not observe protons escaping for $f_{pp} = 0.30$. However, we see that the trajectories of protons injected at the highest latitudes are perturbed and thus certainly unstable, thus some of these protons might be able to escape. Moreover, as can be seen in figure 3.6, some protons do escape but with a very low flux. Due to the limited number of protons in the sample of tracked particles, it cannot capture rare effects and thus we do not have any escaping proton in this sample. Interestingly, simulations at lower resolution show a larger number of protons escaping in the equatorial flow, which allows us to study their trajectories. This difference could result from numerical effects, or longer times required to reach the steady state for higher resolutions,

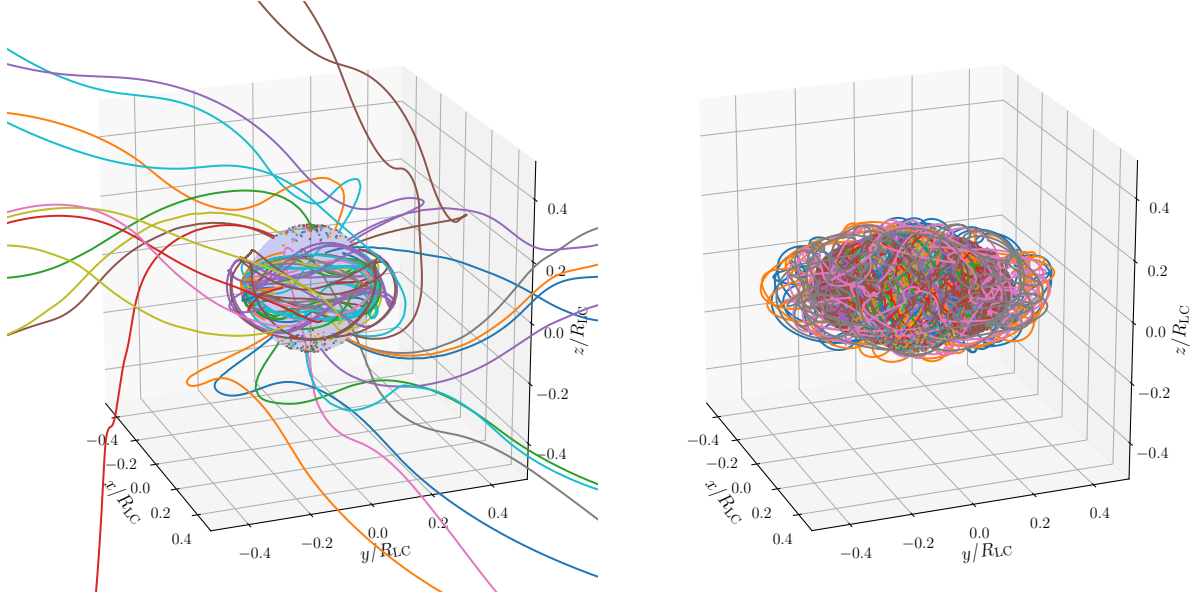


Figure 3.4: Zoom on the trajectories of protons injected at the same time from the neutron star surface, for $f_{pp} = 0.01$ (left) and $f_{pp} = 0.30$ (right). The different colors highlight different trajectories. We note that rare events do not appear, in particular the escape of high energy protons for $f_{pp} = 0.30$.

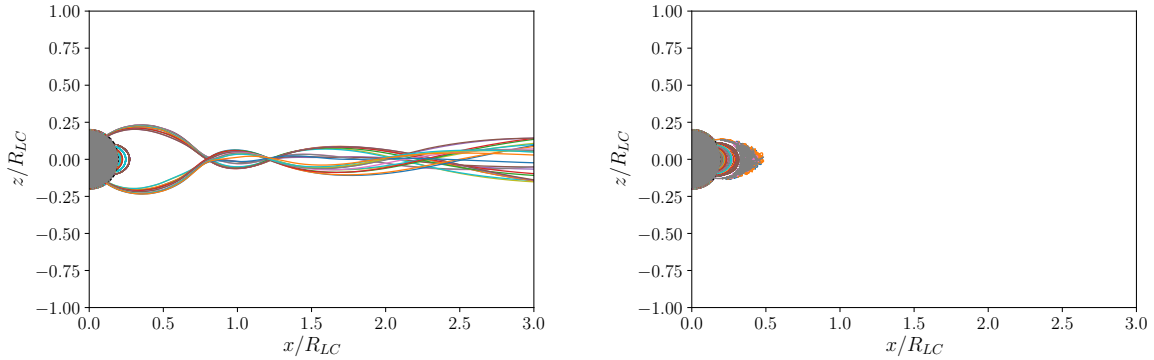


Figure 3.5: Trajectories of protons (projected in the poloidal plane) injected at the same time from the neutron star surface, for $f_{pp} = 0.01$ and $f_{pp} = 0.30$. The different colors highlight different trajectories.

and is currently under study.

In the range of tested parameters, protons experience different fates: they are not injected from the same latitudes, do not experience the same electromagnetic fields during their propagation. Therefore they show different final energies and fluxes, which is illustrated in figure 3.6 where we compare the spectra of escaping particles for $f_{pp} = 0.01$ and $f_{pp} = 0.30$. To compute these spectra, we calculate at a given timestep the total number of particle comprised in the spherical shell between $0.8r_{\max}$ and $0.9r_{\max}$, such as $u_r > 0$. This number is divided by the typical time required for relativistic particles to escape this volume $0.1r_{\max}/c$. We see that for high production of pairs, a large amount of accelerated electrons and positrons can escape. As shown in Cerutti et al. (2015), positrons get accelerated to higher energies than electrons, due to their trajectories next to the Y-point and in the current sheet. For a low production of pairs, almost no positrons are produced and due to their confinement in the polar flows, escaping electrons get accelerated to lower energies than in the previous case. Interestingly, protons escape in both cases, with ten times higher energies in the low pair production regime, but with a lower flux of

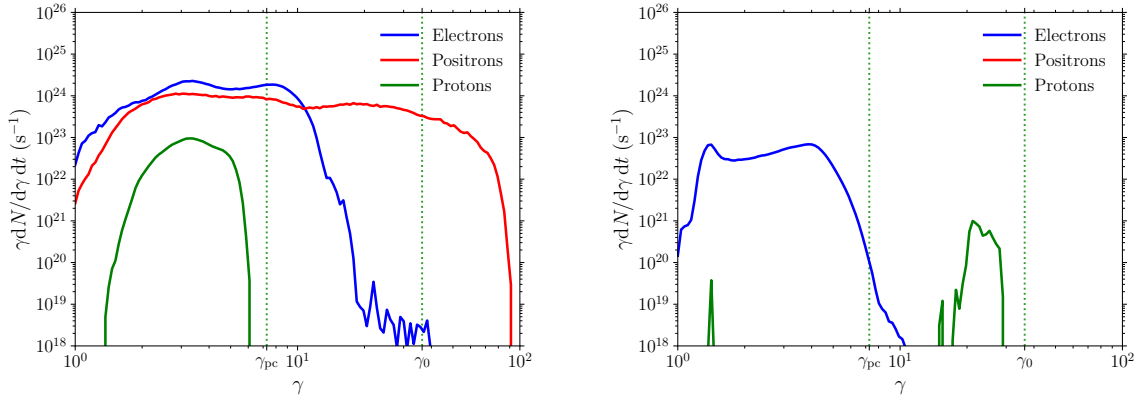


Figure 3.6: Spectra of escaping electrons (blue), positrons (red) and protons (green), for $f_{pp} = 0.01$ (left) and $f_{pp} = 0.30$ (right). The green dotted lines indicate the maximum Lorentz factor of protons accelerated through the full vacuum potential drop from pole to equator γ_0 and through the vacuum potential drop across the polar cap γ_{pc} . Another important quantity is the minimum Lorentz factor of electrons and positrons for pair production $\gamma_{min} = f_{pp}\gamma_0$. For $f_{pp} = 0.01$, $\gamma_{min} \simeq 7$ and for $f_{pp} = 0.30$, $\gamma_{min} \simeq 200$.

more than one order of magnitude compared to the higher pair production regime.

In these simulations, protons get accelerated by the electric field component parallel to their trajectory, as shown in figure 3.7. For one proton that escapes the magnetosphere, we calculate the quantity $\int dt(eE_{||}/mc - \gamma d\beta/dt)/\beta$, where $E_{||} = \mathbf{E} \cdot \mathbf{v}/v$, which gives a good estimate of the Lorentz factor γ . Protons gain a large fraction of their final energy in the inner part of the magnetosphere, in the closed field line region. The strength of the parallel electric field in this region is therefore of prime importance for acceleration. Moreover, protons mostly move along the magnetic field lines in this region, so the electric field parallel to the magnetic field gives a good estimate of the electric field contributing to particle acceleration. As shown in figure 3.8, the electric field parallel to the magnetic field is nearly completely screened for $f_{pp} = 0.01$, and less screened for $f_{pp} = 0.30$, which leads to proton acceleration towards higher energies for low pair productions. We note that magnetic reconnection in the outer part of the magnetosphere and the wind, and especially in the current sheet when it exists, could significantly contribute to proton acceleration. A precise study of magnetic reconnection is however out of the scope of this study, and a larger sample of tracked particle would be required to capture these effects.

We calculate the maximum Lorentz factor of escaping protons from the several configurations tested, as illustrated in figure 3.9. We see that protons experience a fraction of the full vacuum potential drop (higher than the polar cap or the parallel potential drop). This fraction is small for high production of pairs and saturates at a maximum value for low production of pairs. The densities of electrons and positrons in the closed field line region are high for high production of pairs, therefore the high plasma multiplicities screen the parallel electric field and prevent protons from experiencing a large fraction of the full vacuum potential drop. For low production of pairs, only protons are present in the equatorial plane and can experience a large fraction of the full vacuum potential drop. We note that the magnetic field dependence of the proton maximum Lorentz factor, obtained for $\gamma_0 = e\Phi_0/mc^2$, seems to be well reproduced by the simulations.

These estimates cannot be directly related with realistic cases as the magnetic field, neutron star radius and mass ratio are downscaled in our simulations. A rescaling procedure is required, which is a delicate process, due to the large difference of the scales considered. The quantities that we derive should thus be considered with care. We assume that a constant fraction of

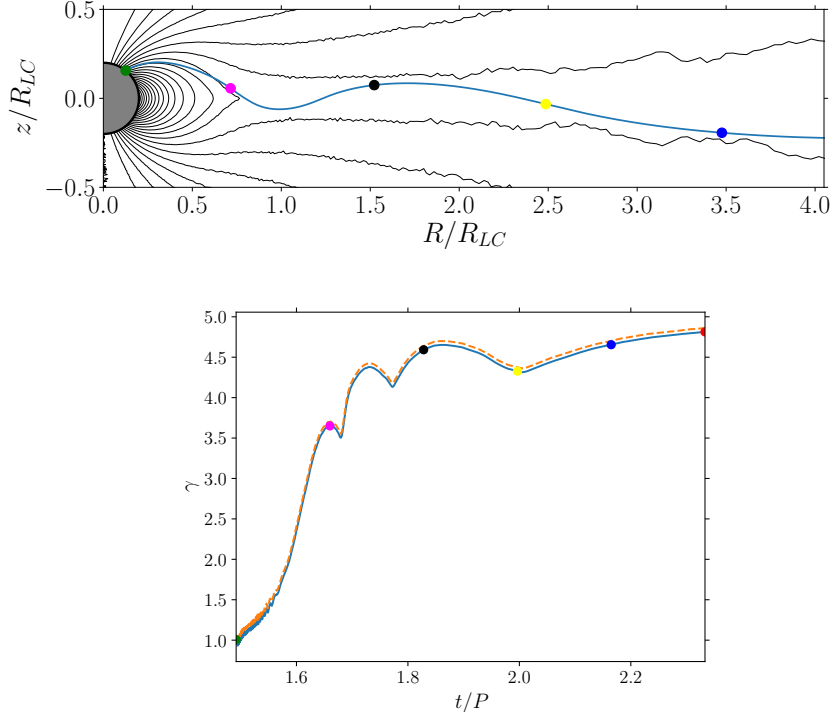


Figure 3.7: Example of a proton escaping the magnetosphere, trajectory (upper panel) and corresponding Lorentz factor (lower panel), for $f_{pp} = 0.01$. Markers of different colors link the two figures. On the lower panel, we compare $\int dt(eE_{\parallel}/mc - \gamma d\beta/dt)/\beta$ (solid line) and γ (dashed line).

the full vacuum potential drop can be channelled into proton acceleration. In our simulations, we obtain maximum Lorentz factors between $\gamma_{s,\min} = 5$ and $\gamma_{s,\max} = 28$, thus 15% to 85% of the γ_0 . As $\gamma_0 = 3.3 \times 10^7 m_{r,1836}^{-1} B_{\star,9} R_{\star,6}^2 P_{-3}^{-1}$, we see that protons can get accelerated up to $E_p \simeq 5 \times 10^{15} \text{ eV } B_{\star,9} R_{\star,6}^2 P_{-3}^{-1}$ for a high pair production and up to $E_p \simeq 3 \times 10^{16} \text{ eV } B_{\star,9} R_{\star,6}^2 P_{-3}^{-1}$ for a low pair production. These estimates have been derived for typical properties of millisecond pulsars $B_{\star} = 10^9 \text{ G}$ and $P = 10^{-3} \text{ s}$, we note however that similar results are obtained for $B_{\star} = 10^{12} \text{ G}$ and $P = 1 \text{ s}$. Millisecond magnetars, with $B_{\star} = 10^{15} \text{ G}$ and $P = 10^{-3} \text{ s}$ could produce cosmic rays up to $E_p \sim 10^{22} \text{ eV}$. However, such configurations are difficult to explore with our simulations due to the large distance between the star and the light cylinder radius, or the high magnetic fields.

One last important quantity to infer is the total energy dissipated and channelled into particles, which allows to estimate the proton luminosity. The production of pairs has a strong impact on the outgoing Poynting flux, which can be a small fraction of the analytic spin-down power of an aligned pulsar $L_0 = cB_{\star}^2 R_{\star}^6 / 4R_{LC}^4$ (e.g. Contopoulos et al., 1999; Spitkovsky, 2006) for low pair productions, as illustrated in figure 3.10. Thus aligned pulsars with low pair production barely spin-down, as expected for the disc-dome solution (Cerutti et al., 2015). At distance $r > R_{LC}$, the outgoing Poynting fluxes decrease only slightly, showing that in our simulations a large part of the energy dissipation occurs below $r = R_{LC}$.

Energy dissipation is illustrated in figure 3.11, where we show the outgoing Poynting flux and the luminosity in electrons, in positrons and in protons for $f_{pp} = 0.01$ and $f_{pp} = 0.30$. The sum of these quantities should be constant for a dissipation of Poynting flux into particle kinetic energy. We note that this is not exactly the case, especially below R_{LC} , which could be due to numerical effects. For high pair production, we see clearly the effect of energy dissipation below R_{LC} and the energy is mostly dissipated into positron kinetic energy. For low pair production, the source of the dissipation below R_{LC} is not clear, and a small fraction of the Poynting flux

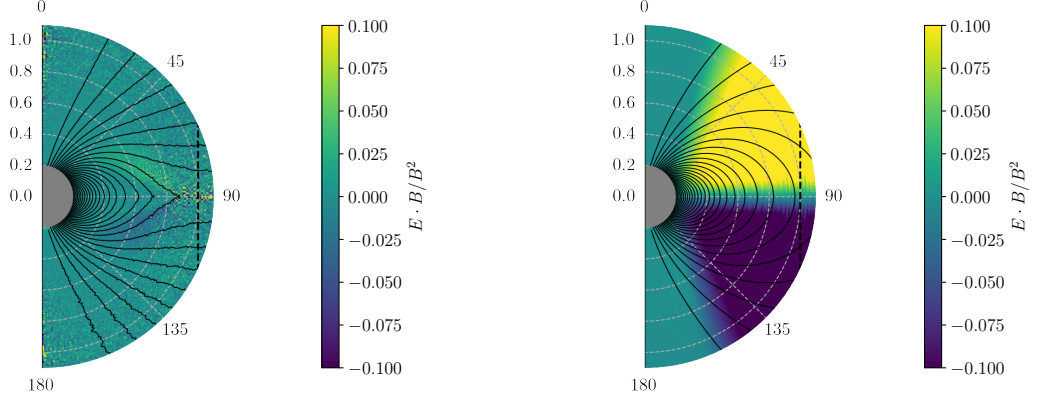


Figure 3.8: Parallel electric field $\mathbf{E} \cdot \mathbf{B}/B^2$ in the inner part of the magnetosphere ($r \leq R_{LC}$), for $f_{pp} = 0.01$ (left) and $f_{pp} = 0.30$ (right).

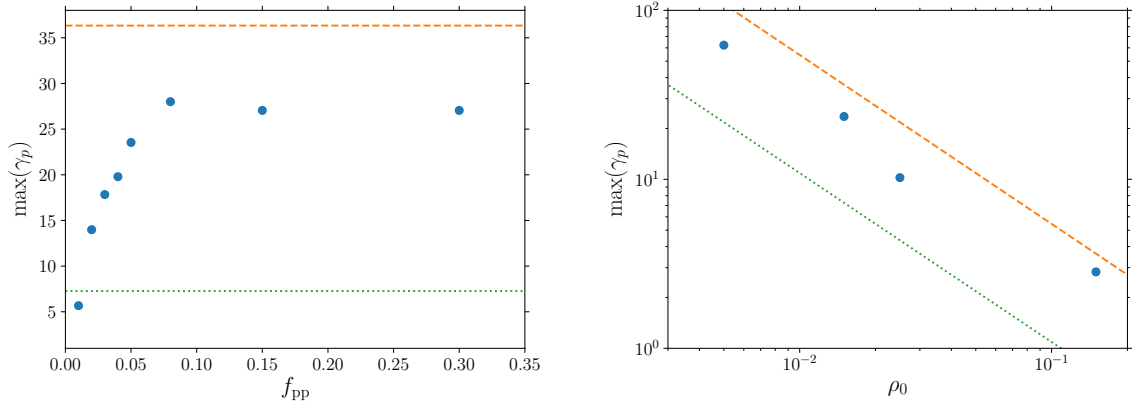


Figure 3.9: Maximum Lorentz factor of escaping protons, as a function of f_{pp} for $\rho_0 = 0.015$ (left) and of $\rho_0 = m_e c^2 / eB$ for $f_{pp} = 0.05$ (right). The dots correspond to simulation results, whereas the lines represent the maximum Lorentz factor of protons experiencing the vacuum potential drop, from pole to equator (orange, dashed) or across the polar cap (green, dotted).

is dissipated into electron and proton kinetic energy. These two extreme cases allow to evaluate the typical proton luminosity. We obtain $L_p = 5 \times 10^{-4} L_0$ for a low production of pairs and $L_p = 2 \times 10^{-2} L_0$ for a high production of pairs. Assuming that we can use these fractions for typical pulsar properties, and considering the value of the spin-down power of an aligned pulsar $L_0 = 1.4 \times 10^{37} \text{ erg s}^{-1} B_{*,9}^2 R_{*,6}^6 P_{-3}^{-4}$ for millisecond pulsar properties, we obtain $L_p \simeq 7 \times 10^{33} \text{ erg s}^{-1} B_{*,9}^2 R_{*,6}^6 P_{-3}^{-4}$ for a low production of pairs and $L_p \simeq 3 \times 10^{35} \text{ erg s}^{-1} B_{*,9}^2 R_{*,6}^6 P_{-3}^{-4}$ for a high production of pairs. For millisecond magnetars with a high production of pairs, $L_p \simeq 3 \times 10^{47} \text{ erg s}^{-1} B_{*,15}^2 R_{*,6}^6 P_{-3}^{-4}$ which is comparable to luminous blazar or jetted tidal disruption events bolometric luminosities.

This work allows to identify promising configurations for the acceleration of protons, by considering a highly magnetized rotating conductor, on which a dipolar magnetic field is anchored. The simulations show that pulsars are good candidates for the acceleration of protons and their escape from the magnetosphere, regardless of the amount of pair production. For a high production of pairs, about 1% of the pulsar spin-down power is channelled into protons, which is of the same order than the fraction required to fit the UHECR spectrum (Fang et al., 2013b). For a low production of pairs, less than 0.05% of the pulsar spin-down power is channelled into protons. However, despite these low luminosities, it appears also that protons get ac-

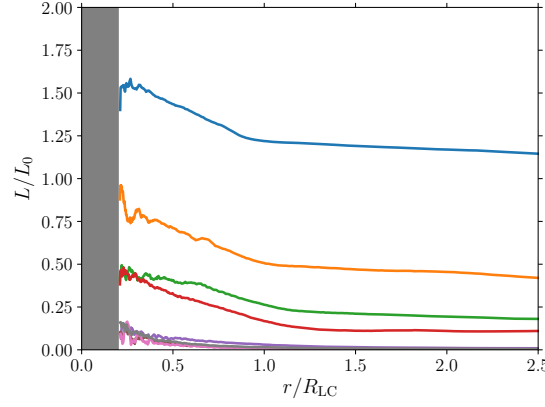


Figure 3.10: Outgoing Poynting flux integrated over a sphere of radius r as a function of radius for $f_{pp} = 0.01$, $f_{pp} = 0.02$, $f_{pp} = 0.03$, $f_{pp} = 0.04$, $f_{pp} = 0.05$, $f_{pp} = 0.08$, $f_{pp} = 0.15$, $f_{pp} = 0.30$, from top to bottom. All the quantities are normalized by the analytic spin-down power of an aligned pulsar.

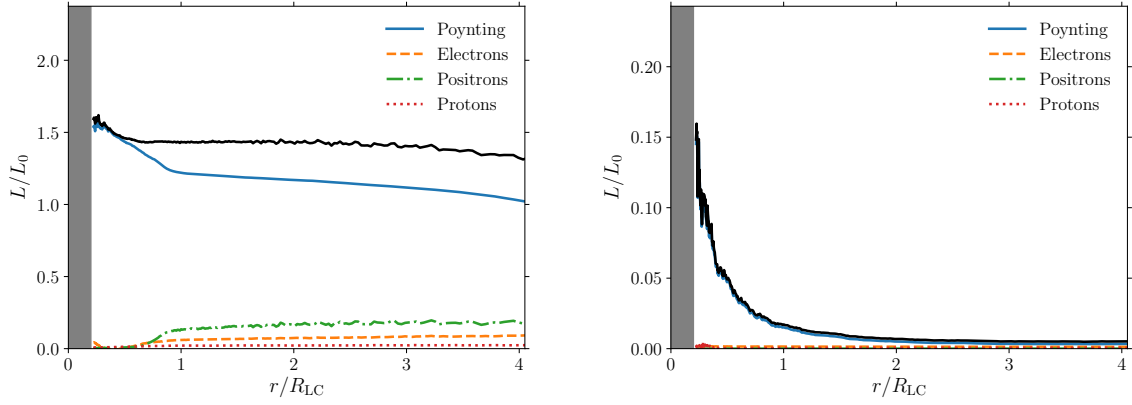


Figure 3.11: Energy dissipation as a function of radius for $f_{pp} = 0.01$ (left) and $f_{pp} = 0.30$ (right). We show the radial Poynting flux integrated over a sphere of radius r (blue line), the luminosity in electrons (orange dashed line), in positrons (green dot-dashed line) and in protons (red dotted line), and the sum of all these components (black line), normalized by L_0 .

celerated to higher energies for a low production of pairs. A simple rescaling allows to estimate the maximum energy and luminosity of accelerated protons, which gives energies above 1 PeV and luminosities above $L_p \simeq 3 \times 10^{35} \text{ erg s}^{-1}$ for typical properties of millisecond pulsars, for high production of pairs. This might have interesting observational consequences for the production of gamma rays as we will see in chapter 4. Moreover, for typical properties of millisecond magnetars, UHECR could be produced. Considering that 1% of the pulsar spin-down power is channelled into proton luminosity during approximately the spin-down time $t_{sd} = 9Ic^3P^2/8\pi^2B_\star^2R_\star^6 \simeq 3 \times 10^3 \text{ s } I_{45}B_{\star,15}^{-2}R_{\star,6}^{-6}P_{-3}^2$, we obtain the energetic budget of $\sim 10^{51} \text{ erg}$. Thus a birth rate of magnetars above $10^2 \text{ Gpc}^{-3} \text{ yr}^{-1}$ is required to match the cosmic-ray flux above 10^{19} eV , which requires $E_{\text{UHECR}}\dot{n} = 10^{53} \text{ erg Gpc}^{-3} \text{ yr}^{-1}$ where E_{UHECR} is the total energy in UHECR above 10^{19} eV and \dot{n} is the event rate (Katz et al., 2009).

However, this work is restrictive as only a small fraction of the pulsar wind is comprised in our simulations, and we do not account for energy losses or re-acceleration of protons at larger distances, for instance at a shock front. Moreover, we consider the case of an aligned pulsar, and the structure of the magnetosphere should be modified in the misaligned case (Pétri, 2016). However, the structure of the magnetosphere below the light cylinder radius, where most of

the acceleration seems to take place, should be similar for the misaligned configuration. We highlight that reconnection taking place in the striped wind or Fermi-type acceleration taking place at the termination shock between the pulsar wind and its nebula (e.g. Lemoine et al., 2015) should enhance the proton maximum energy.

To conclude, these PIC simulations allow to identify interesting features, that could be applied to future models encompassing larger scales. Further work will be required to better characterize the escape of protons by a detailed modeling of their trajectories. The link between the simulated amount of pair production and pair multiplicities in realistic environments should be explored. For this purpose, a self-consistent modeling of pair production, but also of other types of interactions will be required.

The theoretical framework described in the previous chapters allows to gain more insight into the mechanisms involved in the acceleration, propagation and interactions of cosmic rays, and can benefit the modeling of multi-messenger signals from astrophysical sources. In the following, we present direct applications of this framework, in the context of multi-messenger astronomy. We highlight the importance of two sources populations, the galactic population of pulsars and the extragalactic population of tidal disruptions by massive black holes, that could significantly contribute to observed emissions in gamma rays, cosmic rays and neutrinos, at the highest energies.

Chapter 4

Millisecond pulsars as pevatrons: multi-wavelength signatures in the galactic center region

Pulsars appear as good candidate sources for the acceleration of cosmic rays, both from analytical estimates and detailed numerical simulations, as developed in chapters 2 and 3. Interestingly, our galaxy contains many of these objects and they could make a significant contribution to the flux of galactic cosmic rays. This would lead to a large variety of observational consequences, and we discuss one possible implication in this chapter.

Recent gamma-ray measurements provide evidence that the galactic center hosts very high energy sources that produce diffuse gamma-ray emission ranging from GeV to > 10 TeV energies (Aharonian et al., 2006; HESS Collaboration et al., 2016; Fermi-LAT Collaboration, 2017). Whether this emission results from one single source or a population of sources, whether the GeV and TeV observations are connected at all, whether they are produced via similar processes or are the signatures of different particles accelerated in the same sources, whether they stem from leptonic or hadronic models, are all highly debated topics. Strong arguments have however been put forward in favor of a yet-unresolved population of millisecond pulsars (MSP), being responsible for the GeV gamma rays observed by Fermi known as the galactic center excess, through a leptonic channel (Fermi-LAT Collaboration, 2017). At higher energies, the HESS observations are interpreted as a convincing proof that protons are accelerated up to PeV energies (HESS Collaboration et al., 2016).

These salient conclusions can be connected in a unified model: we propose that the MSP that are most likely the emitters of the GeV galactic center gamma rays observed by Fermi are also loaded in baryons, and are thus possible PeV proton accelerators, producing the HESS diffuse TeV emission. In this scenario, the pulsars accelerate cosmic rays up to very high energies. After escaping the sources and diffusing in the galactic center region, these accelerated cosmic rays interact with the molecular clouds during their propagation in the interstellar medium, producing gamma rays. We demonstrate that our model is consistent in terms of energetics and population features. Furthermore, by taking into account spatial diffusion of cosmic rays, we can successfully account for the observations from 100 GeV to > 10 TeV, and put constraints on key parameters of the millisecond pulsar population. In particular, the cosmic-ray acceleration efficiency within the pulsars, as well as the spatial, magnetic field and initial spin distributions, and the total number of MSP in this population, influence the gamma-ray emission.

We first review in Section 4.1 the Fermi-LAT and HESS observations, their interpretations available in the literature, and show in Section 4.2 how our millisecond pulsar model can reproduce the derived energetics at first order. Modeling the diffusion of cosmic rays around the galactic center and the production of cosmic rays by the MSP are key issues in this study. We examine the diffusion of particles from one source and two populations of MSP in Section 4.3, study

the injection of cosmic rays by MSP and calculate the associated diffuse gamma-ray flux in Section 4.4. Section 4.5 is devoted to a discussion of the results.

This chapter is based on Guépin et al. (2018a), with only minor changes: the analytical treatment of cosmic-ray diffusion have been completed, in order to account more precisely for the impact of spallation for instance. Moreover, a discussion about the pulsar population and luminosity distribution has been added.

4.1 Multi-wavelength observations of the galactic center

The quality and amount of data towards the galactic center collected over the last decade from radio to gamma rays have boosted our understanding of high-energy processes taking place in this region (see, for instance, van Eldik, 2015 for a review). The last couple of years have been even more exciting with the measurements in gamma rays of several extended sources, and the refined measurements of GeV-to-TeV diffuse emissions around the galactic center. We will discuss in this section two major detections that are relevant for the present study: the HESS and Fermi-LAT observations of *a priori* independent diffuse emissions around the galactic center, and the corresponding interpretations that are being discussed in the literature. We caution that the observations that are relevant to us exclude the GeV and TeV sources, 1FGL J1745-290 and HESS J1745-290, respectively, which are spatially coincident with the supermassive black hole Sagittarius A*. This object is not considered to be the source of the GeV-TeV diffuse emission that we aim to model. We first recall some basics of the structure of the galactic center and of the millisecond pulsar distribution that are relevant to understanding the interpretations of the high-energy gamma-ray emission.

4.1.1 The galactic center region

Radio observations of pulsars combined with information from star formation rates show that the bulk of the pulsar population is concentrated in the Galactic disk, and that it could contain thousands of objects (Levin et al., 2013; Lorimer, 2004; Lorimer, 2013). The Galactic disk can be modeled as a cylinder of height ~ 1 kpc, and of gas density $n_{\text{gas}} \sim 1 \text{ cm}^{-3}$ (see figure 4.1).

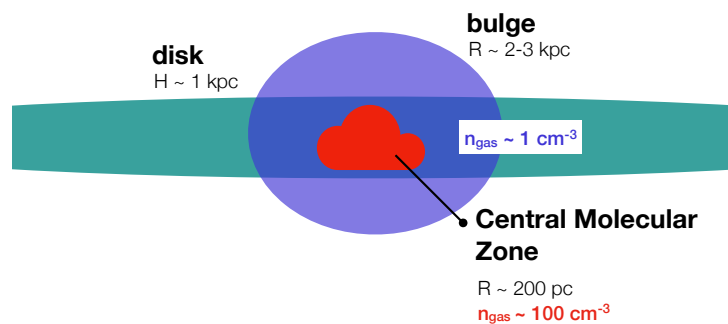


Figure 4.1: Sketch of the regions of the galactic center at play in our model, with indications on the approximate size, gas density and millisecond pulsar numbers, as detailed in Section 4.1.1.

The inner few kiloparsecs of our Galaxy are commonly referred to as the *bulge* of the Galaxy. It consists of an elongated structure stretched over 2 – 3 kpc, populated by old (~ 10 Gyr old) stars, and thus putatively hosting an important population of millisecond recycled pulsars (Zoccali and Valenti, 2016; Fermi-LAT Collaboration, 2017). Except for the very inner region

hosting molecular clouds known as the central molecular zone, the gas density in the bulge can be roughly approximated to be similar to that in the disk.

One specificity of the galactic center region is that it is filled with giant molecular clouds, that represent about 10% of the total gas amount of the Galaxy (see Mills (2017) for a review). The emission in this region is dominated by non-thermal radiation from accelerated particles, with several identified powerful objects such as supernova remnants and pulsar wind nebulae. As a consequence, the energy density in the central molecular zone is estimated to be an order of magnitude larger than that of the average Galactic cosmic rays. The molecular clouds, with a mean gas density $n_{\text{gas}} \sim 100 \text{ cm}^{-3}$, are believed to be prime targets for the production of the observed gamma rays. The radio, infrared and submillimeter images reveal a ridge-like, elongated morphology for the gas distribution, mostly concentrated in a radius of $\lesssim 200 \text{ pc}$ around the galactic center.

4.1.2 The diffuse TeV emission

Deep observations of the galactic center region carried out by the HESS collaboration revealed an extended diffuse emission over a few hundred parsecs around the galactic center from -1.1° to $+1.5^\circ$ in Galactic longitude (Aharonian et al., 2006). The statistics accumulated over 10 years together with improved analysis techniques have enabled us to map this region with increased accuracy, and have revealed diffuse emission in the inner 50 pc around Sagittarius A*, reaching gamma-ray energies $E > 10 \text{ TeV}$ (HESS Collaboration et al., 2016; Abdalla, 2018). This diffuse emission is illustrated in figure 4.2. This region, hereafter referred to as the inner 50 pc region, is defined as an annulus centered of Sgr A* of inner and outer radii of 0.15° and 0.45° , respectively. Angles between 304° and 10° in Galactic coordinates are excluded from the integration region. This emission is spatially correlated with the central molecular zone, and hence points towards the acceleration of protons in this region. Indeed, a leptonic scenario with electrons and positrons that undergo Inverse Compton scattering off the radiation field is unlikely, as the leptons would dominantly suffer severe synchrotron radiative losses that would prevent them from propagating over the scale of the central molecular zone. A hadronic scenario seems more favorable in this perspective, where energetic protons interacting with the gas in the interstellar medium produce very-high-energy (VHE, $E \gtrsim 100 \text{ GeV}$) gamma rays from $\pi^0 \rightarrow \gamma\gamma$ decay. The total γ -ray luminosity injected in this region is measured to be of order of $L_{\gamma > 1 \text{ TeV}} \sim 5 \times 10^{34} \text{ erg s}^{-1}$.

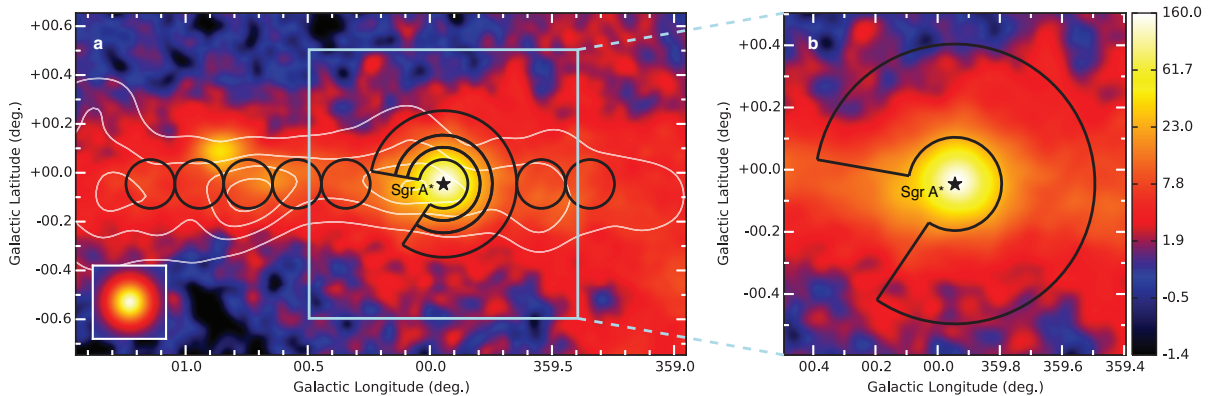


Figure 4.2: Galactic center region in very-high-energy gamma rays, from HESS Collaboration et al. (2016). The color scale indicate counts, white contours indicate the molecular gas density distribution. The right panel is a zoomed view around Sagittarius A*, and the black contour define the 50 pc region used to extract the diffuse emission spectrum.

The detection of VHE gamma rays in the 10 TeV energy range requires the acceleration of

CR protons to PeV energies, which implies either one or a population of accelerators of such particles, called as *pevatrons*, in the galactic center region. The central supermassive black hole Sagittarius A* could accelerate ultra-relativistic protons to PeV energies, thus acting as a Pevatron. In the scenario of a central single PeV source, the radial dependency of the CR proton profile up to a few hundred parsecs from Sagittarius A* suggests continuous injection of protons over timescales of at least thousands of years. It was initially suggested that a single supernova explosion could explain this emission, by the injection and diffusion of particles, and their interaction with the molecular clouds. However, a single supernova can hardly sustain efficient PeV proton acceleration over such a timescale (Bell et al., 2013).

4.1.3 The diffuse GeV emission

A high-energy gamma-ray excess with respect to the interstellar emission models has been detected using Fermi-LAT observations with a spatial extension up to about 20 degrees from the galactic center (see, for instance, Refs. (Goodenough and Hooper, 2009; Abazajian and Kaplinghat, 2012; Hooper and Slatyer, 2013; Abazajian et al., 2014; Calore et al., 2015; Daylan et al., 2016)). Several gamma-ray emission scenarii have been suggested, however there is no definite conclusion on the origin of the excess. Among them are dark matter annihilations in the inner region of the Galactic dark matter halo (Goodenough and Hooper, 2009; Hooper and Slatyer, 2013; Abazajian et al., 2014; Calore et al., 2015; Daylan et al., 2016), as well as outflows from the supermassive black hole Sagittarius A* injecting energetic cosmic-ray protons (Carlson and Profumo, 2014) or leptons (Petrović et al., 2014; Gaggero et al., 2015) in the interstellar medium from outflows. While the former may be in tension with the non-observation of gamma-ray excesses towards dwarf galaxy satellites of the Milky Way (Ackermann, 2015), the latter would hardly reproduce the morphology of the galactic center excess. An alternative hypothesis is the presence of an additional SNR population that could steadily inject protons (Gaggero et al., 2015; Carlson et al., 2016), being however not observed at any other wavelength so far.

More recently, a hypothetical population of MSP in the Galactic disk and the Galactic bulge has been shown to well match the morphology of the galactic center excess (Wang et al., 2005; Cholis et al., 2015; Lee et al., 2015; Bartels et al., 2016). The presence of this unresolved pulsar population has been independently put forward by Fermi-LAT (Fermi-LAT Collaboration, 2017) using 7.5 years of data of Pass 8 analysis¹. The disk population follows a Lorimer Galactocentric spatial distribution $\rho(R) \approx R^n e^{-(R/\sigma)}$ with $n = 2.35$ and $\sigma = 1.528$ kpc, and a distribution as a function of the distance from the Galactic disc $\rho(z) \approx e^{-(|z|/z_0)}$ with scale height $z_0 = 0.70$ kpc. The luminosity function for the gamma-ray emission is modelled as a power-law with slope -1.7 in the luminosity range $[10^{33}, 10^{36}] \text{ erg s}^{-1}$. The number of expected pulsars in the disk was derived to be $N_d = [4000 - 16000]$, based on the known pulsars and the unassociated 3FGL sources compatible with pulsar characteristics. Besides the pulsar population of the Galactic disk, an additional distinct bulge pulsar population is needed, for radial distance $r < 3$ kpc from the galactic center. This additional pulsar population is described by a spherically symmetric distribution $dN/dr \propto r^{-\alpha_b}$, with $\alpha_b = 2.6$. The bulge luminosity function is modelled as for the disk and the normalization is determined in order to reproduce the galactic center excess. The number of pulsars in the bulge is estimated to be in the range $N_b = [800 - 3600]$ in the luminosity range $[10^{33}, 10^{36}] \text{ erg s}^{-1}$.

These estimates can be affected by systematic uncertainties in the modelling of the MSP populations. Among them are the construction of the interstellar emission model, the modelling of the MSP disk population, and the assumed luminosity functions of the disk and bulge populations.

¹The unresolved bulge pulsar population is robustly detected against the underlying interstellar emission models possibly including the Fermi bubble component (Fermi-LAT Collaboration, 2017).

Interestingly, in Ploeg et al. (2017), the authors derived $N_b = (4.0 \pm 0.9) \times 10^4$ for MSP luminosities greater than $10^{32} \text{ erg s}^{-1}$. Extrapolating the derived luminosity function from Fermi-LAT Collaboration (2017) down to $10^{32} \text{ erg s}^{-1}$ provides compatible with the results of Ploeg et al. (2017) within errors. A recent bayesian study of gamma-ray emitting MSP (Bartels et al., 2018) suggest the presence of $2 \times 10^4 - 10^5$ MSP in the Galactic disk, a number that is in agreement with the population derived from radio catalogs (Levin et al., 2013). The authors find that the luminosity function in the disk population preferably follows a Lorimer power-law profile as we assume in the current work. They report that they lack sensitivity to place strong constraints on the bulge population of MSP.

4.2 Millisecond pulsars as pevatrons

The evidence of PeV protons in the galactic center, together with the report that a millisecond pulsar population may be responsible of the galactic center diffuse emission observed by Fermi-LAT, led us to elaborate the following scenario. A millisecond pulsar population emits the diffuse Fermi GeV gamma rays via leptonic processes, and the diffuse TeV excess observed by HESS via hadronic processes, hence acting as pevatrons. In this scenario, MSP accelerate protons up to very high energies, that can reach PeV energies for initial spin periods of $P_i \sim 1 \text{ ms}$ and dipole magnetic fields $B \gtrsim 10^9 \text{ G}$. These cosmic rays interact with the interstellar medium and molecular clouds through hadronic processes and produce neutral pions that decay into gamma rays. The millisecond pulsar population is characterized by a spatial distribution around the galactic center, and by period, magnetic field and age distributions.

The diffusion of cosmic rays emitted from each pulsar leads to a typical radial extension of the cosmic-ray density that can be compared to the data. We model the propagation of protons in the turbulent Galactic magnetic field by following the estimates of Blasi and Amato (2012) for the diffusion coefficient, as we will explain in detail in Section 4.3.1. Typical estimates of proton-proton interaction and diffusion timescales, written as

$$\begin{aligned} t_{pp} &= 1/cn_H\sigma_{pp}, \\ &\sim 10^{13} \text{ s } (n_H/100 \text{ cm}^{-3})^{-1}, \end{aligned} \quad (4.1)$$

and

$$\begin{aligned} t_{\text{diff}} &= r_{\text{diff}}^2/2D, \\ &\sim 10^{11} \text{ s } (r_{\text{diff}}/200 \text{ pc})^2, \end{aligned} \quad (4.2)$$

respectively, where $\sigma_{pp} \simeq 50 \text{ mb}$ is the hadronic cross section for a proton energy of $E = 10^{14} \text{ eV}$, n_H the gas density (see Section 4.1.1) and $D \simeq 10^{30} \text{ cm}^2 \text{ s}^{-1} E_{14}$ is the diffusion coefficient for protons at $E = 10^{14} \text{ eV}$ (see Section 4.3.1 for more details). As $t_{pp} > t_{\text{diff}}$, one expects a large radial extension of the cosmic-ray density distribution.

We only consider the impact of proton-proton interactions and neglect other energy loss processes, as synchrotron or inverse Compton processes. The typical interaction timescales of these processes are respectively $t_{\text{syn}}^{-1} \sim 4/3 \sigma_{T,p} c \gamma_p^2 U_B E^{-1}$ and $t_{\text{IC}}^{-1} \sim 4/3 \sigma_{T,p} c \gamma_p^2 U_{\text{rad}} E^{-1}$ (in the Thomson regime), where $\sigma_{T,p}$ is the Thomson cross section for protons, U_{rad} is the CMB energy density and $U_B = B^2/8\pi$ is the magnetic energy density. We obtain the estimates $t_{\text{syn}} \sim 7 \times 10^{14} \text{ yr } E_{13}^{-1} B_{-4}^{-2}$ and $t_{\text{IC}} \sim 1 \times 10^{18} \text{ yr } E_{13}^{-1}$ for $E_{13} = 10^{13} \text{ eV}$, $B_{-4} = 100 \mu\text{G}$ and $U_{\text{rad}} \sim 0.3 \text{ eV cm}^{-3}$. These are well above the typical proton-proton energy-loss timescale $t_{pp} \sim 5 \times 10^7 \text{ yr } n_{H,1}$ for $E_{13} = 10^{13} \text{ eV}$ and $n_{H,1} = 1 \text{ cm}^{-3}$, which confirms that these processes are sub-dominant when compared to proton-proton interactions.

Considering the MSP population inferred to explain the diffuse GeV emission, we assess if the energy reservoir in this population is sufficient to reach the level required to fit the gamma-ray flux. In the following, B is the polar magnetic field strength of the star, R_\star its radius and P_i the initial spin period, and $\Omega = 2\pi/P$ the angular speed. The radiation from a rotating dipole seen from infinity (Shapiro and Teukolsky, 1986) reads $\dot{E} = -2|\ddot{\mathbf{m}}|^2/3c^3$, where $\mathbf{m} = BR_\star^3(\cos\alpha\mathbf{e}_\parallel + \sin\alpha\cos\Omega t\mathbf{e}_\perp + \sin\alpha\sin\Omega t\mathbf{e}'_\perp)/2$ is the dipole magnetic moment, α the angle between the rotation and magnetic axis, \mathbf{e}_\parallel is a unit vector parallel to the rotation axis, \mathbf{e}_\perp and \mathbf{e}'_\perp are unit vectors building an orthonormal basis with \mathbf{e}_\parallel . As $|\ddot{\mathbf{m}}|^2 = B^2R_\star^6\Omega^4\sin^2\alpha/4$, we have $\dot{E} = -B^2R_\star^6\Omega^4\sin^2\alpha/6c^3$. We note that this estimate gives no radiation for the aligned rotator, and that other estimates of the energy dissipation have been inferred from numerical simulations (e.g. Spitkovsky, 2006), as mentioned in chapter 3. The averaged value of this electromagnetic luminosity is obtained by integration over a sphere $\dot{E}_{\text{ave}} = -\int_{\phi=0}^{2\pi}\int_{\alpha=0}^{\pi}d\alpha d\phi (B^2R_\star^6\Omega^4\sin^3\alpha/6c^3)/4\pi$ and we retrieve the electromagnetic luminosity of pulsars presented in Arons (2003)

$$\begin{aligned} |\dot{E}_{\text{rot}}| &= 16\pi^4 B^2 R_\star^6 P^{-4}/9c^3, \\ &\simeq 6.4 \times 10^{36} \text{ erg s}^{-1} B_9^2 R_{\star,6}^6 P_{i,-3}^{-4}, \end{aligned} \quad (4.3)$$

We consider that this luminosity is converted to kinetic luminosity $\dot{N}E$, with efficiency $\eta_{\text{acc}} \leq 1$. The particle rest mass power is $\dot{N}mc^2 \equiv \dot{N}_{\text{GJ}}(2\kappa m_e + Am_p/Z)c^2$, where

$$\begin{aligned} \dot{N}_{\text{GJ}} &\sim \mathcal{A}_{\text{PC}} \rho_{\text{GJ}} c/e = 2\pi^2 B R_\star^3 P^{-2}/ec, \\ &\simeq 1.4 \times 10^{33} \text{ s}^{-1} B_9 R_{\star,6}^3 P_{i,-3}^{-2}, \end{aligned} \quad (4.4)$$

is the Goldreich-Julian rate (Goldreich and Julian, 1969; Arons, 2003), with $\mathcal{A}_{\text{PC}} \simeq 2\pi^2 R_\star P^{-1}/c$ the area of a polar cap and $\rho_{\text{GJ}} \simeq BP^{-1}/c$ the Goldreich-Julian charge density (Goldreich and Julian, 1969). Therefore millisecond-pulsars can accelerate protons up to very high energies (Kotera et al., 2015):

$$\begin{aligned} E_0 &= \eta_{\text{acc}} |\dot{E}_{\text{rot}}|/\dot{N}, \\ &\sim 1.4 \times 10^{15} \text{ eV } \eta_{\text{acc}} \kappa_3^{-1} (1 + m_p/2m_e \kappa_3)^{-1} B_9 R_{\star,6}^3 P_{i,-3}^{-2}. \end{aligned} \quad (4.5)$$

where κ is the pair multiplicity, which can range between $10 - 10^8$ in theory (a highly debated quantity) and $\eta_{\text{acc}} = 1$. For $\kappa \sim 10^3$, a substantial fraction of the pulsar power goes into ions, as $m_p/2\kappa m_e \sim 0.9$. Taking into account the pulsar spin-down, with a braking index of $n = -\Omega\ddot{\Omega}/\dot{\Omega}^2 = 3$ (obtained for the magnetic dipole model), as $E(t) \propto P^{-2} \propto P_i^{-2}(1 + 8\pi^2 B^2 R_\star^6 t/9Ic^3 P_i^2)$, the cosmic-ray energy at time t is $E_{\text{CR}}(t) = E_0(1 + t/t_{\text{sd}})^{-1}$, where $t_{\text{sd}} = 9Ic^3 P^2/8\pi^2 B^2 R_\star^6 \sim 9.8 \times 10^7 \text{ yr } I_{45} B_9^{-2} R_{\star,6}^{-6} P_{i,-3}^2$ is the spin-down timescale. Following Blasi et al. (2000) and Arons (2003), as $\dot{N} = \Omega^2 m/ec$, $-d\Omega/dt = \dot{E}/I\Omega = 4\Omega^3 m^2/9Ic^3$ and $d\Omega/dE = \Omega/2E$ the spectrum of cosmic-rays accelerated is $dN/dE = -\dot{N}(dt/d\Omega)(d\Omega/dE) = 9Ic^2/4eBR_\star^3 E$. The cosmic-ray luminosity is therefore

$$\begin{aligned} L_{\text{CR}}(t) &= \frac{9}{4} \frac{c^2 I E^2}{e B R_\star^3} \frac{d}{dt} \left(\frac{1}{E} \right), \\ &= \frac{9}{4} \frac{c^2 I}{e B R_\star^3} E_{\text{CR}}(t) (t + t_{\text{sd}})^{-1}, \\ &\simeq 3.1 \times 10^{36} \text{ erg s}^{-1} \eta_{\text{acc}} \kappa_3^{-1} (1 + m_p/2m_e \kappa_3)^{-1} B_9^2 R_{\star,6}^6 P_{i,-3}^{-4} (1 + t/t_{\text{sd}})^{-2}, \end{aligned} \quad (4.6)$$

where the latter value is obtained for $\eta_{\text{acc}} = 1$ and $\kappa = 10^3$. In the following we neglect the potential interaction of accelerated cosmic rays in the vicinity of the source, with the ambient photon fields or hadronic debris, which is out of the scope of the present study. From the millisecond pulsar luminosity $L_{\text{MSP}} \sim 10^{36} \text{ erg s}^{-1}$, and the luminosity in baryons $L_p = \eta_p L_{\text{MSP}}$,

where η_p is the fraction of the pulsar luminosity channelled into protons, we have $L_{\text{MSP,tot}} = N_{\text{MSP}} L_{\text{MSP}}$ where N_{MSP} is the number of MSP in the region considered. Therefore the gamma-ray luminosity L_γ related to proton-proton interactions is

$$\begin{aligned} L_\gamma &\sim \tau_{pp} \eta_p L_{\text{MSP,tot}}, \\ &\sim 10^{36} \text{ erg s}^{-1} \eta_p \left(\frac{N_{\text{MSP}}}{100} \right) \left(\frac{r_{\text{diff}}}{200 \text{ pc}} \right)^2 \left(\frac{n_{\text{H}}}{100 \text{ cm}^{-3}} \right), \end{aligned} \quad (4.7)$$

where $\tau_{pp} = \min(1, t_{\text{diff}}/t_{pp})$. Note that the diffuse excess observed by HESS is about $L_{\gamma > 1 \text{ TeV}} \sim 5 \times 10^{34} \text{ erg s}^{-1}$ in the inner 50 pc region, thus the energetic budget estimated above is sufficient to explain the diffuse excess, and leaves room for low injection rate and inefficient sources.

Considering this population of MSPs, we predict the gamma-ray flux profile as a function of distance from the galactic center and the inferred cosmic-ray density, as well as the TeV gamma-ray flux energy spectrum in the inner 50 pc region. In order to reproduce the observational data with our predictions, only a limited number of free parameters are required to be determined: namely, the magnetic field distribution $F_B(B)$, the acceleration efficiency η_{acc} and the number of MSP in the population considered.

4.3 Cosmic-ray spatial density distribution

The diffusion of cosmic rays is the key process to estimate their density and its spatial dependency. First, we consider the case of one source and generalize our results to the case of two different MSP populations, in the Galactic bulge and in the disk, respectively. In the following, we focus on the case of accelerated protons.

4.3.1 Cosmic-ray density for a single source

After escaping from a source, cosmic rays diffuse and interact with the surrounding medium. Following Blasi and Amato (2012), we can model the diffusive propagation of protons with the diffusive transport equation

$$\frac{\partial n(E, \vec{r}, t)}{\partial t} = \nabla [D(E) \nabla n(E, \vec{r}, t)] - \Gamma^{\text{sp}}(E) n(E, \vec{r}, t) + N(E) \delta(t - t_s) \delta^3(\vec{r} - \vec{r}_s), \quad (4.8)$$

where cosmic rays are injected at a time t_s from a point source located at $\vec{r}_s = (x_s, y_s, z_s)$, with a spectrum $N(E)$; $n(E, \vec{r}, t)$ is the density of particles with energy E at the location \vec{r} and time t , $D(E)$ is the diffusion coefficient assumed to be spatially constant and $\Gamma^{\text{sp}}(E)$ is the spallation rate of protons. As explained in Section 4.5, we neglect proton energy losses, which are typically described by the term $\partial [P(E) n(E, \vec{r}, t)] / \partial E$. The energy-dependent diffusion coefficient writes

$$D(E) = 10^{28} D_{28} \left(\frac{R}{3 \text{ GV}} \right)^\delta \text{ cm}^2 \text{ s}^{-1}, \quad (4.9)$$

where $R = E/Z$ is the rigidity (with E in eV). The best fit to the existing data of boron-to-carbon ratio is obtained for $D_{28} = 4$ with $\delta = 1/3$ (Kolmogorov-type) (Kolmogorov, 1941; Aguilar et al., 2016; Strong and Moskalenko, 1998). The rate of spallation $\Gamma^{\text{sp}}(E)$ depends on the gas density n_{gas} , the nucleus velocity v (we can assume $v = c$) and the cross section σ_{pp}

$$\Gamma^{\text{sp}}(E) = n_{\text{gas}} c \sigma_{pp}. \quad (4.10)$$

At GeV energies and above, the spallation cross-section can be well parametrized by $\sigma_{pp}(E) \simeq 30 \{0.95 + 0.06 \ln[(E - m_p c^2)/1 \text{ GeV}]\} \text{ mb}$ (Aharonian, 2004).

The following Green's function is a solution of Eq. (4.8) without boundary conditions

$$\mathcal{G}(\vec{r}, t; \vec{r}_s, t_s) = \frac{N(E)}{[4\pi D(E)\tau]^{3/2}} \exp[-\Gamma^{\text{sp}}(E)\tau] \exp\left[-\frac{|\vec{r} - \vec{r}_s|^2}{4D(E)\tau}\right], \quad (4.11)$$

where $\tau = t - t_s$ (Blasi and Amato, 2012). For a constant source injection rate $\dot{Q}_p(E)$ during the time T , we can calculate the cosmic-ray density, at a time $t = T$ and position \vec{r} , by integrating over the injection time t_{inj}

$$\begin{aligned} w_{\text{CR}}(E, \vec{r}, t) &= \int_{t_{\text{inj}}=0}^t dt_{\text{inj}} \dot{Q}_p(E) \mathcal{G}(\vec{r}, t; \vec{r}_s, t_{\text{inj}}), \\ &= \int_{t'=0}^t dt' \dot{Q}_p(E) \mathcal{G}(\vec{r}, t'; \vec{r}_s, 0), \\ &= \frac{\dot{Q}_p(E)}{8\pi D(E)|\vec{r} - \vec{r}_s|} \left[\text{erfc}\left(\frac{|\vec{r} - \vec{r}_s|}{\sqrt{4D(E)t}} - \sqrt{\Gamma^{\text{sp}}(E)t}\right) \exp\left(\frac{-|\vec{r} - \vec{r}_s|}{\sqrt{D(E)/\Gamma^{\text{sp}}(E)}}\right) \right. \\ &\quad \left. + \text{erfc}\left(\frac{|\vec{r} - \vec{r}_s|}{\sqrt{4D(E)t}} + \sqrt{\Gamma^{\text{sp}}(E)t}\right) \exp\left(\frac{|\vec{r} - \vec{r}_s|}{\sqrt{D(E)/\Gamma^{\text{sp}}(E)}}\right) \right]. \end{aligned} \quad (4.12)$$

The above density can be simplified in specific cases. For a continuous injection over a time smaller than the proton-proton interaction timescale, the cosmic-ray density writes (HESS Collaboration et al., 2016)

$$w_{\text{CR}}(E, \vec{r}, t) = \frac{\dot{Q}_p(E)}{4\pi D(E)|\vec{r} - \vec{r}_s|} \text{erfc}\left(\frac{|\vec{r} - \vec{r}_s|}{\sqrt{4D(E)t}}\right), \quad (4.13)$$

and for times longer than the proton-proton interaction timescale, interactions induce an exponential cut-off, such as

$$w_{\text{CR}}(E, \vec{r}, t) = \frac{\dot{Q}_p(E)}{4\pi D(E)|\vec{r} - \vec{r}_s|} \exp\left(\frac{-|\vec{r} - \vec{r}_s|}{\sqrt{D(E)/\Gamma^{\text{sp}}(E)}}\right). \quad (4.14)$$

The diffusion radius r_{diff} is typically ~ 200 pc following the spatial extension of the TeV emission measured by HESS (HESS Collaboration et al., 2016). The corresponding radial cosmic-ray densities obtained in the above-mentioned cases are plotted in figure 4.3, with and without the spallation process. The solution used in HESS Collaboration et al. (2016) is accurate over a large range of distances: the cosmic-ray density integrated over injection time is compatible with a solution $\propto r^{-1}$ close to the source, typically at distances smaller than 100 pc. At large distances from the location of the source ($r \gg 100$ pc), we see the effect of diffusion for injection times smaller than the proton-proton interaction timescale and the effect of interactions for longer times. We note that $d_{\text{max,sp}}(E) \equiv \sqrt{D(E)/\Gamma^{\text{sp}}(E)} \sim 7 \times 10^2$ pc for $n_p = 100 \text{ cm}^{-3}$ and $E = 10^{13}$ eV.

4.3.2 Millisecond-pulsar distributions

We consider two distinct populations of millisecond-pulsars, one in the bulge and one in the disk, using the spatial distributions derived in Fermi-LAT Collaboration (2017).

In the bulge: the distribution of MSPs is described by $F_b(r_s, \theta, \phi) = K_b r^{-\alpha_b}$ in spherical coordinates, with K_b a normalization constant and $\alpha_b = 2.6$. By normalizing this distribution to the total number of millisecond-pulsars in the bulge N_b , we obtain

$$F_b(r_s, \theta, \phi) = \frac{(3 - \alpha_b)N_b}{4\pi r_{\text{max}}^{3-\alpha_b}} r_s^{-\alpha_b} \quad \text{for } 0 < r_s < r_{\text{max}}, \quad (4.15)$$

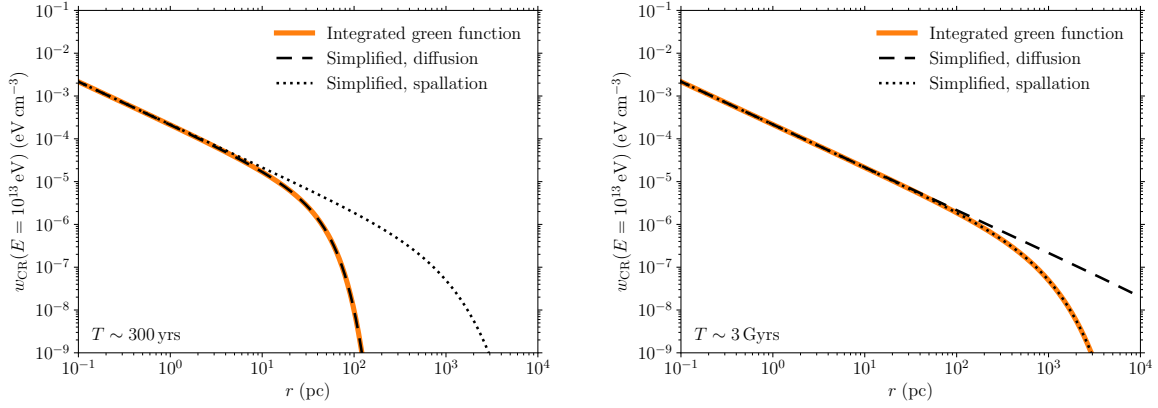


Figure 4.3: Cosmic-ray density for one source (orange, equation 4.12), compared with the simplified solution without spallation (dashed black, (HESS Collaboration et al., 2016), equation 4.13), and with the one with spallation (dotted black, equation 4.14), for $E = 10^{13}$ eV. We compare the results for continuous injection times $T \sim 300$ yrs (left) and $T \sim 3$ Gyrs (right). The three formalisms agree out to distances of a few 100 pc.

where $r_{\max} = 3.1 \times 10^3$ pc is the radial extension of the bulge (Mezger et al., 1996). Above r_{\max} , the disk contribution dominates over the bulge one. In this region, the precise behaviour of the radial dependency of the bulge distribution is neglected. The radial distribution normalized to 1 is therefore $F_b(r_s) = (3 - \alpha_b) r_s^{2-\alpha_b} / r_{\max}^{3-\alpha_b}$ for $0 < r_s < r_{\max}$.

In the disk: the distribution of MSPs, normalized to the total number of millisecond-pulsars in the disk N_d , is described by

$$F_d(r_s, \theta, z) = \frac{r_s^n \exp(-r_s/\sigma) \exp(-|z_s|/z_0) N_d}{4\pi z_0 \sigma^{n+2} \Gamma(n+2)}, \quad (4.16)$$

in cylindrical coordinates, with $n = 2.35$, $\sigma = 1.528 \times 10^3$ pc and $z_0 = 700$ pc. The radial distribution normalized to 1 is therefore $F_d(r_s) = r_s^{n+1} \exp(-r_s/\sigma) / \sigma^{n+2} \Gamma(n+2)$. The two radial distributions normalized to 1 are illustrated in figure 4.4.

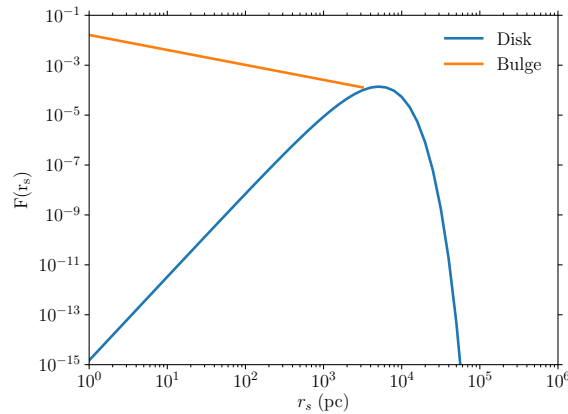


Figure 4.4: Normalized radial distribution functions of the bulge (orange line) and disk (blue line) populations of MSP.

4.3.3 Total cosmic-ray density

First, we focus on the impact of the spatial distribution of MSP on the cosmic-ray density profile, and thus consider a continuous injection of cosmic rays from each pulsar, during $T \sim 3$ Gyrs, and an observation time $t = T$. This preliminary assumption of continuous injection, which is not realistic in the case of MSP, should be considered as a preliminary step required to study the cosmic-ray radial distribution, as in this section we only aim at comparing the shape of the radial cosmic-ray density profile and not its normalization. As we will see in the next section, a more realistic cosmic-ray injection from MSP is needed to determine the pulsar population parameters required to reproduce the data. These parameters only impact the normalization of the profile and not its general shape. Moreover, the cosmic-ray density derived from the HESS measurements HESS Collaboration et al. (2016) displayed in figure 4.5 are obtained under different assumptions than ours. The luminosity of several regions is associated with the cosmic-ray density, using in particular the mass estimate in each region is based on tracer molecules.

As a first step, we assume that the cosmic-ray density for one source is well described by Eq. (4.13), where we neglect the error function component. As shown in Section 4.3.1, this approximation is reasonable for a continuous cosmic-ray injection from the source, and for short distances from the central source (see figure 4.3). With this assumption, the total cosmic-ray density is calculated analytically by integrating the one-source density over the distribution of millisecond-pulsars in the bulge and the disk.

In the bulge: the total cosmic-ray density is given by

$$\begin{aligned} w_{\text{CR,tot}}(E, r, t) &= \int_{r_s=0}^{\infty} \int_{\theta=0}^{\pi} \int_{\phi=0}^{2\pi} r_s^2 dr_s \sin \theta d\theta d\phi F(r_s, \theta, \phi) w_{\text{CR}}(E, |\vec{r} - \vec{r}_s|, t), \\ &= \frac{(3 - \alpha_b) \dot{Q}_p(E) N_b}{16\pi^2 D(E) r_{\text{max}}^{3-\alpha_b}} \int_{r_s=0}^{r_{\text{max}}} \int_{\theta=0}^{\pi} \int_{\phi=0}^{2\pi} \frac{r_s^{2-\alpha_b} dr_s \sin \theta d\theta d\phi}{\sqrt{r^2 + r_s^2 - 2rr_s \cos \theta}}. \end{aligned} \quad (4.17)$$

For $r < r_{\text{max}}$

$$w_{\text{CR,tot}}(E, r, t) = \frac{\dot{Q}_p(E)(3 - \alpha_b) N_b}{4\pi D(E)(2 - \alpha_b) r_{\text{max}}} \left[1 - \frac{1}{3 - \alpha_b} \left(\frac{r}{r_{\text{max}}} \right)^{2-\alpha_b} \right], \quad (4.18)$$

and for $r \geq r_{\text{max}}$

$$w_{\text{CR,tot}}(E, r, t) = \frac{\dot{Q}_p(E) N_b}{4\pi D(E) r}. \quad (4.19)$$

In the disk: the total cosmic-ray density is given by

$$\begin{aligned} w_{\text{CR,tot}}(E, r, t) &= \int_{r_s=0}^{\infty} \int_{\theta=0}^{2\pi} \int_{z_s=-\infty}^{\infty} r_s dr_s d\theta dz_s F(r_s, \theta, z_s) w_{\text{CR}}(E, |\vec{r} - \vec{r}_s|, t), \\ &= \frac{\dot{Q}_p(E) N_d}{16\pi^2 D(E) z_0 \sigma^{n+2} \Gamma(n+2)} \\ &\quad \times \int_{r_s=0}^{\infty} \int_{\theta=0}^{2\pi} \int_{z_s=-\infty}^{\infty} \frac{r_s^{n+1} dr_s d\theta dz_s \exp(-r_s/\sigma) \exp(-|z_s|/z_0)}{\sqrt{r^2 + r_s^2 - 2rr_s \cos \theta + (z - z_s)^2}}. \end{aligned} \quad (4.20)$$

Integrating over θ we obtain

$$w_{\text{CR,tot}}(E, r, t) = \frac{\dot{Q}_p(E) N_d}{\pi^2 D(E) z_0 \sigma^{n+2} \Gamma(n+2)} \int_{r_s=0}^{\infty} \int_{z_s=0}^{\infty} dr_s dz_s \times \frac{r_s^{n+1} \exp(-r_s/\sigma) \exp(-|z_s|/z_0)}{(r-r_s)^2 + z_s^2} \mathcal{K} \left(\frac{-4rr_s}{(r-r_s)^2 + z_s^2} \right). \quad (4.21)$$

where \mathcal{K} is the complete elliptic integral of the first kind. This integral is computed numerically. Moreover, we can examine the characteristics of the disk cosmic-ray density in this simple case. The disk distribution peaks around $\sigma \sim 10^4$ pc. At order zero, for $|\vec{r} - \vec{r}_s| \ll r_{\text{diff}}$

$$w_{\text{CR,tot}}(E, r, t) \approx \frac{\dot{Q}_p(E) N_{\text{disk}}}{4\pi D(E) \sigma (n+1)} \quad \text{for } r \ll \sigma, \quad (4.22)$$

$$\approx \frac{\dot{Q}_p(E) N_{\text{disk}}}{4\pi D(E) r} \quad \text{for } r \gg \sigma. \quad (4.23)$$

We note that the limit obtained at $r \gg \sigma$ is similar to the cosmic-ray density of the bulge population at $r \geq r_{\text{max}}$.

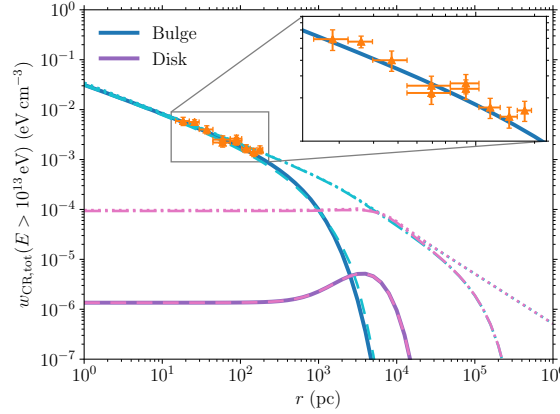


Figure 4.5: Total cosmic-ray density profiles for the bulge and disk populations of MSP (respectively, blue and purple lines), for $E > 10^{13}$ eV and a continuous injection time $T \sim 3$ Gyrs. We examine the joint effect of diffusion radius and spallation (equation 4.12, solid line), the effect of diffusion radius only (equation 4.13, dot-dashed line), the effect of spallation only (equation 4.14, dashed line) and the simplest case (r^{-1} component in equation 4.13, dotted line). The injection parameters have been chosen to enable a comparison with the cosmic-ray densities derived in HESS (orange points), where specific assumptions are made, see text. The vertical error bars correspond to 1σ confidence levels and the horizontal ones to the bin sizes. A population in the disk alone fails to reproduce the observed CR distribution.

The total cosmic-ray densities for the two different populations are illustrated in figure 4.5. The MSP populations considered extend over large distances, thus the corrections due to diffusion or interaction times have a significant impact on the total cosmic-ray density profiles. For distances $r < 200$ pc, the disk component is characterised by a constant cosmic-ray density profile. Hence we can readily see that the disk population alone cannot be sufficient to reproduce the results obtained in HESS Collaboration et al. (2016), and that a bulge component is needed. Interestingly, the spatial distribution of the bulge MSP population allows to reproduce the radial dependency of the CR densities derived in HESS Collaboration et al. (2016). For such a long injection time ($T \sim 3$ Gyrs), diffusion only affects the cosmic-ray density at large distances from the Galactic center ($r > 10^3$ pc). Moreover, proton-proton interactions affect significantly the cosmic-ray density at large distances ($r > 10^3$ pc), but also at small distances for the disk MSP population. Indeed, the disk distribution peaks at a large distance from the Galactic center, and protons injected at these distances interact before propagating towards the Galactic center, which strongly reduces the cosmic-ray density at small distances.

4.4 Diffuse gamma-ray emission

In order to compute the diffuse gamma-ray flux associated with the total cosmic-ray densities, we first need to give more details on the cosmic-ray injection from MSP. As stated before, energetic particles are continuously injected for a typical duration $t_{\text{sd}} = 9Ic^3P^2/8\pi^2B^2R_\star^6$ –the so-called spin-down timescale (Shapiro and Teukolsky, 1986). A *transient* flux of cosmic rays can be naturally modeled assuming that the electromagnetic energy of the pulsar wind, stemming from the combination of the stellar rotation and dipole magnetic field, is dissipated at each instant into particles. Following the notations and assumptions used in Section 4.2, the flux can be characterized by a mono-energetic injection at each time t with energy $E_{\text{CR}}(t) = E_0(1+t/t_{\text{sd}})^{-1}$. This type of injection produces a hard injection spectrum in E^{-1} . However, this first injection can be reprocessed, for instance at a shock front, producing a power-law injection spectrum with a possibly softer index, if the acceleration process is stochastic for instance. This flux can then be modeled as a *uniform* power-law spectrum that lasts over t_{sd} .

The total cosmic-ray density is calculated by accounting for the spatial distribution of MSP and diffusion of cosmic rays (see Section 4.3) but also for the variety of MSP in the population considered. We model the initial spin period distribution by a log-normal $F_P[P(\text{ms})] \propto P^{-1} \exp[(\log P - \mu)^2/2\sigma^2]$ with $\mu = 1.5$ and $\sigma = 0.58$ (Lorimer et al., 2015), and the magnetic field distribution by a power-law $F_B(B) \propto B^{-1}$ for $B_{\text{min}} < B < B_{\text{max}}$ (Story et al., 2007), where we set $B_{\text{min}} = 10^8 \text{ G}$. The value of B_{max} is adjusted to reproduce the HESS observations.

The predictions for the gamma-ray diffuse emission can be compared with the HESS observations (HESS Collaboration et al., 2016). The gamma-ray diffuse flux and integrated luminosity are measured in different regions close to the galactic center. Considering that the gamma-ray emission is entirely produced by pp interactions, we can calculate the gamma-ray spectrum $dN_\gamma/d\epsilon dt$, where ϵ is the photon energy, from the differential cross section for the gamma-ray production $d\sigma_{pp,\gamma}(\epsilon, E)/d\epsilon$, the cosmic-ray density $w_{\text{CR}}(E, r)$ and the mass of the target M in the region of interest, centred at r (where we consider that w_{CR} is constant):

$$\begin{aligned} \frac{dN_\gamma}{d\epsilon dt} &= \eta_N \int dE \frac{dN_p}{dE dt} \frac{d\sigma_{pp,\gamma}}{d\epsilon}(\epsilon, E), \\ &= \frac{\eta_N M c}{m_p} \int dE w_{\text{CR}}(E, r) \frac{d\sigma_{pp,\gamma}}{d\epsilon}(\epsilon, E). \end{aligned} \quad (4.24)$$

The factor η_N accounts for the presence of nuclei ($Z > 1$) in interstellar matter and m_p is the proton mass. The differential cross sections for the gamma-ray production are generated with the EPOS LHC model (Werner et al., 2006; Pierog et al., 2015b) and are illustrated in figure 4.6, for different proton energies between $E = 1 \text{ TeV}$ and $E = 10^4 \text{ TeV}$. We note that in the energy range of interest (above $\epsilon = 1 \text{ TeV}$), the differential cross section shows a strong dependence on the incident proton energy since the maximum energy is directly linked to the latter. In Kelner et al. (2006), these distributions have been parametrized as a function of the fraction of energy $x = \epsilon/E$ to remove this explicit dependence. Since for our study we are not interested in the detailed contributions of each hadronic component like in Kelner et al. (2006), we preferred a more straightforward approach using the up-to-date hadronic interaction model EPOS LHC Werner et al. (2006) and Pierog et al. (2015b) now widely used to study soft QCD results at LHC and air showers. The differential cross section for the photon production is simulated directly taking into account the decay of all unstable particles (mainly neutral pions and eta resonances) at different energies and then interpolated for the calculation of the integral in equation 4.24.

We note that HESS Collaboration et al. (2016) calculate gamma-ray luminosity as follows: $L_\gamma(\epsilon) \sim \eta_N w_{\text{CR}}(10\epsilon)M/n_H m_p t_{pp \rightarrow \gamma}$, where n_H is the hydrogen gas density and $t_{pp \rightarrow \gamma}$ is the proton energy-loss timescale related to gamma ray production. In our work, we integrate over the differential cross section for the gamma-ray production. Therefore, each proton energy is not

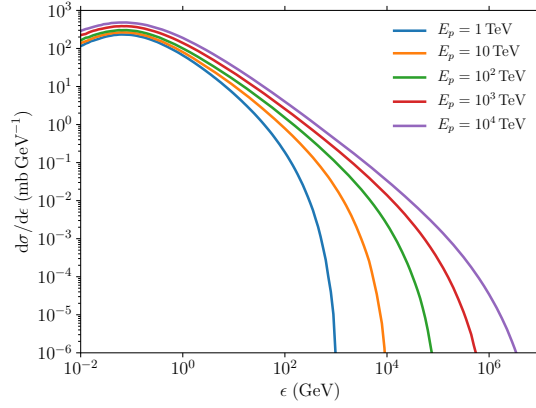


Figure 4.6: Differential cross sections for the gamma-ray production $d\sigma_{pp,\gamma}(\epsilon, E)/d\epsilon$ (mb GeV $^{-1}$), as a function of gamma-ray energy ϵ (GeV), for various proton energies $E = 1 - 10^4$ TeV.

related to a unique photon energy but to a distribution of photon energies, which is characterized by the differential cross section. For a monoenergetic proton injection at the energy E , the peak of the gamma-ray spectrum $\epsilon^2 dN_\gamma/d\epsilon$ is located around $\epsilon \approx E/10$.

We can compare our predictions in the inner 50 pc region for the transient and uniform injection models, with HESS measurements extracted from HESS Collaboration et al. (2016), and Fermi-LAT data extracted from Gaggero et al. (2017). The diffuse gamma-ray flux in this region is obtained from the gamma-ray luminosity: $\epsilon^2 \Phi_\gamma(\epsilon) = L_\gamma(\epsilon)/4\pi D_{GC}^2 \Delta\Omega$, where $D_{GC} \sim 8 \times 10^3$ pc is the distance from the galactic center and $\Delta\Omega \simeq \Delta\phi(\cos\theta_{\min} - \cos\theta_{\max})$ is the solid angle of the inner 50 pc region.

The uniform injection case, with a power-law injection, a constant maximum acceleration energy and luminosity over the pulsar spin-down time, is first treated in Section 4.4.1. The transient injection is then studied in more detail in Section 4.4.2.

4.4.1 Uniform power-law cosmic-ray injection

The uniform injection of accelerated protons from each millisecond-pulsar $\dot{Q}_p(E)$ is modeled by a simple power-law $dN/dE \propto E^{-\beta}$ for $E_{p,\min} < E < E_{p,\max}$, with β the injection spectral index. Each pulsar injects protons during the typical duration $T = t_{sd}$. We obtain the following proton injection rate

$$\dot{Q}_p(E) = \frac{\eta_p L_{CR}(t_{sd})(2 - \beta)}{1 - [E_{p,\min}/E_{p,\max}(t_{sd})]^{2-\beta}} \left[\frac{E}{E_{p,\max}(t_{sd})} \right]^{2-\beta}, \quad (4.25)$$

where η_p is the baryon loading, $L_{CR}(t_{sd}) \sim 2.5 \times 10^{35} \text{ erg s}^{-1} \eta_{\text{acc}} B_9^2 R_{\star,6}^6 P_{i,-3}^{-4}$ is the pulsar luminosity in cosmic rays at $t_{sd} \sim 9.8 \times 10^7 \text{ yr } I_{45} B_9^{-2} R_{\star,6}^{-6} P_{i,-3}^2$ and $E_{p,\max}(t_{sd}) \sim 2.3 \times 10^{14} \text{ eV } A \eta_{\text{acc}} \kappa_4^{-1} B_9 R_{\star,6}^3 P_{i,-3}^{-2}$ is the maximum energy of accelerated protons at t_{sd} . In this case, the cosmic-ray luminosity and maximum energy do not vary, and we choose the fiducial minimum injection energy $E_{p,\min} = 10^{10} \text{ eV}$. If we neglect the impact of spallation on the diffusion, and assume a constant pulsar birth rate τ_{birth} during the time t , the cosmic-ray density for one source is given by equation. (4.13). For each sub-class of pulsars with fixed P and B , the cosmic-ray density is weighted by t_{sd}/t , ensuring a uniform emission during the time t . This formalism is valid as long as the average timescale between two millisecond pulsar births is shorter than the spin-down timescale $1/\tau_{\text{birth}} \ll t_{sd}$, which is usually the case, as $t_{sd} \gtrsim 10^7 \text{ yrs}$ for MSP, and the typical birth rate is $\tau_{\text{birth}} \gtrsim 1/345000 \text{ yr}^{-1}$ (Ferrario and Wickramasinghe, 2007; Story et al., 2007; Lorimer, 2008). We calculate the cosmic-ray density integrated over the spin and magnetic

field distributions. Without the additional factor t_{sd}/t , the cosmic-ray density spectrum would be well described by a power-law of index $\beta + \delta$, but in our case the situation is more complex. The cosmic-ray density as a function of distance is still well described by a power-law $\propto r^{-1}$, as it is not influenced by the integration over the distributions.

The total cosmic-ray injection is obtained after the integration over the spatial distribution of the bulge MSP population, which gives the dominant contribution for $N_d \lesssim 10^3 N_b$ in the region of interest $r \lesssim 200$ pc (see figure 4.5). As $w_{\text{CR}}(E, r, t) \propto r^{-1}$ for $r \lesssim 200$ pc, we can use the analytical expressions derived in Section 4.3, especially the equation 4.18. Finally, we calculate the diffuse gamma-ray spectrum and luminosity, illustrated on figure 4.7 for $\beta = 1.1$, $E_{p,\text{min}} = 10^{10}$ eV, $\eta_{\text{acc}} \sim 0.03$, $\kappa = 10^3$ and $\eta_p N_b \sim 10^6$. In general the HESS data can be reproduced for $\eta_{\text{acc}}(m_p/2m_e\kappa)/(1 + m_p/2m_e\kappa) \sim 10^{-2}$. Concerning the magnetic field distribution, $B_{\text{max}} \geq 10^{11}$ eV allows to reproduce the HESS observations, whereas lower values do not allow to reproduce the HESS data over the whole energy range. The number of pulsars required increases with B_{max} .

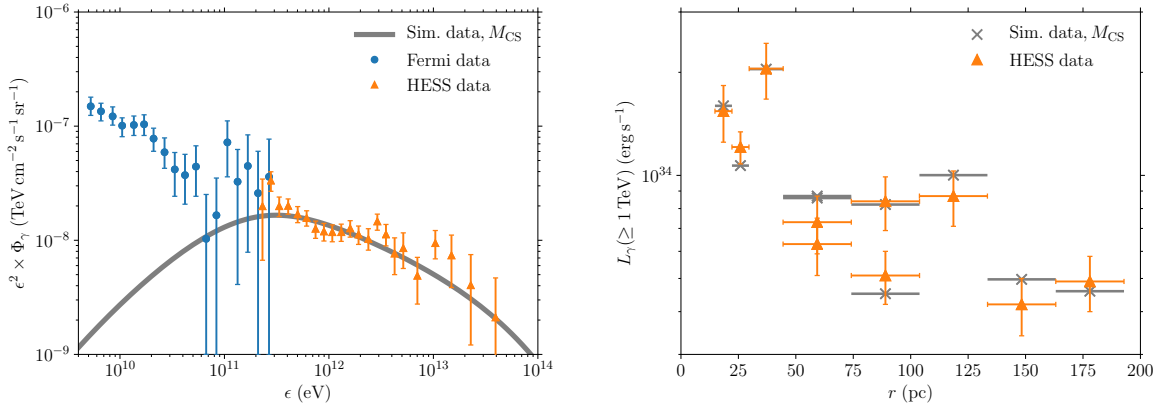


Figure 4.7: Diffuse gamma-ray spectrum in the central region (*left*), as predicted by our uniform power-law injection model for $\beta = 1.1$, $E_{p,\text{min}} = 10^{10}$ eV, $\eta_{\text{acc}} \sim 0.03$ and $\eta_p N_b \simeq 2 \times 10^6$ (grey thick line) and measured by Fermi (blue dots) and HESS (orange triangles). Gamma-ray luminosity as a function of the distance to the galactic center (*right*), from our model with the same parameters (grey crosses) and measured by HESS (orange triangles). The horizontal bars show the bin size and the vertical ones, the 1σ confidence level of the HESS data.

One drawback of this uniform injection model is that the value of the parameter $E_{p,\text{min}} = 10^{10}$ eV is quite arbitrary, but determines the energy range covered by the modeled diffuse gamma-ray spectrum. Moreover, we note that hard injection spectra $\beta \sim 1 - 2$ are needed to fit the HESS data. Such spectra can be achieved in pulsars, for example via reconnection processes in the striped wind, as shown by hybrid and particle-in-cell simulations (e.g., Bennett and Ellison (1995), Dieckmann and Bret (2009), Spitkovsky (2008), and Sironi and Spitkovsky (2011)). More simply, the unipolar induction toy-model in the transient monoenergetic injection scenario described in the next section produces naturally hard injection spectra with $\beta = 1$ Shapiro and Teukolsky (1986), without involving additional parameters as the minimum injection energy.

4.4.2 Transient monoenergetic cosmic-ray injection

From Eq. (4.6), the transient flux of cosmic rays injected into the wind is given by

$$\frac{d^2 N}{dE dt}(E, t) = \frac{9}{4} \frac{c^2 I}{ZeBR_\star^3} E^{-1} (t + t_{\text{sd}})^{-1}, \quad (4.26)$$

with a mono-energetic injection at each time t at $E_{\text{CR}}(t) = E_0(1 + t/t_{\text{sd}})^{-1}$, where $t_{\text{sd}} \sim 3.1 \times 10^{15} \text{ s } I_{45} B_9^{-2} R_{\star,6}^{-6} P_{1,-3}^2$. Following the approach of Blasi and Amato (2012), we calculate the CR density at position \vec{r} , energy E and time t , for a transient CR injection from a single millisecond-pulsar located at \vec{r}_s and starting at t_s

$$\begin{aligned} w_{\text{CR}}(E, \vec{r}, t) &= \int_{t^*=0}^{t-t_s} dt^* E^2 \frac{d^2 N}{dE dt}(E, t^*) \mathcal{G}(\vec{r}, t; \vec{r}_s, t^*), \\ &= \int_{t^*=0}^{t-t_s} dt^* \frac{9}{4} \frac{c^2 I}{ZeBR_{\star}^3} E(t^* + t_{\text{sd}})^{-1} \delta\left(\frac{E(1 + t^*/t_{\text{sd}})}{E_0} - 1\right) \mathcal{G}(\vec{r}, t; \vec{r}_s, t^*), \\ &= \frac{9}{4} \frac{c^2 I E}{ZeBR_{\star}^3} \mathcal{G}(\vec{r}, t; \vec{r}_s, t_s + t_{\text{sd}}(E_0/E - 1)), \end{aligned} \quad (4.27)$$

which is non zero only for $E_0[1 + (t - t_s)/t_{\text{sd}}]^{-1} \leq E \leq E_0$. For a given energy E , this solution is only valid after the injection of cosmic rays, for $t > t_s + t_{\text{sd}}(E_0/E - 1)$.

We assume a uniform distribution for the birth time of the pulsars t_s between $t_s = 0$ and $T_{s,\text{max}} = t$. We integrate the one-source cosmic-ray density over the birth time, spin and magnetic field distributions

$$\begin{aligned} w_{\text{CR}}(E, \vec{r}, t) &= \int_{B=0}^{\infty} dB \int_{P=0}^{\infty} dP \int_{t_s=0}^{t_{s,\text{max}}} dt_s \frac{9}{4} \frac{c^2 I E F_B(B) F_P(P)}{e B R_{\star}^3 T_{s,\text{max}}} \mathcal{G}[\vec{r}, t; \vec{r}_s, t_s + t_{\text{sd}}(E_0/E - 1)] \\ &= \int_{B=0}^{\infty} dB \int_{P=0}^{\infty} dP \int_{t'_s=t'_{s,\text{min}}}^{t'_{s,\text{max}}} dt'_s \frac{9}{4} \frac{c^2 I E F_B(B) F_P(P)}{e B R_{\star}^3 T_{s,\text{max}}} \mathcal{G}(\vec{r}, t'_s; \vec{r}_s, 0), \end{aligned} \quad (4.28)$$

with $t_{s,\text{max}} = \min\{\max[t - t_{\text{sd}}(E_0/E - 1), 0], T_{s,\text{max}}\}$, $t'_{s,\text{min}} = t - t_{\text{sd}}(E_0/E - 1) - t_{s,\text{max}}$ and $t'_{s,\text{max}} = t - t_{\text{sd}}(E_0/E - 1)$. Note that t_{sd} and E_0 depend on B and P_1 . The influence of the P , B and t_s distributions on the cosmic-ray densities is illustrated in figure 4.8. It highlights the importance of the B^{-1} dependence of the magnetic field distribution, required to obtain the correct power-law shape of the cosmic-ray density and diffuse gamma-ray spectra, and therefore a good match to the HESS measurements.

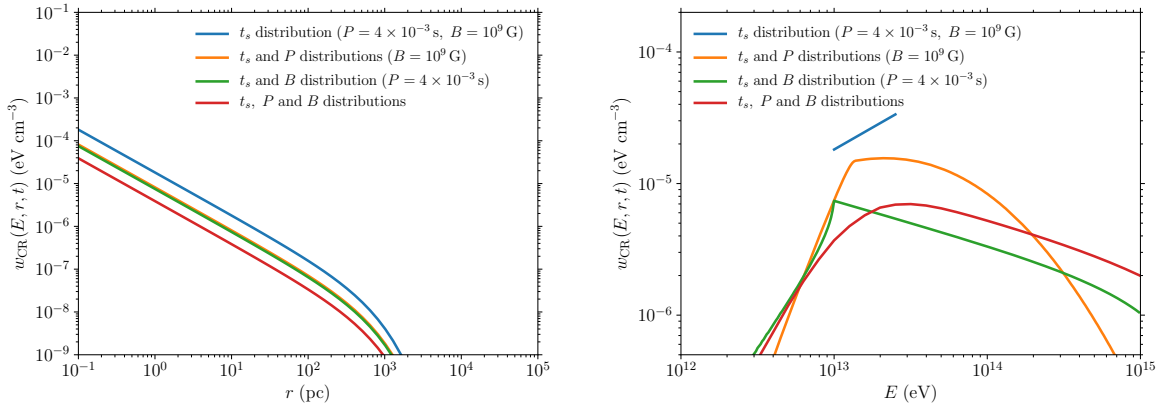


Figure 4.8: Cosmic-ray density for $\eta_{\text{acc}} = 1$ and $t = T_{s,\text{max}} = 10^{17} \text{ s}$, as a function of distance for $E = 10^{13} \text{ eV}$ (left) and as a function of energy for $r = 1 \text{ pc}$ (right). We show the cosmic-ray densities integrated on: t_s distribution, for $P = 4 \times 10^{-3} \text{ s}$ and $B = 10^9 \text{ G}$ (blue); t_s and P distributions, for $B = 10^9 \text{ G}$ (orange); t_s and B distributions, for $P = 4 \times 10^{-3} \text{ s}$ (green); t_s , P and B distributions (red).

For a given set of MSP parameters (P_1, B, R_{\star}, t_s) , the maximum and minimum energies of cosmic rays can be very close for a small observation time $t > t_s$, as $E_{\text{max}} = E_0$ and $E_{\text{min}} = E_0\{1 + [\min(t, T_{s,\text{max}}) - t_s]/t_{\text{sd}}\}^{-1}$. For $t_{\text{obs}} > T_{s,\text{max}}$, the cosmic-ray density is attenuated very rapidly. In this study, we focus on the case $t_{\text{obs}} \leq T_{s,\text{max}}$, considering that the birth of MSP in

the galactic center still arise today. The value of $T_{s,\max}$ influences the normalization of the birth time distribution; from the typical age of our galaxy, we set $T_{s,\max} = 10^{17}$ s.

As shown in Section 4.3.1, for $r \lesssim 200$ pc, the cosmic-ray density as a function of distance r is well described by a power-law $\propto r^{-1}$. Therefore, the total cosmic-ray density can be obtained by using the results of Section 4.3.3, which accounts for the integration of the above density over the spatial distribution of MSP in the bulge. As stated before, the contribution of the bulge population is dominant for $N_d \lesssim 10^3 N_b$ at $r \lesssim 200$ pc. Therefore, depending on the relative number of MSP in both populations, the disk population could contribute to the diffuse flux: for $N_d/N_b \sim 1$, it would give a contribution above $r \sim 5 \times 10^3$ pc (see figure 4.5).

Considering the bulge contribution only, for a mass estimate based on CS tracers, a moderate acceleration efficiency $\eta_{\text{acc}} \sim 0.03$ for $\kappa = 10^3$, a total number of pulsars $\eta_p N_b \sim 10^6$, $\eta_N = 1.5$ and a power-law distribution of the magnetic field of index -1 between $B_{\min} = 10^8$ G and $B_{\max} = 10^{11}$ G, we obtain a gamma-ray spectrum and a luminosity profile that are compatible with the HESS measurements. Our results are shown in figure 4.9.

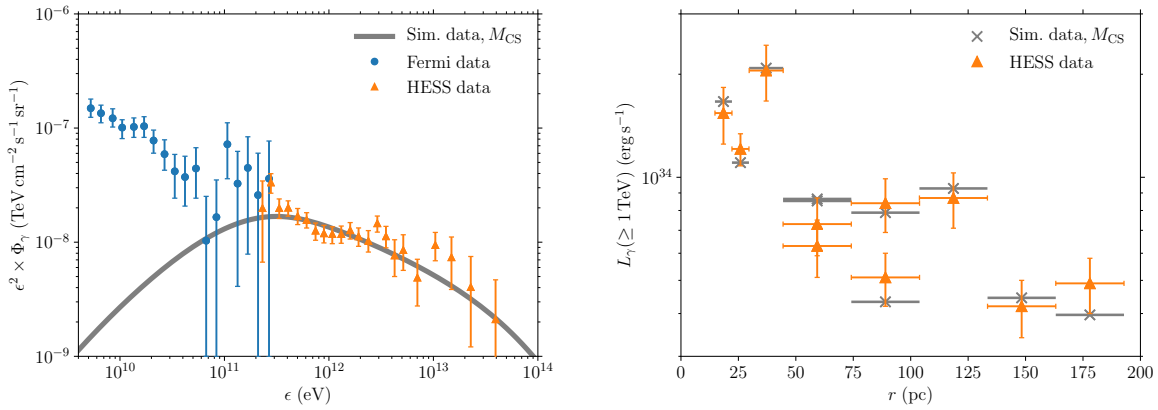


Figure 4.9: Diffuse gamma-ray spectrum in the central region (*left*), as predicted by our transient monoenergetic injection model for a mass estimate based on CS tracers, $\eta = 0.03$, $\eta_p N_b \simeq 10^6$ (grey thick line) and measured by Fermi (blue dots) and HESS (orange triangles). Gamma-ray luminosity as a function of the distance to the galactic center (*right*), from our model with the same parameters (grey crosses) and measured by HESS (orange triangles).

4.4.3 Bulge population of pulsars

Our two injection models require a total number of pulsars $\eta_p N_b \sim 10^6$ in the bulge in order to reproduce the HESS data. This number is subject to large uncertainties, as it depends on the baryon loading η_p – a poorly constrained quantity, on the acceleration efficiency and on the various distributions characterizing our pulsar population. Better observational constraints would be required to obtain a more accurate estimate of this quantity. Moreover, we note that this number corresponds to the total number of MSP in the bulge population, for a uniform birth time distribution. Therefore a large fraction of these pulsars do not contribute to the emission observed by HESS as they have already dissipated a large fraction of their rotational energy. Moreover, the population analysis in the literature consider frequently luminosities $> L_{\gamma,\min} \sim 10^{33}$ erg s $^{-1}$ for gamma rays produced through leptonic processes. Therefore, the number of pulsars with cosmic-ray luminosities lying in a given range would be a better quantity to compare with other MSP pulsation studies. The initial spin and magnetic field distributions, as well as the proton maximum energy and luminosity distributions at t_{obs} are illustrated in figure 4.10 for $\eta_{\text{acc}} = 0.03$ and $\kappa = 10^3$. The cosmic-ray energy distribution peaks at $\sim 10^{12}$ eV

and the cosmic-ray luminosity distribution peaks at $\sim 10^{32} \text{ erg s}^{-1}$. The cosmic-ray luminosity distribution can be approximated by a power-law between $\sim 10^{34} - 10^{36} \text{ erg s}^{-1}$, with a profile $\propto L_{\text{CR}}^{-1.4}$. This result is qualitatively compatible with the typical luminosity distribution of pulsars in gamma rays, which is described by a harder profile.

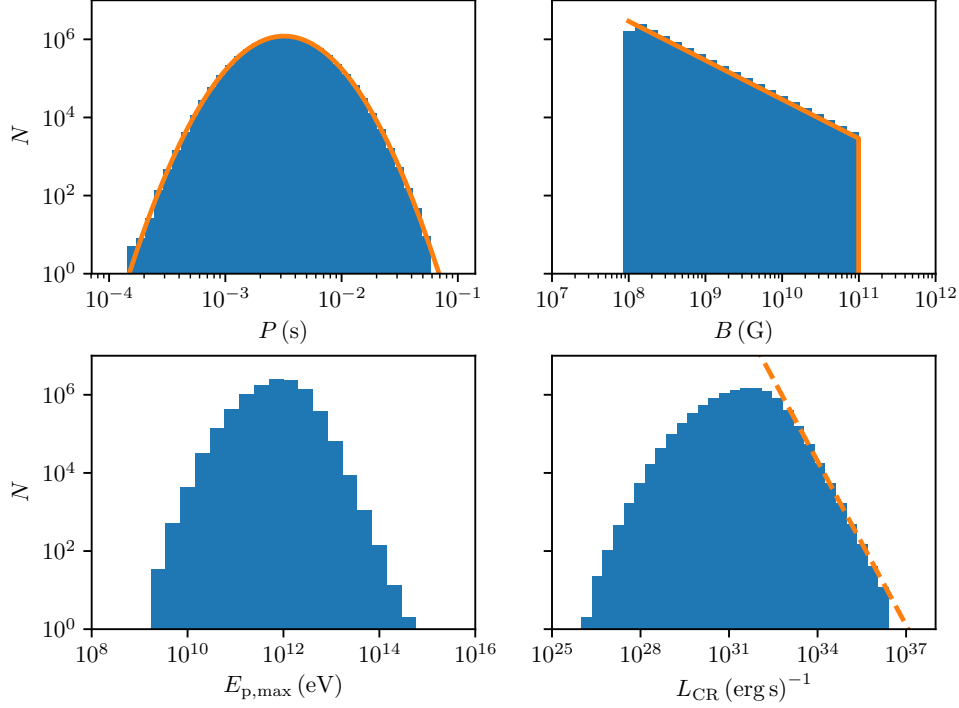


Figure 4.10: From left to right and up to down, initial spin, dipole magnetic field, cosmic-ray energy and cosmic-ray luminosity distribution histograms, for a random draw of 10^7 initial spin and dipole magnetic field values. The adjusted analytic distributions are also shown for initial spin and dipole magnetic field distributions (orange).

Using these distributions, we can estimate that a sub-population of MSP with $L_{\text{CR}}(t_{\text{sd}}) > 10^{33} \text{ erg s}^{-1}$ represents $\sim 4\%$ of the total MSP population, for $\eta_{\text{acc}} = 0.03$ and $\kappa = 10^3$. The corresponding number of MSP in this sub-population is then $N_{\text{b}}(L_{\text{CR}}(t_{\text{sd}}) > 10^{33} \text{ erg s}^{-1}) \sim 4 \times 10^4$, which is of the same order that the one derived in Ploeg et al. (2017). Note that a higher lower bound for $L_{\text{CR}}(t_{\text{sd}})$ would lead to a smaller fraction of the total population, for instance $N_{\text{b}}(L_{\text{CR}}(t_{\text{sd}}) > 10^{34} \text{ erg s}^{-1}) \sim 2 \times 10^3$, which lies in the range suggested by Fermi-LAT Collaboration (2017). More precise comparison between leptonic and hadronic models would require a joint modeling of leptonic and hadronic emissions from pulsars.

4.5 Discussion

The contribution of heavier nuclei appears only as a pre-factor η_N in the gamma-ray luminosity calculation. This value is commonly chosen to be $\eta_N = 1.5$, e.g., HESS Collaboration et al. (2016). However, a more refined treatment would be required to account for the various and more complex effects appearing if pulsars accelerate protons as well as heavier nuclei. For instance the accelerated nuclei would reach energies higher than protons, as typically $E_{N,\text{max}} \sim Z E_{p,\text{max}}$. The spallation of nuclei would also create secondary nuclei during the diffusion process. Such effects are left for future studies.

We have modeled the diffusion process of cosmic rays using a standard diffusion coefficient (Strong and Moskalenko, 1998). Recent detections of extended TeV emissions around young pulsars with HAWC has led to a measurement of the diffusion coefficient, that the collaboration claims as a general value for the interstellar medium (Abeysekara et al., 2017). Hooper and Linden (2017) however argues that this measurement should be only valid locally, around the Geminga and Monogem pulsars. Note also that the statistical significance of these measurements is still low and to be confirmed. We tested the influence of the diffusion coefficient on our results: for a 100-times lower diffusion coefficient, the radial extension of the gamma-ray excess is reduced, and therefore the gamma-ray luminosity as a function of the distance to the galactic center cannot match with the HESS observations. This result is illustrated in figure 4.11, where we compare two different diffusion coefficients, $D(E)$ and $D(E)/100$, where $D(E) = 10^{28} D_{28} (R/3 \text{ GV})^\delta \text{ cm}^2 \text{ s}^{-1}$, $R = E/Z$, $D_{28}/H_{\text{kpc}} = 1.33$ and $\delta = 1/3$ (see Eq. (4.9)).

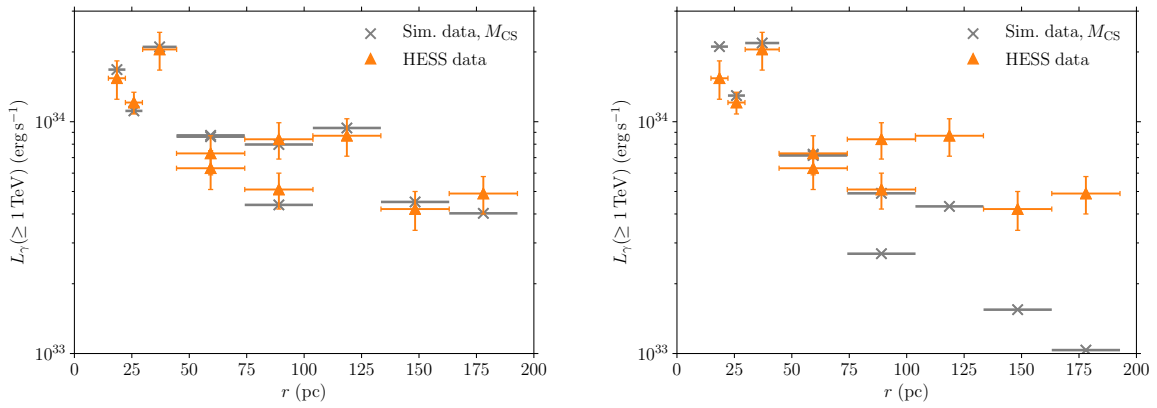


Figure 4.11: Gamma-ray luminosity as a function of the distance to the galactic center, for our model (grey crosses) and measured by HESS (orange triangles). We compare the results obtained for the diffusion coefficient $D(E)$ of Eq. (4.9) (left) and for $D(E)/100$ (right).

The modelling of our population of MSP is subject to uncertainties. In particular, the dipole magnetic field distribution of such objects is still not well constrained by the observations. However, we noted in this work that this distribution has a strong impact on the predictions, especially on the shape of the gamma-ray spectrum. Whereas B_{max} has a minor impact as long as $B_{\text{max}} \geq 10^{11} \text{ G}$, the index -1 of this power-law distribution is decisive in order to match the HESS measurements.

We focussed in this work on the gamma-ray spectrum at the highest energies, *i.e.* $\sim 1 \text{ TeV}$, and obtained a reasonable match to the diffuse emission measured by HESS with our two cosmic-ray injection models, for a bulge population of MSP. However, these hadronic models do not account for the Fermi gamma-ray observations at lower energies. As mentioned in Section 4.1.3, standard leptonic scenarios involving populations of pulsars can explain the flux observed by Fermi up to $\sim 10 \text{ GeV}$ energies. This would imply that the hadronic and leptonic emissions from MSP would fail to explain the gamma-ray flux observed by Fermi between 10 GeV and 100 GeV , shown in figure 4.7 and 4.9. On the other hand, several theoretical models have been discussed in the literature that enable the acceleration of electron and positron pairs in pulsars up to $\sim 10 \text{ TeV}$ energies (Kisaka and Kawanaka, 2012; Bednarek and Sobczak, 2013; Venter et al., 2015). Observationally, two young pulsars (Geminga, Monogem) have been identified by HAWC as emitters of gamma rays up to 100 GeV via leptonic components (Abeysekara et al., 2017). Hints of TeV halos around MSP have been reported to be found in the HAWC data Hooper and Linden (2018). Moreover, Petrović et al. (2015) and Yuan and Ioka (2015) suggest that the up-scattering of low-energy photons by electron-positron pairs emitted by the MSPs could contribute to the gamma-ray diffuse emission above a few GeV. These arguments can be

invoked to suggest that the gamma-ray emission observed by Fermi could be explained up to ~ 100 GeV by leptonic emission from MSP, and that the hadronic component would then take over. MSP would appear as the dominant sources of the gamma-ray diffuse emission at very high energies in the galactic center.

Nearby pulsars such as Geminga and Monogem may contribute to the CR density at Earth. In particular, assuming a baryon loading of 0.05 in the Geminga pulsar and the diffusion coefficient used in this study away from the inner tens of pc around Geminga, a qualitative estimate of the Geminga CR contribution at Earth of about 10^{-9} eVcm $^{-3}$ from the electron luminosity derived in Abeysekara et al. (2017). Assuming the value of the diffusion coefficient inferred in the inner tens of pc around Geminga to be valid on the Geminga-to-Earth spatial scale would drastically increase the CR contribution. However, given the electron energy losses, such a low diffusion coefficient would not enable one to measure electrons up to 20 TeV, for which local CR electron sources such as Geminga are natural sources.

4.6 Conclusion

A total population of $\eta_p N_b \sim 10^6$ millisecond pulsars (MSP) accelerating protons up to very high energies with baryon loading η_p , and located in a 10^3 pc bulge around the galactic center, appears as an acceptable candidate to explain the diffuse gamma-ray excess observed by HESS in the galactic center region. A disk population cannot reproduce the spatial characteristics of the data. The ratio between the number of pulsars in the disk and the bulge components N_d/N_b should be smaller than $\sim 10^3$, so that the bulge component remains predominant. Moreover, only a sub-population contributes to the observed emission, with typically $\eta_p N_b (L_{CR}(t_{sd}) > 10^{34} \text{ erg s}^{-1}) \sim 2 \times 10^3$ and $\eta_p N_b (L_{CR}(t_{sd}) > 10^{33} \text{ erg s}^{-1}) \sim 4 \times 10^4$. Regarding the properties of these pulsars, moderate acceleration efficiencies $\eta_{acc} \sim 0.03$ with pair multiplicities $\kappa = 10^3$, specific initial spin and dipole magnetic field distributions are required to reproduce the spectral and spatial characteristics of the data. We note that η_{acc} and κ are interlinked/correlated parameters. The magnetic field distribution has a strong impact on the gamma-ray spectrum. A standard diffusion coefficient is required to reproduce the spatial extension of the gamma-ray excess.

More precise measurements above 50 TeV using deeper observations of the galactic center region with HESS and future high-sensitivity instruments such as CTA, whether or not indicating the presence of a high energy cut-off in the VHE diffuse emission spectrum, would put strong constraints on several parameters of our model, as the acceleration efficiency η_{acc} or the magnetic field distribution –especially on its upper bound B_{max} , the value of B_{min} being already better constrained by observations. A high energy cut-off would be associated with a low η_{acc} or a low B_{max} .

Chapter 5

Tidal disruptions by massive black holes, as promising source candidates of ultra-high-energy cosmic rays and high-energy neutrinos

Accelerating cosmic rays at the highest energies is not an easy task, as seen in chapter 3 in the case of pulsars, and even for the most extremely magnetized of these objects called magnetars. Following the hint of the extragalactic origin of ultra-high-energy cosmic rays (UHECR), many extragalactic source categories have been suggested. The most promising candidates involve mostly relativistic jets launched by the accretion of matter into massive black holes, where particles get accelerated. By the same reasoning, tidal disruptions by massive black holes (hereafter referred to as TDE for Tidal Disruption Event), and especially the ones powering relativistic jets, appear as good candidate sources for the acceleration of cosmic rays. Tidal disruptions can occur when stars approach massive black holes located at the center of galaxies at distances smaller than the tidal disruption radius. If this radius is larger than the Schwarzschild radius of the black hole, tidal forces can violently disrupt the star and produce luminous and long-lasting flares. After the disruption of the stellar object, which might be a main sequence star or in some extreme cases a white dwarf, part of its material escapes and part is accreted, launching simultaneously a wind or a relativistic outflow. These transient events were predicted theoretically about 20 years before their first detections, and TDEs lasting for months (or sometimes years) have been observed in the UV, X-rays and γ rays (e.g., Komossa, 2015). The emission mostly shows a fast rising phase and a luminosity decay $L \propto t^{-5/3}$, coherent with fallback accretion (Phinney, 1989). The most luminous events show a higher variability, with sequences of flares of ~ 1000 s alternating with quiescent periods of $\sim 5 \times 10^4$ s. As they can reach luminosities of $L_{\text{max}} = 10^{48} \text{ erg s}^{-1}$, and can maintain very high bolometric luminosities ($L_{\text{bol}} \sim 10^{47} \text{ erg s}^{-1}$) lasting about 10^6 s, these powerful emissions are very likely to come from a relativistic jet launched from the central massive black hole e.g., Bloom et al., 2011; Burrows et al., 2011. To date, it is still not clear if non-jetted and jetted TDEs constitute two distinct populations.

The transient nature of jetted TDEs suggest potentially a large injection of hadronic material inside the relativistic jet and an enhanced magnetic field boosting particle acceleration. Therefore, they could be an ideal site for the production of UHECR and for the production of high-energy neutrinos, produced later by the interaction of the accelerated hadrons with the ambient radiative and/or hadronic backgrounds. Moreover, the material from the disrupted star could contain some elements heavier than proton and helium, required to match the elementary composition detected by the Pierre Auger observatory. However, further modeling would be required to confirm these statements. Although only a handful of jetted TDEs have been detected so far, these objects have already attracted great interest in the high-energy astroparticle community.

High-energy neutrino production in TDE jets was considered before the discovery of IceCube neutrinos (e.g., Murase, 2008a; Murase and Takami, 2009; Wang et al., 2011), and contributions to IceCube neutrinos have been studied (Senno et al., 2016b; Dai and Fang, 2017; Lunardini and Winter, 2016; Wang and Liu, 2016). The UHECR production in TDE jets was originally suggested by Farrar and Gruzinov (2009), and the external shock scenario was also considered in detail (Farrar and Piran, 2014). However, it should be kept in mind that the rate of TDEs is too tight to fit the observed UHECR fluxes, as can be deduced from the constraints derived by Murase and Takami (2009), who obtained $\dot{n}_{\text{tde}} > 1 \text{ Gpc}^{-3} \text{ yr}^{-1}$. Hence a pure proton case is disfavored and the nucleus scenario is required. Recent studies attempted to inject a mixed composition and fit the UHECR flux and composition simultaneously in both the internal and external shock scenarios (Alves Batista and Silk, 2017; Zhang et al., 2017).

So far, the existing studies have not attempted to model the production of UHECRs in the inner part of the TDE jet (with acceleration occurring at internal shocks for instance). Modeling this effect requires taking into account the interaction of accelerated nuclei inside the jet in order to calculate consistently the resulting chemical composition. In this work, we focus on the interaction of accelerated nuclei inside the TDE jet, and the signatures they can produce in UHECR and high-energy neutrinos. For this purpose we use the interaction code described in section 1.2.3. In order to calculate the diffuse fluxes of UHECRs and neutrinos, we also introduce a new model for the event rate evolution and luminosity function of TDEs powering jets. The semi-analytic galaxy formation model of Barausse (2012) is used to model the cosmological evolution of massive black holes, which can be related to the jetted TDE comoving event rate density, and thus to the diffuse UHECR and neutrino fluxes. The properties of TDEs powering jets are subject to large uncertainties. Therefore, we scan the parameter space allowed by TDE observations to model the radiation region (Sect. 5.1.1) and the typical photon field inside a TDE jet (Sec. 5.1.2). Inside this region, we consider different interaction processes, detailed in Sect. 5.1.3. We then calculate mean free path (MFP) tables for the interaction of protons and heavier nuclei with the photon field of the jet. We use these tables in our code to predict UHECR and neutrino signatures (Sect. 5.2) for single sources. In order to estimate the diffuse particle fluxes from a population of jetted TDEs, we derive the luminosity function and occurrence rate evolution of these events (Sect. 5.3). We find in Sect. 5.4 that we can fit the latest UHECR spectrum and composition results of the Auger experiment for a range of reasonable parameters. The diffuse neutrino flux associated with this scenario is found to be detectable with IceCube in the next decade. Transient neutrino signals from single sources would be difficult to detect with IceCube or the upcoming GRAND experiment, except for sources located within $\sim 50 \text{ Mpc}$, associated with a very low event rate.

This chapter is fully based on Guépin et al. (2018b), but a few modifications have been made. A more accurate normalization procedure of the simulation outputs have slightly modified our neutrino spectra predictions. A bug in the large-scale propagation has been corrected, leading to an increase of the diffuse proton flux below 10^{19} eV and a slight decrease of the diffuse neutrino flux, see figures 5.7 and 5.9. The corresponding sections have been revised, and an erratum is in preparation. These changes do not impact our conclusions.

5.1 Interaction of UHE nuclei inside TDE jets

In the following, all primed quantities are in the comoving frame of the emitting region. Other quantities are in the observer frame. Quantities are labeled $Q_x \equiv Q/10^x$ in cgs units unless specified otherwise, and except for particle energies, which are in $E_x \equiv E/10^x \text{ eV}$.

The tidal disruption of a stellar object can occur if it gets close enough to a black hole, and will

produce observable flares if it happens outside the black hole event horizon. A part of the stellar material forms a thick accretion disk, and a fraction of this material accretes onto the black hole, most likely in a super-Eddington regime. For most TDEs, the observed radiation comes from the dissipation inside the accretion disk, characterized by a thermal spectrum peaking in extreme ultraviolet or soft X-rays; for a rotating black hole launching a relativistic jet, a non-thermal hard X-ray radiation can be detected, presumably produced through synchro-Compton radiation (e.g., Burrows et al., 2011). The jet radiation should dominate the observed spectrum for black holes with low mass and high spin, jets oriented toward the observer, and large radiative efficiency of the jet.

In the jet comoving frame, using a condition of causality, $R' \sim \Gamma c t_{\text{var}}$ can be considered as the size of the emitting region. In the internal shock model, the distance of the emission region from the black hole is estimated to be $r \sim \Gamma^2 c t_{\text{var}} = 3 \times 10^{14} \text{ cm } \Gamma_1^2 t_{\text{var},2}$, where $t_{\text{var}} = 10^2 t_{\text{var},2}$ s and $\Gamma = 10\Gamma_1$ are the typical variability timescale and bulk Lorentz factor for jetted TDEs, respectively. This radius coincides with the radius estimated from high-latitude emission with a duration of $\sim t_{\text{var}}$ (e.g., Piran, 2004). Here we note that from these estimates $r \sim \Gamma R'$, but more generally the relationship between R and R' can be modified, for example by subsequent internal shocks caused by merged shells and the existence of multiple emission regions such as subjets (e.g., Murase and Nagataki, 2006a; Bustamante et al., 2017). However, as long as we consider internal shocks in the jet that expand conically, it is reasonable to consider the expression of r obtained for the one-zone calculation, as has been done in the literature of GRBs.

First, we assume that cosmic rays are injected at the center of a non-evolving radiation region in the comoving frame. The evolution of the region would mainly result in the dilution over time of the radiation and magnetic energy densities, together with adiabatic losses, associated with observable spectral changes. We account for these effects, to a first approximation, by considering two dominant stages for our TDEs: the early stage, when the source is in a high state, at its maximum brightness; and a medium state, reached later, for which the source is typically 1 – 1.5 orders of magnitude less luminous, but for a longer integrated time. We argue in the following that these two states have different impacts on the production of UHECRs and their associated high-energy neutrinos.

5.1.1 UHECR injection and energetics

Cosmic ray nuclei from the stellar material can be accelerated to ultra-high energies inside the TDE jet via one of the various mechanisms advocated for GRBs or AGN jets. We assume that acceleration leads to a rigidity-dependent spectrum $dN_{\text{CR}}/dE' = \mathcal{A} \sum_Z f_Z E'^{-\alpha} \exp(-E'/E'_{Z,\text{max}})$ with an exponential cutoff at $E'_{Z,\text{max}}$ for nuclei of charge Z . Here \mathcal{A} is a normalization constant and f_Z is the fraction of elements with charge number Z , such that $\sum_Z f_Z = 1$. The spectral index α can vary (typically between $\alpha \sim 1$ and $\alpha \gtrsim 2$) depending on the acceleration mechanism (e.g., magnetic reconnection or diffusive shock acceleration). The cosmic-ray composition depends on the composition of the disrupted object, but it also strongly depends on what happens to the elements before they get injected and accelerated in the jet. Heavy nuclei could indeed undergo fragmentation during the disruption of the stellar object, or a large fraction of light nuclei could escape as part of the expelled stellar envelope. In this work, the elements injected in the radiation region are protons (p), helium (He), carbon and oxygen (CO), silicium (Si), and iron (Fe).

From the energetics point of view, the luminosity injected into cosmic rays is considered related to the bolometric luminosity in photons, such that $L_{\text{CR}} = \xi_{\text{CR}} L_{\text{bol}}$, where we define the baryon loading fraction ξ_{CR} as the fraction of the bolometric luminosity that is injected into cosmic rays of energy $E \geq E_{\text{min}} \equiv 10^{16} \text{ eV}$. The maximum injection energy $E'_{Z,\text{max}}$ is determined by the

competition between the acceleration timescale for a nucleus of charge Z , $t'_{\text{acc}} = \eta_{\text{acc}}^{-1} E' / c Z e B'$, and the energy loss timescales $t'_{\text{loss}} = \min(t'_{\text{dyn}}, t'_{\text{syn}}, t'_{\text{IC}}, t'_{\text{BH}}, t'_{p\gamma}, \dots)$, where $t'_{\text{dyn}} = R' / c$ is the dynamical timescale. We recall that the factor $\eta_{\text{acc}} \leq 1$ describes the efficiency of the acceleration process; for a maximally efficient acceleration, $\eta_{\text{acc}} = 1$. In this study we neglect the re-acceleration of secondary particles, and leave it for future work. Estimates of the maximum energy of accelerated particles are given in section 5.1.3.

5.1.2 Modeling the TDE spectral energy distribution

As suggested in Senno et al. (2016b), we model the spectral energy distribution (SED) inside the TDE jet as a log-parabola with three free parameters: the peak luminosity L_{pk} , peak energy ϵ_{pk} , and width \hat{a} . The photon energy density then reads

$$\epsilon'^2 n'_{\epsilon'} \simeq \frac{L_{\text{pk}}}{4\pi\Gamma^4 R'^2 c} (\epsilon' / \epsilon'_{\text{pk}})^{-\hat{a} \log(\epsilon' / \epsilon'_{\text{pk}})}. \quad (5.1)$$

The peak luminosity and peak energy set the maximum of the SED. The data can help to constrain the width of the log-parabola and a potential high-energy cutoff. However, there are large uncertainties on the observed photon density, due to galaxy absorption, and even more on the photon density inside the jet (see Burrows et al., 2011; Bloom et al., 2011 for the spectrum of Swift J1644+57). From our SED model, the bolometric luminosity can then be defined as the luminosity integrated over the entire spectrum: $L_{\text{bol}} = \int d\epsilon' L_{\text{pk}} / \epsilon' (\epsilon' / \epsilon'_{\text{pk}})^{-\hat{a} \log(\epsilon' / \epsilon'_{\text{pk}})}$. As we consider a constant photon field during the two states, this bolometric luminosity is larger than the peak luminosity. Moreover, as we model the radiation field inside the jet, we should have $L_{\text{jet,obs}} \sim L_{\text{bol}}$. We note that in most cases, the main contribution to the observed luminosity is the jet luminosity, but for high black hole masses ($M_{\text{bh}} > 5 \times 10^7 M_{\odot}$), the thermal luminosity is of the same order of magnitude as the jet luminosity (Krolik and Piran, 2012).

In this work, we examine several cases summarized in Table 5.1 and illustrated in figure 5.1. We choose to only vary the width \hat{a} and the peak luminosity L_{pk} of the log-parabola, and to consider a typical peak energy $\epsilon_{\text{pk}} = 70 \text{ keV}$, which is compatible with Swift J1644+57 observations (e.g., Burrows et al., 2011). Each case corresponds to a different magnetic field, and therefore corresponds to a maximum proton energy $E'_{p,\text{max}}$ (Eq. 5.4). The magnetic field is inferred assuming equipartition between the radiative and magnetic energy densities: $\xi_B \int d\epsilon' \epsilon' n'_{\epsilon'} = B'^2 / 8\pi$ with $\xi_B = 1$. Rough equipartition is a standard hypothesis for jets that can be argued from measurements of the energy repartition in extragalactic objects, for example blazar jets (Celotti and Ghisellini, 2008). It also naturally arises if relativistic reconnection is at play in the outflow, dissipating electromagnetic energy into kinetic energy (Sironi et al., 2015).

The TDE photon spectra evolve in time. As mentioned earlier, although we do not account for proper time evolutions of the SED in this paper, we consider two states of the SED, inferred from the observations of Swift J1644+57, and which are important for our framework: an early state, corresponding to a high state that can typically last $t_{\text{dur}} \sim 10^5 \text{ s}$ with a bright luminosity, a high jet efficiency, and a narrow jet opening angle; and a medium state, 1 – 1.5 orders of magnitude less bright, but lasting $t_{\text{dur}} \sim 10^6 \text{ s}$, with a lower jet efficiency and a similar jet opening angle. For both states, we set a width $\hat{a} = 0.07$. These parameters are overall compatible with Swift J1644+57 SED models corrected for galactic absorption (e.g., Burrows et al., 2011).

5.1.3 Interaction processes

All relevant interaction processes for nucleons and heavier nuclei are taken into account in our calculations, see sections 1.2.2 and 1.2.3 for more detail on the interactions at play and the

$L_{\text{bol}}[L_{\text{pk}}] \text{ (erg s}^{-1}\text{)}$	\hat{a}	$B' \text{ (G)}$	$E'_{p,\text{max}} \text{ (eV)}$
$3.5 \times 10^{48} [10^{48}]$	0.25	5.1×10^3	1.8×10^{18}
$6.8 \times 10^{48} [10^{48}]$	0.07	7.0×10^3	2.4×10^{18}
$1.0 \times 10^{49} [10^{48}]$	0.03	8.7×10^3	2.2×10^{18}
$6.8 \times 10^{46} [10^{46}]$	0.07	7.0×10^2	6.3×10^{18}
$6.8 \times 10^{47} [10^{47}]$	0.07	2.2×10^3	4.3×10^{18}
$6.8 \times 10^{48} [10^{48}]$	0.07	7.0×10^3	2.4×10^{18}

Table 5.1: Properties of the different TDE photon fields considered in this work for a cosmic-ray acceleration efficiency $\eta_{\text{acc}} = 1$. All the photon fields are modeled by a log-parabola (Eq. 5.1), with bolometric luminosity L_{bol} , peak luminosity L_{pk} , peak energy ϵ_{pk} , and width \hat{a} .

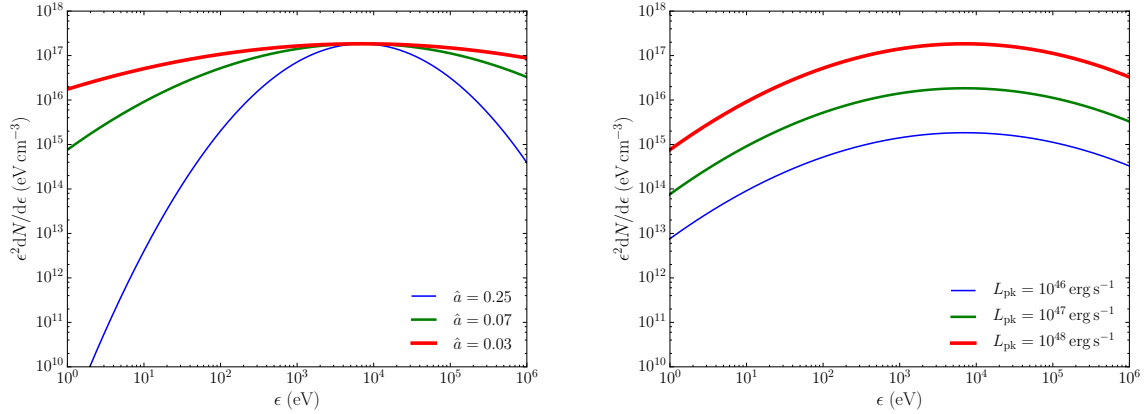


Figure 5.1: Comparison between photon densities for a log-parabola model with fixed peak luminosity $L_{\text{pk}} = 10^{48} \text{ erg s}^{-1}$ (left) and with fixed width $\hat{a} = 0.07$ (right).

computation method. We note that photonuclear cross sections and EBL models have a strong influence on the spectrum and composition of cosmic rays for extragalactic propagation, as discussed in Alves Batista et al. (2015). For different EBL models, the discrepancy between cosmic-ray spectra can reach $\sim 40\%$. The impact of photonuclear models is also strong, whereas more difficult to quantify, especially regarding the channels involving α -particles.

We show in figure 5.2 the MFPs or energy loss lengths derived for different photon fields, for carbon and iron nuclei. In the top panel, we compare the mean free paths obtained for log-parabola models of the photon densities, for $\hat{a} = 0.25$ and $\hat{a} = 0.03$, with a fixed $L_{\text{pk}} = 10^{48} \text{ erg s}^{-1}$. The width of the log-parabola has a strong influence on the MFPs as it substantially changes the radiation energy density. We see that overall, photonuclear interactions dominate over a wide range of particle Lorentz factors γ , up to ultra-high energies where synchrotron losses start taking over. Changing the width of the log-parabola modifies the MFPs by several orders of magnitude, with shorter paths for narrower SED. In the bottom panel, we compare the mean free paths obtained for $L_{\text{pk}} = 10^{46} \text{ erg s}^{-1}$ and $L_{\text{pk}} = 10^{48} \text{ erg s}^{-1}$, with a given width $\hat{a} = 0.07$. The influence of peak luminosity on the MFPs is more moderate; as expected, the MFPs are a power of the peak luminosity, and a higher L_{pk} leads to shorter MFP.

Several interesting estimates can be derived by comparing the energy-loss and energy-gain timescales of nuclei. For the following estimates, we consider a log-parabola SED with peak luminosity $L_{\text{pk}} = 10^{46} \text{ erg s}^{-1}$ and a width $\hat{a} = 0.07$, which gives the mean magnetic field

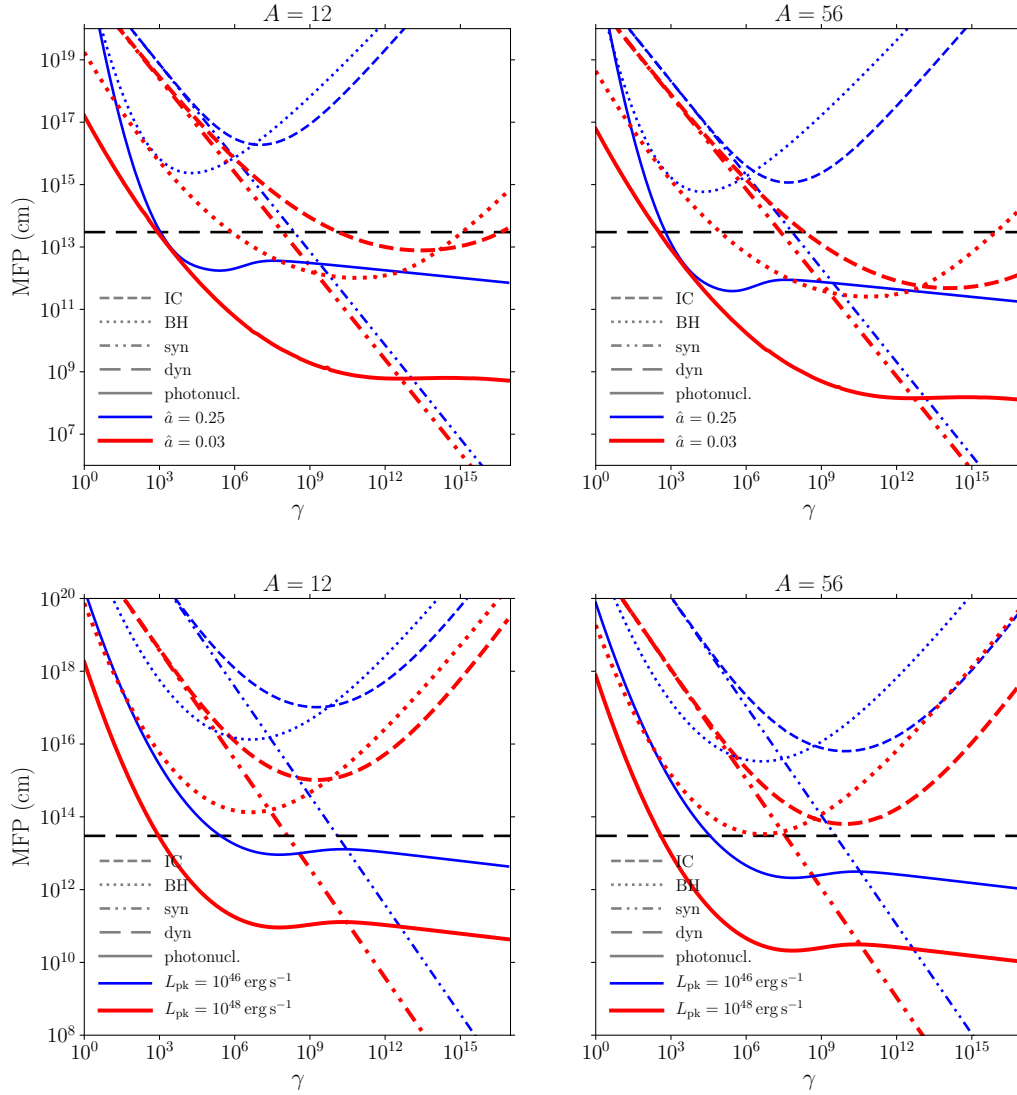


Figure 5.2: Influence of the log-parabola width \hat{a} for $L_{\text{pk}} = 10^{48} \text{ erg s}^{-1}$ (top) and peak luminosity L_{pk} for $\hat{a} = 0.07$ (bottom), on the mean free paths and energy loss lengths in the comoving frame for carbon (left) and iron (right) nuclei of Lorentz factor γ . Top panel: we compare $\hat{a} = 0.25$ (blue) and $\hat{a} = 0.03$ (red). Bottom panel: we compare $L_{\text{pk}} = 10^{46} \text{ erg s}^{-1}$ (blue) and $L_{\text{pk}} = 10^{48} \text{ erg s}^{-1}$ (red). The different line styles correspond to different processes: photonuclear (solid), inverse Compton (dashed), Bethe–Heitler (dotted), and synchrotron (double dot-dashed). The black long-dashed line corresponds to the typical comoving size of the region. Wider SED lead to larger MFPs.

$B' = (8\pi \int d\epsilon' \epsilon' n'_{\epsilon'})^{0.5} \simeq 10^{2.85} \text{ G}$. These can be considered as typical parameters of jetted TDEs (e.g., the characteristics of Swift J1644+57). An upper bound of the maximum energy of accelerated particles is given by the competition between the acceleration timescale (t'_{acc}) and the dynamical timescale (t'_{dyn}):

$$\begin{aligned} E'_{Z,\text{max,dyn}} &\sim c Z e B' (1+z)^{-1} \Gamma t_{\text{var}} \eta_{\text{acc}}, \\ &\simeq 6.3 \times 10^{17} \text{ eV } Z_1 B'_{2.8} \Gamma_{10} t_{\text{var},2} \eta_{\text{acc},-1}, \\ &\simeq 1.6 \times 10^{19} \text{ eV } Z_{26} B'_{2.8} \Gamma_{10} t_{\text{var},2} \eta_{\text{acc},-1}. \end{aligned} \quad (5.2)$$

Moreover, the competition between acceleration (t'_{acc}) and synchrotron (t'_{syn}) timescales gives

$$\begin{aligned} E'_{Z,\text{max,syn}} &\sim \left[\frac{6\pi(m_{\text{u}}c^2)^2 e}{(m_e/m_{\text{u}})^2 \sigma_{\text{T}}} \right]^{\frac{1}{2}} A^2 Z^{-3/2} B'^{-1/2} \eta_{\text{acc}}^{1/2}, \\ &\simeq 2.4 \times 10^{18} \text{ eV } A_1^2 Z_1^{-3/2} B'_{2.8}{}^{-1/2} \eta_{\text{acc},-1}^{1/2}, \\ &\simeq 5.7 \times 10^{19} \text{ eV } A_{56}^2 Z_{26}^{-3/2} B'_{2.8}{}^{-1/2} \eta_{\text{acc},-1}^{1/2}. \end{aligned} \quad (5.3)$$

The upper bound given by the competition between the acceleration timescale (t'_{acc}) and the photohadronic timescale ($t'_{\text{p}\gamma}$) is computed numerically. For the parameters considered above, we obtain for protons $E'_{p,\text{up,p}\gamma} \simeq 2.5 \times 10^{18} \text{ eV}$. The comparison between the different energy loss timescales allows us to determine the limiting energy loss process: for the previous example the dynamical timescale is the limiting timescale.

The competition between the energy loss processes in the radiation region influences the outgoing cosmic-ray spectrum, and in particular the high-energy cutoffs. By considering the competition between synchrotron losses (t'_{syn}) and escape (t'_{esc}) for protons, we can derive the corresponding high-energy cutoff

$$\begin{aligned} E'_{p,\text{up}} &\sim \frac{6\pi(m_p c^2)^2}{(m_e/m_p)^2 \sigma_{\text{T}} c B'^2 \Gamma t_{\text{var}}}, \\ &\simeq 9.0 \times 10^{18} \text{ eV } B'_{2.8}{}^{-2} \Gamma_1^{-1} t_{\text{var},2}^{-1}. \end{aligned} \quad (5.4)$$

The competition between synchrotron losses (t'_{syn}) and pion production ($t'_{p\gamma}$) for a transient event characterized by a hard spectrum gives

$$\begin{aligned} E'_{p,\text{up}} &\simeq \frac{3(m_p c^2)^2 \langle \sigma_{p\gamma} \kappa_{p\gamma} \rangle L_{\text{pk}}}{2(m_e/m_p)^2 \sigma_{\text{T}} c^3 B'^2 \Gamma^5 t_{\text{var}}^2 \epsilon_{\text{pk}}}, \\ &\simeq 5.0 \times 10^{21} \text{ eV } B'_{2.8}{}^{-2} \Gamma_1^{-5} L_{\text{pk},46} t_{\text{var},2}^{-2}, \end{aligned} \quad (5.5)$$

where we consider $\epsilon_{\text{pk}} = 70 \text{ keV}$. For nuclei, the high-energy cutoffs depend on the mass and atomic numbers. As $\gamma_N = E'_N / A m_{\text{u}} c^2$, for the competition between synchrotron losses (t'_{syn}) and escape (t'_{esc}) we obtain $E'_{N,\text{max}} \simeq 1.4 \times 10^{20} \text{ eV } B'_{2.8}{}^{-2} \Gamma_1^{-1} t_{\text{var},2}^{-1} A_{56}^4 Z_{26}^{-4}$ where $A_{56} = A/56$ and $Z_{26} = Z/26$ for iron nuclei. These estimates can be seen in figure 5.2.

5.2 UHECRs and neutrinos from single TDEs

We calculate the cosmic-ray and neutrino spectra after the propagation of protons or nuclei through the photon field of a jetted TDE. First, we consider one single source. The production of neutrinos should be dominated by the high state when the photon field is brightest (and the opacities greatest). During the high state, UHECR should experience strong photodisintegration and thus their production should be dominated by the medium state, characterized by a lower

luminosity but a longer duration than the high state. We show in figure 5.3 an example of outgoing cosmic-ray spectrum for a pure iron injection from a single TDE in its high state SED characterized by $L_{\text{pk}} = 10^{47.5} \text{ erg s}^{-1}$ and $\hat{a} = 0.07$, and in its medium state SED characterized by $L_{\text{pk}} = 10^{46} \text{ erg s}^{-1}$ and $\hat{a} = 0.07$. As is shown below, these two states are associated in our model with a black hole of mass $M_{\text{bh}} = 7 \times 10^6 M_{\odot}$. We consider that the injection of iron nuclei is characterized by power-law spectrum of spectral index $\alpha = 1.8$, minimum and maximum energies $E'_{\text{N,min}} = ZE'_{\text{p,min}}$ and $E'_{\text{N,max}} = ZE'_{\text{p,max}}$. As explained previously, $E'_{\text{p,max}}$ is determined by the competition between acceleration timescale and energy-loss timescales. The minimum energy is less constrained, and we consider the fiducial value $E'_{\text{p,min}} = 10^{15} \text{ eV}$. Thus the acceleration process produces a power-law of cosmic rays extending over about three orders of magnitude. We also consider an acceleration efficiency $\eta_{\text{acc}} = 0.2$. Here we do not account for the extragalactic propagation of cosmic rays, and the spectrum is normalized by considering the luminosity distance of Swift J1644+57: $d_{L,1} \simeq 1.88 \text{ Gpc}$ ($z \simeq 0.354$). Two associated neutrino spectra are shown in figure 5.4. One spectrum is normalized by considering the luminosity distance of Swift J1644+57, $d_{L,1} \simeq 1.88 \text{ Gpc}$, and the other by considering a luminosity distance $d_{L,2} = 50 \text{ Mpc}$. The IceCube sensitivity is characterized by a minimum fluence $\mathcal{S}_{\text{IC}} = 5 \times 10^{-4} \text{ TeV cm}^{-2}$ over the energy range $10 \text{ TeV} - 10 \text{ PeV}$, which corresponds to a detection limit $s_{\text{IC}} \sim 10^{-11} \text{ TeV cm}^{-2} \text{ s}^{-1}$ for a one-year data collection (Aartsen et al., 2015). We give the IceCube sensitivity from the effective area presented in Aartsen et al. (2014b) for the optimal declination range $0^\circ < \delta < 30^\circ$ (thin lines), and for the declination range $30^\circ < \delta < 60^\circ$ (thick lines) associated with the Swift event J1644+57. We also give the future GRAND sensitivity (GRAND Collaboration et al., 2018), averaged over one day in order to account for the limited coverage in the direction of the source.

The peak luminosity and width of the photon SED have a strong effect on the cosmic-ray and neutrino spectra as they influence strongly photohadronic and synchrotron losses, which are the two dominant energy loss processes in our framework. For cosmic rays, energy losses due to photohadronic interactions are mainly dominant at low energies, while synchrotron losses dominate at high energies. If the radiation energy density is sufficiently low, the escape time of cosmic rays can be the limiting time at low energies. Regarding the cosmic-ray spectrum, we see in figure 5.3 that for a medium state SED with $L_{\text{pk}} = 10^{46} \text{ erg s}^{-1}$, iron strongly interacts and produces many secondary particles with a large number of nucleons below $E_{\text{cut}}/56 \sim 10^{19} \text{ eV}$. Despite these high interaction rates, nuclei can still survive and escape from the region with energies up to 10^{20} eV . For a high state SED with $L_{\text{pk}} = 10^{47.5} \text{ erg s}^{-1}$, the iron strongly interacts, as do the secondary cosmic rays produced through iron interactions. No nuclei can survive and escape the region; only protons escape, with a maximum energy around $\max(E_p) \sim 10^{18} \text{ eV}$. The high-energy cutoff for each element with $Z > 1$ results from the competition between the energy loss processes or from the maximum injection energy. For instance in figure 5.3, the competition between acceleration and dynamical timescales sets the maximum energy for $L_{\text{pk}} = 10^{46} \text{ erg s}^{-1}$, whereas it is the competition between photonuclear and dynamical timescales for $L_{\text{pk}} = 10^{47.5} \text{ erg s}^{-1}$.

figure 5.4 shows that the high-energy neutrino spectrum peaks around $E_\nu \sim 10^{16} \text{ eV}$. A nearby medium state TDE at distance 50 Mpc with peak luminosity $L_{\text{pk}} = 10^{46} \text{ erg s}^{-1}$ would not be detectable, even with future neutrino detectors such as GRAND (Fang et al., 2017). On the other hand, at early times and in their high states, TDEs would lead to massive production of high-energy neutrinos, and should be marginally detectable with IceCube for a nearby distance of 50 Mpc . It would not be detectable with GRAND at the high-energy end, because the source would not be observed during its entire duration, which reduces the GRAND sensitivity. We note that the rate of TDEs at distances smaller than 50 Mpc is $4 \times 10^{-6} \text{ yr}^{-1}$ for a comoving event rate density $\sim 0.03 \text{ Gpc}^{-3} \text{ yr}^{-1}$, which is extremely low. TDEs in their high states at distances $> 50 \text{ Mpc}$ would not be detectable with IceCube or GRAND because of the flux decrease and

the low high-energy cutoff of the neutrino spectrum. We note that our chosen parameter set is consistent with the non-detection of neutrinos from Swift J1644+57 (as was already highlighted in chapter 2) and allows for baryonic loading at the source ξ_{CR} up to \sim a few 100 to remain consistent with this non-detection.

The presence of a plateau in the neutrino spectrum is due to the contributions of muon and electron neutrinos. The high-energy cutoff is due to pions and muons experiencing energy losses (mainly synchrotron losses) before they decay. We account for synchrotron and inverse Compton losses, but do not account for the kaon contribution. We note that electron neutrinos have a lower energy cutoff than muon neutrinos. Electron neutrinos are produced through muon decay, and muons are produced through pion decay; therefore, the energy of electron neutrinos is influenced by pion losses and muon losses before they decay. Muon neutrinos, in turn, are produced through pion decay or muon decay. Hence the energy of those produced through pion decay is only influenced by pion energy losses before the decay, which explains the higher energy cutoff for muon neutrinos.

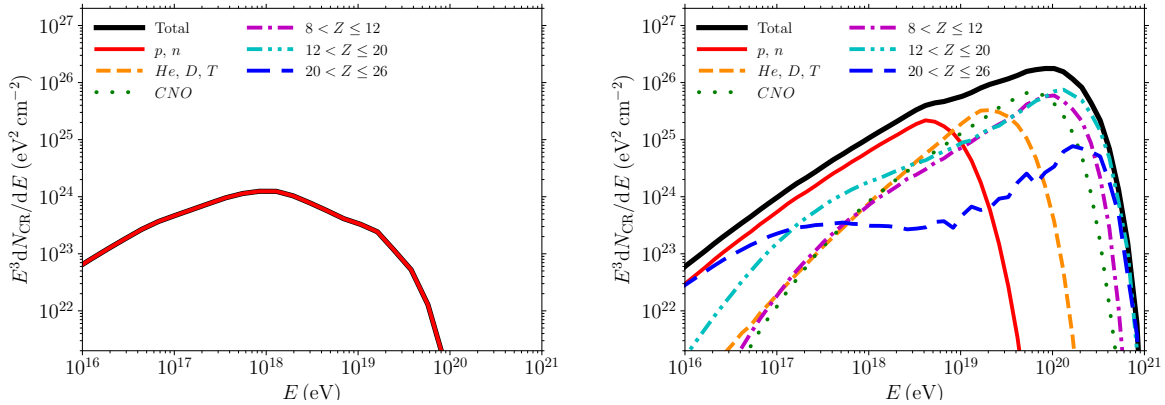


Figure 5.3: Cosmic-ray spectra for one source with pure iron injection with spectral index $\alpha = 1.8$, photon field with $\hat{a} = 0.07$, and acceleration efficiency $\eta_{\text{acc}} = 0.2$. We show the total spectrum (black) and the composition (other colors), as indicated in the legend, for TDE around a black hole of mass $M_{\text{bh}} = 7 \times 10^6 M_{\odot}$, with a corresponding SED in its high state with $L_{\text{pk}} = 10^{47.5} \text{ erg s}^{-1}$ and $t_{\text{dur}} = 10^5 \text{ s}$ (left) and in its medium state with $L_{\text{pk}} = 10^{46} \text{ erg s}^{-1}$ and $t_{\text{dur}} = 10^6 \text{ s}$ (right) for a source distance $d_{L,1} = 1.88 \text{ Gpc}$. We assume here $\xi_{\text{CR}} = 1$.

5.3 Modeling the population of TDEs contributing to UHECR and neutrino fluxes

A derivation of the comoving density rate of TDEs can be found in Sun et al. (2015). These authors define the comoving density rate as $\dot{n}(z, L) = \dot{n}_0 \Lambda(L) f(z)$, where \dot{n}_0 is the total local event rate density, $f(z)$ the TDE redshift distribution, and $\Lambda(L)$ the TDE luminosity function. The luminosity function is given by a power-law, $\Lambda_{\text{TDE}}(L_{\gamma}) \propto (L_{\gamma, \text{pk}}/L_{\text{m, pk}})^{-\alpha_L}$, with $L_{\text{m, pk}} = 10^{48} \text{ erg s}^{-1}$, $\int_{L_{\text{min}}}^{L_{\text{max}}} dL_{\gamma} \Lambda_{\text{TDE}}(L_{\gamma}) = 1$, $L_{\text{min}} = 10^{45} \text{ erg s}^{-1}$, $L_{\text{max}} = 10^{49} \text{ erg s}^{-1}$ and $\alpha_L = 2$. However, the Sun et al. (2015) model is not well adapted to our framework as their comoving rate density accounts for the entire TDE population and not the subpopulation powering jets. Moreover, the redshift evolution of the luminosity function is neglected, due to the small size of their observational sample. Thus, in the following we present a prediction for the comoving event rate density of TDEs powering jets by combining the TDE rate per galaxy \dot{N}_{TDE} and the black hole comoving number density per luminosity $dn_{\text{bh}}(z, L)/dL$ (i.e., the number of black holes per comoving volume and per bin of jet luminosity).

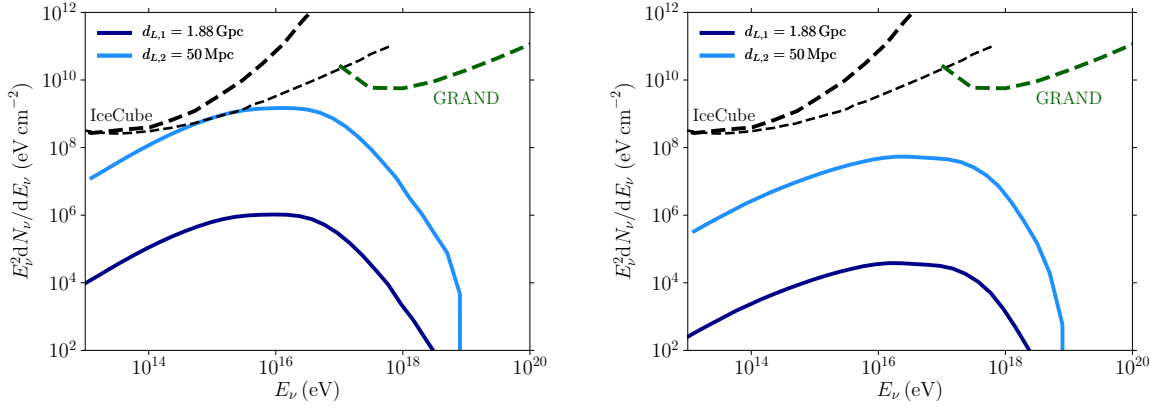


Figure 5.4: Neutrino spectra for three flavors for one source with same characteristics as in figure 5.3. We show the total spectra (in eV cm^{-2}) for a high state SED with $L_{\text{pk}} = 10^{47.5} \text{ erg s}^{-1}$ (left) and a medium state SED with $L_{\text{pk}} = 10^{46} \text{ erg s}^{-1}$ (right). We consider two different distances $d_{L,1} = 1.88 \text{ Gpc}$ (dark blue) and $d_{L,2} = 50 \text{ Mpc}$ (light blue). The IceCube and projected GRAND sensitivities (GRAND Collaboration et al., 2018) are also shown (dashed black and green lines). For the IceCube sensitivities, we show two cases depending on the declination: $0^\circ < \delta < 30^\circ$ (most favorable case, thin line) and $30^\circ < \delta < 60^\circ$ (Swift J1644+57 case, thick line) (Aartsen et al., 2014a).

5.3.1 TDE rate per galaxy

The TDE rate per galaxy \dot{N}_{TDE} depends on the galaxies considered. Following Wang and Merritt (2004), we consider a lower bound in the case of core galaxies and an upper bound in the case of power-law galaxies. Indeed, for core galaxies, $\dot{N}_{\text{TDE}} \approx 10^{-5} \text{ yr}^{-1}$. For power-law galaxies, combining $\dot{N}_{\text{TDE}} \approx 7.1 \times 10^{-4} \text{ yr}^{-1} (\sigma/70 \text{ km s}^{-1})^{7/2} M_{\text{bh},6}^{-1}$, where $M_{\text{bh},6} = M_{\text{bh}}/10^6 M_\odot$ and σ is the stellar velocity dispersion of the bulge, and the relation between the black hole mass and the bulge velocity dispersion from Kormendy and Ho (2013): $\log_{10} M_{\text{bh},9} = -0.51 + 4.4 \log_{10} (\sigma/200 \text{ km s}^{-1})$, we obtain a TDE rate per galaxy which depends on the black hole mass $\dot{N}_{\text{TDE}} \approx 3 \times 10^{-4} \text{ yr}^{-1} M_{\text{bh},6}^{-0.2}$.

5.3.2 Identifying the black hole masses leading to observable TDEs

First, we identify the population of black holes that can lead to observable TDEs. TDEs can occur for stellar objects of mass M_\star at distances $d_\star \leq r_t = R_\star (M_{\text{bh}}/M_\star)^{1/3}$ (Hills, 1975). Following Krolik and Piran (2012), $r_t \simeq 10 R_s M_{\star,\odot}^{2/3-\xi} M_{\text{bh},6}^{-2/3} [(k_\star/f_\star)/0.02]^{1/6}$ is the tidal disruption radius, where $R_s = 2GM_{\text{bh}}/c^2$ is the Schwarzschild radius, $M_{\star,\odot}$ is the mass of the star in solar units, $M_{\text{bh},6} = M_{\text{bh}}/10^6 M_\odot$, k_\star is related to the star's radial density profile, and f_\star is its binding energy in units of GM_\star^2/R_\star . This radius is obtained for a main sequence star with a typical mass-radius relation $R_\star \approx R_\odot M_{\star,\odot}^{1-\xi}$ with $\xi \simeq 0.2$ for $0.1 M_\odot < M_\star \leq M_\odot$ or $\xi \simeq 0.4$ for $M_\odot < M_\star < 10 M_\odot$ (Kippenhahn and Weigert, 1994). Moreover, we consider here and in what follows fully radiative stars, thus $k_\star/f_\star = 0.02$ (Phinney, 1989). For white dwarfs, typically $R_\star \sim M_\star^{-1/3}$ with $0.5 M_\odot < M_\star \leq 0.7 M_\odot$. Their tidal disruption radii are smaller due to the smaller dimensions of these objects; an approximate formula gives $r_t \simeq 7.4 \times 10^9 (M_{\text{bh},3.3}/\rho_{\star,7})^{1/3}$ (Luminet and Pichon, 1989), where ρ_\star is the white dwarf core density.

With this tidal disruption radius, we can estimate the maximum black hole mass enabling the production of flares. The first-order requirement for flares to be produced reads $r_t \gtrsim R_s$. For a Schwarzschild black hole, this leads to $M_{\text{bh}} \lesssim 4 \times 10^7 M_\odot M_{\star,\odot}^{1-3\xi/2} [(k_\star/f_\star)/0.02]^{1/4}$, which ranges from $M_{\text{bh}} \lesssim 10^7 M_\odot$ to $M_{\text{bh}} \lesssim 10^8 M_\odot$ for $0.1 M_\odot < M_\star \leq 10 M_\odot$. However, jetted TDEs are

likely to be powered by black holes with moderate to high spin; a general-relativistic treatment accounting for the black hole spin increases the maximum mass of black holes that are able to disrupt a solar-like star: $M_{\text{bh}} \sim 7 \times 10^8 M_{\odot}$ (Kesden, 2012).

5.3.3 Relation between black hole mass and jet luminosity

The black hole mass function $dn_{\text{bh}}(z, M_{\text{bh}})/dM_{\text{bh}}$ (i.e., the number of black holes per comoving volume and per mass bin) is obtained with the semi-analytic galaxy formation model reviewed in Sect. 5.3.4, and we derive $dn_{\text{bh}}(z, L)/dL$ by relating the black hole mass and the jet luminosity. Following Krolik and Piran (2012), we consider a TDE which forms a thick accretion disk, powering a jet through the Blandford–Znajek mechanism. We estimate the maximum accretion rate by considering that about 1/3 of the stellar mass is accreted after one orbital period P_{orb} (Lodato et al., 2009). From Krolik and Piran (2012),

$$P_{\text{orb}}(a_{\text{min}}) \approx 5 \times 10^5 \text{ s } M_{\star, \odot}^{(1-3\xi)/2} M_{\text{bh}, 6}^{1/2} \left(\frac{k_{\star}/f_{\star}}{0.02} \right)^{1/2} \beta^3, \quad (5.6)$$

where a_{min} is the minimum semi-major axis. The parameter ξ comes from the main sequence mass–radius relation $R_{\star} \approx R_{\odot} M_{\star, \odot}^{(1-\xi)}$ and $\beta \lesssim 1$ is the penetration factor. It leads to the following accretion rate:

$$\dot{M} \approx 20 M_{\odot} \text{ yr}^{-1} M_{\star, \odot}^{(1+3\xi)/2} M_{\text{bh}, 6}^{-1/2} \left(\frac{k_{\star}/f_{\star}}{0.02} \right)^{-1/2} \beta^{-3}. \quad (5.7)$$

The luminosity of a jet powered by a black hole depends on the regime of accretion. In the super-Eddington regime, i.e., for $M_{\text{bh}} \lesssim M_{\text{bh}, \text{jet}}$, where

$$M_{\text{bh}, \text{jet}} = 4 \times 10^8 M_{\odot} \left(\frac{\dot{m}}{\dot{m}_0} \right)^{2/3} M_{\star, \odot}^{(1+\xi)/3} \left(\frac{k_{\star}/f_{\star}}{0.02} \right)^{-1/2} \beta^{-3}, \quad (5.8)$$

the jet luminosity is given by Krolik and Piran (2012),

$$L_{\text{jet}} \approx 8 \times 10^{46} \text{ erg s}^{-1} \frac{f(a)}{\beta_h \alpha_s} M_{\text{bh}, 6}^{-1/2} q \left(\frac{\dot{m}}{\dot{m}_0} \right) M_{\star, \odot}^{(1+3\xi)/2} \left(\frac{k_{\star}/f_{\star}}{0.02} \right)^{-1/2} \beta^{-3}, \quad (5.9)$$

where α_s is the ratio of inflow speed to orbital speed of the disk, and β_h the ratio of the midplane total pressure near the ISCO to the magnetic pressure in the black hole’s stretched horizon, such that $\alpha_s \beta_h \sim 0.1 - 1$; the function $f(a) \approx a^2$ encodes the dependence of the jet luminosity on the dimensionless spin of the black hole (Piran et al., 2015), a , which ranges from $a = 0$ (for a Schwarzschild black hole) to $a = 1$ (for a maximally spinning black hole); $\dot{m} = \dot{M} c^2 / L_{\text{Edd}}$ is the normalized accretion rate in the outer disk (with L_{Edd} the Eddington luminosity); \dot{m}_0 is the peak normalized accretion rate; and q is the fraction of \dot{m} arriving at the black hole, thus accounting for possible outflows. We do not consider the sub-Eddington regime as it involves black holes with higher masses, which should not be able to tidally disrupt main sequence stars. We recall that in the following we assume default values $q = 1$, $a = 1$, $\alpha_s \beta_h = 1$, $k_{\star}/f_{\star} = 0.02$ for the parameters appearing in the jet luminosity. In particular, the choice to set the spin $a = 1$ is justified by iron- $K\alpha$ measurements of AGN spins (Brenneman, 2013; Reynolds, 2013), on which our galaxy formation model is calibrated (Sesana et al., 2014). Clearly, if all black holes had low spins $a \ll 1$ our jetted TDE rates would be significantly decreased, but such a choice seems hard to reconcile with iron- $K\alpha$ observations (see discussion in Sesana et al. 2014).

The total energy release per TDE is given by

$$\mathcal{E}_{\text{jet}} \approx L_{\text{jet}} P_{\text{orb}} \simeq 4 \times 10^{52} \text{ erg } M_{\star, \odot} \frac{f(a)}{\beta_h \alpha_s} q \left(\frac{\dot{m}}{\dot{m}_0} \right), \quad (5.10)$$

which should be less than $\dot{M}c^2$. We note that a jet luminosity $L_{\text{jet}} = \eta_{\text{jet}}\dot{M}c^2$ and $\eta_{\text{jet}} \sim 1$ are achieved if the disk is magnetically arrested, but the efficiency factor may be smaller. Also, the gravitational binding energy is much lower, so we need to rely on an energy extraction, for example via the Blandford–Znajek mechanism to have powerful jets.

The observable non-thermal luminosity (which, as mentioned before, is identified with the bolometric luminosity of our SED model) is related to the jet luminosity by accounting for the efficiency of energy conversion from Poynting to photon luminosity η_{jet} and for the beaming factor $\mathcal{B} = \min(4\pi/\Delta\Omega, 2\Gamma^2)$, where $\Delta\Omega$ is the solid angle occupied by the jet (Krolik and Piran, 2012). For a two-sided jet with a jet opening angle θ_{jet} , we have $\mathcal{B} = \min(1/(1 - \cos\theta_{\text{jet}}), 2\Gamma^2)$. Therefore, $L_{\text{bol}} = L_{\text{jet,obs}} = \eta_{\text{jet}}\mathcal{B}L_{\text{jet}} = 2\eta_{\text{jet,-2}}L_{\text{jet}}$ for $\theta_{\text{jet}} \sim 5^\circ$, $\Gamma = 10$, and $\eta_{\text{jet}} = 0.01$.

Considering the theoretical local rate density $\dot{n}_{\text{tde},0} = 150 \text{ Gpc}^{-3} \text{ yr}^{-1}$ estimated from the semi-analytic galaxy formation model of Barausse (2012) (see section 5.3.4), the luminosity density is estimated to be

$$\begin{aligned} Q_{\text{TDEjet}} &\approx \eta_{\text{jet}} \mathcal{B} \mathcal{E}_{\text{jet}} \dot{n}_{\text{tde},0}, \\ &\simeq 10^{46} \text{ erg Mpc}^{-3} \text{ yr}^{-1} \eta_{\text{jet,-2}} M_{\star,\odot} \frac{f(a)}{\beta_h \alpha_s} q \left(\frac{\dot{m}}{\dot{m}_0} \right) \frac{\dot{n}_{\text{tde},0}}{150 \text{ Gpc}^{-3} \text{ yr}^{-1}}. \end{aligned} \quad (5.11)$$

We note that $\sim 10^{43} \text{ erg Mpc}^{-3} \text{ yr}^{-1}$ above $10^{19.5} \text{ eV}$ is required to account for the observed flux of UHECR for a hard injection spectral index, (e.g. Katz et al., 2009). This estimate can be modified for a heavy composition due to the contribution of secondary cosmic rays below 10^{20} eV . However, the uncertainties remain high on the local event rate density given the small number of jetted TDEs observed.

5.3.4 Redshift evolution of the black hole mass function

To model the cosmological evolution of massive black holes in their galactic hosts, we utilize the semi-analytic galaxy formation model of Barausse (2012) (with incremental improvements described in Sesana et al., 2014; Antonini et al., 2015a; Antonini et al., 2015b; Bonetti et al., 2017a; Bonetti et al., 2017b), adopting the default calibration of Barausse et al. (2017). The model describes the cosmological evolution of baryonic structures on top of Dark Matter merger trees produced with the extended Press–Schechter formalism, modified to more closely reproduce the results of N-body simulations within the Λ CDM model (Press and Schechter, 1974; Parkinson et al., 2008). Among the baryonic structures that are evolved along the branches of the merger trees, and which merge at the nodes of the tree, are a diffuse, chemically primordial intergalactic medium, either shock-heated to the Dark Matter halo’s virial temperature or streaming into the halo in cold filaments (the former is more common at low redshift and high halo masses, and the latter in small systems at high redshifts; Dekel and Birnboim 2006; Cattaneo et al. 2006; Dekel et al. 2009); a cold interstellar medium (with either disk- or bulge-like geometry), which forms from the cooling of the intergalactic medium or from the above-mentioned cold accretion flows, and which can give rise to star formation in a quiescent fashion or in bursts (Sesana et al., 2014); parsec-scale nuclear star clusters, forming from the migration of globular clusters to the galactic center or by in situ star formation (Antonini et al., 2015a; Antonini et al., 2015b); a central massive black hole, feeding from a reservoir of cold gas, brought to the galactic center, for example by major mergers and disk bar instabilities. Our semi-analytic model also accounts for feedback processes on the growth or structures (namely from supernovae and from the jets and outflows produced by AGNs), and for the sub-parsec evolution of massive black holes, for example the evolution of black hole spins (Barausse, 2012; Sesana et al., 2014), migration of binaries due to gas interactions, stellar hardening and triple massive black hole interactions (Bonetti et al., 2017a; Bonetti et al., 2017b), gravitational-wave emission (Klein et al., 2016).

M_{bh} (M_{\odot})	$L_{\text{bol,med}} [L_{\text{pk}}]$ (erg s^{-1})	$L_{\text{bol,high}} [L_{\text{pk}}]$ (erg s^{-1})
7×10^8	$6.8 \times 10^{45} [10^{45}]$	$2.1 \times 10^{47} [10^{46.5}]$
7×10^7	$2.1 \times 10^{46} [10^{45.5}]$	$6.8 \times 10^{47} [10^{47}]$
7×10^6	$6.8 \times 10^{46} [10^{46}]$	$2.1 \times 10^{48} [10^{47.5}]$
7×10^5	$2.1 \times 10^{47} [10^{46.5}]$	$6.8 \times 10^{48} [10^{48}]$

Table 5.2: Observed jet luminosities as a function of black hole mass $M_{\text{bh}} (M_{\odot})$ in the medium state $L_{\text{bol,med}} (\text{erg s}^{-1})$ for $\theta_{\text{jet}} = 5^\circ$ and $\eta_{\text{jet}} = 0.01$, and in the high state $L_{\text{bol,high}} (\text{erg s}^{-1})$ for $\theta_{\text{jet}} = 5^\circ$ and $\eta_{\text{jet}} = 0.35$.

For the purposes of this paper, the crucial input provided by our model is the evolution of the TDE luminosity function. We determine the TDE comoving rate density $\dot{n}_{\text{TDE}}(z, L)$ by combining the TDE rate per galaxy \dot{N}_{TDE} and the black hole comoving density $n_{\text{bh}}(z, M_{\text{bh}})$, and using the black hole mass and jet luminosity relation (Eq. 5.9). For the properties of the jet, we distinguish between the high state, characterized by a high jet efficiency, and the medium state, characterized by a lower jet efficiency. We set these parameters in order to be consistent with the observations of Swift J1644+57, which should be associated with a black hole of mass $M_{\text{bh}} \gtrsim 7 \times 10^6 M_{\odot}$ (Seifna et al., 2017) and reaches a bolometric luminosity $L_{\text{bol}} \gtrsim 10^{48} \text{ erg s}^{-1}$ in the high state. Therefore, we have $\theta_{\text{jet}} = 5^\circ$ and $\eta_{\text{jet}} = 0.35$ in the high state and $\theta_{\text{jet}} = 5^\circ$ and $\eta_{\text{jet}} = 0.01$ in the medium state. For instance, a black hole of mass $M_{\text{bh}} \gtrsim 7 \times 10^6 M_{\odot}$ is associated with $L_{\text{bol}} \simeq 2 \times 10^{48} \text{ erg s}^{-1}$ in the high state and $L_{\text{bol}} \simeq 7 \times 10^{46} \text{ erg s}^{-1}$ in the medium state. The other cases that we consider are shown in Table 5.2. As explained in section 5.3.2, for high masses $M_{\text{bh}} > 10^8 M_{\odot}$, only highly spinning black holes could lead to observable flares. For completeness, we also account for this case in our study.

We compare the black hole mass function predicted by our semi-analytic galaxy formation model with the observational determinations of Shankar (2013) and Lauer et al. (2007) (at $z = 0$), and with those of Merloni and Heinz (2008) and Schulze et al. (2015) (at $z > 0$) in figure 5.5. The model’s predictions are shown as red bars or blue dots, the first referring to a scenario in which black holes form from low-mass seeds of a few hundred M_{\odot} (e.g., the remnants of Pop III stars; Madau and Rees, 2001), and the second representing a model in which black holes descend from “heavy” ($\sim 10^5 M_{\odot}$) seeds arising, for example, from instabilities of protogalactic disks. In more detail, for the latter case we use the model of Volonteri et al. (2008), setting their critical Toomre parameter, which regulates the onset of the instability, to their preferred value $Q_c = 2.5$.) The error bars of the model’s points are Poissonian. As can be seen, the agreement with the data is rather good, especially in the mass range relevant for our purposes ($M_{\text{bh}} < 10^8 M_{\odot}$). As a further test, we also compared the predictions of our model for the AGN (bolometric) luminosity function with the observations of Hopkins et al. (2007), Lacy et al. (2015), La Franca et al. (2005), and Aird et al. (2010), whose envelope we show in figure 5.5 as a shaded orange area. We note that we only consider the luminosity function of Aird et al. (2010) at $z < 3$ as it may be underestimated at larger redshifts (Kalfountzou et al., 2014).

It is interesting to notice that the luminosity function of jetted TDEs is dominated by high luminosities (hence low black hole masses) in our model, unlike the distribution of Sun et al. (2015). This stems from the flat black hole mass functions at low masses (Figures 5.5) combined with the $L_{\text{jet}} \propto M_{\text{bh}}^{-1/2}$ relation (Eq. 5.9). It implies, quite naturally, which of the observed very bright objects such as Swift J1644+57 are the dominant ones in the population. These objects thus set the maximum bolometric luminosity L_{max} in the luminosity function, which we introduce

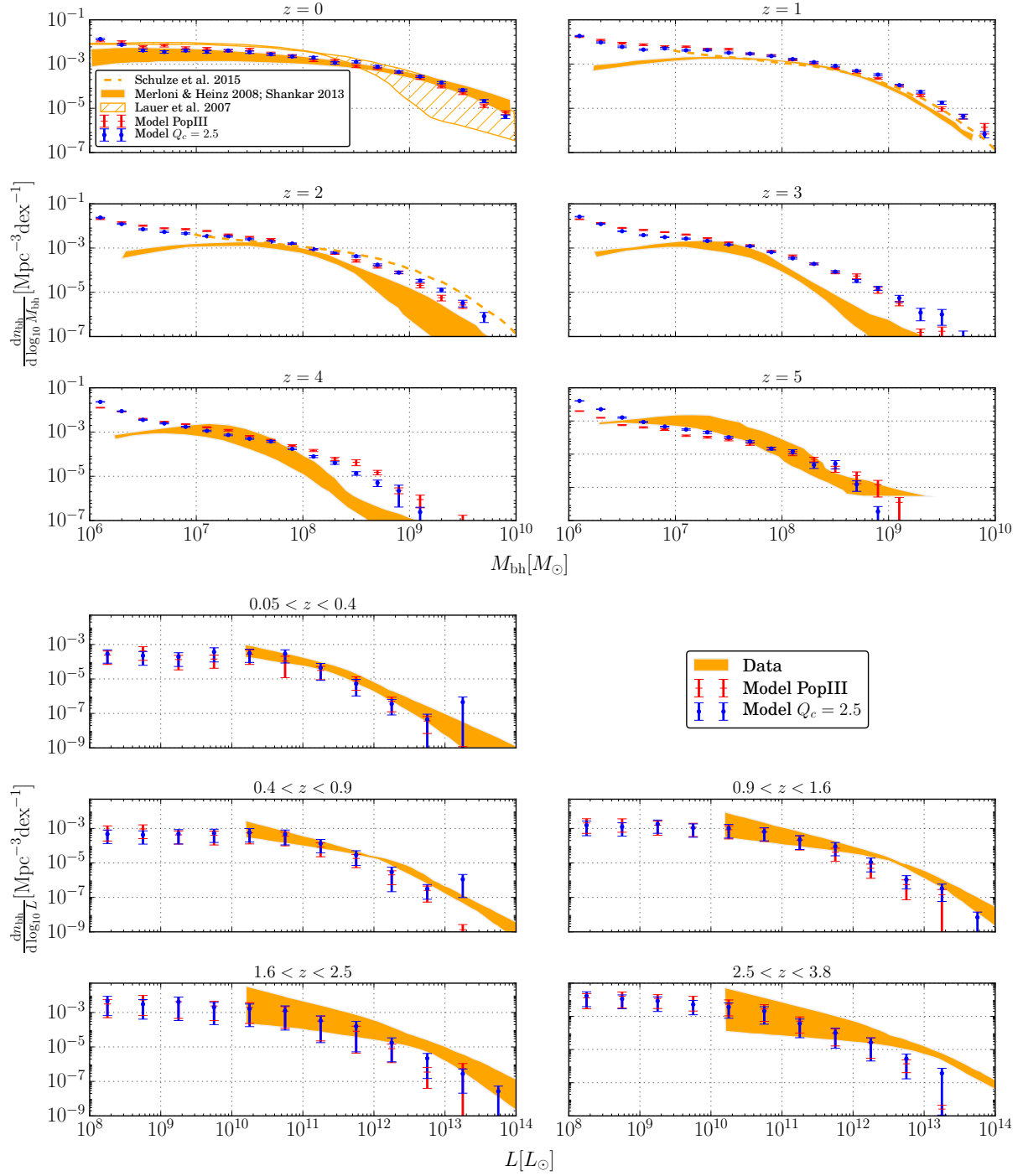


Figure 5.5: Top: predictions of the semi-analytic galaxy formation model of Baraussen (2012) in two different scenarios, light-seed (“Pop III”) and heavy-seed (“ $Q_c = 2.5$ ”), for the mass function of black holes as a function of redshift. The model’s error bars are Poissonian. For comparison, also shown are the observational determinations of Shankar (2013) and Lauer et al. (2007) (at $z = 0$), and those of Merloni and Heinz (2008) and Schulze et al. (2015) (at $z > 0$). Bottom: predictions of our model for the bolometric AGN luminosity function, compared with observational determinations – Hopkins et al. (2007), Lacy et al. (2015), La Franca et al. (2005), and Aird et al. (2010), the last only considered at $z > 3$ –, whose envelope is shown by a shaded orange area.

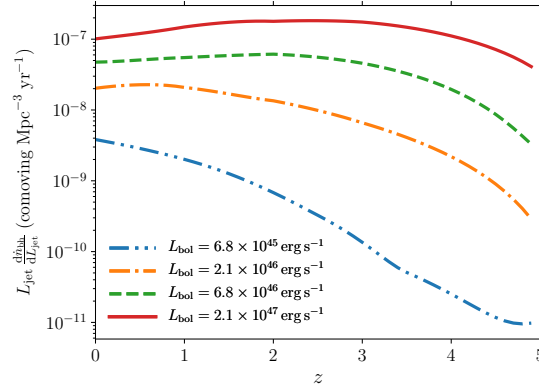


Figure 5.6: Comoving TDE luminosity density in their medium state as a function of redshift, as derived in our model, for $\dot{N}_{\text{TDE}} = 10^{-5} \text{ yr}^{-1}$. The different luminosities correspond to different black hole masses.

as a cutoff in our population model. This also implies that the diffuse flux of UHECRs will be dominantly produced by the most luminous objects in their medium state. Figure 5.6 shows that the corresponding TDE comoving rate density remains almost constant up to redshift ~ 3 for luminosities $\geq 10^{45.5} \text{ erg s}^{-1}$, which dominate in the production of cosmic-ray and neutrino fluxes in our framework.

5.4 Diffuse UHECR and neutrino fluxes from a TDE population

In the following we calculate the diffuse cosmic-ray and neutrino fluxes, and the composition of cosmic rays by considering a population of jetted TDEs. All primed quantities are in the jet comoving frame, all quantities with superscript c are in the source comoving frame, and all other quantities are in the observer frame. The fluxes depend on the spectra produced by each source, on the comoving rate of TDEs, and on the cosmic-ray propagation to the Earth. During the extragalactic propagation, cosmic rays may interact with the cosmic microwave background (CMB) and the extragalactic background light (EBL) through photonuclear interactions. Because of these processes, they may lose energy and create secondary particles in the case of nuclei. In our work we consider EBL models from Kneiske et al. (2004) and Stecker et al. (2006).

First, we give some detail about the calculation of the diffuse neutrino flux. We account for the total number of neutrinos produced by one single source $N_{\nu,s}(E_\nu^c, L)$, which depends on the neutrino energy in the source comoving frame $E_\nu^c = (1+z)E_\nu$ and the bolometric luminosity of the source. Moreover, for a redshift z , we can observe a population of sources characterized by a comoving event rate density $\dot{n}(z, L)$ during an observation time $T_{\text{obs}} = (1+z)T_{\text{obs}}^c$ (where T_{obs} is the time in the observer frame and T_{obs}^c is the time in the source comoving frame), in a comoving volume,

$$\frac{dV(z)}{dz} = \frac{c}{H_0} \frac{4\pi D_c^2}{\sqrt{\Omega_M(1+z)^3 + \Omega_\Lambda}}, \quad (5.12)$$

where $\Omega_M = 0.3$ and $\Omega_L = 0.7$ are our fiducial cosmological parameters, and the Hubble constant is $H_0 = 70 \text{ km s}^{-1} \text{ Mpc}^{-1}$. The comoving event rate density $d\dot{n}(z, L)/dL = \dot{N}_{\text{TDE}} dn_{\text{bh}}(z, L)/dL$ depends on the TDE rate per galaxy \dot{N}_{TDE} and the black hole comoving density per luminosity $dn_{\text{bh}}(z, L)/dL$. Therefore, the diffuse neutrino flux is given by

$$\frac{dN_\nu}{dE_\nu}(E_\nu) = \frac{1}{4\pi} \int_{z_{\text{min}}}^{z_{\text{max}}} \int_{L_{\text{min}}}^{L_{\text{max}}} dz dL f_s \xi_{\text{CR}} \frac{d\dot{n}(z, L)}{dL} \frac{1}{1+z} \frac{dV(z)}{dz} \frac{1}{4\pi D_c^2} \frac{dN_{\nu,s}(E_\nu^c, L)}{dE_\nu^c} \frac{dE_\nu^c}{dE_\nu}. \quad (5.13)$$

We obtain a diffuse neutrino flux

$$\Phi_\nu(E_\nu) = \frac{c}{4\pi H_0} \int_{z_{\min}}^{z_{\max}} \int_{L_{\min}}^{L_{\max}} dz dL \frac{f_s \xi_{\text{CR}} d\dot{n}(z, L)/dL}{\sqrt{\Omega_M(1+z)^3 + \Omega_\Lambda}} F_{\nu,s}^c(E_\nu^c, L) t_{\text{dur}}^c, \quad (5.14)$$

where $\Phi_\nu(E_\nu) = d^2 N_\nu(E_\nu)/dE_\nu dt$ is the diffuse neutrino flux per unit time (observer frame), $F_{\nu,s}^c(E_\nu^c, L) = d^2 N_{\nu,s}(E_\nu^c, L)/dE_\nu^c dt^c$ is the number of neutrinos emitted by one single source per bin of comoving energy and per unit of comoving time, and t_{dur}^c is the duration of the emission in the source comoving frame. Moreover, f_s is the fraction of the jetted TDE population, calculated in Sect. 5.3, which contributes to the production of cosmic rays and neutrinos.

Similarly, the diffuse cosmic-ray flux is given by

$$\Phi_{\text{CR}}(E_{\text{CR}}) = \frac{c}{4\pi H_0} \int_{z_{\min}}^{z_{\max}} \int_{L_{\min}}^{L_{\max}} dz dL \frac{f_s \xi_{\text{CR}} \dot{N}_{\text{TDE}} dn_{\text{bh}}(z, L)/dL}{\sqrt{\Omega_M(1+z)^3 + \Omega_\Lambda}} F_{\text{CR},s,p}^c(E_{\text{CR}}^c, z, L) t_{\text{dur}}^c, \quad (5.15)$$

where $F_{\text{CR},s,p}^c(E_{\text{CR}}^c, z, L)$ is the spectrum obtained after the propagation of cosmic rays from a source at redshift z with luminosity L (per bin of comoving energy E_{CR}^c and per unit of comoving time t^c), and t_{dur}^c is the duration of the emission in the source comoving frame.

Due to the flat evolution of the TDE comoving density rates up to $z \sim 3$, we can safely use the jetted TDE luminosity distribution at $z = 0$ in the above equations and separate the integrals in L and z . We checked in particular that our results were similar when using the distribution function at redshifts $z \lesssim 3$. The impact of the redshift evolution on the cosmic-ray spectrum and on the neutrino flux level is also limited, and close to a uniform evolution as described in Kotera et al. (2010).

5.4.1 Final spectrum and composition of cosmic rays

We show in figure 5.7 the cosmic-ray spectrum obtained for an injection of 70% Si and 30% Fe, a spectral index $\alpha = 1.5$, an acceleration efficiency $\eta_{\text{acc}} = 0.1$, a TDE source evolution, and a fraction $\xi_{\text{CR}} f_s = 2.6 \times 10^{-3}$ of the local event rate density $\dot{n}_{\text{tde},0} = 1.5 \times 10^2 \text{ Gpc}^{-3} \text{ yr}^{-1}$ (or a fraction $\xi_{\text{CR}} f_{s,\text{tot}} = 1.4 \times 10^{-4}$ of the total event rate density $\dot{n}_{\text{tde,tot}} = 2.3 \times 10^3 \text{ Gpc}^{-3} \text{ yr}^{-1}$). This rates are computed from the TDE rate per galaxy obtained in the case of core galaxies, and the first one is integrated over redshift. The population fraction corresponds approximately to the rate density $\sim 0.4 \text{ Gpc}^{-3} \text{ yr}^{-1}$. The heavy composition could be injected for example by the core of disrupted stars. We recall that we consider a production of UHECRs dominated by medium states. Superimposed are the data from the Auger experiment (The Pierre Auger Collaboration et al., 2015) and from the Telescope Array experiment (Fukushima, 2015) shown with their statistical uncertainties. We note that the systematic uncertainty on the energy scale is 14% for the Auger experiment.

We also show in figure 5.8 the corresponding mean and standard deviation for the depth of the maximum of the air showers, $\langle X_{\text{max}} \rangle$ and $\sigma(X_{\text{max}})$. It is represented by a gray band, due to uncertainties related to UHECR-air interaction models EPOS-LHC (Werner et al., 2006; Pierog et al., 2013), SIBYLL 2.1 (Ahn et al., 2009), or QGSJET II-04 (Ostapchenko, 2006; Ostapchenko, 2013). Superimposed are the data from the Auger experiment for the composition of UHECRs, $\langle X_{\text{max}} \rangle$ and $\sigma(X_{\text{max}})$ (Aab et al., 2014). Only statistical uncertainties are displayed; systematic uncertainties are at most $\pm 10 \text{ g cm}^{-2}$ for $\langle X_{\text{max}} \rangle$ and $\pm 2 \text{ g cm}^{-2}$ for $\sigma(X_{\text{max}})$. Our results are in qualitative agreement with the data: they are compatible with a light composition at $10^{18.5} \text{ eV}$, shifting toward a heavier composition for increasing energy.

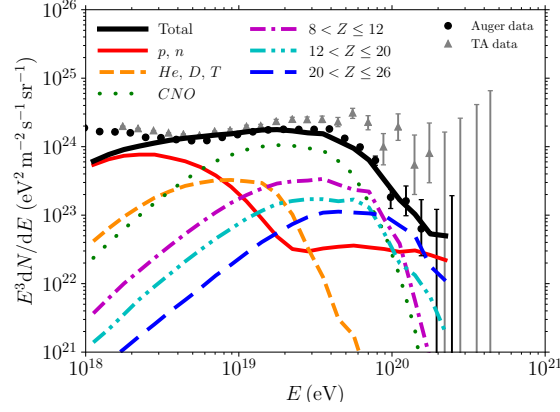


Figure 5.7: Diffuse cosmic-ray spectrum from a population of jetted TDEs (calculated in their medium states) obtained for an injection of 70% Si and 30% Fe, with spectral index $\alpha = 1.5$, $\xi_{\text{CR}} f_s = 2.6 \times 10^{-3}$ and source evolution derived in this work, with maximum bolometric luminosity in the population $L_{\text{max}} = 6.8 \times 10^{46} \text{ erg s}^{-1}$. We show the total spectrum (black) and its composition. We superimpose data from the Auger experiment (black dots, The Pierre Auger Collaboration et al., 2015), and from the Telescope Array experiment (gray dots, Fukushima, 2015) for which only statistical uncertainties are shown.

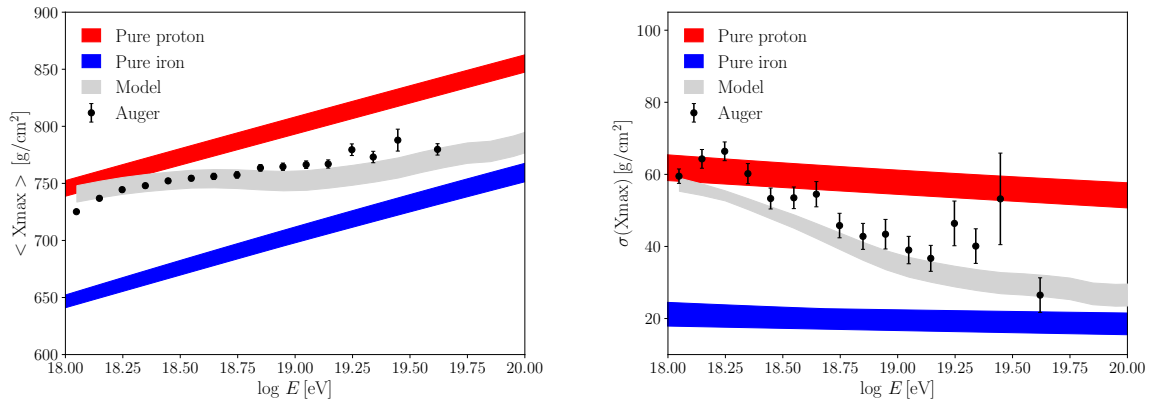


Figure 5.8: Mean and standard deviation of X_{max} for the spectrum shown in figure 5.7 (pale gray band). We also show Auger measurements (Aab et al., 2014) with uncertainties (black dots) and simulation results for pure proton injection (red band) and pure iron injection (blue band). The bands are obtained by accounting for hadronic model uncertainties (EPOS-LHC, SIBYLL 2.1 or QGSJET II-04).

With increased cutoff bolometric luminosities L_{\max} , harder injection spectra are needed in order to compensate for the abundant production of nucleons at low energies, which softens the overall spectrum (typically $\alpha = 1$ is required for $L_{\max} = 10^{47} \text{ erg s}^{-1}$). We present the case of the injection of a dominant fraction of heavy elements; the injection of more intermediate elements, such as the CNO group, is possible at the cost of increasing the acceleration efficiency η_{acc} , and hardening the injection spectrum further in order to achieve the highest energies.

Our model allows to reproduce both the UHECR spectrum and composition of the Auger observations, as long as the dominant sources supply luminosities $\lesssim 10^{46.5} \text{ erg s}^{-1}$, which is a value that is consistent with the observed Swift event. We note that if the high states were dominant for the UHECR production, we would not be able to fit the data; because of the strong photodisintegration of heavy elements in the very dense radiation background, we would obtain a large production of nucleons below 10^{19} eV and no survival of heavy elements at the highest energies. However, because of its limited duration ($t_{\text{dur}} \sim 10^5 \text{ s}$ is chosen as an upper bound), the high state is unlikely to be dominant. Indeed, as shown in figure 5.4, the high state could contribute marginally to the diffuse cosmic-ray flux at the lowest energies. The strong photodisintegration in the high state leads to a strong production of nucleons below 10^{19} eV , which adds a new component to the spectrum and make the composition lighter. In a more refined model we should account for the evolution of the luminosity of the jet, which should decrease during the event duration.

The disrupted stellar object provides material (protons and heavier nuclei) that can be injected and accelerated in a jet. As already emphasized, the composition of this material is poorly constrained; it could be similar to the composition of the stellar object or modified during the disruption process. It is interesting that white dwarfs could be commonly disrupted by black holes with $M_{\text{bh}} \lesssim 10^5 M_{\odot}$. These stars could be a source of copious amounts of CNO nuclei, which seem to be observed in the composition of UHECRs measured by Auger, as noted in Alves Batista and Silk (2017). For completeness, we tested in this study various injection fractions, and we present one case that allows us to fit the Auger data well. We note that a deviation of 5% in the composition does not largely affect the fit to the data within the error bars, given the uncertainties on the other jetted TDE parameters.

Markers of the occurrence of jets associated with TDEs were detected only very recently. Most TDEs should not power jets and only a small fraction of jetted TDEs should point toward the observer, depending on the jet opening angle. Therefore, the properties of these objects are still subject to large uncertainties. From an observational perspective, the jetted TDEs detected recently are very luminous events with a peak isotropic luminosity $L_{\text{pk}} \sim 10^{47} - 10^{48} \text{ erg s}^{-1}$, and a local event rate density is of $\dot{n}_{\text{tde},0} \sim 0.03 \text{ Gpc}^{-3} \text{ yr}^{-1}$ (e.g., Farrar and Piran, 2014). On the other hand, normal TDEs are less luminous and are characterized by a higher local event rate density $\dot{n}_{\text{tde},0} = 10^2 \text{ Gpc}^{-3} \text{ yr}^{-1}$ (e.g., Donley et al., 2002b). However, the characteristics of this new population, mainly their luminosity distribution and comoving event rate density, are difficult to infer due to the scarcity of observations. From our population model, the maximum local event rate density that we can expect reaches $\dot{n}_{\text{tde},0} \sim 2 \times 10^2 \text{ Gpc}^{-3} \text{ yr}^{-1}$ for core galaxies and $\dot{n}_{\text{tde},0} \sim 3 \times 10^3 \text{ Gpc}^{-3} \text{ yr}^{-1}$ for power-law galaxies.

The fraction needed to fit the UHECR spectrum of the Auger observations, $\xi_{\text{CR}} f_s = 2.6 \times 10^{-3}$, can account for example for low UHECR injection rates ξ_{CR} , and/or for population constraints, such as the fraction of TDE jets pointing toward the observer. Assuming the low rate inferred from the observations of $\dot{n}_{\text{tde},0} \sim 0.03 \text{ Gpc}^{-3} \text{ yr}^{-1}$ for the jetted events pointed toward the observer, a baryon loading of $\xi_{\text{CR}} \sim 1$ is required. This value is consistent with the non-detection of neutrinos from Swift J1644+57, which implies an upper limit to the baryon density of a few 100 (Senno et al., 2016b; Guépin and Kotera, 2017).

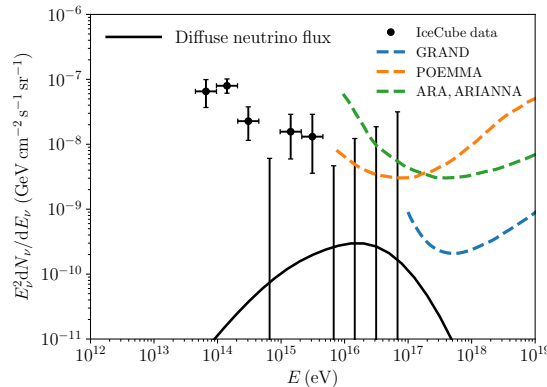


Figure 5.9: Diffuse neutrino flux for three flavors from a population of jetted TDEs with the same properties as in figure 5.7 (neutrino production calculated in their high states). We also show the diffuse neutrino flux measured by the IceCube experiment (IceCube Collaboration et al., 2017), and the projected limits for GRAND (Fang et al., 2017), ARA/ARIANNA (Allison et al., 2015; Barwick et al., 2015), and POEMMA (Neronov et al., 2017a).

5.4.2 Diffuse neutrino flux

The TDE event density obtained by fitting the Auger data with our UHECR spectrum allows us to calculate the diffuse neutrino flux from a population of TDEs, by considering the fraction $\xi_{\text{CR}} f_s$ calculated above. As shown in figure 5.9, the diffuse neutrino flux from jetted TDEs contributes marginally to the total diffuse neutrino flux observed by IceCube (IceCube Collaboration et al., 2017). As it peaks at high energies, around 10^{16} eV, it could be a good target for future generation detectors. However, we note that this flux is too low to be detectable with ARA/ARIANNA, POEMMA, and GRAND at even higher energies. Its high-energy cutoff reduces the flux at higher energies, and therefore it lies below the GRAND sensitivity limit.

5.5 Discussion and conclusion

We assessed in this study the production of UHECRs and neutrinos by a population of TDEs. In our model, the disruption of a stellar object launches a relativistic jet, where internal shocks can accelerate a part of the disrupted material, namely light and heavy nuclei. This scenario is connected to recent observations and analytic studies, favoring a jetted model for some very luminous events. In such a case, material from the disrupted object can be injected and accelerated inside the jet, and can experience interactions before escaping and propagating in some cases toward the Earth. However, other scenarios could be contemplated; for instance, a substantial fraction of the accreted material could be ejected as a wind where particles could be linearly accelerated (even if Zhang et al. (2017) show that UHECR acceleration is difficult in the wind model).

The bulk Lorentz factor Γ and the opening angle of the jet θ_{jet} are two important quantities impacting our results. The bulk Lorentz factor of the jet impacts the observed jet isotropic luminosity and the energy of detected cosmic rays and neutrinos. The dynamical time also scales as Γ and the photon energy density as Γ^{-4} , thus an increase of a factor of a few in Γ could lead to a drastic cut in the photodisintegration rates. Here we use the fiducial value $\Gamma = 10$, but for larger values we expect that the survival of nuclei would be favored, leading to lower nucleon production at lower energies, and thus to a larger parameter space allowing for a good fit for the diffuse UHECR spectrum. Our choice is conservative in this sense. On the other hand, the

neutrino production would be consequently reduced. The opening angle of the jet is also not well constrained; therefore, we adopt a small value $\theta_{\text{jet}} \sim 5^\circ$ for the high and medium states (e.g., Bloom et al., 2011; Burrows et al., 2011). Like the bulk Lorentz factor, this parameter is also involved in the model that we use to link the black hole mass to the isotropic luminosity of the jet. The jet can be seen only if it is pointing toward the observer. However, we note that the effective opening angle for cosmic rays might be higher than the usual opening angle as cosmic rays can experience small deflections inside the jet; thus, misaligned jetted TDEs characterized by a higher rate than aligned events might also contribute to the diffuse cosmic-ray flux.

Biehl et al. (2017) show that the acceleration of nuclei in jets created by the tidal disruption of white dwarfs can lead to a simultaneous fit of the UHECR data and the measured IceCube neutrino flux in the PeV range. One major difference with our study is that we include a detailed jetted TDE population study by modeling the luminosity function and rate evolution in redshift. Our conclusions are also different from theirs, in so far as we cannot fit the observed diffuse IC neutrino flux with our TDE population model. This negative result is consistent with several arguments already highlighted in previous works by Dai and Fang (2017) and Senno et al. (2016b). In particular, the absence of observed neutrino multiplets in the IceCube data gives a lower limit of $\gtrsim 100 - 1000 \text{ Gpc}^{-3} \text{ yr}^{-1}$, which is significantly higher than the rate of jetted TDEs pointing toward us inferred from observations of $\sim 0.03 \text{ Gpc}^{-3} \text{ yr}^{-1}$, and higher than rates with dimmer luminosities also constrained by X-ray observations. In addition, large baryon loadings with $\gtrsim 1000$ are ruled out as such values would imply that Swift J1466+57 would have been observed in neutrinos. Also, a large baryon loading factor implies a total TDE energy of $\gtrsim 10^{54}$ erg, which violates the energetics argument.

Our model is able to reproduce with a reasonable accuracy and for a reasonable range of parameters the observations from the Auger experiments, and TDE powering jets therefore appear to be good candidates for the production of UHECRs. Our results are consistent with other TDE studies that also obtain good fits to UHECR data: Zhang et al. (2017) stress that oxygen-neon-magnesium white-dwarf TDE models could provide good fits, but do not account for photodisintegration in the vicinity of the source because they used a steeper luminosity function. Our model can account for these interactions, and allows us to explore the parameter space for the radiation field, the injection and the composition. This is important for our flatter luminosity function, which predicts that the luminosity density is dominated by the highest-power TDEs, i.e., the effective luminosity is $L \sim 2 \times 10^{48} \text{ erg s}^{-1}$ in the high state. The associated transient HE neutrinos could be detected for single nearby sources (at distances of a few tens of Mpc) with IceCube and upcoming instruments at higher energies such as GRAND or POEMMA. The diffuse flux would be within reach of IceCube in the next decade. Its detection would be more challenging for future generation instruments aiming at the detection of ultra-high-energy neutrinos, due to a high-energy cutoff below 10^{17} eV .

Among the other transient UHECR nuclei models that have been suggested to explain the UHECR data (e.g., fast rotating pulsars, Fang et al., 2012b; Fang et al., 2014; Kotera et al., 2015 or GRBs, Wang et al., 2008; Murase et al., 2008; Globus et al., 2015b; Globus et al., 2015a), the jetted TDE model has the interesting property of presenting two different states (low and high) leading to optimal production of both UHECRs and neutrinos. In addition, the jetted TDE scenario appears mildly constrained by photon observations. Within our model, we demonstrated that the observed Swift J1466+57 can be seen as a typical source that would dominate the production of UHECRs and neutrinos. Even under this constraint, the wide range of variation allowed for several free parameters (for example the Lorentz factor of the outflow, as discussed earlier) enables us to correctly fit the cosmic-ray data. A specific signature of this scenario is thus difficult to infer. A direct multi-messenger signal with TDE photons associated with the emission of neutrinos from a single source appears to be the way to validate this scenario.

Chapter 6

Future detection and reconstruction challenges for very-high energy neutrinos and ultra-high energy cosmic rays

Cosmic rays and neutrinos are key players in multimessenger studies. At the highest energies, a precise knowledge of their properties would provide essential information about energetic phenomena. It is thus critical to detect them with a great accuracy. As explained in chapter 1, the detection of UHECR and the reconstruction of their properties is challenging, due to their low fluxes at the highest energies. Gigantic detectors have been built to study these particles, such as the Pierre Auger observatory, which is constituted of 1660 water surface detector tanks covering about 3000 km^2 and of 27 fluorescence detectors located in four different places. Detectors covering larger surfaces are required to improve the statistics and better understand the features in the UHECR spectrum and composition. The detection of very high-energy neutrinos is even more challenging due to exceedingly long interaction lengths in a neutrino detection medium. Above about $E_\nu \gtrsim 1 \text{ PeV}$ however, the neutrino interaction length shortens to a fraction of the Earth radius (Halzen and Saltzberg, 1998) making it possible for very high-energy neutrinos in skimming trajectories to interact inside the Earth (Domokos and Kovesi-Domokos, 1998a; Domokos and Kovesi-Domokos, 1998b; Feng et al., 2002) and allow for the produced tau lepton to escape the Earth before decaying due to the tau lepton's Lorentz-boosted lifetime, modulated by tau energy loss in the Earth. If the tau lepton decays within the atmosphere, an upward-going extensive air shower will be initiated. The beamed Cherenkov or radio contribution of that shower may be detectable by space-based or ground-based instruments viewing the area near the Earth limb.

The future observatories of very high-energy astroparticles will attempt to detect for the first time very-high energy neutrinos above 10^{17} eV , while performing competitive observations of ultra-high energy cosmic rays, in order to increase the statistics at the highest energies and thus statistically improve the reconstruction of their properties such as their elementary composition. Several projects are currently emerging, and propose to introduce ground-breaking techniques for the detection of very high-energy astroparticle, such as radio detection from ground arrays (e.g. GRAND, ARA) or Cherenkov and fluorescence detection from space (e.g. POEMMA). Prototypes are currently developed, such as GRANDProto300, an array of 300 radio antenna that will be located in China, or SPB2, a super-pressure balloon that will be launched from New Zealand and should serve as a pathfinder for POEMMA. In this chapter, we focus on two aspects related to the projects POEMMA and GRAND, that are important for their development. In the context of the POEMMA project, we conduct a prospective study about the sky coverage of a space VHE neutrino detector from space. For GRAND, we focus on the reconstruction of the elementary composition of UHECR with a sparse radio antenna array. These two studies allow to

identify strengths of weaknesses of these different detection methods, and to start contemplating future developments.

6.1 Towards space detection

In this part, based on Guépin et al. (2019a), we investigate the geometrical constraints of detecting the upward Cherenkov component by a detector located in space, including suborbital altitudes. The general characteristics of a space-based detector dedicated to the detection of VHE Earth-skimming tau neutrinos are described in Section 6.1.1, as well as the geometrical approach used to calculate the effective field of view and the sky exposure related to the observation of VHE tau neutrinos. In Section 6.1.2, we study the influence of several parameters, such as the altitude of the detector and the viewing angle, and of the focal surface design specific to optical Cherenkov detection for a configuration specific to the POEMMA Schmidt telescopes, and present estimates of the sky exposure. The question of the sky coverage is addressed in Section 6.1.3. Finally, the possibility of Target-of-Opportunity (ToO) observations is addressed in Section 6.1.4, where we evaluate the possibility of observing any direction of the sky in a short timescale. Our approach focuses mainly on geometrical calculations, therefore we did not include a consideration of cloud coverage. Moreover, a limited comprehensive study of the influence of the Sun and the Moon on the observations was included. The effects of clouds should be incorporated in a more detailed study as they will influence the sky exposure and sky coverage calculations.

6.1.1 General characteristics of space-based VHE neutrino detector

The basic field-of-view (FOV) characteristics of a space instrument dedicated to the detection of the Cherenkov light arising from a VHE tau neutrino interaction are naturally constrained. The detector needs to point at the Earth limb with the widest possible angular coverage, especially in azimuth (one could envision several individual units mounted in the same satellite like in the CHANT proposal Neronov (2017b)). Its coverage should extend below the limb until the probability of an escaping tau lepton becomes marginal for all detectable neutrino energies. Typically, the instrument should also cover a few degrees above the limb to allow for background estimates, including air glow and UHECR-induced Cherenkov signals. Figure 6.1 shows an example of what the FOV angular coverage of a dedicated generic instrument may look like. In this example, the instrument has a FOV angle $\theta_{\text{FOV}} = 45^\circ$ and covers a region ranging from $\delta = 7^\circ$ below the limb to $\alpha_{\text{off}} = 2^\circ$ above the limb. We note that in practice, it is preferable that the detector is not oriented towards the satellite moving (ram) direction to prevent potential degradation of the optics (unless properly coated) of the Cherenkov detection instrument due to the atomic oxygen present in the upper atmosphere Banks et al. (2004).

However, in what follows we will consider a different FOV configuration. POEMMA is conceived as a system of two satellites in trailing orbits, which aims at detecting both UHECR and VHE neutrinos in a dual-observation mode. The design of the instrument revolves around a uniform 45° FOV equipped with two types of photo-detectors. The top of the FOV, dedicated to the detection of VHE neutrinos, uses Silicon photomultiplier (SiPM) detectors and matches the shape of the dedicated instrument shown in figure 6.1. The bottom of the FOV, dedicated to the detection of UHECRs, uses an arrangement of Multi-Anode-PhotoMultiplier-Tubes (MAPMTs). With the top of the FOV observing the limb, the bottom of the FOV is looking down at the Earth surface, where UHECR showers can be observed. This is what makes the dual purpose FOV of POEMMA so attractive. Figure 6.2 shows the specific angular coverage of POEMMA for VHE neutrinos with $\delta_{\text{off}} = 7^\circ$ and $\alpha_{\text{off}} = 2^\circ$. As can be seen, the Cherenkov-sensitive part

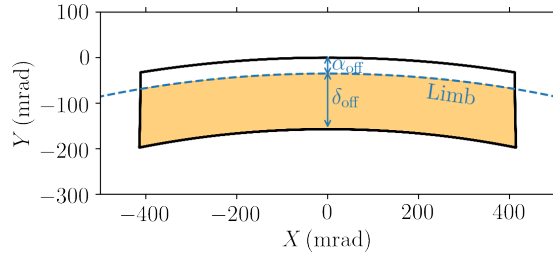


Figure 6.1: Illustration of a generic focal surface for the indirect detection of VHE Earth-skimming tau neutrinos, using the typical opening angle around $45^\circ/2$. The limb of the Earth is shown as a dashed blue line. The orange area corresponds to the part of the focal surface below the limb, that can detect VHE Earth-skimming tau neutrinos.

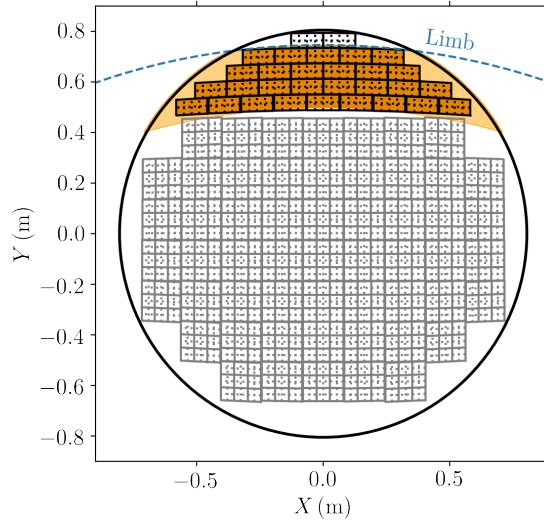


Figure 6.2: Focal surface of the POEMMA detector with the photosensors dedicated to VHE neutrino detection (black tiles) and to the UHECR detection (grey tiles). The projection of the geometrical FOV on the focal surface is shown in light orange and the fraction that can be detected by the tiles is shown in darker orange. The limb of the Earth is shown as a dashed blue line.

of the POEMMA focal surface follows the same philosophy as the generic detector shown in figure 6.1.

To carry out our calculations, we consider one satellite on a circular orbit of inclination angle i , located at an altitude h . The configuration and the notations are illustrated in figure 6.3, in the equatorial coordinate system, with \vec{I} the vernal equinox and \vec{K} the north pole. At a given time, the satellite is characterized by its position (Θ_s, Φ_s) ¹, with $\vec{u}_{\text{sat}} = \sin \Theta_s \cos \Phi_s \vec{I} + \sin \Theta_s \sin \Phi_s \vec{J} + \cos \Theta_s \vec{K}$, such as $\vec{n}_{\text{orb}} \cdot \vec{u}_{\text{sat}} = 0$. For instance for \vec{n}_{orb} in the (\vec{K}, \vec{I}) plane, $\vec{n}_{\text{orb}} = \cos i \vec{K} + \sin i \vec{I}$ and we obtain the constraint $\cos i \cos \Theta_s + \sin i \sin \Theta_s \cos \Phi_s = 0$. The period of the orbit is given by $P = 2\pi \sqrt{(R_\oplus + h)^3 / (GM_\oplus)}$ where G is the gravitational constant and M_\oplus the mass of the Earth; thus for instance $P \approx 1 \text{ h } 45 \text{ min}$ for $h = 1000 \text{ km}$ and $P \approx 1 \text{ h } 35 \text{ min}$ for $h = 525 \text{ km}$. Moreover the orbit precesses around the north pole, with precession rate $\omega_p = (3/2)R_\oplus^2 / (R_\oplus + h)^2 J_2 \omega \cos(i)$, where $\omega = 2\pi/P$ and J_2 is related to the Earth oblateness. For an orbit inclination $i = 28.5^\circ$, the orbit precesses in $P_p \approx 68 \text{ d } 13 \text{ h } 39 \text{ min}$ for $h = 1000 \text{ km}$ and in $P_p \approx 54 \text{ d } 7 \text{ h } 26 \text{ min}$ for $h = 525 \text{ km}$.

The configuration in the plane containing the vectors \vec{u}_{sat} and \vec{n}_d , where \vec{n}_d is the point-

¹ $\Theta_s = \pi/2 - \delta_s$ and $\Phi_s = \alpha_s$ with α_s and δ_s the right ascension and declination of the satellite.

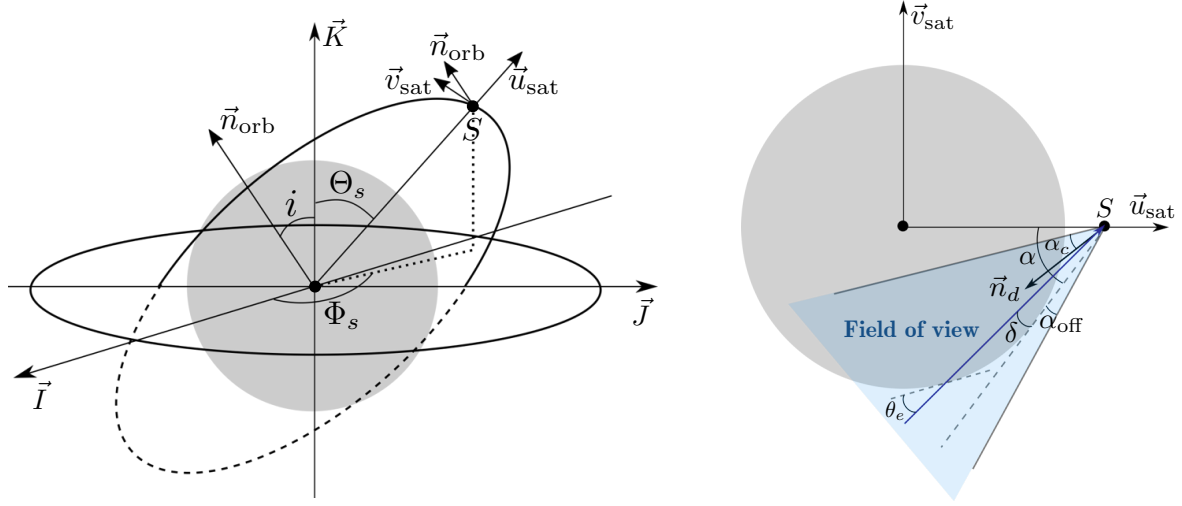


Figure 6.3: Orbital characteristics and notations (left) and illustration of the geometrical configuration in the orbital plane ($\vec{u}_{\text{sat}}, \vec{v}_{\text{sat}}$) (right). The satellite is located at point S . A neutrino arriving at the detector is characterized by its Earth emergence angle θ_e and the corresponding viewing angle δ from the satellite point of view. The detector has a conical FOV of opening angle α_c , with an offset angle α_{off} (away from the Earth limb) and pointing direction \vec{n}_d .

ing axis of the detector, is also illustrated in figure 6.3. The fraction of the Earth crossed by the tau neutrino and the subsequent tau lepton is characterized by its Earth emergence angle θ_e (where $\pi/2 - \theta_e$ is the local zenith angle), or the equivalent viewing angle $\delta = \arcsin[R_{\oplus}/(R_{\oplus} + h)] - \arcsin[R_{\oplus}/(R_{\oplus} + h) \sin(\pi/2 - \theta_e)]$. A comprehensive calculation of the propagation and interaction chain of the tau neutrino and the tau lepton can be found in Hall Reno et al. (2018) and Alvarez-Muniz (2018). As the produced Cherenkov signal is significantly beamed, it is detectable only if the arrival direction points toward the detector, within the FOV determined by the EAS Cherenkov angle, which is $\sim 1.4^\circ$ in air at standard temperature and pressure (STP). In the following, we consider the maximum emergence angle θ_e , above which the probability that a τ lepton escapes the Earth is very small, even considering regeneration effects Alvarez-Muniz (2018) and Hall Reno et al. (2018). Several estimates of the maximum emergence angles have been made for various neutrino energies. From Alvarez-Muniz (2018), $\theta_e = 5^\circ$ appears as a good approximation for $E_\nu = 10^{18}$ eV, as for larger angles the probability that the tau lepton exits the Earth drops. However, these results depend on various factors, for instance the composition of the materials the tau lepton traverses or the neutrino energy. As suggested by recent calculations, we can also consider larger emergence angles and, in the following, the values $\theta_e = 14.4^\circ$ and $\theta_e = 19.6^\circ$ (respectively $\delta = 4^\circ$ and $\delta = 7^\circ$) are also often used and corresponds to VHE tau neutrino energies down to ~ 10 PeV Hall Reno et al. (2018).

In order to determine, for a specific satellite orbital position, the portion of the sky detectable in neutrinos, subsequently called effective or geometrical FOV, we consider two conditions for tau neutrino detectability. The first condition is related to the physical properties of tau neutrino and tau lepton interactions, and thus involves the column depth of Earth crossed or the maximum emergence angle θ_e . The second condition is related to the characteristics of the detector, and thus concerns the arrival direction of the Cherenkov signal (and therefore the arrival direction of the tau neutrino), which should be within the FOV. Note that at VHE energies, the direction of the tau and neutrino are well aligned. We note that only this second condition should be adjusted in the case of a different detector design. The first condition is fulfilled if

$$\arcsin\left[\frac{R_{\oplus}}{R_{\oplus} + h} \sin(\pi/2 - \theta_e)\right] < \arccos(\vec{u} \cdot (-\vec{u}_{\text{sat}})) < \alpha \quad (6.1)$$

where $\alpha = \arcsin[R_{\oplus}/(R_{\oplus} + h)]$, h is the altitude of the satellite and R_{\oplus} the Earth radius. For

$h = 525 \text{ km}$, $\alpha = 67.5^\circ$. The angle between the source direction \vec{u} and nadir $-\vec{u}_{\text{sat}}$ is indeed constrained by the maximum emergence angle (lower bound) and the Earth limb (upper bound). For a conical FOV, the second condition is fulfilled if

$$\vec{u} \cdot \vec{n}_d > \cos \alpha_c, \quad (6.2)$$

where \vec{n}_d is the detector axis and $\alpha_c = \theta_{\text{FOV}}/2$ is the opening angle of the detection cone. In this case, the effective FOV is thus the intersection between a cone of opening angle α_c and a conical shell.

Simplified estimates of the sky exposure can be obtained by following the approach presented in Casadei (2005), which is valid only if the eccentricity of the orbit is zero, the orbit precession period is much larger than the orbital period, and the detector FOV is a cone whose axis lies in the orbital plane and rotates at the satellite orbital angular velocity. Whereas the first two points are in general valid, the last assumption is not true for all orbital configurations. Indeed, the detector is likely to point off orbit, for instance in order to achieve full-sky coverage or meet requirements concerning a specific observation mode (see for instance Sections 6.1.3 and 6.1.4). Alternatively, the effective FOV might not be a cone, and have a more complex structure due to detection constraints: for instance, the interaction of neutrinos with the Earth induces geometrical constraints on the arrival direction of the signal and thus on the detection. Therefore, for any orientation of the detector, we perform more realistic estimates of the portion of the sky available for VHE tau neutrino observation by integrating the exposure time over the observation time for a geometrically constrained FOV.

For a small satellite movement along its orbit, from Φ_s to $\Phi_s + \Delta\Phi_s$, the detector observes approximately the same portion of the sky (for instance the one observable at Φ_s) during the time of displacement $\Delta t_d(\Phi_s) = t_d(\Phi_s + \Delta\Phi_s) - t_d(\Phi_s)$. We consider the equatorial plane $(\vec{I}, \vec{J}, \vec{K})$ as the reference frame (see figure 6.3). The non-rotating orbital plane frame is $(\vec{i}_{\text{orb}}, \vec{j}_{\text{orb}}, \vec{n}_{\text{orb}})$. We focus on the case where $\vec{j}_{\text{orb}} = \vec{J}$, thus $\vec{i}_{\text{orb}} = \cos i \vec{I} - \sin i \vec{K}$ and $\vec{n}_{\text{orb}} = \sin i \vec{I} + \cos i \vec{K}$, where i is the inclination of the orbit. For a position S of the satellite, with an angle α_{sat} in the orbital plane, such as $\vec{u}_{\text{sat}} \equiv \cos \alpha_{\text{sat}} \vec{i}_{\text{orb}} + \sin \alpha_{\text{sat}} \vec{j}_{\text{orb}} = \sin \Theta_s \cos \Phi_s \vec{I} + \sin \Theta_s \sin \Phi_s \vec{J} + \cos \Theta_s \vec{K}$, and projecting on \vec{I}, \vec{J} and \vec{K} , we obtain:

$$\begin{aligned} \vec{u}_{\text{sat}} \cdot \vec{I} &= \cos \alpha_{\text{sat}} \cos i = \sin \Theta_s \cos \Phi_s, \\ \vec{u}_{\text{sat}} \cdot \vec{J} &= \sin \alpha_{\text{sat}} = \sin \Theta_s \sin \Phi_s, \\ \vec{u}_{\text{sat}} \cdot \vec{K} &= \cos \alpha_{\text{sat}} \sin i = \cos \Theta_s. \end{aligned}$$

If $\cos \Theta_s \neq 0$, we have $\alpha_{\text{sat}} = \arctan(\cos i \tan \Phi_s)$ and we obtain the time of displacement

$$\Delta t_d(\Phi_s) = \frac{1}{\omega} |\arctan[\cos i \tan(\Phi_s + \Delta\Phi_s)] - \arctan[\cos i \tan \Phi_s]| \quad (6.3)$$

where ω is the angular speed of the satellite. One needs also to consider some particular cases, for instance when $\cos \Phi_s = 0$ or $\sin \Phi_s = 0$. The above formula allows to calculate the exposure time for any observation time, as a function of the right ascension and the declination, or integrated over the celestial sphere.

6.1.2 Effective field of view and sky exposure estimates

In this section, we illustrate the method described above to calculate the effective FOV and the sky exposure, in the case of a conical FOV, using the characteristics of the POEMMA instrument. As a first step, we consider that the detector is pointing in the direction opposite to the moving direction, with the detector axis in the orbital plane. In the case of POEMMA,

we are only considering the FOV of one satellite as both satellites are in close proximity and observing in the same direction. The pointing direction is chosen such that the edge of the detection cone is above the limb of the Earth with an offset α_{off} , defined as positive when above the Earth limb, thus $\vec{n}_d = -[\cos(\alpha - \alpha_c + \alpha_{\text{off}}) \vec{u}_{\text{sat}} + \sin(\alpha - \alpha_c + \alpha_{\text{off}}) \vec{v}_{\text{sat}}]$. In the following, we calculate the solid angle on the celestial sphere Ω corresponding to the part of the sky observable in neutrinos, which allows to study the impact of several parameters, and to give an example of a focal surface specific to a POEMMA instrument.

Influence of emergence angle, offset angle and altitude

Several estimates of the solid angle Ω are shown in Table 6.1, for a given satellite position at two altitudes $h = 525$ km and $h = 1000$ km, for different emergence angles θ_e and offset angles α_{off} . We note that these estimates varies little along the orbit, thus the following estimates can be considered as typical values. As an example, for $\theta_e = 19.6^\circ$ and $\alpha_{\text{off}} = 2^\circ$, the solid angle varies along one orbit between $\Omega = 6.7 \times 10^{-2}$ sr and $\Omega = 7.1 \times 10^{-2}$ sr for $h = 525$ km, and between $\Omega = 4.9 \times 10^{-2}$ sr and $\Omega = 5.3 \times 10^{-2}$ sr for $h = 1000$ km. The observable fraction of sky projected on the celestial sphere (equatorial coordinates) is illustrated in figure 6.4 for a given satellite position at altitude $h = 525$ km, the emergence angles $\theta_e = 14.4^\circ$ and $\theta_e = 19.6^\circ$ and the offset angles $\alpha_{\text{off}} = 0^\circ$ and $\alpha_{\text{off}} = 2^\circ$. The projection on the Earth surface is also illustrated in figure 6.5 for a given satellite position at altitude $h = 525$ km, an emergence angle $\theta_e = 19.6^\circ$ and the offset angles $\alpha_{\text{off}} = 0^\circ$ and $\alpha_{\text{off}} = 2^\circ$.

	Ω [sr]		Ω [sr]	
	$h = 525$ km		$h = 1000$ km	
	$\alpha_{\text{off}} = 0^\circ$	$\alpha_{\text{off}} = 2^\circ$	$\alpha_{\text{off}} = 0^\circ$	$\alpha_{\text{off}} = 2^\circ$
$\theta_e = 5^\circ$	1.2×10^{-3}	3.4×10^{-3}	7.7×10^{-4}	2.5×10^{-3}
$\theta_e = 14.4^\circ$	2.4×10^{-2}	3.4×10^{-2}	1.6×10^{-2}	2.5×10^{-2}
$\theta_e = 19.6^\circ$	5.4×10^{-2}	6.7×10^{-2}	3.7×10^{-2}	5.0×10^{-2}

Table 6.1: Solid angles for different sets of emergence angles, offset angles and satellite altitudes.

We note that the blue region in figure 6.4 and figure 6.5 gets thicker: as expected, the observable fraction of the sky increases with increasing emergence angle. Similarly, the observable fraction of the sky increases with the FOV angle, which corresponds to an increase of the size of the red region in figure 6.4 and figure 6.5. We note that in figure 6.5, a large fraction of the red area, located outside the outer part of the blue region, lies below the limb, and is therefore not accessible to detection. The addition of an offset angle only influences the condition on the FOV, as can be seen in figure 6.4 and figure 6.5. The observable portion of the sky should increase by increasing the offset angle from 0 to approximately α_c and then decrease. Depending on the characteristics of the detector, such as the constraints on the focal surface, one can maximize the observable fraction of the sky by choosing the optimal offset angle (assuming a conical FOV).

The influence of the altitude is assessed by calculating the solid angle accessible for observation for one given satellite position. We consider two different altitudes $h = 525$ km and $h = 1000$ km as fiducial examples. The altitude of $h = 525$ km is taken as the lowest altitude that yields a stable orbit over a multi-year mission lifetime due to relatively insignificant atmospheric drag. As shown before, the observable portion of the sky depends on the FOV of the detector and on the maximum emergence angle. We draw comparisons at a fixed emergence angle as this quantity is directly related to the path of the neutrino and the tau lepton through the Earth.

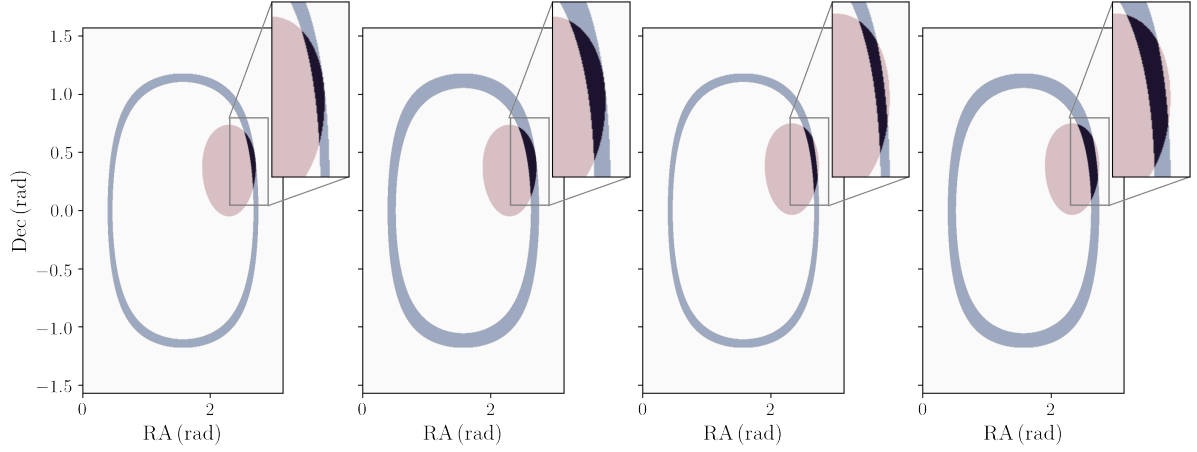


Figure 6.4: Observable portion of the sky as a function of right ascension (RA) and declination (Dec) for a given satellite position at altitude $h = 525$ km, with $\theta_e = 14.4^\circ$ and $\theta_e = 19.6^\circ$, for $\alpha_{\text{off}} = 0^\circ$, and $\alpha_{\text{off}} = 2^\circ$ (from left to right). The red ellipse is related to the condition on the FOV, the blue band to the condition on the emergence angle and the common fraction is shown in black.

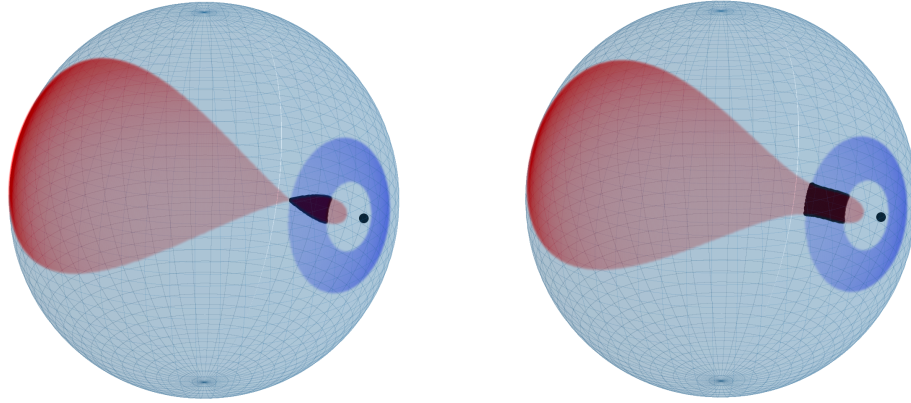


Figure 6.5: Effective FOV projected on the Earth surface, for one satellite position, $\theta_e = 19.6^\circ$ and $h = 525$ km, for $\alpha_{\text{off}} = 0^\circ$ (left) and $\alpha_{\text{off}} = 2^\circ$ (right). The red part is related to the condition on the FOV, the blue part to the condition on the emergence angle and the common area is shown in black.

We note that the viewing angle δ depends on the emergence angle θ_e and the altitude h , which is illustrated in figure 6.6.

For a fixed maximum Earth emergence angle, δ decreases with increasing altitude and as the “lateral” extension of the observable portion of the sky depends on δ , the solid angle accessible for observation actually decreases with increasing altitude. Some numerical estimates are illustrated in Table 6.1, for the various emergence angles, offset angles and altitudes considered in this paper. We also compare in figure 6.6 the observable fraction of the sky projected on the celestial sphere, for one satellite position, for two different altitudes $h = 525$ km and $h = 1000$ km, and for two different emergence angles $\theta_e = 14.4^\circ$ and $\theta_e = 19.6^\circ$. Interestingly, lower altitudes tend to increase the observable solid angle in the sky, for a fixed maximum Earth emergence angle. As shown in Alvarez-Muniz (2018) and Hall Reno et al. (2018), the probability of having a tau lepton escape the Earth for $E_\tau \gtrsim 10$ PeV becomes relatively small for $\theta_e \gtrsim 20^\circ$ assuming nominal values of the cosmogenic neutrino flux, such as those in Kotera et al. (2010). Note that for a fixed delta (viewing angle away from the Earth limb) the maximum Earth emergence angle increases with increasing altitude.

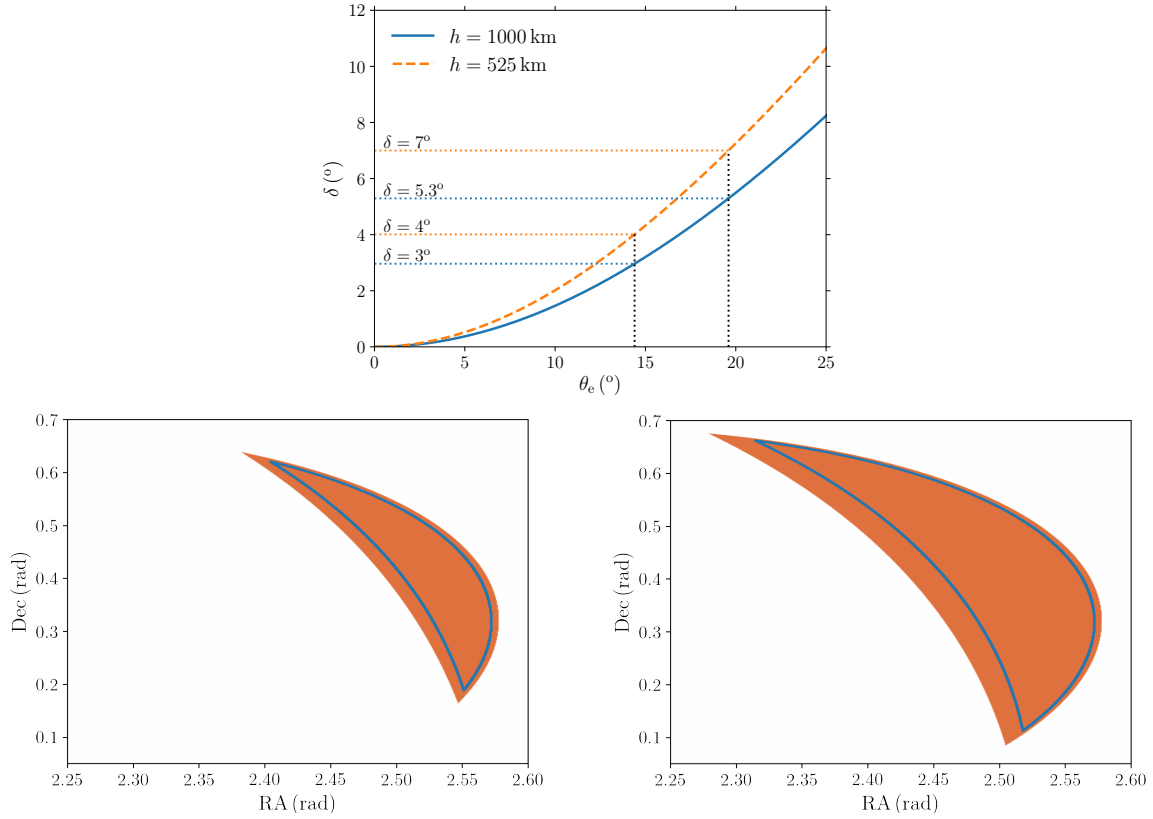


Figure 6.6: Top: viewing angle δ as a function of the emergence angle θ_e for two different altitudes. Bottom: observable portions of the sky for one satellite position and $\alpha_{\text{off}} = 0^\circ$, for two different emergence angles $\theta_e = 14.4^\circ$ (left) and $\theta_e = 19.6^\circ$ (right). The observable portion of the sky is the filled red area for $h = 525$ km and is delimited by the blue contour for $h = 1000$ km.

Accounting for the detection focal surface of the instrument

The calculations presented above are derived from purely geometrical considerations. However, more realistic estimates should account for the dead areas on the focal surface for actual configurations of the optical Cherenkov detection units, as they usually cover only a fraction of this surface. We illustrate this for the configuration adopted within the design of the POEMMA instrument (as shown in figure 6.2). In this case, only a limited part of the focal surface is dedicated to the detection of VHE neutrinos, while the remaining part is dedicated to the detection of UHECRs. The focal surface and the projection of the observable fraction of the geometrical FOV on the celestial sphere and on the Earth surface are illustrated in figure 6.7, for $h = 525$ km, $\theta_e = 19.6^\circ$ and $\alpha_{\text{off}} = 2^\circ$.

Due to the size of the detection units, only a fraction of the geometrical FOV can lead to efficient detections. Regarding the focal surface, because of the orientation of the detector towards the limb, the geometrical FOV overlays only an outlying part of the focal surface. The small uncovered area at the edge of the focal surface is related to the offset angle of the detector. We note that in this configuration, the main part of the two upper detection units will be dedicated to background measurements two degrees above the Earth limb. This effect is illustrated in the left panel of figure 6.7, but not on the right panel as this part of the focal surface is above the limb and thus cannot be projected on the Earth surface. On the one hand, concerning the projection on the Earth surface, we note that important distortions appear, due to projection effects of the relatively small θ_e , as very limited portions of the focal surface represent a significant area on the ground. Indeed, areas are strongly stretched close to the limb. The projection on the celestial sphere, on the other hand, does not lead to significant distortions.

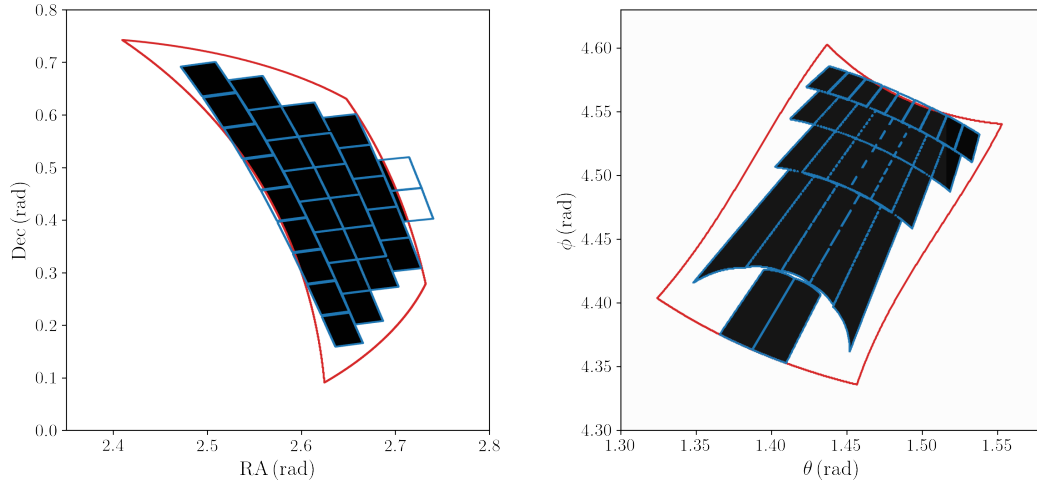


Figure 6.7: Projections of the effective FOV on the celestial sphere as a function of RA and Dec (left), and on the Earth surface as a function of the spherical coordinates (right), for $h = 525$ km, $\theta_e = 19.6^\circ$ and $\alpha_{\text{off}} = 2^\circ$. We compare the geometrical FOV (red), its observable fraction (black) and the delimitation of the edges of the Cherenkov detection units (blue).

For $h = 525$ km and $\alpha_{\text{off}} = 2^\circ$, we can compare the solid angle Ω obtained for the geometrical FOV and its observable fraction: for $\theta_e = 19.6^\circ$, $\Omega_{\text{obs}} = 4.9 \times 10^{-2}$ sr ($\Omega_{\text{obs}}/\Omega = 0.73$), and for $\theta_e = 14.4^\circ$, $\Omega_{\text{obs}} = 2.4 \times 10^{-2}$ sr ($\Omega_{\text{obs}}/\Omega = 0.71$).

Sky exposure

The sky coverage for one orbit is illustrated in figure 6.8. We compare the two geometrical estimates accounting or not for the configuration of the detection units on the focal surface specific to POEMMA. As outlined earlier, the significant change of solid angle coverage alone can lead to significant differences in exposure calculations. The fractional exposure is the total time during which the instrument can detect neutrinos coming from each bin of size $d \cos \Theta d\Phi$, divided by the orbital period. As expected, the lateral extension of the effective FOV appears to be critical in the calculation and a fractional exposure is a bit reduced by accounting for the effect of the finite size of the active area of the Cherenkov detection units in the focal plane. The total exposure during one orbit can be calculated by integrating $t(\Theta, \Phi)$ over the celestial sphere

$$t_{\text{orb}} = \frac{1}{4\pi} \int \int d \cos \Theta d\Phi t(\Theta, \Phi). \quad (6.4)$$

As an example, for $h = 525$ km, $\theta_e = 19.6^\circ$ and $\alpha_{\text{off}} = 2^\circ$ we obtain the following exposure times for one orbit: $t_{\text{orb}} \simeq 31$ s and $t_{\text{orb}} \simeq 23$ s for the geometrical estimate and the realistic estimate including the effect of the detection units. We recall that for $h = 525$ km, the period is $P \simeq 5.7 \times 10^3$ s.

In our calculation we have assumed a fixed orientation of the detector, in the orbital plane and in a direction opposite to the direction of motion. This results in a limited sky coverage as a function of the declination. Indeed, during the observation time allowed by the mission, the precession around the north pole induces a shift of the sky coverage along the right ascension axis, but the declination range remains unchanged. In the next section, we show that the homogeneity of the sky coverage can be significantly increased by rotating the viewing direction out of the orbital plane.

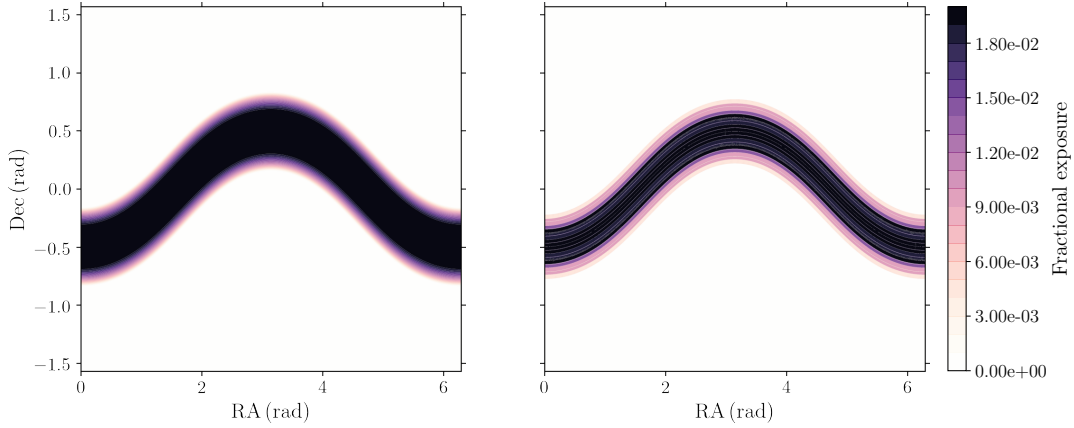


Figure 6.8: Fractional exposure t/P for $i = 28.5^\circ$, $\theta_e = 19.6^\circ$ and $h = 525$ km as a function of right ascension (RA) and declination (Dec), for a detector axis in the orbital plane. Comparison between the geometrical estimates when accounting or not for the effect of the detection units for the POEMMA configuration (respectively right and left panels).

6.1.3 Strategy to achieve full sky coverage

For a fixed orientation of the detector in the orbital frame, only an incomplete portion of the sky can be observed. The minimum and maximum values of declination accessible to observation do not depend on the precession angle of the orbit j , by spherical symmetry – as the orbit precesses around the north pole – but they depend on the orbit inclination i , as illustrated in figure 6.9. For simplicity, we only calculate the minimum and maximum values of declination accessible to observation in the direction of the detector axis, without accounting for the width of the field of view. Accounting for the width of the field of view would only increase the accessible declination range.

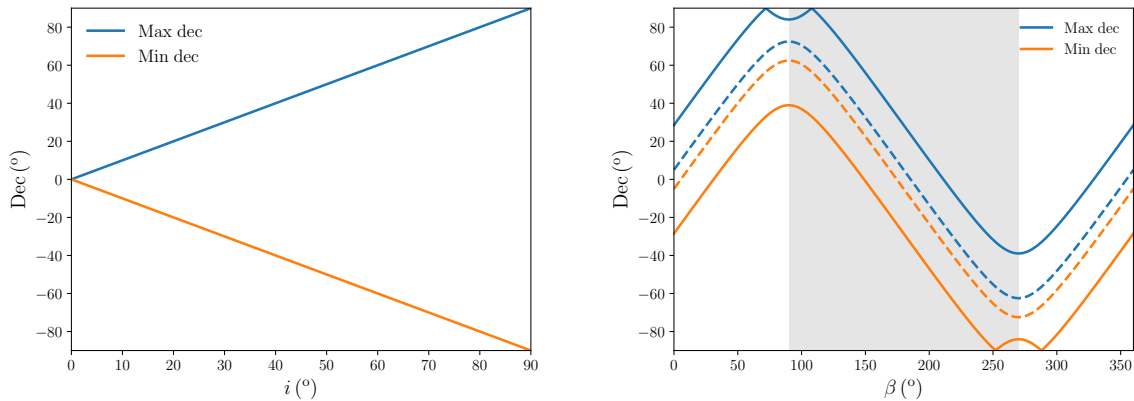


Figure 6.9: Maximum and minimum values of declination which can be observed in the direction of the detector axis (respectively blue and orange lines) for an altitude $h = 525$ km, as a function of the orbit inclination i (left) for $\beta = 0^\circ$, and as a function of the detector inclination β (right) for $i = 28.5^\circ$ (solid) and $i = 5^\circ$ (dashed). The shaded area corresponds to detector inclinations that are disfavored due to being in the ram direction (see text).

The different detector orientations are characterized by the angle β :

$$\vec{n}_d = -[\cos(\alpha - \alpha_c + \alpha_{\text{off}})\vec{v}_{\text{sat}} + \sin(\alpha - \alpha_c + \alpha_{\text{off}})\cos(\beta)\vec{v}_{\text{sat}} + \sin(\alpha - \alpha_c + \alpha_{\text{off}})\sin(\beta)\vec{n}_{\text{orb}}]. \quad (6.5)$$

If $\beta = 0$, the detector axis is in the orbital plane, in an opposite direction to the direction

of motion. Angles around $\beta = \pi$ are not suitable if degradation of the optics from atomic oxygen is an issue. We calculate the minimum and maximum values of declination that can be observed during one orbit. To simplify the calculations, we consider that the detector is only pointing towards the limb. Moreover, we consider an orbit with $\vec{n}_{\text{orb}} = \sin i \cos j \vec{I} + \sin i \sin j \vec{J} + \cos i \vec{K}$ such as $j = 0$. We see in figure 6.9 that the detector inclination, as well as the orbit inclination, have a strong influence on the portion of the sky available for observation. For the study presented here, we make the conservative assumption that the detector axis should not be oriented towards the ram direction. For $i = 5^\circ$, the minimum and maximum declination accessible remain respectively above $-\pi/2$ and below $\pi/2$. For $i = 28.5^\circ$, the values of $-\pi/2$ and $\pi/2$ can be reached for acceptable values of β – following our notations, the values between $\pi/2$ and $3\pi/2$ are excluded. We could therefore consider a detector axis oscillation during one orbit, characterized by a variation of the angle β as a function of the right ascension of the satellite Φ_s , allowing to cover the full declination range, and avoiding values around $\beta = \pi$. This strategy is illustrated in figure 6.10 for one orbit. One can also choose to rotate the detector axis over longer time scales, for instance at the end of a predefined set of orbits.

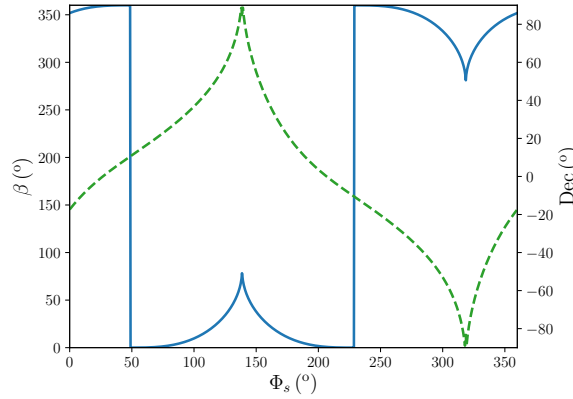


Figure 6.10: Example of detector axis rotation during one orbit, characterized by the angle β as a function of Φ_s (blue, solid) and the corresponding observable values of declination (Dec) as a function of Φ_s (green, dashed).

Using such a strategy, with an oscillation of the detector axis during one orbit, we can calculate the sky coverage for different observation times, as illustrated in figure 6.11 for 380 days of observation, which corresponds to seven precession periods of the satellite orbit $T_{\text{obs}} = 7 \times 2\pi/\omega_p$. In this calculation we consider the geometrical detector layout of POEMMA, but we do not account for the detection units as shown in figure 6.8. We compare the maximum sky exposure, which does not account for the impact of the Sun and the Moon in the calculation, with the exposures obtained when accounting for the impact of the Sun and the Moon. No observation can be performed if the satellite is illuminated by the Sun and if the illumination of the Earth by the Moon is too high. The Moon illumination is given by $p_{\text{moon}}/100 = (1 + \cos \phi)/2$, where ϕ is the phase angle of the Moon. We consider a maximum illumination of the Moon of 50% in our calculations. We find that the Sun and the Moon have a strong impact on the sky exposure, especially on its RA dependence. The link between the precession periods of the satellite, the Sun and the Moon leads to the emergence of ‘hot’ and ‘cold spots’ in the sky exposure map. The exposure becomes more uniform for longer observation times. We note that our strategy allows us to obtain a uniform exposure only if the Sun and the Moon are not taken into account. In order to obtain a more uniform sky exposure, the rotation of the detector axis should be optimized by taking into account the orbits of the Sun and the Moon.

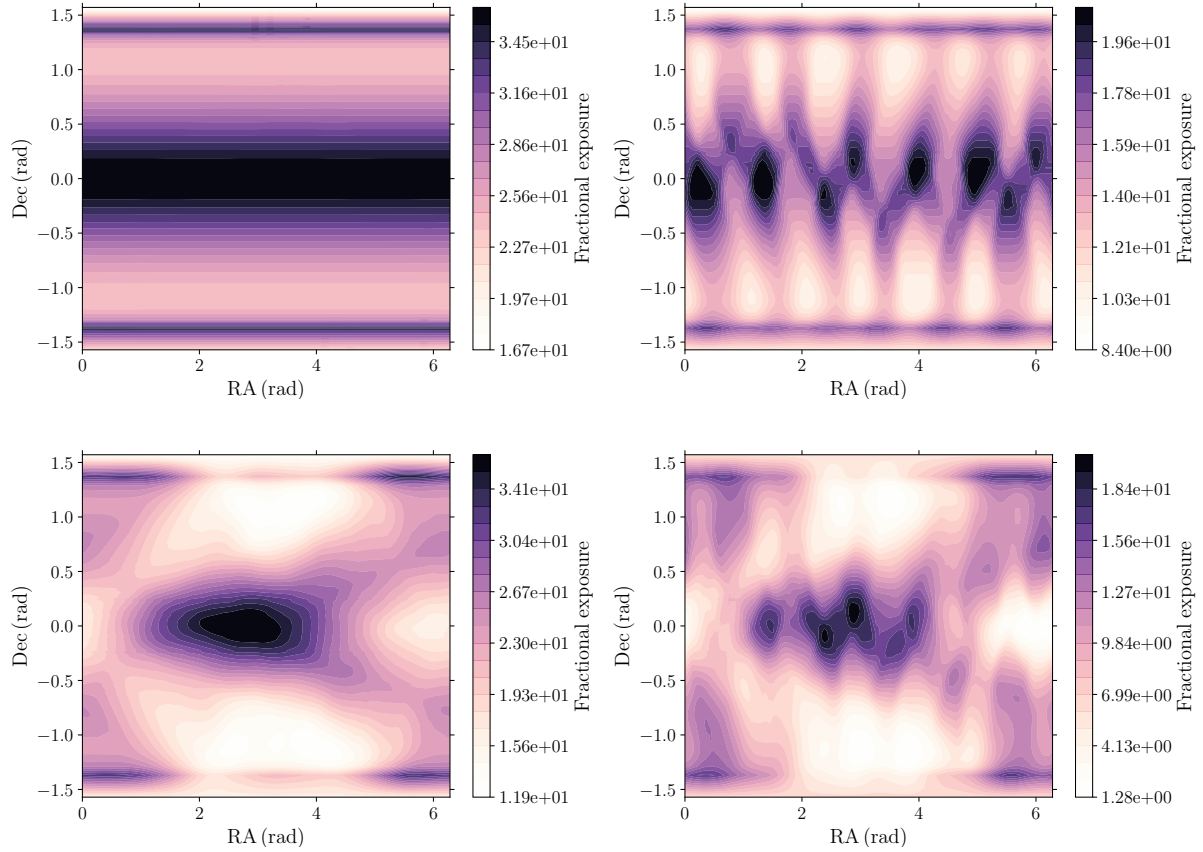


Figure 6.11: Fractional exposure t/P for $i = 28.5^\circ$, $h = 525$ km and $\theta_e = 19.6^\circ$ as a function of right ascension (RA) and declination (Dec), for 380 days of observation ($7 \times 2\pi/\omega_p$), with an optimized rotation of the detector axis during one orbit, for the detector layout of POEMMA. We compare the exposures obtained without the impact of the Sun and the Moon (upper left), with the impact of the Sun (upper right), with the impact of the Moon (lower left) and with the impact of the Sun and the Moon (lower right).

6.1.4 Target of opportunity follow-up

In the case of an external alert of an interesting transient event, for instance following a localized gravitational wave detection, the neutrino space detector could enter a specific ToO observation mode, designed to maximize its exposure to a given region in the sky. In this section we do not focus on a specific instrument, as we only use the condition of the emergence angle (see equation 6.1) in order to evaluate the observable portion of the sky during one orbit. Indeed, in the case of the POEMMA instrument, the rotation of the detector axis changes the orientation of the FOV, and the observable portion of the sky corresponds to the blue band, see figure 6.12, which is related to the condition on the emergence angle. As the detector axis should not be oriented towards the direction of motion, only half of this blue region is accessible to observation. By adding the exposures related to the only accessible region, we simply calculate the maximum fractional exposure that we can obtain for every direction in the sky, which is illustrated in figure 6.12.

We note that even if the entire declination range was accessible during one orbit (see section 6.1.3), it would not be accessible at each satellite position: in figure 6.12 (left) we see that the condition on the emergence angle (blue band) gives minimum and maximum values of the declination accessible for observation, with a declination range of $2\alpha < \pi$ which depends on the satellite altitude. Therefore, during one orbit, some regions of the sky cannot be observed: two

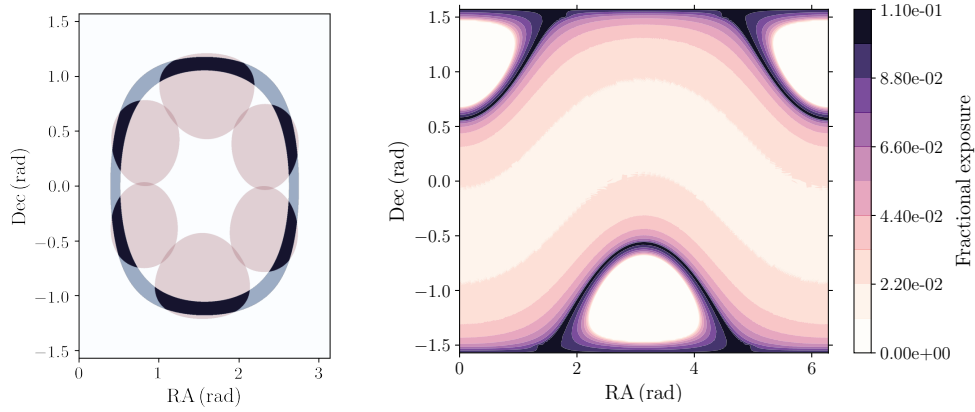


Figure 6.12: Left: observable portion of the sky using six non-overlapping detector orientations, as a function of right ascension and declination, for $i = 28.5^\circ$, $h = 525$ km, $\theta_e = 19.6^\circ$ and $\alpha_{\text{off}} = 2^\circ$. The blue band is related to the condition on the emergence angle, the red region to the condition on the FOV and the black regions to their intersection. Right: maximum fractional exposure for every direction of the sky, as a function of right ascension and declination.

blind spots appear at high declinations. For $i = 28.5^\circ$, $h = 525$ km, $\theta_e = 19.6^\circ$ and $\alpha_{\text{off}} = 2^\circ$, about $P_{\text{obs}} = 91\%$ of the sky is available for observation during one orbit, given

$$P_{\text{obs}} = \frac{1}{4\pi} \iint_{t(\Theta, \Phi) > 0} d\cos\Theta d\Phi, \quad (6.6)$$

where $t(\Theta, \Phi)$ is the exposure time for any direction of the sky. As the orbit precesses slowly, with a precession period of about 54 days for $i = 28.5^\circ$ and $h = 525$ km, some regions of the sky will not be accessible for short duration transient phenomena.

As emphasized previously, the Sun and the Moon illuminations have a strong impact on the observations and cannot be neglected. During about half of the orbit, the satellite is illuminated by the Sun, and thus about 49% of the sky is available for observation during one orbit, for the parameters given above. The regions of the sky occulted by the Sun will remain inaccessible for up to half a year. The ability to carry out timely follow-up observations of a ToO will be extremely dependent on its relative position with respect to the Sun. The Moon illumination varies throughout the lunar cycle. If the illumination is too high, observations can only be performed when the Sun and the Moon are hidden by the Earth. The observable portion of the sky during one orbit is illustrated in figure 6.13 for several dates, and thus various Moon illuminations. For illustration purposes, we consider that observations can be performed for a Moon illumination below 50%. We see that the observable portion of the sky can be strongly reduced during the periods of highest illumination.

We should add that our calculation does not take into account considerations related to the cloud coverage, which could hinder further the ability of an optical instrument, such as POEMMA, to search for VHE tau neutrinos from a flaring source for example, unless one considers that useful Cherenkov signal is produced in cloud-free regions or above the cloud height.

6.1.5 Conclusion

In this paper we show that space-based experiments that use the optical Cherenkov signal from tau-induced EASs from VHE Earth-skimming tau neutrinos can achieve full sky coverage assuming at least a year observation time, using POEMMA as an example. These results

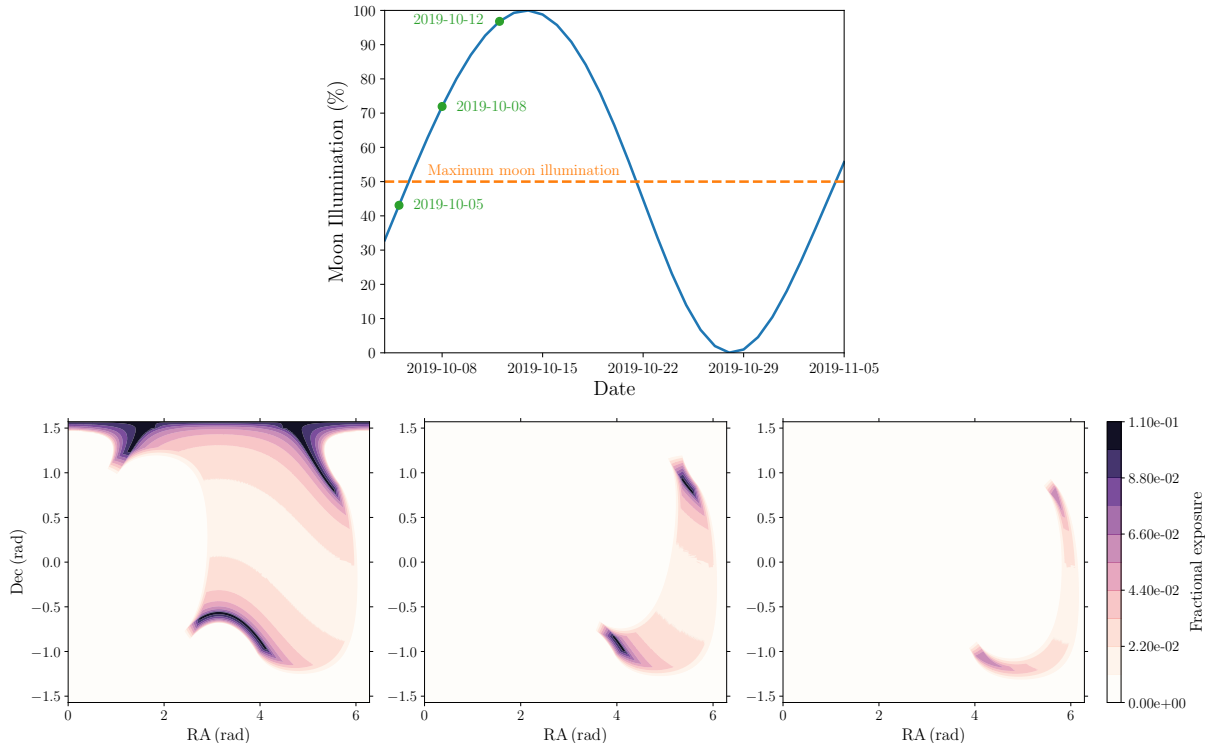


Figure 6.13: Top: Moon illumination during one lunar cycle (blue line), fiducial maximum Moon illumination (orange dashed line) and three dates used as examples (green points). Bottom: maximum fractional exposure for every direction of the sky, as a function of right ascension and declination, for the three dates (left: 2019-10-5, middle: 2019-10-8, right: 2019-10-12), including the impact of the Sun and the Moon.

highlight one benefit of space-based observations versus ground-based observations at a fixed geographic location. Our result is based on geometrical calculations of the FOV that also details the dependence of the sky exposure and sky coverage for various configurations, including different assumptions of the satellite altitude, maximum Earth emergence angle of the tau lepton, offset angle when viewing the Earth limb, orientation of the director axis relative to the orbit trajectory, and constraints imposed by the finite active area of photo-detectors in the focal plane of the Cherenkov telescope. Calculations of the Earth emerging tau lepton spectrum induced from tau neutrino interactions in the Earth Alvarez-Muniz (2018) and Hall Reno et al. (2018) show that for a given tau energy threshold, the tau flux becomes significantly reduced at a specific Earth emergence angle, thus effectively setting a maximum useful Earth emergence angle. Once this is fixed, our calculations show, perhaps counter-intuitively, that the sky exposure decreases for an increasing satellite altitude. This is due to the satellite viewing angle away from the horizon decreasing as the altitude increases when the maximum Earth emergence angle is fixed.

Without accounting for the impact of the Sun, for a maximum emergence angle $\theta_e = 19.6^\circ$ and a detector offset angle $\alpha_{\text{off}} = 2^\circ$ above the Earth limb, about 91% of the sky is available for observation during one orbit for a satellite altitude of $h = 525$ km against 87% for $h = 1000$ km. With the impact of the Sun, we obtain 49% for $h = 525$ km and 45% for $h = 1000$ km for one orbit. A lower altitude increased therefore the sky coverage and could also be advantageous for photon collection. As expected, the maximum Earth emergence angle strongly affects the exposure, and as this maximum angle depends on the incoming neutrino spectrum, one should observe a distribution in energy as a function of the emergence angle that in turn influences the sensitivity of the instrument.

The rotation of the detector axis during the observation time is critical in order to cover the entire declination range and thus to achieve full sky coverage. It should be noted that the POEMMA satellites can slew 90 degrees within several minutes. By rotating the detector axis during one orbit or over longer time scales, one can scan the entire declination range for $h = 525$ km, but the highest declinations cannot be reached for $h = 1000$ km. Without accounting for the impact of the Sun and the Moon and with an appropriate detector orientation change strategy, about one precession period is therefore needed to achieve full sky coverage. However, if we account for the presence of the Sun, some regions of the sky are simply not available for observations for up to six months. Follow-up Target-of-Opportunity observations of a transient source are therefore strongly constrained by its relative position with respect to the Sun. This is a limitation of using the optical Cherenkov from tau-induced EAS. It should be noted that measuring the radio emission from upward-moving EAS would not have the solar or lunar constraints that are required for optical Cherenkov EAS measurements, although radio detection from space presents its own set of unique challenges.

6.2 Towards radio detection with a gigantic ground array

The detection of very high-energy astroparticles by gigantic radio arrays is almost as challenging as their detection from space. As stated before, the interaction of very energetic astroparticles –such as UHECR, gamma rays or VHE neutrinos– with the atmosphere and/or the Earth initiate large particle showers in the atmosphere. Their propagation through the geomagnetic field induces a radio emission that experiences little attenuation in the atmosphere, and can therefore be detected at a large distance from the shower. Two effects contribute to the radio emission of particle showers on Earth. First, positive and negative charges are separated by the geomagnetic field, and the induced time-varying electric current produces the geomagnetic radio emission (Kahn et al., 1966). Second, an excess of negative charges due to Compton scattering also induces a radio emission, known as the Askaryan effect (Askar’yan, 1962; Askar’yan, 1965). In the atmosphere, the geomagnetic effect dominates whereas in dense media such as ice, the Askaryan effect dominates. These two emission mechanisms are illustrated in figure 6.14.

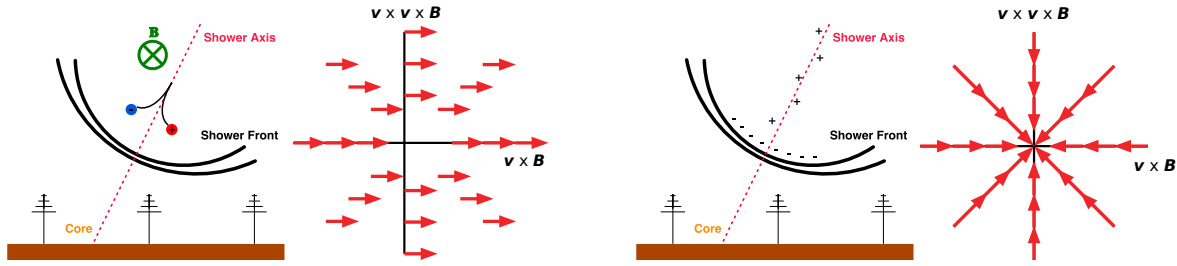


Figure 6.14: Illustration of the geomagnetic (left) and charge excess (right) radiation mechanisms. The arrows show the direction of linear polarization in the plane perpendicular to the shower axis. From Schoorlemmer (2012) and de Vries et al. (2012).

The future experiment GRAND (GRAND Collaboration et al., 2018), on which we focus in this section, will autonomously detect the radio emission produced by very energetic astroparticles with a giant radio array. GRAND will focus on the detection of inclined air showers. Due to the large footprint of the signal on the ground (a few kilometers for a zenith angle of 80°), a sparse array can be used for detection. The detection principle of VHE neutrinos, UHECR and gamma rays is illustrated in figure 6.15. UHECR and gamma rays interact with the atmosphere and produce an air shower. Tau neutrinos, for their part, interact with the Earth crust (a mountain for instance) and produce a tau particle, that induces an air shower provided that it decays in the atmosphere. Only tau neutrinos are considered in this case as the decay lengths of muons and electrons produced by muon and electron neutrinos are inadequate to induce detectable air showers.

The final stage of the detector will be modular, with 20 separate arrays composed of 10 000 radio antennas deployed over $10\,000\text{ km}^2$. The development of the GRAND project is ongoing, and the deployment of a 300 antenna stage deployed over 300 km^2 is scheduled to 2019-2020. GRANDProto300, that will act as a pathfinder for the later stages of GRAND, will essentially focus on testing the feasibility of autonomous radio detection of horizontal showers initiated by cosmic rays between $10^{16.5-18}\text{ eV}$, and will be complemented with an array of particle detectors optimized for the detection of inclined showers, making it a unique instrument to explore the mysterious energy range where a transition between the Galactic and extragalactic cosmic ray components should happen. Thanks to the drastic advances in radio technology and in our understanding of the radio emission processes in the recent years, the prospects are promising regarding the autonomous radio detection of very energetic astroparticles. This first stage of the project could already lead to important discoveries related to the development of inclined

air showers, which have not yet been studied in detail by the astroparticle physics community. Moreover, we emphasize that a large variety of topics will be studied with GRAND, related to VHE neutrinos (GZK or source neutrinos, neutrino physics), UHECR and gamma-ray astronomy, but also to fast radio bursts, giant radio pulses and the epoch of reionization.

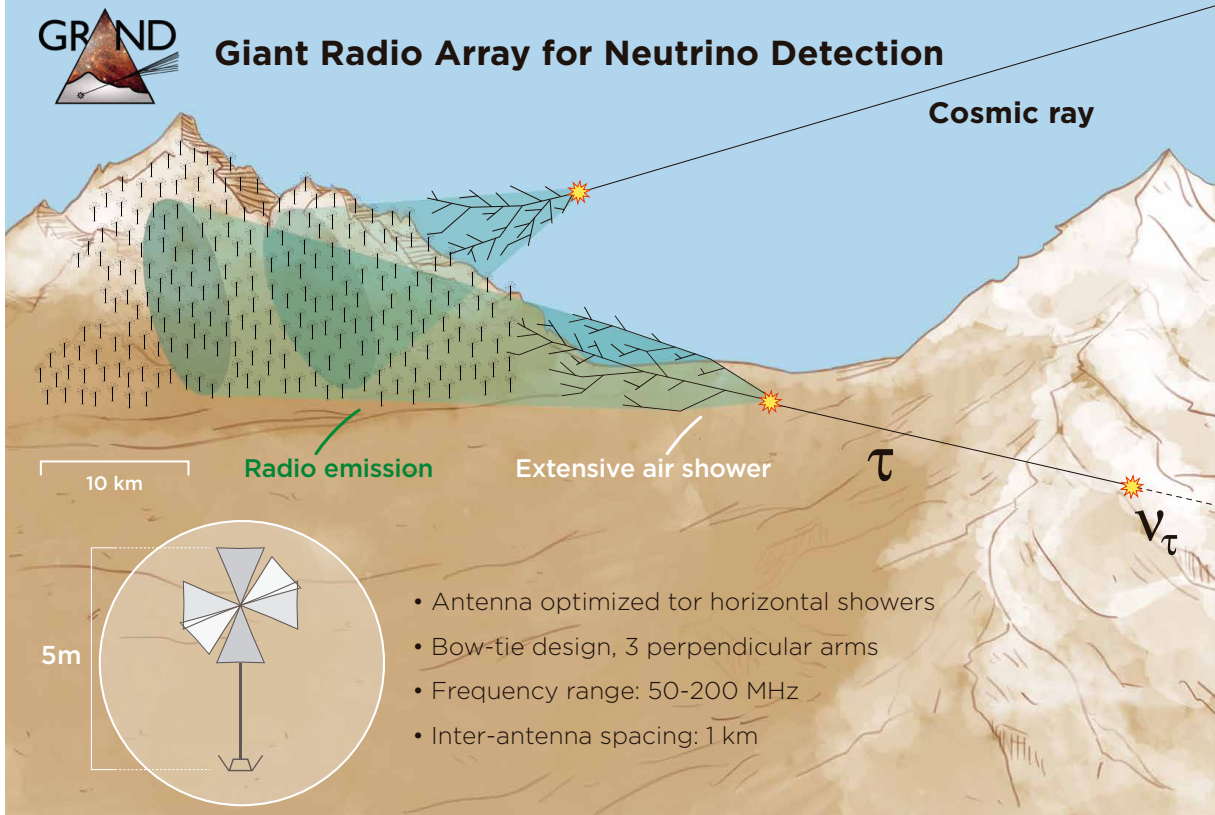


Figure 6.15: Detection of VHE neutrinos, UHECR and gamma rays with a gigantic radio array. See text for more detail on the detection principle. From (GRAND Collaboration et al., 2018).

In particular, the detection of UHECR will help to constrain their properties (elementary composition and spectrum) at the highest energies. In this work, we focus on the reconstruction of the elementary composition of UHECR. Their elementary composition is encoded in the atmospheric depth X_{\max} of the maximum development of the atmospheric air shower that they initiate when they interact with the Earth atmosphere. The X_{\max} reconstruction is purely based on a statistical approach. We note that an uncertainty below 40 g/cm^2 is required to make the distinction between cosmic-ray, gamma-ray and neutrino primaries, whereas an uncertainty below 20 g/cm^2 is required to distinguish between proton and iron primaries, on a single-event base. Inspired from the top-down method from Buitink et al. (2014), we use the information encoded in the radio footprint of proton and iron induced air-showers simulated with the air-shower and radio emission code ZHAireS (Alvarez-Muñiz et al., 2012) to reconstruct their X_{\max} values (GRAND Collaboration et al., 2018).

In this preliminary study, we consider that the only unknown is the nature of the primary particle, assuming that the shower inclination and the primary energy have been reconstructed with perfect accuracy. The topography is also idealized, as we consider that antennas are located exactly in the same plane, which can be inclined from the horizontal to mimic the effect of a mountain slope. Therefore, we can assess the influence of the shower inclination, the primary energy, the mountain slope and the spacing between the antennas, on the reconstruction of the nature of the primary particle.

6.2.1 The X_{\max} reconstruction procedure

Simulation sets of 50 proton-initiated and 20 iron-initiated showers are generated with identical energy and arrival direction. In these simulations, the radio signal induced by the air shower is recorded by 160 antenna (perfect dipoles) which form a star shape pattern in the $\mathbf{v} \times \mathbf{B} - \mathbf{v} \times \mathbf{v} \times \mathbf{B}$ plane, where \mathbf{v} is the direction of particles and \mathbf{B} is the geomagnetic field (vectorial quantities). For one set of parameters, one test shower among the simulated events is chosen. The footprint of the test shower on the realistic array is compared to the footprint of all the other simulated showers with a least-squares fit, to obtain the best-fit value of X_{\max} for the test shower. This procedure is repeated for all the showers of the simulation set, which enables to evaluate the efficiency of X_{\max} reconstruction, by studying the distribution of the differences between the simulated and reconstructed X_{\max} values, respectively $X_{\max,s}$ and $X_{\max,r}$.

We illustrate the X_{\max} reconstruction procedure on one test shower. Our benchmark example illustrates the case of proton and iron progenitors with energy 10^{19} eV, zenith and azimuth angles of 83° and 40° , mountain slope of 10° and distance between the antenna of 500 m.

The first step consists in applying an antenna model to the simulation outputs, which are electric field traces that correspond to the idealized response of a perfect dipole in the three polarization directions. However, the antenna developed for the GRAND project have a response adapted to the detection of very inclined air showers, with a high detection efficiency along the horizon. The signal detected by the antenna is then filtered in the frequency range chosen by the experiment. We note that in most of the existing arrays, the frequency range is 30 to 80 MHz, and that the Cherenkov ring features appear at higher frequencies. Indeed, due to relativistic time compression, signals add coherently and a ring of amplified emission starts to dominate the emission pattern for frequencies above ~ 100 MHz (de Vries et al., 2011). As Cherenkov rings are very interesting features which could help background rejection and signal reconstruction (e.g. Nelles et al., 2015), the frequency range of the GRAND experiment is 50 to 200 MHz. The signal is also sampled with a sample time of 2 ns. Gaussian noise is randomly added with a root mean square of $15 \mu\text{V}$ in the frequency band 50 to 200 MHz, which corresponds to a low level of noise than could be reached in radio quiet areas. Only antennas with a peak-to-peak voltage higher than $30 \mu\text{V}$ are considered to trigger, and subsequently considered for the analysis (GRAND Collaboration et al., 2018). We illustrate in figure 6.16 the signal detected by one antenna for two different energies of the progenitor. We see that the progenitor energy has a strong impact of the signal amplitude. Therefore noise will strongly limit the detection efficiency at low energies. In particular, the detection of very inclined air showers generated by progenitors with energies below 10^{17} eV with a sparse array is very challenging. Denser sub-arrays could help to access energies below 10^{17} eV, with the detection of less-inclined air showers. This possibility is considered for the experiment GRANDproto300, for which two sub-arrays with antenna spacing of 500 m and 250 m will be encapsulated in a sparser antenna array with a spacing of 1000 m.

In the analysis, the total voltage squared integrated over time is used as a basis to compare the response of the different antennas. In the following we call abusively this quantity power, for simplicity. This quantity is interpolated in the $\mathbf{v} \times \mathbf{B} - \mathbf{v} \times \mathbf{v} \times \mathbf{B}$ plane, to calculate the response of the antennas in the realistic array. Indeed, we consider a squared pattern for the antenna array, and not a star shape pattern. Thus, the realistic array is rotated in shower coordinates and the interpolation allows to obtain the response of each antenna. We note that the interpolation from a star shape pattern can induce some aberrations. We illustrate in figure 6.17 the normalized interpolated power in the $\mathbf{v} \times \mathbf{B} - \mathbf{v} \times \mathbf{v} \times \mathbf{B}$ plane, with the star shape pattern superimposed, and projected on the ground. This latter figure shows the very large extend on the radio footprint on the ground for an inclined air shower, which extends over more than four kilometers. We note that for vertical showers, the extend of the footprint is of the order of only a few hundred

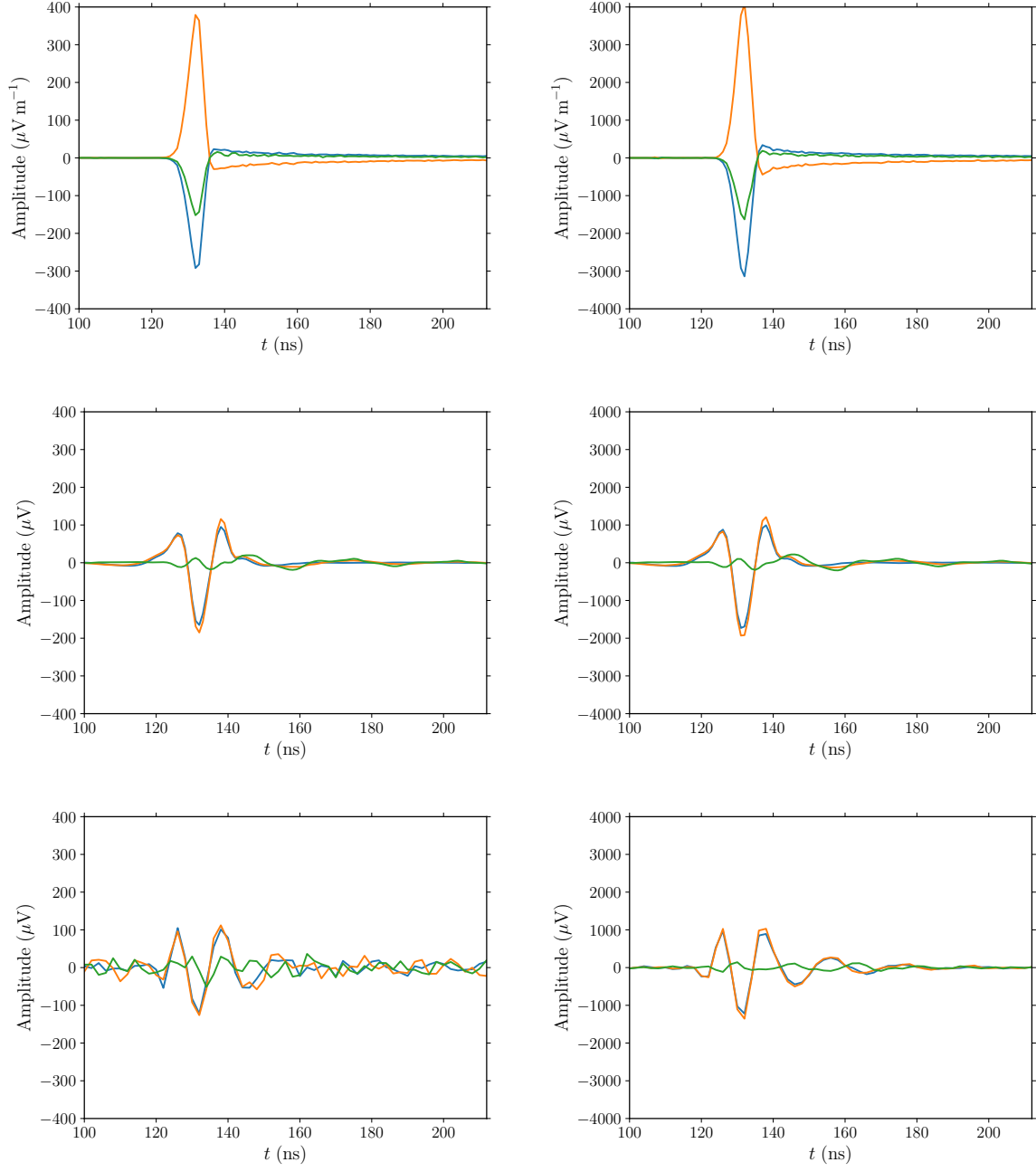


Figure 6.16: Signal detected by one given antenna at the center of the footprint, as a function of time in the three polarization directions, for an idealized dipole antenna (top), by applying the response of the antenna designed for GRAND (middle), and by filtering, sampling and adding noise to the signal (bottom). We compare the cases of a proton progenitor with energy 10^{18} eV (left) and 10^{19} eV (right). The blue, orange and green lines correspond respectively to the north-south, east-west and vertical components of the signal.

meters (Huege, 2016).

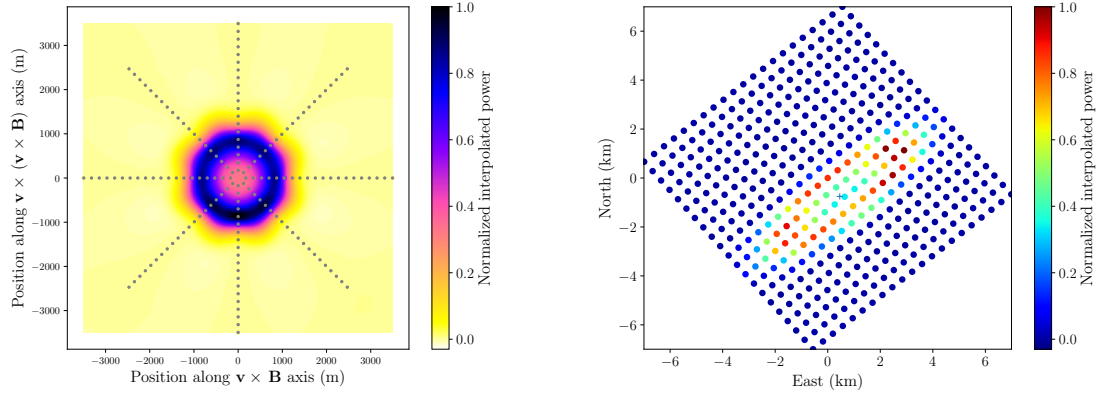


Figure 6.17: For one shower, normalized interpolated power in the $v \times B - v \times v \times B$ plane with the star shape pattern superimposed (left) and projected on the ground on the antenna array (right).

After these first steps, the X_{\max} reconstruction itself is performed by using a least squares method. From a general perspective, the maximization of the likelihood (Bevington and Robinson, 2003)

$$P(a_j) = \prod \left[\frac{1}{\sigma_i \sqrt{2\pi}} \right] \exp \left\{ -\frac{1}{2} \sum \left[\frac{y_i - y(x_i)}{\sigma_i} \right]^2 \right\}, \quad (6.7)$$

with respect to the parameters (a_j) corresponds to the minimization of $\chi^2 = \sum [y_i - y(x_i)]^2 / \sigma_i^2$ with respect to each parameter, and allows to find the optimum values of the parameters (a_j). In our case, for each test shower (the fake data) chosen among the simulated showers, the core of the shower is randomly shifted, and the two-dimensional radiation map is then fitted by minimizing (Buitink et al., 2014)

$$\chi^2 = \sum_{\text{antennas}} \left[\frac{P_{\text{ant}} - f P_{\text{sim}}(x_{\text{ant}} - x_0, y_{\text{ant}} - y_0)}{\sigma_{\text{ant}}} \right]^2, \quad (6.8)$$

where P_{ant} is the power of the antenna located at $(x_{\text{ant}}, y_{\text{ant}})$ for the fake data, σ_{ant} is the noise level and P_{sim} is the power of the antenna for the other simulated showers. Three parameters are included in the fit: the position of the shower axis (x_0, y_0) and a scaling parameter f for the radio power. Only antennas that have triggered are included in the fit. The χ^2 value (which is divided by the number of degrees of freedom of the least-squares fit) is then used to reconstruct the atmospheric depth of the shower maximum X_{\max} , as this quantity has a strong impact on the radiation profile. However, X_{\max} is not the only shower parameter that influence the radiation profile, and shower-to-shower fluctuations induce other variations in the shower development.

In order to reconstruct the X_{\max} value, the χ^2 data are fitted by a parabola in the $X_{\max} - \chi^2$ plane. The minimum is taken to be the reconstructed X_{\max} value (see e.g. Buitink et al., 2014). Indeed, for a large event sample, as the likelihood becomes a Gaussian of each parameter centred on the (a'_j) minimizing χ^2 , such that $P(a_j) \propto \exp[-(a_j - a'_j)^2 / 2\sigma_j^2]$, we can write $\chi^2 = (a_j - a'_j)^2 / \sigma_j^2 + C$ where C is a constant (Bevington and Robinson, 2003). The χ^2 variation in a vicinity of a minimum corresponds thus to a parabola. In order to improve the parabola fitting, we also separate the X_{\max} range in several bins and only select for the fit the χ^2 values between $\min(\chi^2)$ and $\min(\chi^2) + \text{std}(\chi^2)$, where $\min(\chi^2)$ and $\text{std}(\chi^2)$ are respectively the minimum and the standard deviation of the χ^2 in the X_{\max} range. Another fitting procedure has been tested for which a parabola is fitted to the edge of the χ^2 “cloud”. This last procedure

improves the accuracy of the reconstruction but should be examined in more detail, in particular to ensure that it does not introduce a statistical bias.

Two examples of parabola fitting are shown in figure 6.18 for a test shower initiated by a proton and an iron nucleus. We note that in the $X_{\max} - \chi^2$ plane, points are highly scattered around the parabolic shape, which makes the fitting procedure difficult. As emphasized in Carvalho and Alvarez-Muñiz (2019), the uncertainty on X_{\max} reconstruction should increase with shower inclination, mostly because of a more symmetric radiation pattern on the ground. This is due to the fact that for very inclined showers, the shower develops higher in the atmosphere, and because of the lower air density, the geomagnetic emission contribution is enhanced with respect to the Askaryan emission.

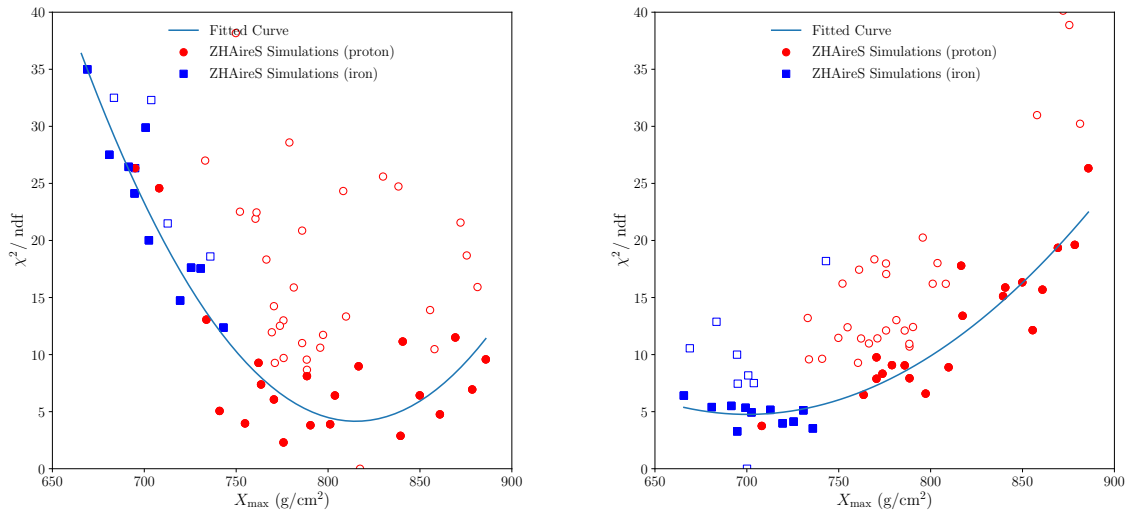


Figure 6.18: Two examples of parabola fitting in the $X_{\max} - \chi^2$ plane, for proton (left) and iron (right) progenitors. The red circles correspond to simulations with proton progenitors and the blue squares simulations with iron progenitors. Only the filled symbols are considered for the fitting procedure, and the resulting curve is shown in blue.

The last step consists on studying the distribution of $X_{\max,r} - X_{\max,s}$, that can be characterized it by its mean and standard deviation, in order to evaluate the uncertainty on X_{\max} . It is expected that this distribution is centred around 0. The standard deviation allows then to evaluate if the X_{\max} reconstruction efficiency and the ability to distinguish between various messengers (below 40 g cm⁻²) and between proton and iron primaries (below 20 g cm⁻²). One histogram example is shown in figure 6.19. For our benchmark example, we obtain a broad distribution with mean ~ 5 g cm⁻² and standard deviation ~ 23 g cm⁻². With this simple example, we already see that the X_{\max} reconstruction for very inclined air showers is promising but also challenging. In some extreme cases, the reconstructed value of X_{\max} differs by more than 40 g cm⁻² from the simulated value. This cases correspond to outliers of the distribution, with very high or very low values of X_{\max} in the simulation sample. Increasing the number of simulations and better sampling the X_{\max} values across the accessible range could help to limit this effect.

6.2.2 Reconstruction performance

As mentioned before, we test the impact of several parameters on the X_{\max} reconstruction: we focus on the distance between the antennas d , the energy of the primary particle E , and the incoming direction of the air shower, mainly encoded in the zenith angle θ . The results

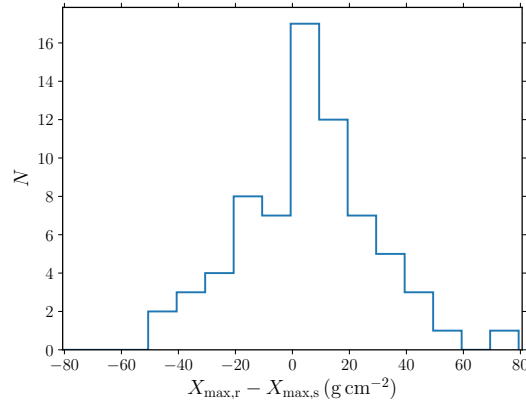


Figure 6.19: Histogram of $X_{\max,r} - X_{\max,s}$ obtained for our benchmark example (see text).

are illustrated in figure 6.20 where we compare the standard deviations of the $X_{\max,r} - X_{\max,s}$ distributions, as a function of the distance between the antenna (denoted ‘step’), for step = 250 m, 500 m, 750 m, 1000 m and 1250 m.

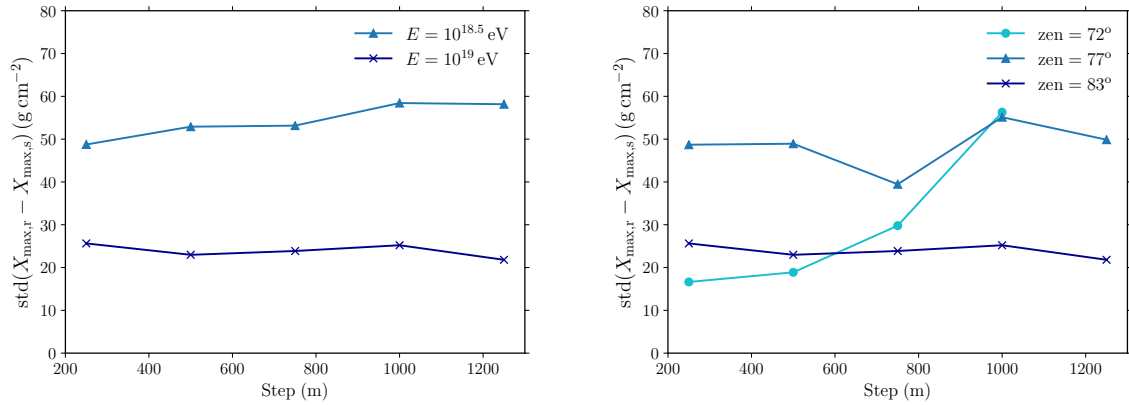


Figure 6.20: Standard deviation of the $X_{\max,r} - X_{\max,s}$ distributions as a function of distances between the antenna (step). We show the impact of primary energy for $\theta = 83^\circ$ and $\alpha = 10^\circ$ (left), for two primary energies $E = 10^{18.5} \text{ eV}$ (rectangles) and $E = 10^{19} \text{ eV}$ (crosses). We also show the impact of zenith angle for $E = 10^{19} \text{ eV}$ and $\alpha = 10^\circ$ (right), for three zenith angles $\theta = 72^\circ$ (circles), $\theta = 77^\circ$ (rectangles) and $\theta = 83^\circ$ (crosses).

First, we study the impact of primary energy, for the same zenith angle $\theta = 83^\circ$ and mountain slope $\alpha = 10^\circ$. For energies above 10^{19} eV , the level of noise is low and the reconstruction gives $\text{std}(X_{\max,r} - X_{\max,s})$ of the order of 30 g cm^{-2} , which allows to distinguish between cosmic rays and other astroparticles but does not allow to distinguish between proton and iron primaries. We note that there is only a weak dependence of the reconstruction on the distance between the antenna, as long as a sufficient number of antennas trigger, which is the case for the spacing considered. For energies below $10^{18.5} \text{ eV}$, the noise starts to affect the X_{\max} reconstruction, and $\text{std}(X_{\max,r} - X_{\max,s})$ is between 50 g cm^{-2} and 60 g cm^{-2} , increasing with the distance between the antenna. Additional work will be therefore required to improve the reconstruction at lower energies.

The zenith angle of the incoming particle has also an impact on the X_{\max} reconstruction. For the same primary energy 10^{19} eV and mountain slope $\alpha = 10^\circ$, we compare the reconstruction for $\theta = 72^\circ$, $\theta = 77^\circ$ and $\theta = 83^\circ$. We note that small zenith angles are more sensitive to the distance between the antenna, as the size of the footprint on the ground decreases with decreasing zenith

angles, as illustrated in figure 6.21. Thus dense arrays, with step ≤ 750 m, would be required to reconstruct the elementary composition of air showers induced by UHECR with zenith angles $\theta \leq 72^\circ$. Interestingly, the X_{\max} reconstruction is efficient for $\theta = 72^\circ$ and step ≤ 500 m, giving $\text{std}(X_{\max,r} - X_{\max,s}) < 20 \text{ g cm}^{-2}$, whereas $\theta = 77^\circ$ gives $\text{std}(X_{\max,r} - X_{\max,s}) \simeq 50 \text{ g cm}^{-2}$ for step ≤ 500 m, and the results for $\theta = 83^\circ$ lie in between. As shown in Carvalho and Alvarez-Muñiz (2019), we observe a degradation of the X_{\max} reconstruction with increasing zenith angle by comparing the results for $\theta = 72^\circ$ and $\theta = 83^\circ$. The result obtained for $\theta = 77^\circ$ could result from the antenna response considered in this study, as the antenna gain varies strongly with zenith angle. Thus no simple dependence of the X_{\max} reconstruction as a function of zenith angle can be established, as it depends on the antenna response.

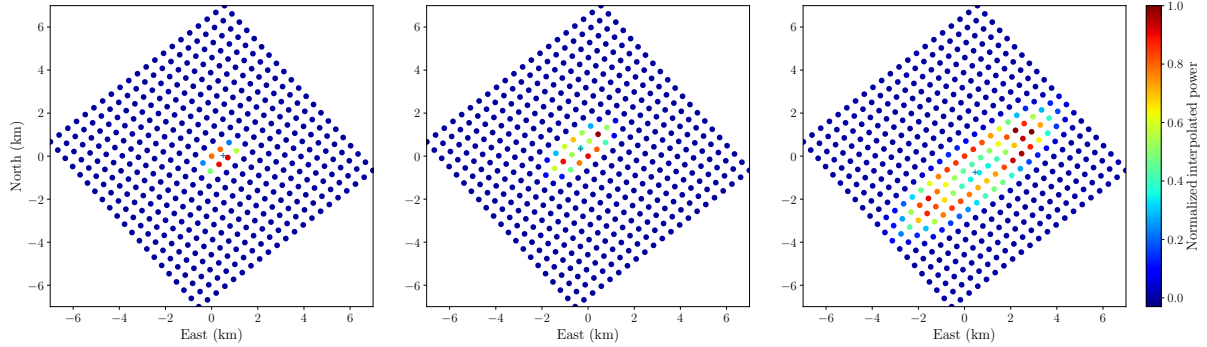


Figure 6.21: Comparison between the normalized and interpolated antenna power projected on the ground for one shower, for $E = 10^{19}$ eV, step = 500 m and $\alpha = 10^\circ$. We compare three footprints for $\theta = 72^\circ$ (left), $\theta = 77^\circ$ (middle) and $\theta = 83^\circ$ (right).

To conclude, we highlight with this numerical study the influence of primary energy and direction of the incoming particle on the statistical X_{\max} reconstruction. For GRANDProto300, which aims at studying the transition region between Galactic to extragalactic cosmic rays, the mass composition is an absolutely crucial parameter. These results could thus be used in future developments of the GRAND project, and especially in the context of GRANDProto300 applied to real data. The preliminary results are promising as they indicate that an X_{\max} resolution of $< 40 \text{ g cm}^{-2}$ could be reached for GRAND. We emphasize that the energy and the direction of the primary are known, and that we consider an idealized topography. In particular, the footprint is fully contained in the array (except for step = 250 m) and we did not consider X_{\max} reconstruction in the case where only a part of the footprint is detected by the array. More refined methods and dedicated setups should lead to better accuracy.

Conclusion

I took my first steps in the field of astroparticle physics, driven by the advent of time-domain and multimessenger astronomy and intrigued by the mysterious origins of ultra-high-energy cosmic rays and high-energy neutrinos. From my experience, the study of energetic astrophysical sources greatly benefits from a comprehensive approach across many domains of physics and astrophysics, fuelled by a continuous dialog between theory and observations. In this perspective, while focussing on theoretical aspects of the modeling of energetic phenomena, I also participated in the development of future observatories of high-energy astroparticles.

Cosmic rays appear to be key players in the production of non-thermal and, more generally, multimessenger emissions. Thus we developed analytical and numerical tools to study the acceleration and interactions of cosmic rays in the vicinity of energetic sources. We highlighted the importance of high-energy neutrino detection by focussing on the detectability of high-energy neutrino flares from transient sources. Indeed, their association with one astrophysical source would be the evidence for cosmic-ray acceleration and interactions in the vicinity of this source, and would have important consequence for the modeling of non-thermal emissions from energetic phenomena. Our analytical model can be applied to different detectors and various categories of sources. It allows to point the most promising sources for the detection of high-energy neutrino flares, which could guide future target searches. Moreover, it highlights the difficulty of detecting high-energy neutrinos from currently known transient sources and motivate the development of detectors with higher sensitivities. A precise modeling of acceleration and interaction processes was required to go further in our investigation of the properties of energetic sources. We identified two interesting categories of sources, pulsars and tidal disruption events, that guided our future theoretical work.

The specific properties of pulsars, and especially the configuration of their magnetosphere, triggered a precise study on cosmic-ray acceleration in highly magnetized environments. With particle-in-cell simulations, we were able to account for the complex interaction between particles and electromagnetic fields during the acceleration process. It allowed to characterize the energy and luminosity of protons escaping from these environments, and support the idea that pulsars could be good candidates for the acceleration of high-energy cosmic rays in our Galaxy, and that highly magnetized and rapidly spinning pulsars -the hypothetical millisecond magnetars- could produce cosmic rays up to ultra-high-energies. We focussed on the fate of protons in the magnetosphere, thus our work should be extended to larger scales to study the impact of proton reacceleration at a shock front for instance, or in the current sheet through magnetic reconnection. Moreover, a more precise treatment of particle interactions, such as the pair production, but also photohadronic interactions, could lead to interesting consequences such as the production of high-energy neutrinos and gamma rays.

Facing the difficulty of a self-consistent and efficient modeling of all the interaction processes at play in a source and the production of secondary particles, we developed a numerical treatment of cosmic-ray interactions in any kind of radiative backgrounds. This tool allows to study in detail the interaction of accelerated cosmic rays in the vicinity of energetic sources, which accounts for nuclear cascades, and to predict the emitted fluxes of ultra-high-energy cosmic rays and

neutrinos. It can be applied to various categories of sources, in keeping with our first analytical study of transient sources. In the future, new modules could be added to calculate gamma-ray emissions and produce self-consistently interaction backgrounds from the radiation of accelerated particles, such as electrons and positrons. A more precise calculation of cosmic-ray acceleration could be implemented, including the possibility of re-acceleration of cosmic rays and secondary particles during their propagation. Thus the competition between acceleration and interaction processes could be more precisely studied.

Several observational consequences could be deduced from this theoretical framework. First, we demonstrated that a population of millisecond pulsars located in the Galactic bulge could explain the diffuse gamma-ray emission observed by the HESS detector. In our model, gamma rays are produced through hadronic processes, when cosmic rays accelerated by pulsars interact with molecular clouds. Interestingly, this same population has been proposed as a possible candidate to explain the diffuse gamma-ray emission observed by Fermi in the same region, and could also possibly contribute to molecular ionization in the central molecular zone. Our model could be extended to account for leptonic emissions and could be applied to emissions from globular clusters of close-by galaxies. Second, we examined the production of ultra-high-energy cosmic rays and high-energy neutrinos from tidal disruptions by massive black holes powering relativistic jets. Considering a population of these transient events, we were able to find a set of source parameters allowing to fit the spectrum and composition of ultra-high-energy cosmic rays measured by the Auger experiment. Using these parameters, we showed that this population cannot produce the high-energy neutrinos detected by the IceCube experiment, but produces neutrinos at higher energies, that could be detected with future very-high-energy neutrino observatories. The contribution of this population of sources in the diffuse gamma-ray background is still to be calculated. In the future, the detection of additional events will help to constrain and adapt this model. In this study, it was fundamental to account for the evolution of the luminosity of the system, even very simply by considering two phases, as we found that high-energy neutrinos and protons below 10^{18} eV were principally emitted during the early and most luminous phase, because of the numerous interactions of ultra-high-energy cosmic rays, whereas ultra-high-energy cosmic rays were principally emitted during the later phase characterized by a lower luminosity. This example showed the importance of accounting for time-dependent properties of transient sources to model precisely their multimessenger emissions. Therefore, in the future, the time-dependence of transient sources, and in particular the evolution of interaction backgrounds, could be included directly in our simulation tool.

Finally, the 21st century will certainly see the advent of high-energy and very-high-energy neutrino astronomy, from 10^{13} eV to 10^{18} eV. Ground-breaking techniques have been and will be developed to face the challenge of detecting this scarcely interacting messengers and associating them with astrophysical sources. On the one hand, we focussed on the detection of very-high-energy neutrinos from space with a Cherenkov detector, as proposed by the POEMMA project, and studied the sky coverage from geometrical estimates. We emphasized that this detection technique could be interesting for the detection of transient sources, due to the possibility of full sky coverage and the possibility of pointing, and a dedicated study is on-going. On the other hand, the detection by a giant radio antenna array of the radio emission, induced by inclined air showers, is a new detection technique proposed by the GRAND experiment. This antenna array could also detect ultra-high-energy cosmic rays and gamma rays, and in this context we studied the reconstruction of the elementary composition of ultra-high-energy cosmic rays. The reconstruction technique appears to be adequate for ultra-high energies, but the reconstruction of the elementary composition below 10^{18} eV will be challenging due to the noise level. New techniques will be developed in the future in order to deal with high noise levels.

Acronyms

AGN Active Galactic Nucleus

AMON Astrophysical Multimessenger Observatory Network

ANITA Antarctic Impulsive Transient Antenna

ARIANNA Antarctic Ross Ice-Shelf ANtenna Neutrino Array

CMB Cosmic Microwave Background

EBL Extragalactic Background Light

GRAND Giant Radio Array for Neutrino Detection

GRB Gamma-Ray Burst

HE High-Energy ($> 10^{12}$ eV)

HESS High Energy Stereoscopic System

LHC Large Hadron Collider

LIGO Laser Interferometer Gravitational-Wave Observatory

LISA Laser Interferometer Space Antenna

MFP Mean Free Path

MHD Magnetohydrodynamics

MSP Millisecond Pulsars

PIC Particle-In-Cell

POEMMA Probe of Extreme Multi-Messenger Astrophysics

TDE Tidal Disruption Event

UHECR Ultra-High-Energy Cosmic Ray ($> 10^{18}$ eV)

VHE Very-High-Energy ($> 10^{17}$ eV)

Bibliography

- Aab, A. et al. (2014). “Depth of maximum of air-shower profiles at the Pierre Auger Observatory. I. Measurements at energies above $10^{17.8}$ eV”. *Phys. Rev. D* 90.12, p. 122005. arXiv: 1409.4809 [astro-ph.HE].
- Aab, A. et al. (2016). “Evidence for a mixed mass composition at the ‘ankle’ in the cosmic-ray spectrum”. *Physics Letters B* 762, pp. 288–295. arXiv: 1609.08567 [astro-ph.HE].
- Aab, A. et al. (2018). “Large-scale Cosmic-Ray Anisotropies above 4 EeV Measured by the Pierre Auger Observatory”. *ApJ* 868, p. 4. arXiv: 1808.03579 [astro-ph.HE].
- Aartsen, M. G. et al. (2013a). “First Observation of PeV-Energy Neutrinos with IceCube”. *Physical Review Letters* 111.2, p. 021103. arXiv: 1304.5356 [astro-ph.HE].
- (2013b). “Search for Time-independent Neutrino Emission from Astrophysical Sources with 3 yr of IceCube Data”. *ApJ* 779, p. 132. arXiv: 1307.6669 [astro-ph.HE].
- Aartsen, M. G. et al. (2014a). “Observation of High-Energy Astrophysical Neutrinos in Three Years of IceCube Data”. *Physical Review Letters* 113.10, p. 101101. arXiv: 1405.5303 [astro-ph.HE].
- (2014b). “Searches for Extended and Point-like Neutrino Sources with Four Years of IceCube Data”. *ApJ* 796, p. 109. arXiv: 1406.6757 [astro-ph.HE].
- Aartsen, M. G. et al. (2015). “Searches for Time-dependent Neutrino Sources with IceCube Data from 2008 to 2012”. *ApJ* 807, p. 46. arXiv: 1503.00598 [astro-ph.HE].
- Aartsen, M. G. et al. (2016a). “An All-sky Search for Three Flavors of Neutrinos from Gamma-ray Bursts with the IceCube Neutrino Observatory”. *ApJ* 824, p. 115. arXiv: 1601.06484 [astro-ph.HE].
- Aartsen, M. G. et al. (2016b). “Lowering IceCube’s Energy Threshold for Point Source Searches in the Southern Sky”. *ApJ Lett.* 824, p. L28. arXiv: 1605.00163 [astro-ph.HE].
- Abazajian, Kevork N. and Manoj Kaplinghat (2012). “Detection of a Gamma-Ray Source in the Galactic Center Consistent with Extended Emission from Dark Matter Annihilation and Concentrated Astrophysical Emission”. *Phys. Rev.* D86. [Erratum: *Phys. Rev.* D87,129902(2013)], p. 083511. arXiv: 1207.6047 [astro-ph.HE].
- Abazajian, Kevork N. et al. (2014). “Astrophysical and Dark Matter Interpretations of Extended Gamma-Ray Emission from the Galactic Center”. *Phys. Rev.* D90.2, p. 023526. arXiv: 1402.4090 [astro-ph.HE].
- Abbasi, R. et al. (2009). “Search for High-Energy Muon Neutrinos from the “Naked-Eye” GRB 080319B with the IceCube Neutrino Telescope”. *ApJ* 701, pp. 1721–1731. arXiv: 0902.0131 [astro-ph.HE].
- Abbasi, R. et al. (2012a). “Neutrino Analysis of the 2010 September Crab Nebula Flare and Time-integrated Constraints on Neutrino Emission from the Crab Using IceCube”. *ApJ* 745, p. 45. arXiv: 1106.3484 [astro-ph.HE].
- Abbasi, R. et al. (2012b). “Time-dependent Searches for Point Sources of Neutrinos with the 40-string and 22-string Configurations of IceCube”. *ApJ* 744, p. 1. arXiv: 1104.0075 [astro-ph.HE].
- Abbasi, R. U. et al. (2017). “Search for EeV protons of galactic origin”. *Astroparticle Physics* 86, pp. 21–26. arXiv: 1608.06306 [astro-ph.HE].

- Abbasi, R. U. et al. (2018). “Depth of Ultra High Energy Cosmic Ray Induced Air Shower Maxima Measured by the Telescope Array Black Rock and Long Ridge FADC Fluorescence Detectors and Surface Array in Hybrid Mode”. *The Astrophysical Journal* 858.2, p. 76.
- Abbott, B. P. et al. (2016a). “GW151226: Observation of Gravitational Waves from a 22-Solar-Mass Binary Black Hole Coalescence”. *Physical Review Letters* 116.24, p. 241103. arXiv: 1606.04855 [gr-qc].
- (2016b). “Observation of Gravitational Waves from a Binary Black Hole Merger”. *Physical Review Letters* 116.6, p. 061102. arXiv: 1602.03837 [gr-qc].
- Abbott, B. P. et al. (2017). “GW170817: Observation of Gravitational Waves from a Binary Neutron Star Inspiral”. *Physical Review Letters* 119.16, p. 161101. arXiv: 1710.05832 [gr-qc].
- Abdalla, H. et al. (2018). “Characterising the VHE diffuse emission in the central 200 parsecs of our Galaxy with H.E.S.S”. *Astron. Astrophys.* 612, A9. arXiv: 1706.04535 [astro-ph.HE].
- Abdo, A. A. et al. (2011). “Gamma-Ray Flares from the Crab Nebula”. *Science* 331, p. 739. arXiv: 1011.3855 [astro-ph.HE].
- Abdo, A. A. et al. (2013). “The Second Fermi Large Area Telescope Catalog of Gamma-Ray Pulsars”. *ApJS* 208, p. 17. arXiv: 1305.4385 [astro-ph.HE].
- Abeysekara, A. U. et al. (2017). “Extended gamma-ray sources around pulsars constrain the origin of the positron flux at Earth”. *Science* 358, pp. 911–914. arXiv: 1711.06223 [astro-ph.HE].
- Abu-Zayyad, T. et al. (2012). “The surface detector array of the Telescope Array experiment”. *Nuclear Instruments and Methods in Physics Research A* 689, pp. 87–97. arXiv: 1201.4964 [astro-ph.IM].
- Ackermann, M. et al. (2014). “Fermi establishes classical novae as a distinct class of gamma-ray sources”. *Science* 345, pp. 554–558. arXiv: 1408.0735 [astro-ph.HE].
- Ackermann, M. et al. (2015). “Searching for Dark Matter Annihilation from Milky Way Dwarf Spheroidal Galaxies with Six Years of Fermi Large Area Telescope Data”. *Phys. Rev. Lett.* 115 (23), p. 231301.
- Ageron, M. et al. (2011). “ANTARES: The first undersea neutrino telescope”. *Nuclear Instruments and Methods in Physics Research A* 656, pp. 11–38. arXiv: 1104.1607 [astro-ph.IM].
- Aguilar, M. et al. (2016). “Precision Measurement of the Boron to Carbon Flux Ratio in Cosmic Rays from 1.9 GV to 2.6 TV with the Alpha Magnetic Spectrometer on the International Space Station”. *Phys. Rev. Lett.* 117 (23), p. 231102.
- Aharonian, F. et al. (2006). “Discovery of very-high-energy γ -rays from the Galactic Centre ridge”. *Nature* 439, pp. 695–698. eprint: astro-ph/0603021.
- Aharonian, F. et al. (2007). “An Exceptional Very High Energy Gamma-Ray Flare of PKS 2155-304”. *ApJ* 664, pp. L71–L74. arXiv: 0706.0797.
- Aharonian, F. A. (2004). *Very high energy cosmic gamma radiation : a crucial window on the extreme Universe*. World Scientific Publishing Co.
- Aharonian, F. A. and A. M. Atoyan (1996). “On the emissivity of π^0 -decay gamma radiation in the vicinity of accelerators of galactic cosmic rays.” *A&A* 309, pp. 917–928.
- Ahn, E.-J. et al. (2009). “Cosmic ray interaction event generator SIBYLL 2.1”. *Phys. Rev. D* 80.9, p. 094003. arXiv: 0906.4113 [hep-ph].
- Aird, J. et al. (2010). “The evolution of the hard X-ray luminosity function of AGN”. *MNRAS* 401, pp. 2531–2551. arXiv: 0910.1141.
- Aleksić, J. et al. (2012). “Phase-resolved energy spectra of the Crab pulsar in the range of 50-400 GeV measured with the MAGIC telescopes”. *A&A* 540, A69. arXiv: 1109.6124 [astro-ph.HE].
- Aliu, E. et al. (2008). “Observation of Pulsed γ -Rays Above 25 GeV from the Crab Pulsar with MAGIC”. *Science* 322, p. 1221. arXiv: 0809.2998.

- Allison, P. et al. (2012). “Design and Initial Performance of the Askaryan Radio Array Prototype EeV Neutrino Detector at the South Pole”. *Astropart. Phys.* 35, pp. 457–477. arXiv: 1105.2854 [astro-ph.IM].
- Allison, P. et al. (2015). “First constraints on the ultra-high energy neutrino flux from a prototype station of the Askaryan Radio Array”. *Astroparticle Physics* 70, pp. 62–80. arXiv: 1404.5285 [astro-ph.HE].
- Alvarez-Muñiz, J. et al. (2012). “Coherent radiation from extensive air showers in the ultrahigh frequency band”. *Phys. Rev. D* 86.12, p. 123007. arXiv: 1208.0951 [astro-ph.HE].
- Alvarez-Muniz, Jaime et al. (2018). “Comprehensive approach to tau-lepton production by high-energy tau neutrinos propagating through the Earth”. *Phys. Rev. D* 97.2, p. 023021. arXiv: 1707.00334 [astro-ph.HE].
- Alves Batista, R. and J. Silk (2017). *Ultra-high-energy cosmic rays from tidally-ignited stars*. arXiv: 1702.06978 [astro-ph.HE].
- Alves Batista, R. et al. (2015). “Effects of uncertainties in simulations of extragalactic UHECR propagation, using CRPropa and SimProp”. *J. Cosmology Astropart. Phys.* 10, p. 063. arXiv: 1508.01824 [astro-ph.HE].
- Alves Batista, R. et al. (2019). “Open Questions in Cosmic-Ray Research at Ultrahigh Energies”. *arXiv e-prints*. arXiv: 1903.06714 [astro-ph.HE].
- Amaro-Seoane, Pau et al. (2017). “Laser Interferometer Space Antenna”. *arXiv e-prints*, arXiv:1702.00786. arXiv: 1702.00786 [astro-ph.IM].
- Antonini, F., E. Barausse, and J. Silk (2015a). “The Coevolution of Nuclear Star Clusters, Massive Black Holes, and Their Host Galaxies”. *ApJ* 812, p. 72. arXiv: 1506.02050.
- (2015b). “The Imprint of Massive Black Hole Mergers on the Correlation between Nuclear Star Clusters and Their Host Galaxies”. *ApJ* 806, p. L8. arXiv: 1504.04033.
- Armengaud, E. et al. (2007). “CRPropa: A numerical tool for the propagation of UHE cosmic rays, γ -rays and neutrinos”. *Astroparticle Physics* 28, pp. 463–471. eprint: arXiv:astro-ph/0603675.
- Arnett, W. D. (1980). “Analytic solutions for light curves of supernovae of Type II”. *ApJ* 237, pp. 541–549.
- Arnett, W. D. et al. (1989). “Supernova 1987A”. *ARA&A* 27, pp. 629–700.
- Arons, J. (1981). “Particle acceleration by pulsars”. *Origin of Cosmic Rays*. Ed. by G. Setti, G. Spada, and A. W. Wolfendale. Vol. 94. IAU Symposium, pp. 175–204.
- (1983). “Pair creation above pulsar polar caps - Geometrical structure and energetics of slot gaps”. *ApJ* 266, pp. 215–241.
- (2003). “Magnetars in the Metagalaxy: An Origin for Ultra-High-Energy Cosmic Rays in the Nearby Universe”. *ApJ* 589, pp. 871–892. eprint: astro-ph/0208444.
- Askar’yan, G. A. (1962). “Excess negative charge of an electron-photon shower and its coherent radio emission”. *Sov. Phys. JETP* 14.2. [Zh. Eksp. Teor. Fiz.41,616(1961)], pp. 441–443.
- Askar’yan, G. A. (1965). “Coherent Radio Emission from Cosmic Showers in Air and in Dense Media”. *Soviet Journal of Experimental and Theoretical Physics* 21, p. 658.
- Atoyan, A. M. and C. D. Dermer (2003). “Neutral Beams from Blazar Jets”. *ApJ* 586, pp. 79–96. eprint: astro-ph/0209231.
- Baerwald, P., M. Bustamante, and W. Winter (2015). “Are gamma-ray bursts the sources of ultra-high energy cosmic rays?” *Astroparticle Physics* 62, pp. 66–91. arXiv: 1401.1820 [astro-ph.HE].
- Balbo, M. et al. (2011). “Twelve-hour spikes from the Crab Pevatron”. *A&A* 527, p. L4. arXiv: 1012.3397 [astro-ph.HE].
- Banks, B. A., K. K. de Groh, and S. K. Miller (2004). *Low Earth Orbital Atomic Oxygen Interactions With Spacecraft Materials*. Tech. rep. NASA/TM—2004-213400. Glenn Research Center.

- Barausse, E. (2012). “The evolution of massive black holes and their spins in their galactic hosts”. *MNRAS* 423, pp. 2533–2557. arXiv: 1201.5888.
- Barausse, E. et al. (2017). “Selection bias in dynamically measured supermassive black hole samples: scaling relations and correlations between residuals in semi-analytic galaxy formation models”. *MNRAS* 468, pp. 4782–4791. arXiv: 1702.01762.
- Bartels, R. T., T. D. P. Edwards, and C. Weniger (2018). “Bayesian Model Comparison and Analysis of the Galactic Disk Population of Gamma-Ray Millisecond Pulsars”. *ArXiv e-prints*. arXiv: 1805.11097 [astro-ph.HE].
- Bartels, Richard, Suraj Krishnamurthy, and Christoph Weniger (2016). “Strong Support for the Millisecond Pulsar Origin of the Galactic Center GeV Excess”. *Phys. Rev. Lett.* 116 (5), p. 051102.
- Barwick, S. (2011). “ARIANNA - A New Concept for High Energy Neutrino Detection”. *International Cosmic Ray Conference* 4, p. 238.
- Barwick, S. W. et al. (2015). “A first search for cosmogenic neutrinos with the ARIANNA Hexagonal Radio Array”. *Astroparticle Physics* 70, pp. 12–26. arXiv: 1410.7352 [astro-ph.HE].
- Baty, H., J. Petri, and S. Zenitani (2013). “Explosive reconnection of double tearing modes in relativistic plasmas: application to the Crab flares”. *MNRAS* 436, pp. L20–L24. arXiv: 1308.0906 [astro-ph.HE].
- Beall, J. H. and W. Bednarek (2002). “Neutrinos from Early-Phase, Pulsar-driven Supernovae”. *ApJ* 569, pp. 343–348. eprint: astro-ph/0108447.
- Bednarek, W. and W. Idec (2011). “On the variability of the GeV and multi-TeV gamma-ray emission from the Crab nebula”. *MNRAS* 414, pp. 2229–2234. arXiv: 1011.4176 [astro-ph.HE].
- Bednarek, W. and T. Sobczak (2013). “Gamma-rays from millisecond pulsar population within the central stellar cluster in the Galactic Centre”. *MNRAS* 435, pp. L14–L18. arXiv: 1306.4760 [astro-ph.HE].
- Bednarek, W., G. F. Burgio, and T. Montaruli (2005). “Galactic discrete sources of high energy neutrinos”. *New A Rev.* 49, pp. 1–21. eprint: astro-ph/0404534.
- Bednarz, J. and M. Ostrowski (1998). “Energy Spectra of Cosmic Rays Accelerated at Ultrarelativistic Shock Waves”. *Physical Review Letters* 80, pp. 3911–3914. eprint: astro-ph/9806181.
- Bell, A. R. (1978a). “The acceleration of cosmic rays in shock fronts. I”. *MNRAS* 182, pp. 147–156.
- (1978b). “The acceleration of cosmic rays in shock fronts. II”. *MNRAS* 182, pp. 443–455.
- Bell, AR et al. (2013). “Cosmic ray acceleration and escape from supernova remnants”. *Mon. Not. Roy. Astron. Soc.* 431, p. 415. arXiv: 1301.7264 [astro-ph.HE].
- Bellido, Jose (2018). “Depth of maximum of air-shower profiles at the Pierre Auger Observatory: Measurements above $10^{17.2}$ eV and Composition Implications”. *PoS ICRC2017*. [40(2017)], p. 506.
- Beloborodov, A. M. (2014). “Magnetically powered outbursts from white dwarf mergers”. *MNRAS* 438, pp. 169–176. arXiv: 1311.0668 [astro-ph.HE].
- Bennett, L and D. C. Ellison (1995). “Investigation of intrinsic variability in one-dimensional parallel shocks using steady state hybrid simulations”. *J. Geophys. Res.* 100, pp. 3439–3448.
- Berezinsky, V. S. and G. T. Zatsepin (1969). “Cosmic rays at ultrahigh-energies (neutrino?)” *Phys. Lett.* 28B, pp. 423–424.
- Bevington, P. R. and D. K. Robinson (2003). *Data reduction and error analysis for the physical sciences*.
- Biehl, D. et al. (2017). “Tidally disrupted stars as a possible origin of both cosmic rays and neutrinos at the highest energies”. *ArXiv e-prints*. arXiv: 1711.03555 [astro-ph.HE].
- Birdsall, C. K. and A. B. Langdon (1991). *Plasma Physics via Computer Simulation*.
- Blackburn, L. et al. (2016). “IceCube-160427A: Fermi GBM Observations.” *GRB Coordinates Network* 19364.

- Blackman, E. G. and G. B. Field (1994). “Kinematics of relativistic magnetic reconnection”. *Physical Review Letters* 72, pp. 494–497.
- Blandford, R. D. and J. P. Ostriker (1978). “Particle acceleration by astrophysical shocks”. *ApJ* 221, pp. L29–L32.
- Blandford, R. D. and R. L. Znajek (1977). “Electromagnetic extraction of energy from Kerr black holes”. *MNRAS* 179, pp. 433–456.
- Blasi, P. and E. Amato (2012). “Diffusive propagation of cosmic rays from supernova remnants in the Galaxy. I: spectrum and chemical composition”. *J. Cosmology Astropart. Phys.* 1, p. 010. arXiv: 1105.4521 [astro-ph.HE].
- Blasi, P., R. I. Epstein, and A. V. Olinto (2000). “Ultra-High-Energy Cosmic Rays from Young Neutron Star Winds”. *ApJ* 533, pp. L123–L126. eprint: astro-ph/9912240.
- Blaufuss, E. (2016). “ICECUBE-160427A neutrino candidate event: updated direction information.” *GRB Coordinates Network* 19363.
- Block, Martin M., Loyal Durand, and Phuoc Ha (2014). “Connection of the virtual γ^*p cross section of ep deep inelastic scattering to real γp scattering, and the implications for γN and ep total cross sections”. *Phys. Rev. D* 89.9, p. 094027. arXiv: 1404.4530 [hep-ph].
- Bloom, J. S. et al. (2009). “Observations of the Naked-Eye GRB 080319B: Implications of Nature’s Brightest Explosion”. *ApJ* 691, pp. 723–737. arXiv: 0803.3215.
- Bloom, J. S. et al. (2011). “A Possible Relativistic Jetted Outburst from a Massive Black Hole Fed by a Tidally Disrupted Star”. *Science* 333, p. 203. arXiv: 1104.3257 [astro-ph.HE].
- Boggs, S. et al. (2005). “SGR 1806-20, RHESSI observations of the 041227 giant flare.” *GRB Coordinates Network* 2936.
- Bonetti, M. et al. (2017a). “Post-Newtonian evolution of massive black hole triplets in galactic nuclei – II. Survey of the parameter space”. *ArXiv e-prints*. arXiv: 1709.06088.
- Bonetti, M. et al. (2017b). “Post-Newtonian evolution of massive black hole triplets in galactic nuclei – III. A robust lower limit to the nHz stochastic background of gravitational waves”. *ArXiv e-prints*. arXiv: 1709.06095.
- BORIS, J. P. (1970). “Relativistic plasma simulation-optimization of a hybrid code”. *Proc. 4th Conf. Num. Sim. Plasmas*, pp. 3–67.
- Borkowski, J. et al. (2004). “Giant flare from Sgr 1806-20 detected by INTEGRAL.” *GRB Coordinates Network* 2920.
- Brenneman, L. (2013). *Measuring the Angular Momentum of Supermassive Black Holes*.
- Britzen, S. et al. (2007). “The soft X-ray properties of AGN from the CJF sample. A correlation analysis between soft X-ray and VLBI properties”. *A&A* 476, pp. 759–777. arXiv: 0802.4347.
- Bromberg, O., E. Nakar, and T. Piran (2011). “Are Low-luminosity Gamma-Ray Bursts Generated by Relativistic Jets?” *ApJ* 739, p. L55. arXiv: 1107.1346 [astro-ph.HE].
- Brown, G. C. et al. (2015). “Swift J1112.2-8238: a candidate relativistic tidal disruption flare”. *MNRAS* 452, pp. 4297–4306. arXiv: 1507.03582 [astro-ph.HE].
- Bucciantini, N., J. Arons, and E. Amato (2011). “Modelling spectral evolution of pulsar wind nebulae inside supernova remnants”. *MNRAS* 410, pp. 381–398. arXiv: 1005.1831 [astro-ph.HE].
- Budnik, R. et al. (2008). “Cosmic Rays from Transrelativistic Supernovae”. *ApJ* 673, pp. 928–933. arXiv: 0705.0041.
- Buehler, R., F. D’Ammando, and E. Hays (2010). “Fermi LAT confirmation of enhanced gamma-ray emission from the Crab Nebula region”. *The Astronomer’s Telegram* 2861.
- Buehler, R. et al. (2012). “Gamma-Ray Activity in the Crab Nebula: The Exceptional Flare of 2011 April”. *ApJ* 749, p. 26. arXiv: 1112.1979 [astro-ph.HE].

- Buitink, S. et al. (2014). “Method for high precision reconstruction of air shower X_{max} using two-dimensional radio intensity profiles”. *Phys. Rev. D* 90.8, p. 082003. arXiv: 1408.7001 [astro-ph.IM].
- Burrows, D. N. et al. (2011). “Relativistic jet activity from the tidal disruption of a star by a massive black hole”. *Nature* 476, pp. 421–424. arXiv: 1104.4787 [astro-ph.HE].
- Bustamante, M., K. Murase, and W. Winter (2016). *Multi-messenger light curves from gamma-ray bursts in the internal shock model*. arXiv: 1606.02325 [astro-ph.HE].
- Bustamante, M. et al. (2017). “Multi-messenger Light Curves from Gamma-Ray Bursts in the Internal Shock Model”. *ApJ* 837, p. 33. arXiv: 1606.02325 [astro-ph.HE].
- Bykov, A. et al. (2012). “Particle Acceleration in Relativistic Outflows”. *Space Science Reviews* 173, pp. 309–339. arXiv: 1205.2208 [astro-ph.HE].
- Calore, Francesca, Ilias Cholis, and Christoph Weniger (2015). “Background model systematics for the Fermi GeV excess”. *Journal of Cosmology and Astroparticle Physics* 2015.03, p. 038.
- Carlson, Eric and Stefano Profumo (2014). “Cosmic Ray Protons in the Inner Galaxy and the Galactic Center Gamma-Ray Excess”. *Phys. Rev. D* 90.2, p. 023015. arXiv: 1405.7685 [astro-ph.HE].
- Carlson, Eric, Stefano Profumo, and Tim Linden (2016). “Cosmic-Ray Injection from Star-Forming Regions”. *Phys. Rev. Lett.* 117 (11), p. 111101.
- Carvalho, W. R. and J. Alvarez-Muñiz (2019). “Determination of cosmic-ray primary mass on an event-by-event basis using radio detection”. *Astroparticle Physics* 109, pp. 41–49. arXiv: 1712.03544 [astro-ph.HE].
- Casadei, D. (2005). “Sky coverage of orbital detectors. Analytical approach”. *ArXiv Astrophysics e-prints*. eprint: astro-ph/0511674.
- Cattaneo, A. et al. (2006). “Modelling the galaxy bimodality: shutdown above a critical halo mass”. *MNRAS* 370, pp. 1651–1665. eprint: astro-ph/0601295.
- Celotti, A. and G. Ghisellini (2008). “The power of blazar jets”. *MNRAS* 385, pp. 283–300. arXiv: 0711.4112.
- Cenko, S. B. et al. (2011). “GRB 110328A / Swift J164449.3+573451: PTF quiescent optical counterpart.” *GRB Coordinates Network* 11827.
- Cerutti, B. and A. M. Beloborodov (2017). “Electrodynamics of Pulsar Magnetospheres”. *Space Sci. Rev.* 207, pp. 111–136. arXiv: 1611.04331 [astro-ph.HE].
- Cerutti, B., D. A. Uzdensky, and M. C. Begelman (2012). “Extreme Particle Acceleration in Magnetic Reconnection Layers: Application to the Gamma-Ray Flares in the Crab Nebula”. *ApJ* 746, p. 148. arXiv: 1110.0557 [astro-ph.HE].
- Cerutti, B. et al. (2013a). “Simulations of Particle Acceleration beyond the Classical Synchrotron Burnoff Limit in Magnetic Reconnection: An Explanation of the Crab Flares”. *ApJ* 770, p. 147. arXiv: 1302.6247 [astro-ph.HE].
- (2013b). “Simulations of Particle Acceleration beyond the Classical Synchrotron Burnoff Limit in Magnetic Reconnection: An Explanation of the Crab Flares”. *ApJ* 770, p. 147. arXiv: 1302.6247 [astro-ph.HE].
- (2014). “Gamma-ray flares in the Crab Nebula: A case of relativistic reconnection?” *Physics of Plasmas* 21.5, p. 056501. arXiv: 1401.3016 [astro-ph.HE].
- Cerutti, B. et al. (2015). “Particle acceleration in axisymmetric pulsar current sheets”. *MNRAS* 448, pp. 606–619. arXiv: 1410.3757 [astro-ph.HE].
- Chen, A. Y. and A. M. Beloborodov (2014). “Electrodynamics of Axisymmetric Pulsar Magnetosphere with Electron-Positron Discharge: A Numerical Experiment”. *ApJ* 795, p. L22. arXiv: 1406.7834 [astro-ph.HE].
- Chen, P., T. Tajima, and Y. Takahashi (2002). “Plasma Wakefield Acceleration for Ultrahigh-Energy Cosmic Rays”. *Physical Review Letters* 89.16, pp. 161101–+. eprint: arXiv:astro-ph/0205287.

- Cheng, K. S., C. Ho, and M. Ruderman (1986). “Energetic radiation from rapidly spinning pulsars. I - Outer magnetosphere gaps. II - VELA and Crab”. *ApJ* 300, pp. 500–539.
- Cheng, K. S., M. Ruderman, and L. Zhang (2000). “A Three-dimensional Outer Magnetospheric Gap Model for Gamma-Ray Pulsars: Geometry, Pair Production, Emission Morphologies, and Phase-resolved Spectra”. *ApJ* 537, pp. 964–976.
- Chevalier, R. A. and C. M. Irwin (2011). “Shock Breakout in Dense Mass Loss: Luminous Supernovae”. *ApJ Lett.* 729, p. L6. arXiv: 1101.1111 [astro-ph.HE].
- Chodorowski, M. J., A. A. Zdziarski, and M. Sikora (1992). “Reaction rate and energy-loss rate for photopair production by relativistic nuclei”. *ApJ* 400, pp. 181–185.
- Cholis, Ilias, Dan Hooper, and Tim Linden (2015). “Challenges in Explaining the Galactic Center Gamma-Ray Excess with Millisecond Pulsars”. *JCAP* 1506.06, p. 043. arXiv: 1407.5625 [astro-ph.HE].
- Ciprini, S. and S. Cutini (2013). “Swift detection of increased X-ray activity from gamma-ray flaring blazar PKS 1424-41”. *The Astronomer’s Telegram* 4770.
- Clausen-Brown, E. and M. Lyutikov (2012). “Crab nebula gamma-ray flares as relativistic reconnection minijets”. *MNRAS* 426, pp. 1374–1384. arXiv: 1205.5094 [astro-ph.HE].
- Contopoulos, I., D. Kazanas, and C. Fendt (1999). “The Axisymmetric Pulsar Magnetosphere”. *ApJ* 511, pp. 351–358. eprint: astro-ph/9903049.
- Corbel, S. and S. S. Eikenberry (2004). “The connection between W31, SGR 1806-20, and LBV 1806-20: Distance, extinction, and structure”. *A&A* 419, pp. 191–201. eprint: astro-ph/0311313.
- Coroniti, F. V. (1990). “Magnetically striped relativistic magnetohydrodynamic winds - The Crab Nebula revisited”. *ApJ* 349, pp. 538–545.
- Cummings, J. R. et al. (2011). “GRB 110328A: Swift detection of a burst.” *GRB Coordinates Network* 11823.
- Dai, L. and K. Fang (2016). *Can tidal disruption events produce the IceCube neutrinos?* arXiv: 1612.00011 [astro-ph.HE].
- (2017). “Can tidal disruption events produce the IceCube neutrinos?” *MNRAS* 469, pp. 1354–1359. arXiv: 1612.00011 [astro-ph.HE].
- Daugherty, J. K. and A. K. Harding (1982). “Electromagnetic cascades in pulsars”. *ApJ* 252, pp. 337–347.
- Daylan, Tansu et al. (2016). “The characterization of the gamma-ray signal from the central Milky Way: A case for annihilating dark matter”. *Physics of the Dark Universe* 12, pp. 1–23. ISSN: 2212-6864.
- de Gouveia dal Pino, E. M. and A. Lazarian (2005). “Production of the large scale superluminal ejections of the microquasar GRS 1915+105 by violent magnetic reconnection”. *A&A* 441, pp. 845–853.
- de Jager, O. C. (2007). “Lower Limits on Pulsar Pair Production Multiplicities from H.E.S.S. Observations of Pulsar Wind Nebulae”. *ApJ* 658, pp. 1177–1182.
- de Vries, K. D. et al. (2011). “Coherent Cherenkov Radiation from Cosmic-Ray-Induced Air Showers”. *Physical Review Letters* 107.6, p. 061101. arXiv: 1107.0665 [astro-ph.HE].
- de Vries, Krijn D., Olaf Scholten, and Klaus Werner (2012). “Macroscopic geo-magnetic radiation model: polarization effects and finite volume calculations”. *Nuclear Instruments and Methods in Physics Research A* 662, S175–S178. arXiv: 1010.5364 [astro-ph.HE].
- Dekel, A. and Y. Birnboim (2006). “Galaxy bimodality due to cold flows and shock heating”. *MNRAS* 368, pp. 2–20. eprint: astro-ph/0412300.
- Dekel, A. et al. (2009). “Cold streams in early massive hot haloes as the main mode of galaxy formation”. *Nature* 457, pp. 451–454. arXiv: 0808.0553.
- Dermer, C. D. (2002). “Neutrino, Neutron, and Cosmic-Ray Production in the External Shock Model of Gamma-Ray Bursts”. *ApJ* 574, pp. 65–87. eprint: arXiv:astro-ph/0005440.

- Dermer, C. D. and G. Menon (2009). *High Energy Radiation from Black Holes: Gamma Rays, Cosmic Rays, and Neutrinos*. Princeton University Press.
- Dermer, C. D., E. Ramirez-Ruiz, and T. Le (2007). “Correlation of Photon and Neutrino Fluxes in Blazars and Gamma-Ray Bursts”. *ApJ* 664, pp. L67–L70. eprint: [astro-ph/0703219](#).
- Dessart, L. et al. (2012). “Superluminous supernovae: ^{56}Ni power versus magnetar radiation”. *MNRAS* 426, pp. L76–L80. arXiv: 1208.1214 [[astro-ph.SR](#)].
- Deutsch, A. J. (1955). “The electromagnetic field of an idealized star in rigid rotation in vacuo”. *Annales d’Astrophysique* 18, p. 1.
- di Mauro, Mattia et al. (2014). “New evaluation of the antiproton production cross section for cosmic ray studies”. *Phys. Rev. D* 90, p. 085017. arXiv: 1408.0288 [[hep-ph](#)].
- Dieckmann, M.~E. and A. Bret (2009). “Particle-In-Cell Simulation of a Strong Double Layer in A Non-relativistic Plasma Flow: Electron Acceleration to Ultrarelativistic Speeds”. *ApJ* 694, pp. 154–164. arXiv: 0910.0225 [[astro-ph.HE](#)].
- Domokos, G. and S. Kovesi-Domokos (1998a). “Observation of UHE neutrino interactions from outer space”. *Workshop on Observing Giant Cosmic Ray Air Showers From $\gtrsim 10(20)$ eV Particles From Space*. Ed. by J. F. Krizmanic, J. F. Ormes, and R. E. Streitmatter. Vol. 433. American Institute of Physics Conference Series, pp. 390–393. eprint: [hep-ph/9801362](#).
- (1998b). “Observation of Ultrahigh Energy Neutrino Interactions by Orbiting Detectors”. *ArXiv High Energy Physics - Phenomenology e-prints*. eprint: [hep-ph/9805221](#).
- Donley, J. L. et al. (2002a). “Large-Amplitude X-Ray Outbursts from Galactic Nuclei: A Systematic Survey using ROSAT Archival Data”. *AJ* 124, pp. 1308–1321. eprint: [astro-ph/0206291](#).
- (2002b). “Large-Amplitude X-Ray Outbursts from Galactic Nuclei: A Systematic Survey using ROSAT Archival Data”. *AJ* 124, pp. 1308–1321. eprint: [astro-ph/0206291](#).
- eLISA Consortium et al. (2013). “The Gravitational Universe”. *arXiv e-prints*, arXiv:1305.5720. arXiv: 1305.5720 [[astro-ph.CO](#)].
- Engel, R., D. Seckel, and T. Stanev (2001). “Neutrinos from propagation of ultrahigh energy protons”. *Phys. Rev. D* 64.9, p. 093010. eprint: [astro-ph/0101216](#).
- Fan, Y.-Z. et al. (2011). “XRF 100316D/SN 2010bh: Clue to the Diverse Origin of Nearby Supernova-associated Gamma-ray Bursts”. *ApJ* 726, p. 32. arXiv: 1004.5267 [[astro-ph.HE](#)].
- Fang, K., K. Kotera, and A. V. Olinto (2012a). “Newly Born Pulsars as Sources of Ultrahigh Energy Cosmic Rays”. *ApJ* 750, p. 118. arXiv: 1201.5197 [[astro-ph.HE](#)].
- (2012b). “Newly Born Pulsars as Sources of Ultrahigh Energy Cosmic Rays”. *The Astrophysical Journal* 750, p. 118. arXiv: 1201.5197 [[astro-ph.HE](#)].
- (2013a). “Ultrahigh energy cosmic ray nuclei from extragalactic pulsars and the effect of their Galactic counterparts”. *J. Cos. and Astro. Phys.* 3, pp. 10–31. arXiv: 1302.4482 [[astro-ph.HE](#)].
- (2013b). “Ultrahigh energy cosmic ray nuclei from extragalactic pulsars and the effect of their Galactic counterparts”. *J. Cosmology Astropart. Phys.* 3, p. 010. arXiv: 1302.4482 [[astro-ph.HE](#)].
- Fang, K. et al. (2014). “Testing the newborn pulsar origin of ultrahigh energy cosmic rays with EeV neutrinos”. *Phys. Rev. D* 90.10, p. 103005. arXiv: 1311.2044 [[astro-ph.HE](#)].
- (2016). “IceCube constraints on fast-spinning pulsars as high-energy neutrino sources”. *JCAP* 4, p. 010. arXiv: 1511.08518 [[astro-ph.HE](#)].
- Fang, K. et al. (2017). “The Giant Radio Array for Neutrino Detection (GRAND): Present and Perspectives”. *ArXiv e-prints*. arXiv: 1708.05128 [[astro-ph.IM](#)].
- Farrar, G. R. and A. Gruzinov (2009). “Giant AGN Flares and Cosmic Ray Bursts”. *ApJ* 693, pp. 329–332. arXiv: 0802.1074.

- Farrar, G. R. and T. Piran (2014). *Tidal disruption jets as the source of Ultra-High Energy Cosmic Rays*. arXiv: 1411.0704 [astro-ph.HE].
- Feng, J. L. et al. (2002). “Observability of Earth-Skimming Ultrahigh Energy Neutrinos”. *Physical Review Letters* 88.16, p. 161102. eprint: hep-ph/0105067.
- Fermi, E. (1949). “On the Origin of the Cosmic Radiation”. *Physical Review* 75, pp. 1169–1174.
- (1954). “Galactic Magnetic Fields and the Origin of Cosmic Radiation.” *ApJ* 119, p. 1.
- Fermi-LAT Collaboration (2017). *Characterizing the population of pulsars in the inner Galaxy with the Fermi Large Area Telescope*. arXiv: 1705.00009 [astro-ph.HE].
- Ferrario, L. and D. Wickramasinghe (2007). “The birth properties of Galactic millisecond radio pulsars”. *MNRAS* 375, pp. 1009–1016. eprint: astro-ph/0701444.
- Ferrigno, C. et al. (2010). “Chandra follow-up observation of the Crab nebula after the very high energy flare”. *The Astronomer’s Telegram* 2994.
- Foster, R. S. and D. C. Backer (1990). “Constructing a pulsar timing array”. *ApJ* 361, pp. 300–308.
- Fukushima, M. (2015). “Recent results from telescope array”. *European Physical Journal Web of Conferences*. Vol. 99. European Physical Journal Web of Conferences, p. 04004. arXiv: 1503.06961 [astro-ph.HE].
- Gaggero, D. et al. (2017). “Diffuse Cosmic Rays Shining in the Galactic Center: A Novel Interpretation of H.E.S.S. and Fermi-LAT γ -Ray Data”. *Physical Review Letters* 119.3, p. 031101. arXiv: 1702.01124 [astro-ph.HE].
- Gaggero, Daniele et al. (2015). “Towards a realistic astrophysical interpretation of the gamma-ray Galactic center excess”. *JCAP* 1512, p. 056. arXiv: 1507.06129 [astro-ph.HE].
- Gal-Yam, A. and D. C. Leonard (2009). “A massive hypergiant star as the progenitor of the supernova SN 2005gl”. *Nature* 458, pp. 865–867.
- Gal-Yam, A. et al. (2009). “Supernova 2007bi as a pair-instability explosion”. *Nature* 462, pp. 624–627. arXiv: 1001.1156.
- Gallant, Y. A. and A. Achterberg (1999). “Ultra-high-energy cosmic ray acceleration by relativistic blast waves”. *MNRAS* 305, pp. L6–L10. eprint: astro-ph/9812316.
- Ghirlanda, G. et al. (2005). “The peak luminosity-peak energy correlation in gamma-ray bursts”. *MNRAS* 360, pp. L45–L49. eprint: astro-ph/0502488.
- Ghirlanda, G. et al. (2009). “Short versus long gamma-ray bursts: spectra, energetics, and luminosities”. *A&A* 496, pp. 585–595. arXiv: 0902.0983 [astro-ph.HE].
- Ghisellini, G. et al. (1993). “Relativistic bulk motion in active galactic nuclei”. *ApJ* 407, pp. 65–82.
- Ghisellini, G., F. Tavecchio, and M. Chiaberge (2005). “Structured jets in TeV BL Lac objects and radiogalaxies. Implications for the observed properties”. *A&A* 432, pp. 401–410. eprint: astro-ph/0406093.
- Ghisellini, G. et al. (2010). “General physical properties of bright Fermi blazars”. *MNRAS* 402, pp. 497–518. arXiv: 0909.0932.
- Giannios, D. (2010). “UHECRs from magnetic reconnection in relativistic jets”. *MNRAS* 408, pp. L46–L50. arXiv: 1007.1522 [astro-ph.HE].
- Giannios, D., D. A. Uzdensky, and M. C. Begelman (2009). “Fast TeV variability in blazars: jets in a jet”. *MNRAS* 395, pp. L29–L33. arXiv: 0901.1877 [astro-ph.HE].
- Giesen, Gaëlle et al. (2015). “AMS-02 antiprotons, at last! Secondary astrophysical component and immediate implications for Dark Matter”. *Journal of Cosmology and Astro-Particle Physics* 2015, p. 023. arXiv: 1504.04276 [astro-ph.HE].

- Globus, N., D. Allard, and E. Parizot (2015a). “A complete model of the cosmic ray spectrum and composition across the Galactic to extragalactic transition”. *Phys. Rev. D* 92.2, p. 021302. arXiv: 1505.01377 [astro-ph.HE].
- Globus, N. et al. (2015b). “UHECR acceleration at GRB internal shocks”. *MNRAS* 451, pp. 751–790. arXiv: 1409.1271 [astro-ph.HE].
- Goldreich, P. and W. H. Julian (1969). “Pulsar Electrodynamics”. *ApJ* 157, pp. 869–+.
- Goldstein, A. et al. (2013). “The BATSE 5B Gamma-Ray Burst Spectral Catalog”. *ApJS* 208, p. 21. arXiv: 1311.7135 [astro-ph.HE].
- Goodenough, Lisa and Dan Hooper (2009). “Possible Evidence For Dark Matter Annihilation In The Inner Milky Way From The Fermi Gamma Ray Space Telescope”. arXiv: 0910.2998 [hep-ph].
- Gould, R. J. (2005). *Electromagnetic Processes*.
- GRAND Collaboration et al. (2018). “The Giant Radio Array for Neutrino Detection (GRAND): Science and Design”. *ArXiv e-prints*. arXiv: 1810.09994 [astro-ph.HE].
- Greisen, Kenneth (1966). “End to the cosmic ray spectrum?” *Phys. Rev. Lett.* 16, pp. 748–750.
- Guépin, C. and K. Kotera (2017). “Can we observe neutrino flares in coincidence with explosive transients?” *A&A* 603, A76. arXiv: 1701.07038 [astro-ph.HE].
- Guépin, C. et al. (2018a). “Pevatron at the Galactic Center: multi-wavelength signatures from millisecond pulsars”. *J. Cosmology Astropart. Phys.* 7, p. 042. arXiv: 1806.03307 [astro-ph.HE].
- Guépin, C. et al. (2018b). “Ultra-high-energy cosmic rays and neutrinos from tidal disruptions by massive black holes”. *A&A* 616, A179. arXiv: 1711.11274 [astro-ph.HE].
- Guépin, C. et al. (2019a). “Geometrical constraints of observing very high energy Earth-skimming neutrinos from space”. *J. Cosmology Astropart. Phys.* 3, p. 021. arXiv: 1812.07596 [astro-ph.IM].
- Guépin, C., B. Cerutti, and K. Kotera (2019b). “Protons from pulsars”.
- Guo, F. et al. (2014). “Formation of Hard Power Laws in the Energetic Particle Spectra Resulting from Relativistic Magnetic Reconnection”. *Physical Review Letters* 113.15, p. 155005. arXiv: 1405.4040 [astro-ph.HE].
- Gurevich, A. V. and I. N. Istomin (1985). “Electron-positron plasma generation in a pulsar magnetosphere”. *Zhurnal Eksperimentalnoi i Teoreticheskoi Fiziki* 89, pp. 3–21.
- Hall Reno, M., J. F. Krizmanic, and T. Venters (2018). “Cosmogenic tau neutrino detection via Cherenkov signals from air showers from Earth-emerging taus”. *in preparation*.
- Halzen, F. and S. R. Klein (2010). “Invited Review Article: IceCube: An instrument for neutrino astronomy”. *Review of Scientific Instruments* 81.8, pp. 081101–081101. arXiv: 1007.1247 [astro-ph.HE].
- Halzen, F. and D. Saltzberg (1998). “Tau Neutrino Appearance with a 1000 Megaparsec Baseline”. *Physical Review Letters* 81, pp. 4305–4308. eprint: hep-ph/9804354.
- Hasan, I. et al. (2013). “Latest OIR Mags of PKS 1424-41”. *The Astronomer’s Telegram* 4775.
- He, H.-N. et al. (2012). “Icecube Nondetection of Gamma-Ray Bursts: Constraints on the Fireball Properties”. *ApJ* 752, p. 29. arXiv: 1204.0857 [astro-ph.HE].
- HESS Collaboration et al. (2016). “Acceleration of petaelectronvolt protons in the Galactic Centre”. *Nature* 531, pp. 476–479. arXiv: 1603.07730 [astro-ph.HE].
- Hill, C. T. and D. N. Schramm (1985). “Ultrahigh-energy cosmic-ray spectrum”. *Phys. Rev. D* 31, pp. 564–580.
- Hillas, A. M. (1984). “The Origin of Ultra-High-Energy Cosmic Rays”. *ARA&A* 22, pp. 425–444.
- Hills, J. G. (1975). “Possible power source of Seyfert galaxies and QSOs”. *Nature* 254, pp. 295–298.
- Hjorth, J. and J. S. Bloom (2012). *The Gamma-Ray Burst - Supernova Connection*.

- Hooper, D. and T. Linden (2017). “Measuring the Local Diffusion Coefficient with H.E.S.S. Observations of Very High-Energy Electrons”. *ArXiv e-prints*. arXiv: 1711.07482 [astro-ph.HE].
- (2018). “Millisecond Pulsars, TeV Halos, and Implications For The Galactic Center Gamma-Ray Excess”. *ArXiv e-prints*. arXiv: 1803.08046 [astro-ph.HE].
- Hooper, Dan and Tracy R. Slatyer (2013). “Two Emission Mechanisms in the Fermi Bubbles: A Possible Signal of Annihilating Dark Matter”. *Phys. Dark Univ.* 2, pp. 118–138. arXiv: 1302.6589 [astro-ph.HE].
- Hopkins, P. F., G. T. Richards, and L. Hernquist (2007). “An Observational Determination of the Bolometric Quasar Luminosity Function”. *ApJ* 654, pp. 731–753. eprint: astro-ph/0605678.
- Hörandel, J. R., N. N. Kalmykov, and A. V. Timokhin (2007). “Propagation of super-high-energy cosmic rays in the Galaxy”. *Astroparticle Physics* 27, pp. 119–126. eprint: astro-ph/0609490.
- Horns, D. et al. (2010). “Chandra follow-up observation of the Crab nebula after the high energy flare”. *The Astronomer’s Telegram* 3058.
- Hoshino, M. and Y. Lyubarsky (2012). “Relativistic Reconnection and Particle Acceleration”. *Space Sci. Rev.* 173, pp. 521–533.
- Hovatta, T. et al. (2009). “Doppler factors, Lorentz factors and viewing angles for quasars, BL Lacertae objects and radio galaxies”. *A&A* 494, pp. 527–537. arXiv: 0811.4278.
- Huege, Tim (2016). “Radio detection of cosmic ray air showers in the digital era”. *Phys. Rep.* 620, pp. 1–52. arXiv: 1601.07426 [astro-ph.IM].
- Hurley, K. et al. (2004). “IPN localization of giant flare from SGR1806-20.” *GRB Coordinates Network* 2921.
- Hurley, K. et al. (2005). “An exceptionally bright flare from SGR 1806-20 and the origins of short-duration γ -ray bursts”. *Nature* 434, pp. 1098–1103. eprint: astro-ph/0502329.
- IceCube Collaboration et al. (2017). “The IceCube Neutrino Observatory - Contributions to ICRC 2017 Part II: Properties of the Atmospheric and Astrophysical Neutrino Flux”. *ArXiv e-prints*. arXiv: 1710.01191 [astro-ph.HE].
- IceCube Collaboration et al. (2018). “Multimessenger observations of a flaring blazar coincident with high-energy neutrino IceCube-170922A”. *Science* 361, eaat1378. arXiv: 1807.08816 [astro-ph.HE].
- Ioka, K. et al. (2005). “TeV-PeV Neutrinos from Giant Flares of Magnetars and the Case of SGR 1806-20”. *ApJ* 633, pp. 1013–1017. eprint: astro-ph/0503279.
- Jackson, J. D. (1975). *Classical electrodynamics*.
- Jauch, J. M. and F. Rohrlich (1976). *The theory of photons and electrons. The relativistic quantum field theory of charged particles with spin one-half*.
- Jorstad, S. G. et al. (2005). “Polarimetric Observations of 15 Active Galactic Nuclei at High Frequencies: Jet Kinematics from Bimonthly Monitoring with the Very Long Baseline Array”. *AJ* 130, pp. 1418–1465. eprint: astro-ph/0502501.
- Kadler, M. et al. (2016). “Coincidence of a high-fluence blazar outburst with a PeV-energy neutrino event”. *Nature Physics* 12, pp. 807–814. arXiv: 1602.02012 [astro-ph.HE].
- Kahn, Franz Daniel, I. Lerche, and Alfred Charles Bernard Lovell (1966). “Radiation from cosmic ray air showers”. *Proceedings of the Royal Society of London. Series A. Mathematical and Physical Sciences* 289.1417, pp. 206–213. eprint: <https://royalsocietypublishing.org/doi/pdf/10.1098/rspa.1966.0007>.
- Kalfountzou, E. et al. (2014). “The largest X-ray-selected sample of $z \lesssim 3$ AGNs: C-COSMOS and ChaMP”. *MNRAS* 445, pp. 1430–1448. arXiv: 1408.6280.
- Kasen, D. and L. Bildsten (2010). “Supernova Light Curves Powered by Young Magnetars”. *ApJ* 717, pp. 245–249. arXiv: 0911.0680 [astro-ph.HE].

- Kashiyama, K. et al. (2013). “High-energy Neutrino and Gamma-Ray Transients from Trans-relativistic Supernova Shock Breakouts”. *ApJL* 769, p. L6. arXiv: 1210.8147 [astro-ph.HE].
- Kashti, T. and E. Waxman (2005). “Astrophysical Neutrinos: Flavor Ratios Depend on Energy”. *Physical Review Letters* 95.18, p. 181101. eprint: astro-ph/0507599.
- Kasliwal, M. M. (2011). “Bridging the gap : elusive explosions in the local universe”. PhD thesis. California Institute of Technology.
- Katz, B., R. Budnik, and E. Waxman (2009). “The energy production rate & the generation spectrum of UHECRs”. *J. Cosmology Astropart. Phys.* 3, p. 020. arXiv: 0811.3759.
- Kelner, S. R., F. A. Aharonian, and V. V. Bugayov (2006). “Energy spectra of gamma rays, electrons, and neutrinos produced at proton-proton interactions in the very high energy regime”. *Phys. Rev. D* 74.3, p. 034018. eprint: astro-ph/0606058.
- Kesden, M. (2012). “Tidal-disruption rate of stars by spinning supermassive black holes”. *Phys. Rev. D* 85.2, p. 024037. arXiv: 1109.6329 [astro-ph.CO].
- Kippenhahn, R. and A. Weigert (1994). *Stellar Structure and Evolution*, p. 192.
- Kirk, J. G. and P. Schneider (1987). “On the acceleration of charged particles at relativistic shock fronts”. *ApJ* 315, pp. 425–433.
- Kirk, J. G. and O. Skjæraasen (2003). “Dissipation in Poynting-Flux-dominated Flows: The σ -Problem of the Crab Pulsar Wind”. *ApJ* 591, pp. 366–379. eprint: astro-ph/0303194.
- Kirk, J. G. et al. (2000). “Particle Acceleration at Ultrarelativistic Shocks: An Eigenfunction Method”. *ApJ* 542, pp. 235–242. eprint: astro-ph/0005222.
- Kirk, J. G., Y. Lyubarsky, and J. Petri (2009). “The Theory of Pulsar Winds and Nebulae”. *Astrophysics and Space Science Library*. Ed. by W. Becker. Vol. 357. Astrophysics and Space Science Library, p. 421. eprint: astro-ph/0703116.
- Kisaka, S. and N. Kawanaka (2012). “TeV cosmic-ray electrons from millisecond pulsars”. *MNRAS* 421, pp. 3543–3549. arXiv: 1112.5312 [astro-ph.HE].
- Klein, A. et al. (2016). “Science with the space-based interferometer eLISA: Supermassive black hole binaries”. *Phys. Rev. D* 93.2, p. 024003. arXiv: 1511.05581 [gr-qc].
- Kneiske, T. M. et al. (2004). “Implications of cosmological gamma-ray absorption. II. Modification of gamma-ray spectra”. *A&A* 413, pp. 807–815. eprint: arXiv:astro-ph/0309141.
- Koers, H. B. J. and R. A. M. J. Wijers (2007). *Enhanced high-energy neutrino emission from choked gamma-ray bursts due to meson and muon acceleration*. arXiv: 0711.4791.
- Kolmogorov, A. (1941). “The Local Structure of Turbulence in Incompressible Viscous Fluid for Very Large Reynolds’ Numbers”. *Akademiia Nauk SSSR Doklady* 30, pp. 301–305.
- Komissarov, S. S. (2013). “Magnetic dissipation in the Crab nebula”. *MNRAS* 428, pp. 2459–2466. arXiv: 1207.3192 [astro-ph.HE].
- Komissarov, S. S. and M. Lyutikov (2011). “On the origin of variable gamma-ray emission from the Crab nebula”. *MNRAS* 414, pp. 2017–2028. arXiv: 1011.1800 [astro-ph.HE].
- Komossa, S. (2015). “Tidal disruption of stars by supermassive black holes: Status of observations”. *Journal of High Energy Astrophysics* 7, pp. 148–157. arXiv: 1505.01093 [astro-ph.HE].
- Koning, A. J., S. Hilaire, and M. C. Duijvestijn (2005). “TALYS: Comprehensive Nuclear Reaction Modeling”. *AIP Conference Proceedings* 769.1, pp. 1154–1159. eprint: <https://aip.scitation.org/doi/pdf/10.1063/1.1945212>.
- Kormendy, J. and L. C. Ho (2013). “Coevolution (Or Not) of Supermassive Black Holes and Host Galaxies”. *ARA&A* 51, pp. 511–653. arXiv: 1304.7762.
- Kotera, K. and A. V. Olinto (2011). “The Astrophysics of Ultrahigh Energy Cosmic Rays”. *ARAA* 49, pp. 119–153. arXiv: 1101.4256 [astro-ph.HE].

- Kotera, K. and J. Silk (2016). “Ultrahigh-energy Cosmic Rays and Black Hole Mergers”. *ApJ Lett.* 823, p. L29. arXiv: 1602.06961 [astro-ph.HE].
- Kotera, K. et al. (2009). “Propagation of Ultrahigh Energy Nuclei in Clusters of Galaxies: Resulting Composition and Secondary Emissions”. *ApJ* 707, pp. 370–386. arXiv: 0907.2433.
- Kotera, K., D. Allard, and A. V. Olinto (2010). “Cosmogenic neutrinos: parameter space and detectability from PeV to ZeV”. *JCAP* 10, p. 013. arXiv: 1009.1382 [astro-ph.HE].
- Kotera, K., E. S. Phinney, and A. V. Olinto (2013). “Signatures of pulsars in the light curves of newly formed supernova remnants”. *MNRAS* 432, pp. 3228–3236. arXiv: 1304.5326 [astro-ph.HE].
- Kotera, K., E. Amato, and P. Blasi (2015). “The fate of ultrahigh energy nuclei in the immediate environment of young fast-rotating pulsars”. *JCAP* 8, p. 026. arXiv: 1503.07907 [astro-ph.HE].
- Krolik, J. H. and T. Piran (2012). “Jets from Tidal Disruptions of Stars by Black Holes”. *ApJ* 749, p. 92. arXiv: 1111.2802 [astro-ph.HE].
- La Franca, F. et al. (2005). “The HELLAS2XMM Survey. VII. The Hard X-Ray Luminosity Function of AGNs up to $z = 4$: More Absorbed AGNs at Low Luminosities and High Redshifts”. *ApJ* 635, pp. 864–879. eprint: astro-ph/0509081.
- Lacy, M. et al. (2015). “The Spitzer Mid-infrared AGN Survey. II. The Demographics and Cosmic Evolution of the AGN Population”. *ApJ* 802, p. 102. arXiv: 1501.04118.
- Lähteenmäki, A. and E. Valtaoja (1999). “Total Flux Density Variations in Extragalactic Radio Sources. III. Doppler Boosting Factors, Lorentz Factors, and Viewing Angles for Active Galactic Nuclei”. *ApJ* 521, pp. 493–501.
- Landau, L. D. and E. M. Lifshitz (1975). *The classical theory of fields*.
- Lauer, T. R. et al. (2007). “Selection Bias in Observing the Cosmological Evolution of the M_* - σ and M_* - L Relationships”. *ApJ* 670, pp. 249–260. arXiv: 0705.4103.
- Lee, Samuel K., Mariangela Lisanti, and Benjamin R. Safdi (2015). “Distinguishing dark matter from unresolved point sources in the Inner Galaxy with photon statistics”. *Journal of Cosmology and Astroparticle Physics* 2015.05, p. 056.
- Lemoine, M. and B. Revenu (2006). “Relativistic Fermi acceleration with shock compressed turbulence”. *MNRAS* 366, pp. 635–644. eprint: astro-ph/0510522.
- Lemoine, M. and E. Waxman (2009). “Anisotropy vs chemical composition at ultra-high energies”. *J. Cosmology Astropart. Phys.* 11, p. 009. arXiv: 0907.1354 [astro-ph.HE].
- Lemoine, M., G. Pelletier, and B. Revenu (2006). “On the Efficiency of Fermi Acceleration at Relativistic Shocks”. *ApJ* 645, pp. L129–L132. eprint: astro-ph/0606005.
- Lemoine, M., K. Kotera, and J. Pétri (2015). “On ultra-high energy cosmic ray acceleration at the termination shock of young pulsar winds”. *J. Cosmology Astropart. Phys.* 7, p. 016. arXiv: 1409.0159 [astro-ph.HE].
- Levan, A. J. et al. (2011). “An Extremely Luminous Panchromatic Outburst from the Nucleus of a Distant Galaxy”. *Science* 333, p. 199. arXiv: 1104.3356 [astro-ph.HE].
- Levin, L. et al. (2013). “The High Time Resolution Universe Pulsar Survey -VIII. The Galactic millisecond pulsar population”. *MNRAS* 434, pp. 1387–1397. arXiv: 1306.4190 [astro-ph.SR].
- Linsley, J. (1963). “Evidence for a Primary Cosmic-Ray Particle with Energy 10^{20} eV”. *Physical Review Letters* 10, pp. 146–148.
- Lodato, G., A. R. King, and J. E. Pringle (2009). “Stellar disruption by a supermassive black hole: is the light curve really proportional to $t^{-5/3}$?” *MNRAS* 392, pp. 332–340. arXiv: 0810.1288.
- Lorimer, D. R. (2004). “The Galactic Population and Birth Rate of Radio Pulsars”. *Symposium - International Astronomical Union* 218, pp. 105–112.

- Lorimer, D. R. (2013). “The Galactic Millisecond Pulsar Population”. *Neutron Stars and Pulsars: Challenges and Opportunities after 80 years*. Ed. by J. van Leeuwen. Vol. 291. IAU Symposium, pp. 237–242. arXiv: 1210.2746.
- Lorimer, D. R. et al. (2015). “The Parkes multibeam pulsar survey - VII. Timing of four millisecond pulsars and the underlying spin-period distribution of the Galactic millisecond pulsar population”. *MNRAS* 450, pp. 2185–2194. arXiv: 1501.05516 [astro-ph.IM].
- Lorimer, Duncan R. (2008). “Binary and Millisecond Pulsars”. *Living Rev. Relativ.* 11. ISSN: 1433-8351.
- Luminet, J.-P. and B. Pichon (1989). “Tidal pinching of white dwarfs”. *A&A* 209, pp. 103–110.
- Lunardini, C. and W. Winter (2016). “High Energy Neutrinos from the Tidal Disruption of Stars”. *ArXiv e-prints*. arXiv: 1612.03160 [astro-ph.HE].
- Lyubarskii, Y. E. (1996). “A model for the energetic emission from pulsars.” *A&A* 311, pp. 172–178.
- Lyubarsky, Y. E. (2005). “On the relativistic magnetic reconnection”. *MNRAS* 358, pp. 113–119. eprint: astro-ph/0501392.
- Lyutikov, M. (2006). “Magnetar giant flares and afterglows as relativistic magnetized explosions”. *MNRAS* 367, pp. 1594–1602. eprint: astro-ph/0511711.
- (2011). “Electromagnetic power of merging and collapsing compact objects”. *Phys. Rev. D* 83.12, p. 124035. arXiv: 1104.1091 [astro-ph.HE].
- Lyutikov, M. and D. Uzdensky (2003). “Dynamics of Relativistic Reconnection”. *ApJ* 589, pp. 893–901. eprint: astro-ph/0210206.
- Madau, Piero and Martin J. Rees (2001). “Massive black holes as Population III remnants”. *Astrophys.J.* 551, pp. L27–L30. arXiv: astro-ph/0101223 [astro-ph].
- Marcowith, A. et al. (2016). “The microphysics of collisionless shock waves”. *Reports on Progress in Physics* 79.4, p. 046901. arXiv: 1604.00318 [astro-ph.HE].
- Margutti, R. et al. (2008). “Temporal variability of GRB early X-ray afterglows and GRB080319B prompt emission”. *American Institute of Physics Conference Series*. Ed. by Y.-F. Huang, Z.-G. Dai, and B. Zhang. Vol. 1065. American Institute of Physics Conference Series, pp. 259–262. arXiv: 0809.0189.
- Margutti, R. et al. (2013). “The Signature of the Central Engine in the Weakest Relativistic Explosions: GRB 100316D”. *ApJ* 778, p. 18. arXiv: 1308.1687 [astro-ph.HE].
- Martineau-Huynh, Olivier et al. (2016). “The Giant Radio Array for Neutrino Detection”. *EPJ Web Conf.* 116, p. 03005. arXiv: 1508.01919 [astro-ph.HE].
- Maximon, LC (1968). “Simple analytic expressions for the total Born approximation cross section for pair production in a Coulomb field”. *J. Res. Nat. Bur. Stand. B* 72, p. 79.
- Mazets, E. et al. (2004). “The giant outburst from Sgr 1806-20.” *GRB Coordinates Network* 2922.
- Medin, Z. and D. Lai (2010). “Pair cascades in the magnetospheres of strongly magnetized neutron stars”. *MNRAS* 406, pp. 1379–1404. arXiv: 1001.2365 [astro-ph.HE].
- Mereghetti, S. (2008). “The strongest cosmic magnets: soft gamma-ray repeaters and anomalous X-ray pulsars”. *The Astronomy and Astrophysics Review* 15, pp. 225–287. arXiv: 0804.0250.
- Merloni, A. and S. Heinz (2008). “A synthesis model for AGN evolution: supermassive black holes growth and feedback modes”. *MNRAS* 388, pp. 1011–1030. arXiv: 0805.2499.
- Mészáros, P. (2015). *Gamma Ray Bursts as Neutrino Sources*. arXiv: 1511.01396 [astro-ph.HE].
- Metzger, B. D. et al. (2014). “Ionization break-out from millisecond pulsar wind nebulae: an X-ray probe of the origin of superluminous supernovae”. *MNRAS* 437, pp. 703–720. arXiv: 1307.8115 [astro-ph.HE].
- Metzger, B. D. et al. (2015). “Gamma-ray novae as probes of relativistic particle acceleration at non-relativistic shocks”. *MNRAS* 450, pp. 2739–2748. arXiv: 1501.05308 [astro-ph.HE].

- Mezger, P. G., W. J. Duschl, and R. Zylka (1996). “The Galactic Center: a laboratory for AGN?” *A&A Rev.* 7, pp. 289–388.
- Michel, F. C. (1973). “Rotating Magnetospheres: an Exact 3-D Solution”. *ApJ* 180, p. L133.
- (1982). “Theory of pulsar magnetospheres”. *Reviews of Modern Physics* 54, pp. 1–66.
- Mills, E. A. C. (2017). “The Milky Way’s Central Molecular Zone”. *ArXiv e-prints*. arXiv: 1705.05332.
- Modjaz, M. (2011). “Stellar forensics with the supernova-GRB connection”. *Astronomische Nachrichten* 332, pp. 434–447. arXiv: 1105.5297.
- Mücke, A. et al. (1999). “Photohadronic processes in astrophysical environments”. *Publications of the Astronomical Society of Australia* 16, pp. 160–6. eprint: arXiv:astro-ph/9808279.
- Mücke, A. et al. (2000). “Monte Carlo simulations of photohadronic processes in astrophysics”. *Computer Physics Communications* 124, pp. 290–314. eprint: astro-ph/9903478.
- Murase, K. (2007). “High energy neutrino early afterglows from gamma-ray bursts revisited”. *Phys. Rev. D* 76.12, pp. 123001–+. arXiv: 0707.1140.
- (2008a). “Astrophysical High-Energy Neutrinos and Gamma-Ray Bursts”. *American Institute of Physics Conference Series*. Ed. by Y.-F. Huang, Z.-G. Dai, and B. Zhang. Vol. 1065. American Institute of Physics Conference Series, pp. 201–206.
- (2008b). “Prompt high-energy neutrinos from gamma-ray bursts in photospheric and synchrotron self-Compton scenarios”. *Phys. Rev. D* 78.10, p. 101302. arXiv: 0807.0919.
- Murase, K. and J. F. Beacom (2010). “Neutrino background flux from sources of ultrahigh-energy cosmic-ray nuclei”. *Phys. Rev. D* 81.12, pp. 123001–+. arXiv: 1003.4959 [astro-ph.HE].
- Murase, K. and K. Ioka (2013). “TeV-PeV Neutrinos from Low-Power Gamma-Ray Burst Jets inside Stars”. *Physical Review Letters* 111.12, p. 121102. arXiv: 1306.2274 [astro-ph.HE].
- Murase, K. and S. Nagataki (2006a). “High energy neutrino emission and neutrino background from gamma-ray bursts in the internal shock model”. *Phys. Rev. D* 73.6, p. 063002. eprint: astro-ph/0512275.
- (2006b). “High Energy Neutrino Flashes from Far-Ultraviolet and X-Ray Flares in Gamma-Ray Bursts”. *Physical Review Letters* 97.5, p. 051101. eprint: astro-ph/0604437.
- Murase, K. and H. Takami (2009). “Implications of Ultra-High-Energy Cosmic Rays for Transient Sources in the Auger Era”. *ApJ* 690, pp. L14–L17. arXiv: 0810.1813.
- Murase, K. et al. (2006). “High-Energy Neutrinos and Cosmic Rays from Low-Luminosity Gamma-Ray Bursts?” *ApJ* 651, pp. L5–L8. eprint: arXiv:astro-ph/0607104.
- (2008). “High-energy cosmic-ray nuclei from high- and low-luminosity gamma-ray bursts and implications for multimessenger astronomy”. *Phys. Rev. D* 78.2, pp. 023005–023027. arXiv: 0801.2861.
- Murase, K., P. Mészáros, and B. Zhang (2009). “Probing the birth of fast rotating magnetars through high-energy neutrinos”. *Phys. Rev. D* 79.10, pp. 103001–103006. arXiv: 0904.2509.
- Murase, K. et al. (2011). “New class of high-energy transients from crashes of supernova ejecta with massive circumstellar material shells”. *Phys. Rev. D* 84.4, p. 043003. arXiv: 1012.2834 [astro-ph.HE].
- Murase, K. et al. (2012). “The Role of Stochastic Acceleration in the Prompt Emission of Gamma-Ray Bursts: Application to Hadronic Injection”. *ApJ* 746, p. 164. arXiv: 1107.5575 [astro-ph.HE].
- Murase, K., K. Kashiyama, and P. Mészáros (2013). “Subphotospheric Neutrinos from Gamma-Ray Bursts: The Role of Neutrons”. *Physical Review Letters* 111.13, p. 131102. arXiv: 1301.4236 [astro-ph.HE].
- Murase, K., Y. Inoue, and C. D. Dermer (2014). “Diffuse neutrino intensity from the inner jets of active galactic nuclei: Impacts of external photon fields and the blazar sequence”. *Phys. Rev. D* 90.2, p. 023007. arXiv: 1403.4089 [astro-ph.HE].

- Murase, K. et al. (2015). “Gammy-Ray and Hard X-Ray Emission from Pulsar-aided Supernovae as a Probe of Particle Acceleration in Embryonic Pulsar Wind Nebulae”. *ApJ* 805, p. 82. arXiv: 1411.0619 [astro-ph.HE].
- Murase, K. et al. (2016). “Ultrafast Outflows from Black Hole Mergers with a Minidisk”. *ApJ* 822, p. L9. arXiv: 1602.06938 [astro-ph.HE].
- Murase, Kohta and Hajime Takami (2009). “Implications of Ultra-High-Energy Cosmic Rays for Transient Sources”. *Proceedings, 31th International Cosmic Ray Conference (ICRC 2009): Lodz, Poland, 2009*, p. 1181.
- Muslimov, A. G. and A. K. Harding (2003). “Extended Acceleration in Slot Gaps and Pulsar High-Energy Emission”. *ApJ* 588, pp. 430–440. eprint: astro-ph/0301023.
- Nakar, E. (2015). “A Unified Picture for Low-luminosity and Long Gamma-Ray Bursts Based on the Extended Progenitor of 11GRB 060218/SN 2006aj”. *ApJ* 807, p. 172. arXiv: 1503.00441 [astro-ph.HE].
- Nakar, E. and T. Piran (2016). *The Observable Signatures of GRB Cocoons*. arXiv: 1610.05362 [astro-ph.HE].
- Nakar, E. and R. Sari (2012). “Relativistic Shock Breakouts—A Variety of Gamma-Ray Flares: From Low-luminosity Gamma-Ray Bursts to Type Ia Supernovae”. *ApJ* 747, p. 88. arXiv: 1106.2556 [astro-ph.HE].
- Nelles, A. et al. (2015). “Measuring a Cherenkov ring in the radio emission from air showers at 110-190 MHz with LOFAR”. *Astroparticle Physics* 65, pp. 11–21. arXiv: 1411.6865 [astro-ph.IM].
- Nemenashi, P., M. Gaylard, and R. Ojha (2013). “Sharp increase of radio flux in flaring blazar PKS 1424-41”. *The Astronomer’s Telegram* 4819.
- Neronov, A. et al. (2016). *Sensitivity of the space-based Cherenkov from Astrophysical Neutrinos Telescope (CHANT)*. arXiv: 1606.03629 [astro-ph.IM].
- Neronov, A. et al. (2017a). “Sensitivity of a proposed space-based Cherenkov astrophysical-neutrino telescope”. *Phys. Rev. D* 95.2, p. 023004. arXiv: 1606.03629 [astro-ph.IM].
- Neronov, A. et al. (2017b). “Sensitivity of a proposed space-based Cherenkov astrophysical-neutrino telescope”. *Phys. Rev. D* 95.2, p. 023004. arXiv: 1606.03629 [astro-ph.IM].
- Ofek, E. O. et al. (2007). “SN 2006gy: An Extremely Luminous Supernova in the Galaxy NGC 1260”. *ApJ Lett.* 659, pp. L13–L16. eprint: astro-ph/0612408.
- Oikonomou, F., K. Murase, and K. Kotera (2014). “Synchrotron pair halo and echo emission from blazars in the cosmic web: application to extreme TeV blazars”. *A&A* 568, A110. arXiv: 1406.6075 [astro-ph.HE].
- Ojha, R. and M. Dutka (2012). “Increased Gamma-ray Activity from the FSRQ PKS 1424-41”. *The Astronomer’s Telegram* 4494.
- Ojha, R. et al. (2013). “Fermi LAT detection of a new gamma-ray flare from the Crab Nebula region”. *The Astronomer’s Telegram* 4855.
- Olinto, A. V. et al. (2017). “POEMMA: Probe Of Extreme Multi-Messenger Astrophysics”. *ArXiv e-prints*. arXiv: 1708.07599 [astro-ph.IM].
- Ostapchenko, S. (2006). “QGSJET-II: results for extensive air showers”. *Nuclear Physics B Proceedings Supplements* 151, pp. 147–150. eprint: astro-ph/0412591.
- Ostapchenko, S. (2011). “Monte Carlo treatment of hadronic interactions in enhanced Pomeron scheme: QGSJET-II model”. *Phys. Rev. D* 83 (1), p. 014018.
- Ostapchenko, S. (2013). “QGSJET-II: physics, recent improvements, and results for air showers”. *European Physical Journal Web of Conferences*. Vol. 52. European Physical Journal Web of Conferences, p. 02001.
- Palmer, D. M. et al. (2005). “A giant γ -ray flare from the magnetar SGR 1806 - 20”. *Nature* 434, pp. 1107–1109. eprint: astro-ph/0503030.

- Parker, E. N. (1963). “The Solar-Flare Phenomenon and the Theory of Reconnection and Annihilation of Magnetic Fields.” *ApJS* 8, p. 177.
- Parkinson, H., S. Cole, and J. Helly (2008). “Generating dark matter halo merger trees”. *MNRAS* 383, pp. 557–564. arXiv: 0708.1382.
- Pétri, J. (2012). “The pulsar force-free magnetosphere linked to its striped wind: time-dependent pseudo-spectral simulations”. *MNRAS* 424, pp. 605–619. arXiv: 1205.0889 [astro-ph.HE].
- (2016). “Theory of pulsar magnetosphere and wind”. *Journal of Plasma Physics* 82.5, p. 635820502. arXiv: 1608.04895 [astro-ph.HE].
- Petropoulou, M. and A. Mastichiadis (2015). “Bethe-Heitler emission in BL Lacs: filling the gap between X-rays and γ -rays”. *MNRAS* 447, pp. 36–48. arXiv: 1411.1908 [astro-ph.HE].
- Petropoulou, M. et al. (2016a). *The many faces of blazar emission in the context of hadronic models*. arXiv: 1601.06010 [astro-ph.HE].
- Petropoulou, M., G. Vasilopoulos, and D. Giannios (2016b). *The TeV emission of Ap Librae: a hadronic interpretation and prospects for CTA*. arXiv: 1608.07300 [astro-ph.HE].
- Petropoulou, M., S. Coenders, and S. Dimitrakoudis (2016c). “Time-dependent neutrino emission from Mrk 421 during flares and predictions for IceCube”. *Astroparticle Physics* 80, pp. 115–130. arXiv: 1603.06954 [astro-ph.HE].
- Petrović, J., P. D. Serpico, and G. Zaharijas (2015). “Millisecond pulsars and the Galactic Center gamma-ray excess: the importance of luminosity function and secondary emission”. *J. Cosmology Astropart. Phys.* 2, p. 023. arXiv: 1411.2980 [astro-ph.HE].
- Petrović, Jovana, Pasquale Dario Serpico, and Gabriella Zaharijaš (2014). “Galactic Center gamma-ray ”excess” from an active past of the Galactic Centre?” *JCAP* 1410.10, p. 052. arXiv: 1405.7928 [astro-ph.HE].
- Petschek, H. E. (1964). “Magnetic Field Annihilation”. *NASA Special Publication* 50, p. 425.
- Pfeffer, D. N., E. D. Kovetz, and M. Kamionkowski (2015). *Ultra-high-energy-cosmic-ray hot spots from tidal disruption events*. arXiv: 1512.04959 [astro-ph.HE].
- Philippov, A. A. and A. Spitkovsky (2014). “Ab Initio Pulsar Magnetosphere: Three-dimensional Particle-in-cell Simulations of Axisymmetric Pulsars”. *ApJ* 785, p. L33. arXiv: 1312.4970 [astro-ph.HE].
- (2018). “Ab-initio Pulsar Magnetosphere: Particle Acceleration in Oblique Rotators and High-energy Emission Modeling”. *ApJ* 855, p. 94. arXiv: 1707.04323 [astro-ph.HE].
- Philippov, A. A., A. Spitkovsky, and B. Cerutti (2015). “Ab Initio Pulsar Magnetosphere: Three-dimensional Particle-in-cell Simulations of Oblique Pulsars”. *ApJ* 801, p. L19. arXiv: 1412.0673 [astro-ph.HE].
- Phinney, E. S. (1989). “Manifestations of a Massive Black Hole in the Galactic Center”. *The Center of the Galaxy*. Ed. by M. Morris. Vol. 136. IAU Symposium, p. 543.
- Pierog, T. et al. (2013). “EPOS LHC : test of collective hadronization with LHC data”. *ArXiv e-prints*. arXiv: 1306.0121 [hep-ph].
- Pierog, T. et al. (2015a). “EPOS LHC: Test of collective hadronization with data measured at the CERN Large Hadron Collider”. *Phys. Rev. C* 92 (3), p. 034906.
- Pierog, T. et al. (2015b). “EPOS LHC: Test of collective hadronization with data measured at the CERN Large Hadron Collider”. *Phys. Rev. C* 92 (3), p. 034906.
- Pierre Auger Collaboration (2015). “The Pierre Auger Cosmic Ray Observatory”. *Nuclear Instruments and Methods in Physics Research A* 798, pp. 172–213.
- Piran, T. (2004). “The physics of gamma-ray bursts”. *Reviews of Modern Physics* 76, pp. 1143–1210. eprint: arXiv:astro-ph/0405503.
- Piran, T., A. Sądowski, and A. Tchekhovskoy (2015). “Jet and disc luminosities in tidal disruption events”. *MNRAS* 453, pp. 157–165. arXiv: 1501.02015 [astro-ph.HE].

- Piro, A. L. and J. A. Kollmeier (2016). “Ultrahigh-energy Cosmic Rays from the ”En Caul” Birth of Magnetars”. *ApJ* 826, p. 97. arXiv: 1601.02625 [astro-ph.HE].
- Ploeg, H. et al. (2017). “Consistency between the luminosity function of resolved millisecond pulsars and the galactic center excess”. *J. Cosmology Astropart. Phys.* 8, p. 015. arXiv: 1705.00806 [astro-ph.HE].
- Porth, O., S. S. Komissarov, and R. Keppens (2013). “Solution to the sigma problem of pulsar wind nebulae”. *MNRAS* 431, pp. L48–L52. arXiv: 1212.1382 [astro-ph.HE].
- Press, W. H. and P. Schechter (1974). “Formation of Galaxies and Clusters of Galaxies by Self-Similar Gravitational Condensation”. *ApJ* 187, pp. 425–438.
- Press, William H. et al. (1992). *Numerical Recipes in C (2Nd Ed.): The Art of Scientific Computing*. New York, NY, USA: Cambridge University Press. ISBN: 0-521-43108-5.
- Pritchett, P. L. (2003). “Particle-in-Cell Simulation of Plasmas - A Tutorial”. *Space Plasma Simulation*. Ed. by J. Büchner, C. Dum, and M. Scholer. Vol. 615. Lecture Notes in Physics, Berlin Springer Verlag, pp. 1–24.
- Protheroe, R. J. (2002). “Factors Determining Variability Time in Active Galactic Nucleus Jets”. *PASA* 19, pp. 486–498. eprint: astro-ph/0209111.
- Puget, J. L., F. W. Stecker, and J. H. Bredekamp (1976). “Photonuclear interactions of ultrahigh energy cosmic rays and their astrophysical consequences”. *ApJ* 205, pp. 638–654.
- Quimby, R. M. (2012). “Superluminous Supernovae”. *IAU Symposium*. Vol. 279. IAU Symposium, pp. 22–28.
- Quimby, R. M. et al. (2011). “Hydrogen-poor superluminous stellar explosions”. *Nature* 474, pp. 487–489. arXiv: 0910.0059 [astro-ph.CO].
- Rachen, J. P. (1996). “Interaction processes and statistical properties of the propagation of cosmic-rays in photon backgrounds”. PhD thesis. Bonn University.
- Rachen, J. P. and P. Mészáros (1998). “Photohadronic neutrinos from transients in astrophysical sources”. *Phys. Rev. D* 58.12, pp. 123005–+. eprint: arXiv:astro-ph/9802280.
- Racusin, J. L. et al. (2008a). “Broadband observations of the naked-eye γ -ray burst GRB080319B”. *Nature* 455, pp. 183–188. arXiv: 0805.1557.
- Racusin, J. L. et al. (2008b). “GRB 080319B: Swift detection of an intense burst with a bright optical counterpart.” *GRB Coordinates Network* 7427.
- Razzaque, S., P. Mészáros, and E. Waxman (2006). “Enhancement of the ν_e flux from astrophysical sources by two-photon annihilation interactions”. *Phys. Rev. D* 73.10, p. 103005. eprint: astro-ph/0509186.
- Readhead, A. C. S. (1994). “Equipartition brightness temperature and the inverse Compton catastrophe”. *ApJ* 426, pp. 51–59.
- Reynolds, C. S. (2013). “The spin of supermassive black holes”. *Classical and Quantum Gravity* 30.24, p. 244004. arXiv: 1307.3246 [astro-ph.HE].
- Riehn, Felix et al. (2015). “A new version of the event generator Sibyll”. *arXiv e-prints*, arXiv:1510.00568. arXiv: 1510.00568 [hep-ph].
- Romani, R. W. (1996). “Gamma-Ray Pulsars: Radiation Processes in the Outer Magnetosphere”. *ApJ* 470, p. 469.
- Ruderman, M. A. and P. G. Sutherland (1975). “Theory of pulsars - Polar caps, sparks, and coherent microwave radiation”. *ApJ* 196, pp. 51–72.
- Rybicki, G. B. and A. P. Lightman (1979). *Radiative processes in astrophysics*.
- Salafia, O. S. et al. (2016). “Light curves and spectra from off-axis gamma-ray bursts”. *MNRAS* 461, pp. 3607–3619. arXiv: 1601.03735 [astro-ph.HE].

- Scharlemann, E. T. and R. V. Wagoner (1973). “Aligned Rotating Magnetospheres. General Analysis”. *ApJ* 182, pp. 951–960.
- Schoorlemmer, Harm (2012). “Tuning in on cosmic rays. Polarization of radio signals from air showers as a probe of emission mechanisms”. PhD thesis. Nijmegen U.
- Schulze, A. et al. (2015). “The cosmic growth of the active black hole population at $1 < z < 2$ in zCOSMOS, VVDS and SDSS”. *MNRAS* 447, pp. 2085–2111. arXiv: 1412.0754.
- Seifina, E., L. Titarchuk, and E. Virgili (2017). “Swift J164449.3+573451 and Swift J2058.4+0516: Black hole mass estimates for tidal disruption event sources”. *A&A* 607, A38. arXiv: 1707.05898.
- Senno, N., K. Murase, and P. Mészáros (2016a). “Choked jets and low-luminosity gamma-ray bursts as hidden neutrino sources”. *Phys. Rev. D* 93.8, p. 083003. arXiv: 1512.08513 [astro-ph.HE].
- Senno, N., K. Murase, and P. Meszaros (2016b). *High-energy neutrino flashes from x-ray bright and dark tidal disruptions events*. arXiv: 1612.00918 [astro-ph.HE].
- Sesana, A. et al. (2014). “Linking the Spin Evolution of Massive Black Holes to Galaxy Kinematics”. *ApJ* 794, p. 104. arXiv: 1402.7088.
- Shankar, F. (2013). “Black hole demography: from scaling relations to models”. *Classical and Quantum Gravity* 30.24, p. 244001. arXiv: 1307.3289.
- Shapiro, S. L. and S. A. Teukolsky (1986). *Black Holes, White Dwarfs and Neutron Stars: The Physics of Compact Objects*, p. 672.
- Sikora, M. et al. (1987). “Electron injection by relativistic protons in active galactic nuclei”. *ApJ Lett.* 320, pp. L81–L85.
- Singer, L. P. et al. (2016). “IceCube-160427A: iPTF Observations.” *GRB Coordinates Network* 19392.
- Sironi, L. and A. Spitkovsky (2011). “Acceleration of Particles at the Termination Shock of a Relativistic Striped Wind”. *ApJ* 741, p. 39. arXiv: 1107.0977 [astro-ph.HE].
- Sironi, L. and A. Spitkovsky (2014). “Relativistic Reconnection: An Efficient Source of Non-thermal Particles”. *ApJ* 783, p. L21. arXiv: 1401.5471 [astro-ph.HE].
- Sironi, L., A. Spitkovsky, and J. Arons (2013). “The Maximum Energy of Accelerated Particles in Relativistic Collisionless Shocks”. *ApJ* 771, p. 54. arXiv: 1301.5333 [astro-ph.HE].
- Sironi, L., M. Petropoulou, and D. Giannios (2015). “Relativistic jets shine through shocks or magnetic reconnection?” *MNRAS* 450, pp. 183–191. arXiv: 1502.01021 [astro-ph.HE].
- Smartt, S. et al. (2016). “ICECUBE-160427A : Pan-STARRS imaging and optical transients in the field.” *GRB Coordinates Network* 19381.
- Smith, M. W. E. et al. (2013). “The Astrophysical Multimessenger Observatory Network (AMON)”. *Astroparticle Physics* 45, pp. 56–70. arXiv: 1211.5602 [astro-ph.HE].
- Soderberg, A. M. et al. (2006). “Relativistic ejecta from X-ray flash XRF 060218 and the rate of cosmic explosions”. *Nature* 442, pp. 1014–1017. eprint: astro-ph/0604389.
- Spitkovsky, A. (2006). “Time-dependent Force-free Pulsar Magnetospheres: Axisymmetric and Oblique Rotators”. *ApJ* 648, pp. L51–L54. eprint: astro-ph/0603147.
- Spitkovsky, A (2008). “Particle Acceleration in Relativistic Collisionless Shocks: Fermi Process at Last?” *ApJl* 682, pp. L5–L8. arXiv: 0802.3216.
- Starling, R. L. C. et al. (2011). “Discovery of the nearby long, soft GRB 100316D with an associated supernova”. *MNRAS* 411, pp. 2792–2803. arXiv: 1004.2919 [astro-ph.CO].
- Stecker, F. W., M. A. Malkan, and S. T. Scully (2006). “Intergalactic Photon Spectra from the Far-IR to the UV Lyman Limit for $0 < z < 6$ and the Optical Depth of the Universe to High-Energy Gamma Rays”. *ApJ* 648, pp. 774–783. eprint: astro-ph/0510449.
- Story, S. A., P. L. Gonthier, and A. K. Harding (2007). “Population Synthesis of Radio and γ -Ray Millisecond Pulsars from the Galactic Disk”. *ApJ* 671, pp. 713–726. arXiv: 0706.3041.

- Striani, E. et al. (2011). “The Crab Nebula Super-flare in 2011 April: Extremely Fast Particle Acceleration and Gamma-Ray Emission”. *ApJ* 741, p. L5. arXiv: 1105.5028 [astro-ph.HE].
- Strong, A. W. and I. V. Moskalenko (1998). “Propagation of Cosmic-Ray Nucleons in the Galaxy”. *ApJ* 509, pp. 212–228. eprint: astro-ph/9807150.
- Sun, H., B. Zhang, and Z. Li (2015). “Extragalactic High-energy Transients: Event Rate Densities and Luminosity Functions”. *ApJ* 812, p. 33. arXiv: 1509.01592 [astro-ph.HE].
- Suzuki, D. et al. (2011). “GRB 110328A: a second trigger, probably a hard X-ray transient (Swift J164449.3+573451).” *GRB Coordinates Network* 11824.
- Sweet, P. A. (1958). “The Neutral Point Theory of Solar Flares”. *Electromagnetic Phenomena in Cosmical Physics*. Ed. by B. Lehnert. Vol. 6. IAU Symposium, p. 123.
- Tajima, T. and J. M. Dawson (1979). “Laser electron accelerator”. *Physical Review Letters* 43, pp. 267–+.
- Tamborra, I. and S. Ando (2016). “Inspecting the supernova-gamma-ray-burst connection with high-energy neutrinos”. *Phys. Rev. D* 93.5, p. 053010. arXiv: 1512.01559 [astro-ph.HE].
- Tamburini, M. et al. (2010). “Radiation reaction effects on radiation pressure acceleration”. *New Journal of Physics* 12.12, p. 123005. arXiv: 1008.1685 [physics.plasm-ph].
- Tanabashi, M. et al. (2018). “Review of Particle Physics*”. *Phys. Rev. D* 98.3, p. 030001.
- Tavani, M. et al. (2010). “AGILE detection of enhanced gamma-ray emission from the Crab Nebula region”. *The Astronomer’s Telegram* 2855.
- Tavani, M. et al. (2011). “Discovery of Powerful Gamma-Ray Flares from the Crab Nebula”. *Science* 331, p. 736. arXiv: 1101.2311 [astro-ph.HE].
- Tennant, A. et al. (2010). “Chandra observation of the Crab Nebula/PSR following the September 2010 gamma-ray flare.” *The Astronomer’s Telegram* 2882.
- Terasawa, T. et al. (2005). “Repeated injections of energy in the first 600ms of the giant flare of SGR1806 - 20”. *Nature* 434, pp. 1110–1111. eprint: astro-ph/0502315.
- The IceCube-Gen2 Collaboration et al. (2015). *IceCube-Gen2 - The Next Generation Neutrino Observatory at the South Pole: Contributions to ICRC 2015*. arXiv: 1510.05228 [astro-ph.IM].
- The Pierre Auger Collaboration et al. (2015). “The Pierre Auger Observatory: Contributions to the 34th International Cosmic Ray Conference (ICRC 2015)”. *ArXiv e-prints*. arXiv: 1509.03732 [astro-ph.HE].
- The Pierre Auger Collaboration et al. (2017). “Inferences on Mass Composition and Tests of Hadronic Interactions from 0.3 to 100 EeV using the water-Cherenkov Detectors of the Pierre Auger Observatory”. *Phys. Rev. D* 96, p. 122003. arXiv: 1710.07249 [astro-ph.HE].
- Timokhin, A. N. (2007). “Force-free magnetosphere of an aligned rotator with differential rotation of open magnetic field lines”. *Ap&SS* 308, pp. 575–579. arXiv: astro-ph/0607165 [astro-ph].
- (2010). “Time-dependent pair cascades in magnetospheres of neutron stars - I. Dynamics of the polar cap cascade with no particle supply from the neutron star surface”. *MNRAS* 408, pp. 2092–2114. arXiv: 1006.2384 [astro-ph.HE].
- Timokhin, A. N. and J. Arons (2013). “Current flow and pair creation at low altitude in rotation-powered pulsars’ force-free magnetospheres: space charge limited flow”. *MNRAS* 429, pp. 20–54. arXiv: 1206.5819 [astro-ph.HE].
- Timokhin, A. N. and A. K. Harding (2018). “On the maximum pair multiplicity of pulsar cascades”. *arXiv e-prints*. arXiv: 1803.08924 [astro-ph.HE].
- Turolla, R., S. Zane, and A. L. Watts (2015). “Magnetars: the physics behind observations. A review”. *Reports on Progress in Physics* 78.11, p. 116901. arXiv: 1507.02924 [astro-ph.HE].
- Urry, C. M. and P. Padovani (1995). “Unified Schemes for Radio-Loud Active Galactic Nuclei”. *PASP* 107, p. 803. eprint: astro-ph/9506063.

- Uzdensky, D. A. (2011). “Magnetic Reconnection in Extreme Astrophysical Environments”. *Space Science Reviews* 160, pp. 45–71. arXiv: 1101.2472 [astro-ph.HE].
- (2016). “Radiative Magnetic Reconnection in Astrophysics”. *Astrophysics and Space Science Library*. Ed. by W. Gonzalez and E. Parker. Vol. 427. Astrophysics and Space Science Library, p. 473. arXiv: 1510.05397 [astro-ph.HE].
- van Eldik, C. (2015). “Gamma rays from the Galactic Centre region: A review”. *Astroparticle Physics* 71, pp. 45–70. arXiv: 1505.06055 [astro-ph.HE].
- Vanthieghem, A., M. Lemoine, and L. Gremillet (2018). “Stability analysis of a periodic system of relativistic current filaments”. *Physics of Plasmas* 25.7, p. 072115. arXiv: 1804.04429 [physics.plasm-ph].
- Venkatesan, A., M. Coleman Miller, and A. V. Olinto (1997). “Constraints on the Production of Ultra-High-Energy Cosmic Rays by Isolated Neutron Stars”. *ApJ* 484, pp. 323–328. eprint: astro-ph/9612210.
- Venter, C. et al. (2015). “The contribution of millisecond pulsars to the Galactic cosmic-ray lepton spectrum”. *Advances in Space Research* 55, pp. 1529–1536. arXiv: 1410.6462 [astro-ph.HE].
- Verbiest, J. P. W. et al. (2016). “The International Pulsar Timing Array: First data release”. *MNRAS* 458, pp. 1267–1288. arXiv: 1602.03640 [astro-ph.IM].
- Vergani, S. D. et al. (2010). “GRB 100316D: VLT/X-shooter observations.” *GRB Coordinates Network* 10512.
- VERITAS Collaboration et al. (2011). “Detection of Pulsed Gamma Rays Above 100 GeV from the Crab Pulsar”. *Science* 334, p. 69. arXiv: 1108.3797 [astro-ph.HE].
- Verrecchia, F. et al. (2013). “After a gamma-ray flare, AGILE detects the Crab Nebula returning to the normal flux level”. *The Astronomer’s Telegram* 5506.
- Virgili, F. J., E.-W. Liang, and B. Zhang (2009). “Low-luminosity gamma-ray bursts as a distinct GRB population: a firmer case from multiple criteria constraints”. *MNRAS* 392, pp. 91–103. arXiv: 0801.4751.
- Volonteri, M., G. Lodato, and P. Natarajan (2008). “The evolution of massive black hole seeds”. *MNRAS* 383, pp. 1079–1088. arXiv: 0709.0529.
- Vreeswijk, P. M. et al. (2008). “VLT/UVES redshift of GRB 080319B from FeII fine-structure lines.” *GRB Coordinates Network* 7451.
- Wang, J. and D. Merritt (2004). “Revised Rates of Stellar Disruption in Galactic Nuclei”. *ApJ* 600, pp. 149–161. eprint: astro-ph/0305493.
- Wang, W., Z. J. Jiang, and K. S. Cheng (2005). “Contribution to diffuse gamma-rays in the Galactic Centre region from unresolved millisecond pulsars”. *MNRAS* 358, pp. 263–269. eprint: astro-ph/0501245.
- Wang, X.-Y. and R.-Y. Liu (2016). “Tidal disruption jets of supermassive black holes as hidden sources of cosmic rays: Explaining the IceCube TeV-PeV neutrinos”. *Phys. Rev. D* 93.8, p. 083005. arXiv: 1512.08596 [astro-ph.HE].
- Wang, X.-Y., S. Razzaque, and P. Mészáros (2008). “On the Origin and Survival of Ultra-High-Energy Cosmic-Ray Nuclei in Gamma-Ray Bursts and Hypernovae”. *ApJ* 677, pp. 432–440. arXiv: 0711.2065.
- Wang, X.-Y. et al. (2011). “Probing the tidal disruption flares of massive black holes with high-energy neutrinos”. *Phys. Rev. D* 84.8, p. 081301. arXiv: 1106.2426 [astro-ph.HE].
- Waxman, E. and J. Bahcall (1997). “High Energy Neutrinos from Cosmological Gamma-Ray Burst Fireballs”. *Physical Review Letters* 78, pp. 2292–2295. eprint: astro-ph/9701231.
- (1999). “High energy neutrinos from astrophysical sources: An upper bound”. *Phys. Rev. D* 59.2, pp. 023002–023010. eprint: arXiv:hep-ph/9807282.
- Waxman, E. and J. N. Bahcall (2000). “Neutrino Afterglow from Gamma-Ray Bursts: 10^{18} eV”. *ApJ* 541, pp. 707–711. eprint: arXiv:hep-ph/9909286.

- Weisskopf, M. C. et al. (2013). “Chandra, Keck, and VLA Observations of the Crab Nebula during the 2011-April Gamma-Ray Flare”. *ApJ* 765, p. 56. arXiv: 1211.3997 [astro-ph.HE].
- Werner, G. R. et al. (2016). “The Extent of Power-law Energy Spectra in Collisionless Relativistic Magnetic Reconnection in Pair Plasmas”. *ApJ* 816, p. L8. arXiv: 1409.8262 [astro-ph.HE].
- Werner, G. R. et al. (2018). “Non-thermal particle acceleration in collisionless relativistic electron-proton reconnection”. *MNRAS* 473, pp. 4840–4861. arXiv: 1612.04493 [astro-ph.HE].
- Werner, K., F.-M. Liu, and T. Pierog (2006). “Parton ladder splitting and the rapidity dependence of transverse momentum spectra in deuteron-gold collisions at the BNL Relativistic Heavy Ion Collider”. *Physical Review C* 74.4, pp. 044902–+. eprint: arXiv:hep-ph/0506232.
- Wiersema, K. et al. (2010). “GRB 100316D: possible supernova.” *GRB Coordinates Network* 10525.
- Winter, W., J. Becker Tjus, and S. R. Klein (2014). “Impact of secondary acceleration on the neutrino spectra in gamma-ray bursts”. *A&A* 569, A58. arXiv: 1403.0574 [astro-ph.HE].
- Woods, P. M. and C. Thompson (2006). “Soft gamma repeaters and anomalous X-ray pulsars: magnetar candidates”. *Compact stellar X-ray sources*. In: Compact stellar X-ray sources. Edited by Walter Lewin & Michiel van der Klis. Cambridge Astrophysics Series, No. 39. Cambridge, UK: Cambridge University Press, ISBN 978-0-521-82659-4, pp. 547–586.
- Xiao, D. et al. (2016). “High-energy Neutrino Emission from White Dwarf Mergers”. *ApJ* 832, p. 20. arXiv: 1608.08150 [astro-ph.HE].
- Yamada, Masaaki, Russell Kulsrud, and Hantao Ji (2010). “Magnetic reconnection”. *Rev. Mod. Phys.* 82 (1), pp. 603–664.
- Yee, K. (1966). “Numerical solution of initial boundary value problems involving maxwell’s equations in isotropic media”. *IEEE Transactions on Antennas and Propagation* 14, pp. 302–307.
- Yuan, Q. and K. Ioka (2015). “Testing the Millisecond Pulsar Scenario of the Galactic Center Gamma-Ray Excess With Very High Energy Gamma-Rays”. *ApJ* 802, p. 124. arXiv: 1411.4363 [astro-ph.HE].
- Zas, E. and Pierre Auger Collaboration (2017). “Searches for neutrino fluxes in the EeV regime with the Pierre Auger Observatory”. *International Cosmic Ray Conference* 35, p. 972.
- Zatsepin, G. T. and V. A. Kuzmin (1966). “Upper limit of the spectrum of cosmic rays”. *JETP Lett.* 4. [Pisma Zh. Eksp. Teor. Fiz.4,114(1966)], pp. 78–80.
- Zhang, B. and A. K. Harding (2000). “Full Polar Cap Cascade Scenario: Gamma-Ray and X-Ray Luminosities from Spin-powered Pulsars”. *ApJ* 532, pp. 1150–1171. eprint: astro-ph/9911028.
- Zhang, B. T. et al. (2017). “High-energy cosmic ray nuclei from tidal disruption events: origin, survival, and implications”. *ArXiv e-prints*. arXiv: 1706.00391 [astro-ph.HE].
- Zoccali, M. and E. Valenti (2016). “The 3D Structure of the Galactic Bulge”. *PASA* 33, e025. arXiv: 1601.02839.
- Zweibel, E. G. and M. Yamada (2009). “Magnetic Reconnection in Astrophysical and Laboratory Plasmas”. *ARAAS* 47, pp. 291–332.

Subject: Chasing the cosmic accelerators with high energy astroparticles

Abstract: The advent of time-domain and multimessenger astronomy opens new perspectives to study the most energetic phenomena of our universe, and understand the mysterious origins of ultra-high-energy cosmic rays (UHECR) and high-energy (HE) neutrinos. Cosmic rays appear as key players in the production of non-thermal and, more generally, multimessenger emissions. In this thesis, we develop several analytical and numerical tools to study the acceleration and interactions of cosmic rays in the vicinity of energetic sources. As HE neutrinos are clear signatures of these processes, we study the detectability of HE neutrino flares from transient sources. We identify two interesting categories of sources, namely pulsars and tidal disruption events. We show with particle-in-cell simulations that pulsars can accelerate high-energy cosmic rays. We demonstrate that a population of millisecond pulsars located in the Galactic bulge can explain the diffuse gamma-ray emission observed by the HESS detector. Moreover, an extragalactic population of tidal disruptions by massive black holes powering relativistic jets can reproduce the spectrum and composition of UHECRs measured by the Auger experiment, but cannot produce the HE neutrinos detected by the IceCube experiment. Finally, we participate to the development of novel techniques that aim at detecting and reconstructing the properties of very-high-energy (VHE) neutrinos and UHECRs, in the context of the POEMMA and GRAND projects.

Sujet : À la poursuite des accélérateurs cosmiques, à l'aide des particules de haute énergie

Résumé : À l'ère de l'astronomie des messagers multiples et des phénomènes transitoires, des perspectives nouvelles s'ouvrent pour l'étude des phénomènes les plus énergétiques de notre univers, et pour dévoiler l'origine mystérieuse des rayons cosmiques d'ultra-haute énergie (RCUHE) et des neutrinos de haute énergie (HE). Les rayons cosmiques sont des particules clés dans la production de rayonnement non thermique et, plus généralement, d'émissions multimessagers. Dans cette thèse, nous développons plusieurs outils analytiques et numériques pour étudier l'accélération et les interactions des rayons cosmiques au sein des sources énergétiques. Les neutrinos HE attestant que de tels phénomènes sont à l'oeuvre, nous étudions le caractère détectable de sursauts de neutrinos provenant de sources éphémères. Nous identifions alors deux catégories de sources intéressantes, les pulsars et les événements de rupture par effet de marée. Nous montrons, avec des simulations particulières, que les pulsars peuvent accélérer des rayons cosmiques. Nous démontrons qu'une population de pulsars milli-secondes situés au centre de notre Galaxie peut expliquer l'émission diffuse en rayons gamma observée par le détecteur HESS. De plus, une population extragalactique d'événements de rupture par effet de marée produisant des jets relativistes peut expliquer le spectre et la composition des RCUHE mesurées par l'expérience Auger, mais ne peut pas produire les neutrinos HE détectés par l'expérience IceCube. Enfin, nous participons au développement de techniques nouvelles visant à détecter et reconstruire les propriétés des neutrinos de très haute énergie et des RCUHE, dans le cadre des projets POEMMA et GRAND.

